Experimental and Numerical Modelling of Intumescent Protected Flooring Cellular Steel Beams Subjected to Extreme Fire Conditions

Hooman Atefi Aghayan

Civil Structural Engineer, BSc, MSc, CEng

Faculty of Art, Design and the Built Environment of

Ulster University

A thesis submitted for the degree of Doctor of Philosophy

December 2017

I confirm that the word count of this thesis is less than 100,000 words

To the loving Memory of My Mother, Mahin Tabrizi

Content

Chapter 1 - Introduction 20

1.1 Background 20

1.2 Objective 23

1.3 Methodolgy 23

1.4 Outline of thesis 25

Chapter 2 - Literature review 27

2.1 Fire engineering 27

2.1.1 Fire engineering approaches 27

2.1.2 Structural fire engineering 28

2.2 Heat transfer 29

2.2.1 Conduction 29

2.2.2 Convection 29

2.2.3 Radiation 30

2.2.4 Energy balance 31

2.2.5 Lumped capacitance method 31

2.3 Steel temperature prediction 32

2.3.1 Section factor 32

2.3.2 Unprotected steel beam temperature - Simplified method 32

2.3.3 Insulated steel beams temperature - Simplified method 33

2.3.4 Numerical methods 34
2.4 Intumescent coating 34
2.5 Perforated beams 35
2.5.1 Fabrication of cellular beams 35
2.5.2 Failure of perforated beams 36
2.6 Experimental and numerical studies of cellular beams at elevated temperatures 38
2.7 Introduction to numerical methods 41
Chapter 3 - Introduction to Finite Element Theories 43
3.1 Introduction 43
3.2 FEA simulation procedure 43
3.3 Linear and non-linear problems 44
3.4 Mesh 46
3.5 Numerical solution methods & techniques 48
3.5.1 Newtown Raphson 48
3.5.2 Artificial damping 50
3.5.3 Heat transfer 52
3.5.4 Riks analysis 52
3.5.5 Eigenvalue buckling 53
Chapter 4 - Cellular composite beam at ambient temperature 55
4.1 Introduction 55
4.2 Test details 55

4.2.1 General arrangements and material properties....56
4.2.2 Boundary conditions and applied loads....56
4.3 Simulation methodlogy....57
4.3.1 Concrete slab....58
4.3.2 Steel beam....61
4.3.3 Analysis type....61
4.3.4 Load and boundary condition....63
4.4 Results....63
4.5 Discussion....68
4.6 Interim summary....70
Chapter 5 - Unloaded thermal perforated beam....72
5.1 Study strategy....73
5.2 Experimental setup....75
5.3 Material properties....78
5.3.1 Thermal properties of steel....78
5.3.2 Intumescent coating material properties....80
5.4 Simulation methodology....83
5.4.1 Analysis type....83
5.4.2 Mesh type....83
5.4.3 Thermal boundary condition....84
5.4.4 Beam and coating interaction....88

5.5 Parametric study....90
5.5.1 Thickness parametric study....91
5.5.2 Thermal boundary conditions parametric study....91
5.6 Results....92
5.6.1 Unprotected beams....93
5.6.2 Beams with 0.8mm coating thickness....96
5.6.3 Beams with 2.1 mm coating thickness....99
5.6.4 Parametric study....102
5.7 Discussion....103
5.8 Interim summary....108
Chapter 6 - Loaded protected cellular composite beam at elevated temperature....110
6.1 Study strategy....111
6.2 Test set up....114
6.2.1 Steel beam specifications....116
6.2.2 Concrete slab....118
6.2.3 Profiled steel sheeting....119
6.2.4 Intumescent coating....120
6.2.5 Loading....122
6.2.6 Temperature measurement....122
6.2.7 Deformation measurement....123
6.3 Simulation methodology....124

6.3.1 Thermal boundary conditions 124
6.3.2 Thermal properties 129
6.3.3 Specific heat and density of intumescent coating 133
6.3.4 Thermal conductivity of intumescent 134
6.3.5 Mechanical properties 138
6.3.6 Mesh 142
6.3.7 Analysis type 142
6.4 Results 144
6.4.1 Thermal analysis results 145
6.4.2 Beam deflection 155
6.5 Discussion 159
6.6 Interim summery 168
Chapter 7 - parametrical study perforated beams 170
7.1 Study strategy 171
7.2 Parametric study 173
7.2.1 Load ratio study 173
7.2.2 Hydrocarbon fire 176
7.3 Results of the load ratio parametric study 178
7.4 Results of the hydrocarbon fire load 181
7.4.1 Thermal analysis results 181
7.4.2 Beam deflection 190

7.5 Discussion 194
7.5.1 Load ratio study 194
7.5.2 Hydrocarbon fire load 196
7.6 Interim summary 199
Chapter 8 - Conclusion 201
8.1 Future works 206
References 208
Appendix A - Validation of ABAQUS heat transfer functions 214
A.1 Introduction 214
A.2 Benchmarck model 214
A.1 Heat Transfer Analysis 216
A.1.1 Finite Difference Method 216
A.1.1 Finite Element Method 225
A.1.2 FORTRAN Subroutine 225
A.3 Numerical results 228
Appendix B - List of publications 230

List of Figures

Figure 1.1-1 Fabrication of perforated beams 21

Figure 2.5-1 Fabrication of perforated beams [24] 36

Figure 2.5-2 Compression strut for web-post buckling calculations [26] 37

Figure 2.6-1 Intumescent pull back effect [30] 39

Figure 3.3-1 FEA following and non-following load 45

Figure 3.3-2: An example of nonlinearity of boundary conditions 46

Figure 3.5-1 Newton-Raphson method 49

Figure 3.5-2 Riks method [48] 53

Figure 4.2-1 Symmetrical composite Cellular Beam [37] 56

Figure 4.2-2 The general experiment setup [51] 57

Figure 4.3-1 Stress-strain relationships of concrete [2] 60

Figure 4.3-2 High density welded shear studs [51] 61

Figure 4.4-1 Comparison between FEA and test results, relation between displacement at the middle of the concrete slab and the total load applied by the hydraulic jack 64

Figure 4.4-2 Deformed beam under a total 376-kN applied load, Riks analysis, horizontal deformation contour plot 65

Figure 4.4-3 Buckling deformation of the beam 66

Figure 4.4-4 Compressive stress before buckling 67

Figure 4.4-5 Tensile stress before buckling 67

Figure 4.5-1 Warren truss bridge with forces - black for no stress, red is compression, blue is tension 69

Figure 4.5-2 Compression and tension struts 70

Figure 5.2-1 Geometry of solid and perforated beams 76
Figure 5.2-2 Location and name of thermocouples 77
Figure 5.2-3 Not-loaded protected perforated beams tested at Ulster University.....78
Figure 5.3-1 Thermal conductivity of steel - BS 5950-8 79
Figure 5.3-2 Specific heat of steel - BS 5950-8 79
Figure 5.3-3 Temperature - time curve, predicted by variable λ approach and measured 82
Figure 5.4-1 Computational mesh.....84
Figure 5.4-2 Thermal interface surface of the numerical models, blue shows insulated and red shows thermal boundary surfaces 85
Figure 5.4-3 The arrangement of the connections between concrete slab and the tested beams 88
Figure 5.4-4 Schematic arrangement of steel and coating interface mesh and integration nodes, red nodes and orange nodes represent steel and intumescent, respectively 89
Figure 5.4-5 Part of centre of web coated by intumescent coating, section view, the coating is shown by red lines 90
Figure 5.4-6 Schematic arrangement of steel and coating interface mesh and integration nodes. Red nodes, blue nodes and orange nodes represent steel, interface and intumescent, respectively 90
Figure 5.5-1 Boundary conditions of the parametric study.....92
Figure 5.6-1 Temperature history of the solid beam - no coating.....94
Figure 5.6-2 Temperature history of the cellular beam - no coating 94
Figure 5.6-3 Temperature contour plot of solid beam - no coating (°C) 95
Figure 5.6-4 Temperature contour plot of the cellular beam - no coating (°C) 95

Figure 5.6-5 Temperature history of the solid beam - 0.8 mm coating 97
Figure 5.6-6 Temperature history of the cellular beam - 0.8 mm coating 97
Figure 5.6-7 Temperature contour plot of the solid beam - 0.8 mm coating (°C) 98
Figure 5.6-8 Temperature contour plot of the cellular beam - 0.8 mm coating (°C) .98
Figure 5.6-9 Temperature history of the solid beam - 2.1 mm coating 100
Figure 5.6-10 Temperature history of the cellular beam - 2.1 mm coating 100
Figure 5.6-11 Temperature contour plot of the solid beam - 2.1 mm coating (°C) .101
Figure 5.6-12 Temperature contour plot of the cellular beam - 2.1 mm coating (°C) 101
Figure 5.6-13 Maximum temperature of thermocouple nodes with different thicknesses 102
Figure 5.6-14 A2 Temperature, parametric thermal boundary condition study 103
Figure 5.7-1 Temperature of web at the centre area of web, 0.8 mm coating 106
Figure 5.7-2 Temperature of web at the centre area of web, 2.1 mm coating 107
Figure 6.1-1 Compression zone between openings, green and blue regions show compression, red and orange regions show tension 113
Figure 6.1-2 Temperature profile of the 0.8 mm coated beam after 60 minutes, (°C) 113
Figure 6.2-1 The combustion chamber in the FireSERT laboratory.....115
Figure 6.2-2 Configurations of cellular steel beams as they are being prepared for the tests.....117
Figure 6.2-3 The schematic geometry of beams used for FEA simulations 118
Figure 6.2-4 Steel decking 120
Figure 6.2-5 Procedure of application of the intumescent coating 121
Figure 6.2-6 Location of thermocouples on CCBs 123

Figure 6.2-7 Thermocouples on protected CCBs.....123
Figure 6.2-8 General arrangements of the jack and LDVTs.....124
Figure 6.3-1 Schematic burner arrangement [74].....126
Figure 6.3-2 Furnace temperature.....127
Figure 6.3-3 Thermal conductivity of concrete - BS 5950-8.....130
Figure 6.3-4 Specific heat of concrete - BS 5950-8.....130
Figure 6.3-5 Thermal conductivity of steel - BS 5950-8.....132
Figure 6.3-6 Specific heat of steel - BS 5950-8.....132
Figure 6.3-7 Temperature difference between FEA and test results.....135
Figure 6.3-8 Conductivity sensitivity study.....137
Figure 6.3-9 Stress strain relation of concrete [2].....139
Figure 6.3-10 Diagrammatic stress–strain relationships for concrete.....140
Figure 6.3-11 Variation of yield strength and elastic modulus against temperature141
Figure 6.3-12 Computational mesh of Beam 3.....142
Figure 6.3-13 Flowchart of the analysis process.....144
Figure 6.4-1 Temperature history of Beam 1, FEA and experiment results....147
Figure 6.4-2 Temperature contour plot of the steel part of Beam 1 (°C).....148
Figure 6.4-3 Temperature history of Beam 2, FEE and experiment results 150
Figure 6.4-4 Temperature contour plot of the steel section of Beam2 (°C).....151
Figure 6.4-5 Temperature history of Beam 3, FEE and experiment results 154
Figure 6.4-6 Temperature contour plot of the steel section of Beam 3 (°C).....154
Figure 6.4-7 Deformation of the mid span of Beam 1, FEA and experiment results 155
Figure 6.4-8 Vertical deformation of Beam 1 at time of 66 minutes.....156

Figure 6.4-9 Deformation of the mid span of Beam 2, FEA and experiment results 157
Figure 6.4-10 Deformation of Beam 2 at time of 66 minutes.....158
Figure 6.4-11 Deformation of the mid span of Beam 3, FEA and experiment results 158
Figure 6.4-12 Deformation of Beam 3 at time of 66 minutes.....159
Figure 6.5-1 Rotated deformation graph of beam 1 - dashed line shows the maximum Y axis value.....161
Figure 6.5-2 Beam deformations – the dashed lines show the critical times.....163
Figure 6.5-3 Critical temperature profiles.....164
Figure 6.5-4 Compression of the beams at the critical time, N/m^2.....165
Figure 6.5-5 Compression contour plots of beams at 20°C, (N/m^2).....166
Figure 6.5-6 Compression stress at the web and between the two openings which failure occurs.....167
Figure 7.1-1 FEA models of beams 173
Figure 7.2-1 Hydrocarbon and standard fire curves.....177
Figure 7.3-1 Velocity of beam deflection, for every other five load ratio velocities 179
Figure 7.3-2 Maximum bottom flange temperature at failure time versus load ratios 181
Figure 7.4-1 Temperature history of beam 1, FEE and test results.....184
Figure 7.4-2 Temperature contour plot of the steel part of the beam 1 (°C) 184
Figure 7.4-3 Temperature history of beam2, FEE and test results.....187
Figure 7.4-4 Temperature contour plot of the steel part of beam 2 (°C) 187
Figure 7.4-5 Temperature history of beam 3 - FEA and test results.....190

Figure 7.4-6 Temperature contour plot of the steel part of beam 3 (°C) 190
Figure 7.4-7 Deformation of the mid span obtained using FEA and experiment-beam 1 191
Figure 7.4-8 Predicted beam deformation in beam1 under celluloses and hydrocarbon fires 191
Figure 7.4-9 Beam 2 FEA and experiment deformation of the mid. span under the applied load 192
Figure 7.4-10 Predicted beam deformation in beam 2 under celluloses and hydrocarbon fires 193
Figure 7.4-11 FEA and experiment deformation of the mid span, Beam 3 193
Figure 7.4-12 Predicted beam deformation in beam 3 under celluloses and hydrocarbon fires 194
Figure 7.5-1 temperature of beam at the time the rate of deformation is increases, °C 196
Figure 7.5-2 temperature of beam at when the beam deformations reaches span/40, °C 197
Figure 7.5-3 Location of node α (red dot).....198
Figure 7.5-4 Compressive stress of node α 198
Figure A.2-1 Square benchmark model 215
Figure A.1-1 Discretisation of the square plate to nine identical squares.....217
Figure A.1-2 A control volume with a node in the centre 217
Figure A.1-3 Schematic for energy balance - control volume of node 5.....218
Figure A.1-4 Schematic for energy balance - control volume of node 6.....219
Figure A.1-5 Schematic for energy balance - control volume of node 12.....219
Figure A.1-6 Schematic for energy balance - control volume of node 11.....220

Figure A.1-7 Schematic for energy balance - control volume of node 13.....220
Figure A.1-8 Schematic for energy balance - control volume of node 14.....221
Figure A.1-9 Schematic for energy balance on control volume of enclosed air.....221
Figure A.1-10 Schematic for radiation heat exchange inside the benchmark void .223
Figure A.1-11 Square void.....226
Figure A.3-1 Square numerical results, heat transferred by radiation and convection inside the void.....229

List of Tables

Table 5.1-1 FEA model specifications.....74

Table 6.2-1 The geometry of the beams used for FEA simulations.....117

Table 6.3-1 Furnace thermocouples location.....127

Table 6.3-2 Interaction properties.....129

Table 6.3-3 Conductivity sensitivity study.....136

Table A.2-1 Thermal properties of the problem.....215

ACKNOWLEDGMENT

First and foremost, I wish to express my sincere gratitude to my supervisor Professor Ali Nadjai for his invaluable guidance and support during this research. Particularly, I would like to thank him for his continuous advice during the time I was working as an Offshore Structural Engineer away from the University of Ulster.

I am also thankful to the research office at the University of Ulster including, the Dean of Faculty of Art, Design and the Built Environment, Professor Ian Montgomery for their support and guidance throughout my time at the university and for supporting my decision to work as an engineer whilst conducting this research. I would also like to acknowledge the University for providing an opportunity to compete for a research publication grant and selecting me as the winner.

My deepest thanks go to my father, Jamal Atefi for his support and friendship throughout life and my brothers Hamid and Shahriyar who have encouraged me during this period.

Finally, my biggest thanks go to my wife, Dr Mina Ya-alimadad, for her truly selfless support and her love and encouragement during the past few years. Without her none of this would have been possible.

I am dedicating this publication to the memory of my beloved mother, Ms Mahin Tabrizi, whose loving memory sustains me still. She was a great teacher and a mathematician and the most caring parent anyone could ever wish for. She taught me to aim high and work hard in life. This PhD is a testament to all she gave me.

ABSTRACT

National regulations require buildings to be stable for a specific period of time in fire. For steel beams, different standards provide limiting temperature tables for different load ratios. Designers must provide adequate fire insulations for steel elements to prevent their temperature from rising above limiting temperatures and hence maintain the stability of buildings. When it comes to perforated beams, no such tables exist. The standards for solid beams do not apply to perforated beams as they behave differently in fire. On a related note, offshore regulations provide a single limiting temperature for all steel members in hydrocarbon fire and do not account for the effect of the applied loads.

This research, experimentally and numerically investigates the behaviour of intumescent-coated perforated composite beams exposed to cellulose and hydrocarbon fires under different load ratios. In doing so, it provides an understanding of the structural and thermal behaviour of coated perforated beams and determines their limiting temperatures for different load ratios in standard fire and their limiting temperatures in hydrocarbon fire.

To begin with, four unloaded perforated and solid beams with different coating thicknesses in standard fire are examined numerically and experimentally. The results establish the influence of openings on the temperature rise of webs and the effectiveness of the coatings in mitigating this effect.

Secondly, the structural performance of a composite perforated beam at room temperature is examined numerically. The Riks and the general static analysis are employed to simulate the local failure of the beam. A finite element model is developed. It is shown that the numerical results are in good agreement with experiments and that the general static analysis is more suitable in simulating the behaviour of beams with local web failure.

Next, three loaded and intumescent protected perforated beams are investigated numerically and experimentally. The numerical models are comprised of heat transfer and structural analyses. To estimate the experimental beam temperature in the model, the coating surface is exposed to a standard fire. The validity of numerical model and its results is established as they agree with the experimental outcomes.

A comprehensive parametric study is then conducted to define the limiting temperature for the three beams mentioned above. The applied load ratios are changed from 10% to 85% of the ultimate load of the beams. It is shown that the limiting temperatures for load ratios below 30% is around 750°C and it reduces to 450°C by increasing the load ratio to 85%.

Finally, protected perforated beams exposed to hydrocarbon fire are modelled. The thermal load of the three beams is altered from standard to hydrocarbon fire. It is shown that the limiting temperature of perforated beams in hydrocarbon fire is slightly higher than that of standard fire. This is considerably higher than current limiting temperatures in offshore regulations. The findings of this research could lead to reductions in costs as well as the weight of offshore facilities.

NOTE OF ACCESS

"I hereby declare that with effect from the date on which the thesis is deposited in Research Student Administration of Ulster University, I permit

1. the Librarian of the University to allow the thesis to be copied in whole or in part without reference to me on the understanding that such authority applies to the provision of single copies made for study purposes or for inclusion within the stock of another library.

2. the thesis to be made available through the Ulster Institutional Repository and/or EThOS under the terms of the Ulster eTheses Deposit Agreement which I have signed.

IT IS A CONDITION OF USE OF THIS THESIS THAT ANYONE WHO CONSULTS IT MUST RECOGNISE THAT THE COPYRIGHT RESTS WITH THE AUTHOR AND THAT NO QUOTATION FROM THE THESIS AND NO INFORMATION DERIVED FROM IT MAY BE PUBLISHED UNLESS THE SOURCE IS PROPERLY ACKNOWLEDGED".

CHAPTER 1 - INTRODUCTION

Chapter 1 provides an introduction to the objectives of this research. The chapter provides a background of the work in Section 1.1 and introduces the main aims of the research in Section 1.2. The chapter then continues by providing the outline of the thesis in Section 1.3.

1.1 BACKGROUND

Perforated beams, also known as cellular beams, have become popular amongst designers of steel structures. Cellular beams are normally fabricated by cutting the web of a beam along its length and welding its top and bottom tee sections (see Figure 1.1-1). An advantage of cellular beams is that they achieve a higher bending capacity in comparison with their parent sections. Additionally, they provide access for services such as pipes and cables to pass through the beam openings. Passing services through the openings reduces the height of floors, which is a crucial parameter in the design of high-rise buildings.

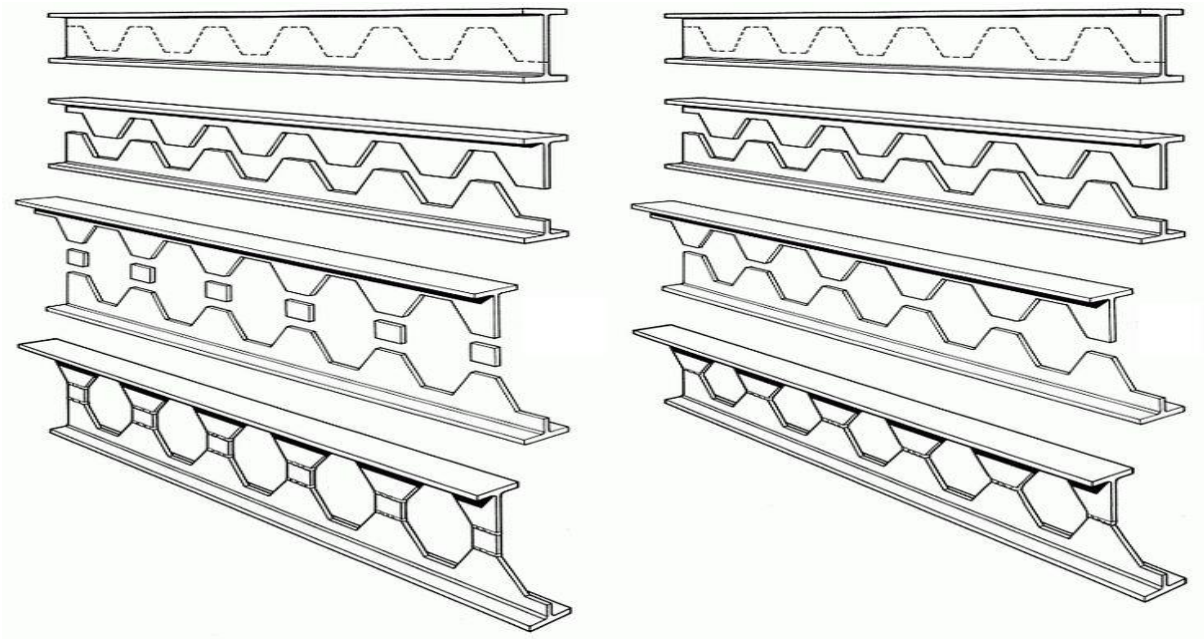

Figure 1.1-1 Fabrication of perforated beams

Similar to any steel members, cellular beams are susceptible to high temperatures. The rise in the temperature of steel in fire causes it to lose its strength and stiffness, until they are no longer able to carry loads. Codes and regulations have forced designers to design structures that maintain their stability for specific periods of time. For instance, residential buildings with more than 5 floors are required to resist against fire for 60 minutes in accordance with The Building Regulations 2010 [1]. This means achieving 60 minutes performance in a standard fire test.

Fire temperature in buildings raises to 900°C after 30 minutes, this temperature is enough to degrade the steel strength and stiffness by 70% [2]. This means that most steel members within structures in fire are not able to carry the design loads at room temperature. Therefore, designers are required to provide fire insulation to create a barrier between steel and fire and delay the temperature rise of steel structures for a required time. There are several types of insulation solutions available for this purpose. Examples include gypsum boards, fire blankets, cement spires, and intumescent coating.

Intumescent coating has become one of the most popular solutions due its advantages such as ease of application, maintenance, favourable appearances for the exposed section, etc. [3]. Intumescent coating is an epoxy based material. When exposed to fire temperature, due to a chain of chemical reactions, it starts to swell and expand between 7 to 20 times of its original thickness, depending on its components [4]. The expanded char is a porous media, which has a very low conductivity. The conductivity of intumescent coating is a function of its material component and its dried thickness. This research is focused on the behaviour of perforated beams coated with intumescent coating during fire.

Designers are required to specify adequate fire protection such as type and thickness of the intumescent coating to keep the structure stable for a required time. In order to specify fire protection systems, it is required to determine the maximum allowable (limiting) temperature i.e. the temperature above which steel members are not able to carry design loads. The allowable steel temperature is provided for different codes and practices such as Table 8 of BS 5950-8 [5]. This standard provides a limiting temperature table that indicates the maximum allowable temperature of different steel structure members. However, this limiting temperature is only provided for solid members. This is because introducing openings to the web, changes the behaviour of beams at temperatures higher than room temperatures. Additionally, due to lack of reliable information on the behaviour of perforated beams at elevated temperatures, no such table of limiting temperatures exists for intumescent coated perforated beams. Moreover, all existing research works have been conducted on perforated beams is based on cellulose fire (standard fire curve). However, perforated beams can be exposed to different types of fire with different temperatures and temperature rise rates such as hydrocarbon fire temperatures in offshore platforms. There is no guideline, codes or standard for design of perforated beams against hydrocarbon fire. The ultimate aim of this research is to narrow down this gap in the current codes and

practices by conducting experimental and numerical investigations and understanding the thermal and structural performance of composite fire protected perforated beams in the event of cellulose and hydrocarbon fires.

In doing so, the project aims to develop a numerical method based on experimental outcomes to predict the thermal and structural performance of intumescent protected composite cellular beams at elevated temperatures.

1.2 OBJECTIVE

The objectives of the present work are:

- To investigate the thermal behaviour of perforated beams.
- To investigate the structural performance of perforated beams at room temperature.
- To investigate the behaviour of perforated beams at elevated temperatures.
- To understand the effect of different load ratios on the performance of cellular beams in fire.
- To investigate the performance of perforated beams subjected to hydrocarbon fire.

1.3 METHODOLGY

- Fours short and not loaded beams are studied experimentally and numerically to examine the influence of intumescent coating on the overall thermal performance of perforated beams. The numerical models are validated against experimental outputs. For the numerical simulations the measured furnace temperatures are used as input only.
- A loaded composite perforated beam at room temperature is modelled numerically in order to develop a numerical model to analyse the behaviour of perforated beams. The numerical model is developed based on the experiments and the outcomes are validated with experimental results.

- Three perforated beams are studied numerically and experimentally at elevated temperatures to understand the performance of composite cellular beams in fire and under structural loads.

  The validated numerical methods mentioned above are used to simulate the performance of fire insulated perforated beams at elevated temperatures. The tests and simulation results are compared against each other to establish the validity of the numerical modelling work.

  In all the existing numerical research studies conducted on the performance of intumescent-coated composite cellular beams in fire, the average recorded temperature from tests are assigned to beams in order to capture the material thermal degradation of perforated beams. Unlike these other numerical works, here coupled thermal and mechanical analysis are conducted. In the other words, in the numerical simulations, the coating surface is exposed to fire, in order to predict the temperature of the beams. This is unlike existing works in which, the beams are divided into several sections depending on the number of thermocouples and the average recorded temperature of each section is then assigned to that section in the numerical model. This approach may give rise to inaccuracies as it assumes that the temperature profile in each section is uniform. This is not true; in particular for web-post sections. Additionally, any errors in the temperatures recorded during the experiment is inherited by the numerical simulations.
- Perform numerical parametric studies to investigate the effect of different load ratios on the performance of cellular beams in fire. A parametric study is conducted on the developed composite cellular beams using finite element models. Different loads are applied to the models to establish the limiting temperature of composite cellular beams.

- A numerical study is performed to understand the response of the composite cellular beams to hydrocarbon fire.

1.4 OUTLINE OF THESIS

Chapter 2 comprises of a literatures review of relevant research in the field, for instance, the importance of using cellular beams in buildings, failure mechanisms of cellular beams. The research has been conducted on the performance of perforated beams at elevated temperatures and the general meaning of numerical study.

Chapter 3 provides an introduction to the theory of finite element methods implemented in this research.

Chapter 4 is a numerical study of a composite cellular beam at room temperature. The developed finite element model is validated against experimental results.

In Chapter 5 the thermal response of perforated and solid beams are experimentally and numerically studied. The beams are unprotected or protected with different coating thickness and they are not loaded. In this chapter, the influence of opening on the web temperature is studied and web-post temperatures are compared against the web temperature of solid beams. The effects of different coating thicknesses on the thermal response of solid and perforated beams are studied.

Chapter 6 numerically and experimentally studies the overall performance of composite cellular beams at elevated temperatures. Three composite perforated beams with different geometries and loads are tested in a furnace at the University of Ulster. These beams are then studied numerically. The numerical models are comprised of heat transfer and structural analysis. Temperatures and deformation of beams achieved using finite element simulations are evaluated against test results. The maximum temperature and compressive stress of web-posts at the failure time of beams are extracted from the numerical models.

Chapter 7 studies the behaviour of composite cellular beams numerically. This chapter consists of two sections. The first section studies the effect of different load ratios on the performance of the beams which are studied in Chapter 6. The outcome of this research provides limiting temperatures for different load ratios on composite cellular beams.

The second part of Chapter 7 investigates the performance of composite cellular beams in the hydrocarbon fire. There is no document, code or standard available for the design of perforated beams against hydrocarbon fire. This section of Chapter 7 provides an understanding on the response of perforated beam against hydrocarbon fire.

Chapter 8 provides conclusions of this research and discusses its findings and outcomes of the objectives is described in this chapter.

CHAPTER 2 - LITERATURE REVIEW

This chapter begins by providing an introduction to fire and structural fire engineering in Section 2.1. Section 2.2 briefly explains the theories of heat transfer used in this research. Section 2.3 discusses the simplified methods to calculate the temperature of beams in fire. This is followed by section 2.4 which describes intumescent coatings. Section 2.5 provides a summary on perforated beams including advantages of cellular beams, fabrication methods and their failure mechanisms. Section 2.6 reviews the research studies conducted on perforated beams to date. The last section of this chapter explains the numerical methods implemented in this work.

2.1 FIRE ENGINEERING

Fire precautions aim to protect lives and minimise the damage that fire could cause societies and the environment by implementing performance-based or prescriptive approaches [5, 6]. Such precautions primarily include the minimisation of the risk of ignition, providing a safe exit for occupants, keeping the spread of fire under control, and reducing the risk of structural collapse to enable the safe exit of occupants and fire fighters. This research is concerned with the latter.

2.1.1 Fire engineering approaches

In general, two broad standards exist to ensure that structural members have sufficient fire resistance. One is the prescriptive approach, in which design recommendations are mainly founded on experience with similar or identical fire tests. This method is precise as it sets clear requirements in terms of permissible materials, insulation thickness, shape and size of structural elements, construction details, etc [6, 7]. This approach is very efficient in

static situations. Its drawback is that it can restrain the development and innovation of designs, which need to evolve to meet architectural and aesthetic requirements. Consequently, the prescriptive designs have been changing for many years towards the second type of standards, i.e. the performance based approach [8].

Performance based design requires specification of performance requirements. Solutions are then developed based on a clear understanding of the underlying scientific and engineering principles rather than experiment alone as in the prescriptive approach.

Due to its simplicity and its capability in producing the desired level of safety in designs, the prescriptive approach should be the first choice when specifying a fire safety strategy. The performance-based approach is appropriate to use when it offers flexibility in design, reduced construction costs and improved safety [9]. Due to its complexity, this method requires much greater understanding of the fundamental principles.

The performance method is based on the evaluation and assessment of three aspects: fire modelling, transfer of heat to the structure and the structural response [8]. This research is comprised of the heat transfer and structural analysis.

2.1.2 Structural fire engineering

Understanding the behaviour of structures in fire enables engineers to develop methods to design and construct structures that remain stable for a required time period. Such methods are provided in relevant structural fire safety codes and standards [5]. This research aims to understand the thermal and mechanical behaviour of perforated beams in fire to provide a guidance for the design of composite cellular beams during fire.

2.2 HEAT TRANSFER

This research is concerned with the amount of heat transferred from a furnace to a composite cellular beam and the temperature of the beam at different locations on the beam during a period of time.

Heat can be transferred by one, or by a combination of three separate modes known as conduction, convection and radiation. In all heat transfer mechanisms, heat energy is transferred from regions with higher temperature to those with lower temperature and between materials [10-12]. This section discusses the fundamental heat transfer mechanisms and introduces the heat transfer theory used for the numerical study of this research.

2.2.1 Conduction

Heat conduction occurs in a microscopic scale. In a material with a temperature gradient, the atoms and molecules in higher temperature regions vibrate, move faster, and have a higher kinetic energy. The particles transfer some of this heat energy to their neighbouring particles by interacting with them (diffusion of energy) without actual motion of the particles.

In a one dimensional case, the rate of heat transfer is proportional to the temperature gradient and the heat flux is expressed as

$$q'' = K\frac{\Delta T}{L}, \qquad \textbf{2.2-1}$$

where q'' is the rate of heat transfer (W/m^2), K is the thermal conductivity coefficient (W/m.K), and $\Delta T / L$ is the temperature gradient [10-12].

2.2.2 Convection

In convection heat transfer mechanism, thermal energy is transferred by the bulk motion of the fluid. Convection heat transfer can be classified into two: free (natural) and forced convection. The rate of heat transfer by convection, whether it is free or forced convection, can be calculated using Newton's law of cooling

$$q'' = h(T_s - T_\infty), \qquad 2.2\text{-}2$$

where q'' is the rate of convective heat flux (W/m^2) and it is function of the temperature difference of the surface (T_s) and the fluid (T_∞), and h (W/m^2.K) is the convection heat transfer coefficient which depends on the surface temperature, temperature and the type of the fluid motion.

2.2.3 Radiation

Electromagnetic waves transfer energy through space in the same way as electromagnetic light waves transfer light. This is referred to as radiation. The same physics laws that govern the transfer of light govern the heat transfer by radiation. This heat transfer mode does not need any intervening medium for heat transfer to occur. Radiation heat transfer can be categorised as outgoing and incoming thermal radiation.

Outgoing radiation

The rate of heat flux emitted by a surface is given by

$$E = \varepsilon\sigma T_s^4, \qquad 2.2\text{-}3$$

where E is the emissivity power (W/m^2), ε is the emissivity coefficient and has values between 0 and 1, σ is the Stefan-Boltzmann constant ($\sigma = 5.67\times10^{-8}$ Wm^{-2}K^{-4}) and T_s is the absolute temperature of the surface. The rate of radiation heat transfer is given by

$$q''_{rad} = \varepsilon\sigma(T_s^4 - T_{sur}^4), \qquad 2.2\text{-}4$$

where T_s is the surface temperature and T_{sur} is the ambient temperature.

Incoming radiation

Incoming radiation can be absorbed, transferred, or reflected. Absorptivity is a thermal surface property of materials, which is the fraction of radiation energy incident on a surface (G) that is absorbed by the exposed surface. The absorbed energy G_{abs} can be expressed as

$$G_{abs} = \alpha \times G, \qquad 2.2\text{-}5$$

where α is the absorptivity coefficient ($0 \leq \alpha \leq 1$).

2.2.4 Energy balance

The heat transfer mechanisms follow the thermodynamics laws. The first law of thermodynamics states that the total energy of a system is conserved. This energy can be altered if energy crosses the system boundaries. According to this law, the energy balance for a heat transfer problem can be written as [10-12]

$$\Delta E_{st} = E_{in} - E_{out} + E_g, \qquad 2.2\text{-}6$$

where ΔE_{st} is the change in the mechanical and thermal energy stored over a time interval Δt. The in and out subscripts refer to the energy entering and leaving the system, and E_g is the thermal energy generated within the system.

2.2.5 Lumped capacitance method

Lumped capacitance method is a technique to avoid complex partial differential heat equations in transient conditions. This method assumes that the heat gradient within the system is equal to zero. According to Fourier's law of heat conduction, the absence of heat gradient implies infinite thermal conductivity [10-12]. Such a condition is impossible. However, if the conductivity resistance within a system is small compared with the heat transfer resistance between the system boundaries and its ambient then the heat gradient can be equal to zero.

Biot number

The Biot number is a dimensionless number that is obtained using [10-12]

$$Bi = hl / K, \qquad 2.2\text{-}7$$

where L is the length of the system. When $Bi<<1$, it is reasonable to neglect the heat gradient within the system. This indicates a uniform temperature distribution within the system [10-12].

2.3 STEEL TEMPERATURE PREDICTION

The steel beam temperature during fire can be calculated by solving the heat transfer analysis energy balance equation. The energy balance equation is a differential equation and it can be solved using complex numerical methods (i.e finite element and finite difference methods).

Additionally, the simplified quasi-steady lumped heat capacity analysis can be used to eliminate space discretization methods to estimate the temperature of beams [13, 14]. This is explained in more detail in the following subsections.

2.3.1 Section factor

Section factor is a parameter that is used widely in fire engineering to determine the heating rate of steel sections. The section factor [*S.F.*] is the ratio of the exposed surface area A_m and the volume V of the steel section [15] i.e.

$$S.F. = A_m / V \qquad 2.3\text{-}1$$

A lower section value means a smaller area exposed to heat and a higher section mass. This leads to a smaller temperature rise of steel sections. Note that section factor is one of the main parameters to predict steel members in fire [15].

2.3.2 Unprotected steel beam temperature - Simplified method

The simplified method uses the combination of the heat transfer energy balance equation, section factor and lumped capacity methods to estimate the temperature of beams in fire. This method assumes that the temperature of beams is uniform within the beams at each

time interval. The temperature rise of a steel beam can be estimated using the simplified heat transfer equation given by [15]

$$\Delta\theta_{a,t} = k_{shadow}\left(\frac{1}{C_a\rho_a}\right)\left(\frac{A}{V}\right)h_{net}^{\bullet}\Delta t \qquad 2.3\text{-}2$$

where k_{shadow} is the correction factor of the exposed radiation, C_a and ρ_a are the specific heat and density of steel, respectively. $\theta_{a,t}$ is the uniform temperature of steel at time t, Δt is the time interval, and $h_{net}^{\bullet}$ is the net amount of heat flux received by the section. The net amount of heat flux is the summation of radiative and convective net heat fluxes i.e. [15]

$$h_{net}^{\bullet} = h_{net,c}^{\bullet} + h_{net,r}^{\bullet} \qquad 2.3\text{-}3$$

where $h_{net,c}^{\bullet}$ and $h_{net,r}^{\bullet}$ are the convective and radiative net heat flux, respectively. The convection heat flux can be expressed as[15]

$$h_{net,c}^{\bullet} = \alpha_c\left(\theta_t - \theta_{a,t}\right) \qquad 2.3\text{-}4$$

where α_c is convection coefficient and θ_t is the ambient temperature. The net rate of heat transfer by radiation is given by [15]

$$h_{net,r}^{\bullet} = \varepsilon_m\varepsilon_f\left(5.67\cdot10^{-8}\right)\left[\left(\theta_t + 273\right)^4 - \left(\theta_{a,t} + 273\right)^4\right] \qquad 2.3\text{-}5$$

where ε_m and ε_f are material and fire emissivity, respectively.

2.3.3 Insulated steel beams temperature - Simplified method

The simplified method predicts the temperature of protected steel beams using the same principal as that used for unprotected beams. The uniform temperature of the beam within each time increment is given by [13, 15]

$$\Delta\theta_{a,t} = \left[\left(\frac{\lambda / d_p}{C_a \rho_a}\right)\left(\frac{A_p}{V}\right)\left(\frac{1}{1+w/3}\right)(\theta_t - \theta_{a,t})\Delta t\right] - \left[\left(e^{w/10} - 1\right)\Delta\theta_t\right] \quad \text{2.3-6}$$

with $w = \left(\frac{C_p \rho_p}{C_a \rho_a}\right) d_p \left(\frac{A_p}{V}\right)$

where λ and d_p are the thermal conductivity and thickness of the coating, respectively. A_p is the inner area of the coatings per unit length, C_p and ρ_p are the specific heat and density of the coating, respectively.

2.3.4 Numerical methods

The simplified method assumes that the temperature of steel is uniform within the whole elements and then the heat energy balance is set for the steel beam. However, the temperature of steel across the beam is not uniform. In the case of asymmetric or perforated beams temperature diffrences within the beam can influence the overall performance of the beam.

For more accurate predictions, beams can be divided into smaller segments. The energy balance equation is then applied at each segment. There are several numerical methods available for the discetrization of solid beams. The finite difference and finite element methods are the preferred methods in modelling heat transfer in solids [16]. These numerical methods are explained in more detail in Section 2.7.

2.4 INTUMESCENT COATING

Intumescent is a paint colour fire insulation which has been used for the past two decades in the UK and the United States. Intumescent coatings have a number of advantages compared to other types of fire protection materials. In addition to their attractive architectural appearance and being lightweight, their installation and maintenance are relatively simple [17, 18]. Intumescent materials consist of two main components: a resin

binder and a mixture of chemicals, which decomposes and releases gas when heated. During this chemical reaction, the intumescent expands by a factor of 7 to 20 times its initial thickness. Following this chemical reaction and thickness expansion, a thick layer of char remains which has low conductivity and insulates the steel from fire [19].

2.5 PERFORATED BEAMS

Perforated beams are currently popular steel sections for two main reasons. Firstly, they provide access for service facilities such as pipes, cables, etc. The other reason is that a perforated beam provides same bending capacity as a solid beam (without opening) with identical size and configuration; but with less weight. The lower weight of the perforated beams with the same capacity has two main advantages. Firstly, using perforated beams contributes towards the sustainability of the design. For a perforated beam about 25% less CO_2 is produced than an equivalent solid beam [20]. Secondly, using perforated beams results in lighter structures, which leads to better performance of the structures against earthquakes [21, 22].

2.5.1 Fabrication of cellular beams

Perforated beams are fabricated from solid sections. Generally, three methods are used to fabricate cellular beams from solid beams [23]:

- The first method is to cut isolated openings in web of solid sections. This technique is implemented for beams with isolated openings.
- Beams are fabricated from plates to form I section beams. The opening can be cut before or after fabrication of the I section beams. The fabrication method is used for regularly spaced or isolated openings.
- I section beams are cut along the web to form two T sections. The top and bottom T are separated and then re-welded to form deeper sections. Heavier sections can be

used for the lower T to optimize the fabricated perforated beams for the application of composite beams. Figure 2.5-1 shows the fabrication process of perforated beams by cutting and welding.

Figure 2.5-1 Fabrication of perforated beams [24]

2.5.2 Failure of perforated beams

Introducing openings to webs changes the failure modes of perforated beams. The failure mode of perforated beams can be categorised as follows [23]:

1- Global bending: perforated beams fail when the applied moment is larger than the bending capacity of the beams. Normally, openings in the web do not lead to a significant reduction in the bending capacity of the beams as most of the bending is taken by the top and bottom flanges.

2- Vertical shear: similar to solid beams, shear failure occurs in the web section of perforated beams. However, due to the introduction of openings the web area of the beams is reduced and the perforated beams are more susceptible to shear failure in comparison with solid beams.

3- Local Vierendeel bending: Vierendeel failure occurs due to the formation of four plastic regions at the corner of an opening of a perforated beam. Shear forces across the perforated beam openings introduce secondary bending moments. The

combination of the secondary movements, global bending, and local axial load leads to the formation of the plastic hinges [25].

4- Web-post horizontal shear and bending: horizontal shear forces at narrow web posts can lead to section failure. Horizontal shear forces are developed within the web-post to transfer the incremental tension force to the bottom flange.

In order to maintain the equilibrium between top and bottom tees in asymmetric beams, the post-webs are subjected to in plane bending moments. This bending may lead to the failure of the post-webs [26].

5- Web post buckling: the shear forces transferred within the web-post could lead to out of plane buckling. The web-post buckling is a function of the width of web-posts, the height of openings and the thickness of web-posts.

Web-post buckling force is calculated based on the concept of an equivalent strut (Figure 2.5-2). The strut length is calibrated against experimental results and numerical modelling of cold and fire conditions [26].

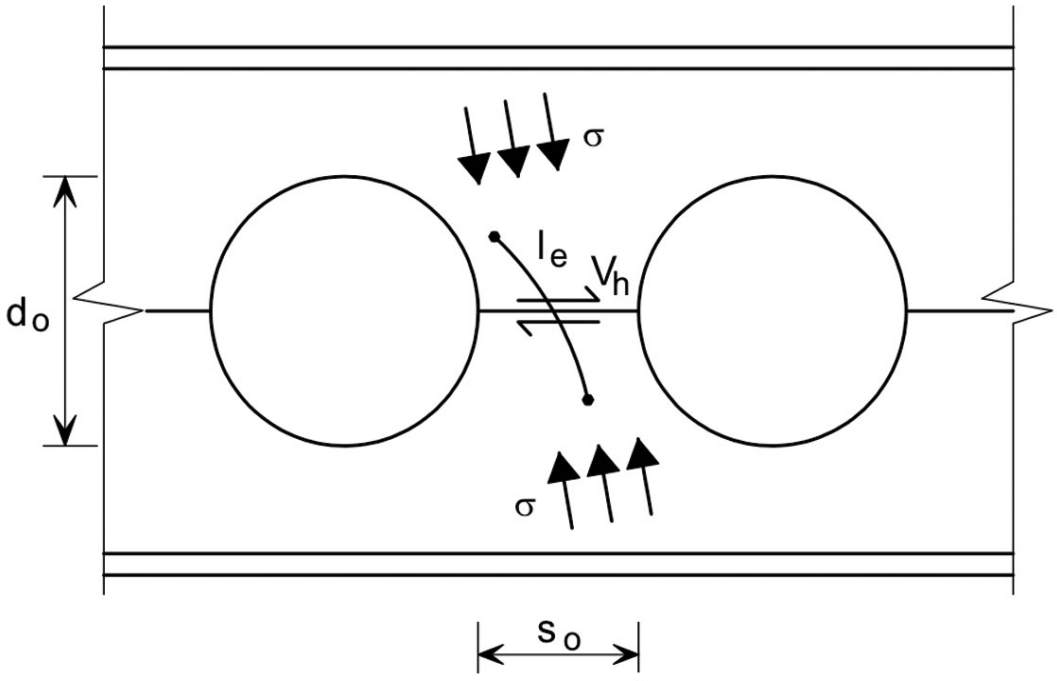

Figure 2.5-2 Compression strut for web-post buckling calculations [26]

2.6 EXPERIMENTAL AND NUMERICAL STUDIES OF CELLULAR BEAMS AT ELEVATED TEMPERATURES

In 2004, Allen published the first experimental results of perforated beams protected with coatings [27]. Allen performed eight fire tests on unloaded and loaded perforated beams. The beam openings were in rectangular or circular shapes. The outcomes of his experiments established that besides the slenderness ratio of web-posts, the opening spacing and dimensions are the main parameter to determine the coating thickness to provide adequate fire protection. The outcomes also showed that the 20% extra coating rule which is in place in "Fire Protection for Structural Steel in Buildings" (known as the Yellow Book) [28], is not conservative. As a result of this, SCI withdrew the 20% rule for intumescent coatings.

Liue and Liew published in 2004 published a paper on their numerical studies on perforated beams at elevated temperatures [29]. Their study looked at the influence of spacing between openings, span and load ratios. Two failure criteria were set for the simulated beams. The first failure criteria was that the deformation of the simulated beams exceeded the deformation limit set by BS 476. The second failure indicator was when the simulation terminated due to instability problems resulting from web buckling.

Bailey in 2004 published a paper based on experiments conducted on unloaded protected solid and perforated beams [30]. The influence of openings on the thermal response of perforated beams was studied by performing the experiments on perforated and solid beams of the same size. Water based and solvent based coatings with two different thickness values of 0.8mm and 2.1mm were used for the protection. The experiment results showed that for the unprotected test, the solid beams have higher temperatures than perforated beams; with a maximum difference of 40°C. The author suggested that the temperature difference might result in different heat exposures within the furnace.

For protected beams, the experimental results show that the web temperature of perforated beams is higher than the web temperaturein identical solid beams. Bailey justified this by the “pulled-back” effect. The coating expands in a way that the edges of the opening are exposed directly to the ambient (Figure 2.6-1) and are consequently exposed to direct heat flux from the furnace.

Figure 2.6-1 Intumescent pull back effect [30]

Wong et. al. [31] studied the behaviour of protected composite floor beams with rectangular web openings in fire. The test was carried out on a full scale fire test on loaded composite beams. The simplified strut method was used to predict the failure of web-post and the ABAQUS software was used for numerical investigation. The recorded temperature during the experiment was used to define the temperature profile of the beam in ABAQUS models. Web-post buckling was identified as the failure mode of the beams during the experiment. This was in agreement with the numerical and analytical results.

Dai et. al. [32] used EN 13381-1 [33] to estimate the conductivity of intumescent coatings based on the conducted test results. The temperature of the partially protected connection was then calculated based on the simple temperature calculation methods given by EN

1993-1-2 [34]. The estimated temperature was in good agreement with the experimental results.

The Dai approach was later developed by Krishnamoorthy [35]. The EN 13381-1 was used to estimate the thermal conductivity of the coatings. FEA models were then developed to simulate the behaviour of protected connections in fire. A thermal analysis was performed in order to predict the temperature of the connections. The predicted temperature was in good agreement with experimental results.

Guo-Qiang et al [36] used the Daio approach for predicting the intumescent conductivity. However, instead of using temperature dependent conductivity (variable conductivity), a constant thermal conductivity was used to predict the temperature of fire tested connections. The temperature predicted using this method was in good agreement with the experimental results 15 minutes after the initiation of the test.

Nadjai et al [37] conducted a numerical and experimental investigation on the performance of cellular composite beams. Four 4.5 m asymmetric loaded beams were exposed to the standard fire curve. The beams were not fire protected and the failure of all four beams was web-post buckling. The results showed that the failure mode of the beams could not be predicted using the stiffness reduction factor recommend by Eurocode. Four numerical models were developed using the SAFIR software package based on the tests. The simulated structural response of perforated beams was in good agreement with the test results.

Vassart [38] developed a range of numerical models for long span perforated beams to study the failure of perforated beams by web-post buckling and Virendeel bending. His numerical investigation was based on the Nadjai experiments [37]. These experiments (which were performed on four loaded composite beams) were used to develop advanced

numerical models using the DIANA software package [39]. The numerical results were in good agreement with experimental and analytical prediction of web-post failure.

Bake [40] developed a numerical method based on the experiment conducted by Nadjai [37]. He conducted a series of parametric studies to determine the sensitivity of loaded perforated beams to the restraining of upper flanges. His numerical study shows that the restraining of the upper flange can change the failure mode from web post buckling to Vierendeel.

Nadjai conducted a new series of fire tests on six cellular composite beams. Three of the beams were protected by intumescent and three of them were unprotected to investigate the effect of the coating on the general performance of the beams. The geometry of each protected beam was similar to an un-protected beam. Naili [41] used the DIANA software package to develop a numerical method based on these unprotected beams tests. Petrou [42] used DIANA to develop a numerical method based on the protected beams test. Both E. Naili [35] and Petrou [36] assigned the recorded temperature during the tests to their structural model to capture the effect of temperature degradation and their numerical work did not include a heat transfer analysis.

2.7 INTRODUCTION TO NUMERICAL METHODS

The rate of heat transfer is a second order differential equation. Most differential equations higher than first order cannot be solved analytically. Hence numerical methods are used to solve these equations based on approximation processes. The finite difference method (FDM) and finite element method (FEM) are two of such methods which are used widely for solving heat transfer and stress-strain equations. For instance, the general partial differential equation governing a transient heat transfer problem can be expressed as

$$\frac{d^2T}{dx^2} - \frac{h_c P}{kA_c}(T - T_S) - \frac{\varepsilon\sigma P}{KA_c}(T^4 - T_s^4) = \frac{\rho C_v}{K}\frac{dT}{dt} \qquad \textbf{2.7-1}$$

where h_c is the convective coefficient, ε is the emissivity of the surface of the object, K is the thermal conductivity of the material, P is perimeter, A_c is the cross-sectional area of the object, T_s is the temperature of the surrounding ambient air, and σ is the Stefan-Boltzmann constant. Note that equation 2.7-1 includes a second order derivative of temperature with respect to space (d^2T/dx^2) on the Left Hand Side (LHS) and a first order derivative of temperature with respect time (dT/dt) on the Right Hand Side (RHS). The former n can be approximated with a finite difference formulae in which the domain of the solution is divided into N subintervals (mesh) with ($N+1$) defined points (mesh points). This changes the LHS into an algebraic equation which can be solved analytically.

Similarly, the first order derivative requires discretisation in time. Two general time discretisations are available for all numerical methods; explicit and implicit. In explicit methods, the unknown variable is approximated based on its estimated value from the previous time step. The explicit method is easy to use but the time step lengths are limited with a stability criterion [43-45].

A heat transfer problem is defined as a test case to validate the heat transfer functions of the FEA used package. Appendix A presents the validation problem and its results. Validation practices also provide an insight into the numerical methods used throughout this research work.

CHAPTER 3 - INTRODUCTION TO FINITE ELEMENT THEORIES

This chapter discusses the numerical methods used in the finite element simulation of this research. It starts with a brief introduction to the ABAQUS software package and continues with expanding the general procedure of modelling a physical problem in Section 3.2. Section 3.3 discusses the differences between linear and non-linear analysis. Section 3.4 provides a summary on the properties of the different type of mesh which are used in this research. Section 3.5 explains the analysis methods which are used for this project.

3.1 INTRODUCTION

The numerical simulations in this project are carried out in the ABAQUS FEA software package. This software is used widely in both academia and industry, in many fields such as aerospace, soil mechanics, and biomedical engineering. This has made ABAQUS a well-validated and reliable FEA package. The software is one of the most powerful tools for non-linear simulations available in the market, making it a suitable choice for this project. Besides, ABAQUS is one of the very few packages that employ the Riks analysis (see section 3.5.4 for details) which is used in some parts of this project.

3.2 FEA simulation procedure

FEA simulations consist of three general steps, namely pre-processing, processing and post processing. The former entails all the necessary steps required in defining the problem that is being solved. In other words, variables, material properties, boundary and initial

condition are specified and the model is discretised in space (mesh) to define the physical problem as a set of finite difference equations. The parameters and variables used in this research are discussed in details in this chapter.

Processing is the step in which the defined differential equations are solved using appropriate numerical algorithms. It is important to note that every solution algorithm has its own limitation and thus the pre-processing and processing steps should be defined with extra care to lead to numerically stable solutions with numerically acceptable errors.

Once the equations are solved, any desired results are processed and presented in appropriate formats such as graphs, numbers, and contour plots(post-processing). Note that when using FEA packages, the required results should be requested in the pre-processing step.

3.3 LINEAR AND non-linear PROBLEMS

Linear and non-linear FEA refer to the differential equations defining the physical problem. Problems described using linear and non-linear differential equations lead to linear and non-linear FEA models, respectively. The general form of a linear differential equation can be expressed as

$$a_n(t)y^{(n)}(t) + a_{n-1}(t)y^{(n-1)}(t) + \ldots + a_1(t)y'(t) + a_0(t)y(t) = g(t) \qquad 3.3\text{-}1$$

which contains no products of the function $y(t)$ and its derivatives. Both the function or its derivatives occur only to the first power. The coefficients $a_n(t),\ldots,a_0(t)$ and g_t can be zero or non-zero, constant or non-constant, and linear or non-linear functions. A differential equation that cannot be expressed in the form of Eq. 3.3-1 is classed as non-linear.

FEA models are generally described using the simplified form of the principal equation given by [46]

$$F=Kd \qquad 3.3\text{-}2$$

where F is the known vector of nodal loads, K is the known stiffness matrix and d in equation 3.3-2 is the unknown vector of nodal displacements. This equation may consist of a large number of linear algebraic equations, depending on the number of integration points (mesh type and size). The stiffness matrix K is dependent on the geometry, material properties, and restraints.

For the linear problems K is constant and hence the equations are solved once. This results in a direct numerical solution algorithm, which is obtained in minutes or seconds. Conversely, in a non-linear problem, as the material deforms, K changes. Thus, in a non-linear analysis K must be updated as the solver progresses through an iterative solution algorithm. Consequently, a longer time is needed to obtain accurate solutions.

In general, non-linearity of a model originates from its geometry, boundary conditions, or material, each of which are explained below [46].

Non-linearity due to geometry: this happens when changes in the geometry of a model under loading leads to changes in the stiffness matrix. This is normally the case when large deformations occur (typically larger than 1/20th of the largest dimension of the model [47]). Note that when large deformations occur, the load direction may vary as the model deforms. In most FEA programs two options exist to account for this change: following and non-following load. The former retains its direction in relation to the deformed model as shown in Figure 3.3-1.a, whilst in the latter the load direction stays unchanged as the model deforms (see Figure 3.3-1.b)

a) Non-following b) Following

Figure 3.3-1 FEA following and non-following load

Non-linearity due to boundary condition: this happens when support conditions, including contacts, change under loading. A simple example is shown in Figure 3.3-2, in which the free end of the cantilever deflects under the applied load and comes in contact with the cube, leading to the nonlinear response of the beam.

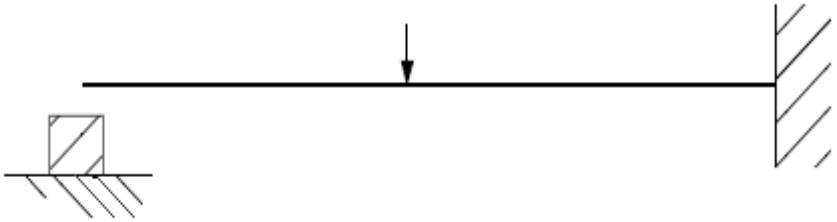

Figure 3.3-2: An example of nonlinearity of boundary conditions

Initially, the beam undergoes a vertical deflection, which has a linear relationship with the load when the deformations are small and until the beam contacts the stop. The contact causes a sudden change in the conditions at that boundary and stops the beam from further vertical deflection. Thus, the stiffness of the beam changes during the analysis, making the problem non-linear.

Non-linearity due to material: this occurs when material properties and hence the stiffness matrix changes under operating conditions. A linear material model assumes that stress remains proportional to strain. This assumption is no longer valid when large deformations take place or when the model undergoes permanent deformations as the model does not return to its original shape once the load is removed. This is the case in rubbers and elastomers which experience very high strains (sometimes greater than 50%), and in most plastics which undergo permanent deformations. In such cases a nonlinear material model must be used for the numerical modelling [47].

3.4 MESH

This section describes the different types of elements used in ABAQUS for this research.

Continuum elements

Solid (or continuum) elements are employed for linear and nonlinear analysis (including modelling of contacts, plasticity and large deformations). These elements are available for structural, heat transfer, and coupled thermal-structural analysis.

Several types of solid elements are available in ABAQUS. One is the 3D linear brick which is a cubic element with a node at each corner (8 nodes). Such elements are regarded as linear as they use linear interpolations between the two nodes on each edge. The 8 node 3D element used for stress/displacement analyses is referred to as C3D8.

Shell elements

Shell elements are employed in the modelling of structures in which one dimension (the thickness) is considerably smaller than other dimensions. Conventional shell elements define the geometry at a reference surface and the thickness of material is defined as the material property in the property section module. Conventional shell elements have all degrees of freedom.

Robust and accurate solutions are obtainable using general-purpose shell elements. This is true for thin and thick shell models, under all loading conditions. The thickness as a function of in-plane deformation, is allowed in their formulation. Such elements do not suffer from transverse shear locking and they do not have any unconstrained hourglass modes. This suits the purposes of this work as ABAQUS numerically calculates the stresses and strains independently. This calculation is performed at each integration point through the thickness of the shell and hence it allows nonlinear material behaviour to occur. For instance, an elastic-plastic shell element may yield at the outer section points while remaining elastic at the inner section points.

Mesh and time increment size

With regards to heat transfer analysis, a time increment limit exists, below which solutions can become inaccurate and unstable. This minimum time increment is a function of mesh size and material properties and is defined as

$$\Delta t > \frac{\rho c}{6k} \Delta l^2 \qquad \textbf{3.4-1}$$

where delta is the time step size, ρ and k are the density and conductivity of the material, respectively, and l is the mesh size. Hence a fine mesh is not essential to more accurate results and therefore extra care is required to determine the mesh sizes.

3.5 NUMERICAL SOLUTION METHODS & TECHNIQUES

Section 3.5 discusses the fundamental principals and limitations of the numerical methods and techniques used in this research.

3.5.1 Newtown Raphson

The Newton-Raphson method solves an equation of the form *f(x) =0* where *f(x)* is continuous and differentiable. This method is illustrated in Figure 3.5-1.

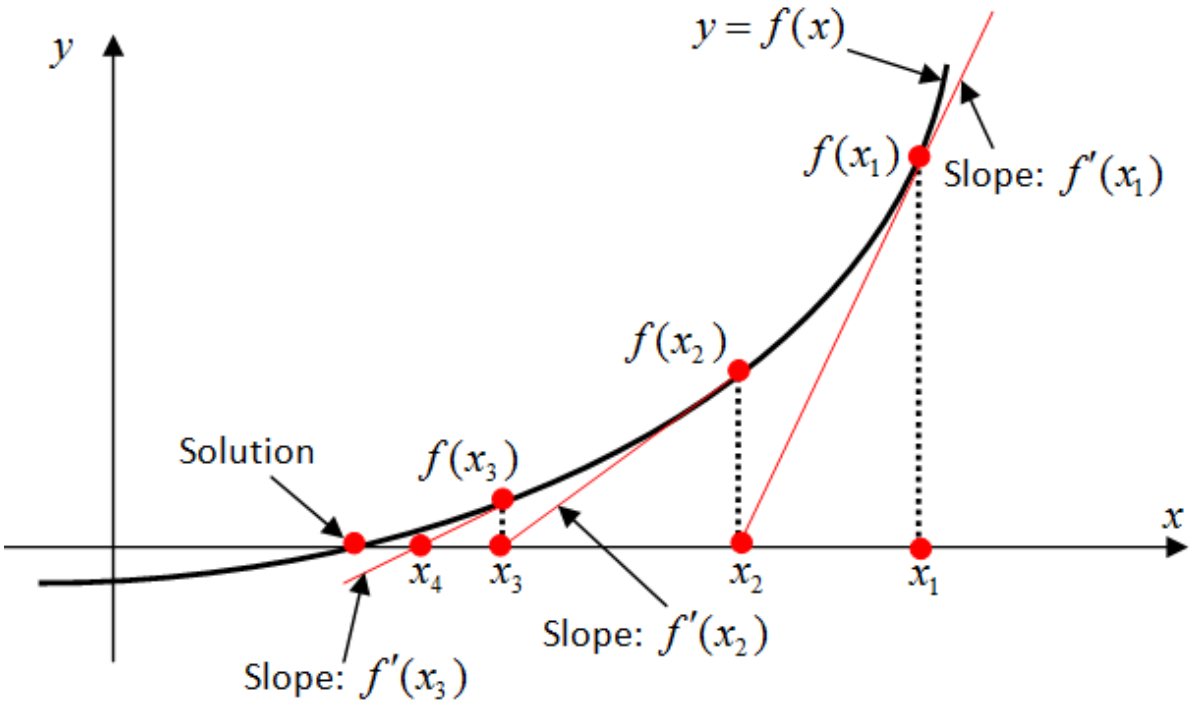

Figure 3.5-1 Newton-Raphson method

To begin with, a point x_1 is chosen as the initial estimate of the solution. A second estimate x_2 is then found by taking a tangent line to $f(x)$ at $(x_1, f(x_1))$ and finding the point at which the tangent line crosses the x-axis. This process continues until convergence is obtained. A solution x_{i+1} at each iteration (i) is obtained using

$$x_{i+1} = x_i - \frac{f(x_i)}{f'(x_i)} \qquad \textbf{3.5-1}$$

where $f'(x_i)$ is the slope of the tangent and $f(x_i)$ is the solution at x_i. Note that Newton's method can also be derived using Taylor series expansion of $f(x)$ about x_1 which is given by

$$f(x) = f(x_1) + (x - x_1) f'(x_1) + \frac{1}{2!}(x - x_1)^2 f''(x_1) + \ldots \qquad \textbf{3.5-2}$$

where f' and f'' are the first and second differentials with respect to x, respectively.

The Newton-Raphson method arrives at a solution fast, provided that the initial guess is close to the solution. Convergence problems also occur when the value of $f'(x)$ is close to zero near the solution [43].

3.5.2 Artificial damping

Static problems can become unstable for different reasons. The instability in numerical methods can be categorized as local and global instability [48] .Global instability may happen due to snap trough/back or buckling of the whole structure. Local instability can be geometrical such as local buckling or material softening. Any type of instability in a general static analysis leads to failure of simulations due to a convergence problem. Riks analysis (see section 3.5.4) can be used for the global and post buckling simulation of structures. However, the Riks method does not provide an accurate model for localised instability [48].

In localised failures, the problem essentially becomes dynamic i.e. it releases accumulated strain energy. The problems with local instability can be analysed via the introduction of damping in a static analysis or dynamically. In the former, damping is used to dissipate the released strain energy. This is because static analysis aims to capture a stable configuration and hence it is not possible for the released strain energy to be dissipated into kinetic energy. In the dynamic case, strain energy is released locally from buckling and is transformed into kinetic energy. Note that solving a quasi-static problem dynamically is often an expensive approach [48].

ABAQUS [48] offers an automatic mechanism for stabilising unstable quasi-static problems via the addition of a volume-proportional damping to the model. Viscous forces Fv given by

$$F_v = CMv \qquad \textbf{3.5-3}$$

are added to the global equilibrium equations given by [49]

$$P - Q - F_v = O \qquad \textbf{3.5-4}$$

where M is an artificial mass matrix calculated, C is a damping factor, $v = \Delta u / \Delta t$ is the vector of nodal velocities, Δu is the vector of incremental displacement, Δt is the time increment, P is the total applied load, and Q is the internal force [49].

When local instability happens and the rate of deformation of that portion increases, the appended damping effect dissipates the released strain energy. In reality, the energy dissipated by the artificial damping equals the energy released as the inertia effect. Replacing kinetic energy with artificial damping energy enables the unstable phenomenon to be analysed stably by obtaining an equilibrium solution within the static analysis [49].

An alternative method is the adaptive automatic stabilisation scheme in ABAQUS. In this method, the damping factor can vary with time and in space. This factor is controlled by the convergence history and the ratio of the energy dissipated by viscous damping to the total strain energy. In cases where convergence problems occur, ABAQUS/Standard automatically increases the damping factor. For instance, if an analysis includes severe discontinuities or requires decreases in the time increment, the damping factor may increase. Conversely, the damping factor may automatically be reduced if instabilities or rigid body modes decrease.

The ratio of the energy dissipated by viscous damping to the total strain energy can be limited using an accuracy tolerance applied on the global level for an entire model. If this ratio for the model is greater than the accuracy tolerance, the damping factor at each individual element is modified so that the ratio of the stabilisation energy to the strain energy does not exceed the accuracy tolerance on both the global and local element level [49].

3.5.3 Heat transfer

Nonlinearities specific to heat transfer problems can arise due to the material properties being temperature dependent or due to nonlinear boundary conditions. Often, the nonlinearities due to the former are mild as the material properties vary slowly with temperature.

ABAQUS tackles nonlinear heat transfer problems using the Newton Raphson method with some modifications to enhance stability of the iteration process. To integrate in time, the software uses the backward differencing scheme due to its unconditional stability [48].

3.5.4 Riks analysis

Riks method is able to find static equilibrium states during an unstable phase of a structural response. This is done by reducing the applied load such that the maximum load that the structure can handle before failing at each stage can be identified (see Figure 3.5-2) [50]. Fundamentally, The Riks algorithm is Newton's method in which the magnitude of the load is an additional unknown. Therefore, there is no control over the load applied in subsequent iterations. Riks method simultaneously solves for loads and displacements. The progress of the solution is measured using the arc-length along the static equilibrium path of the load-deflection curve (see Figure 3.5-2). This scheme produces solutions regardless of whether the response is stable or unstable [48].

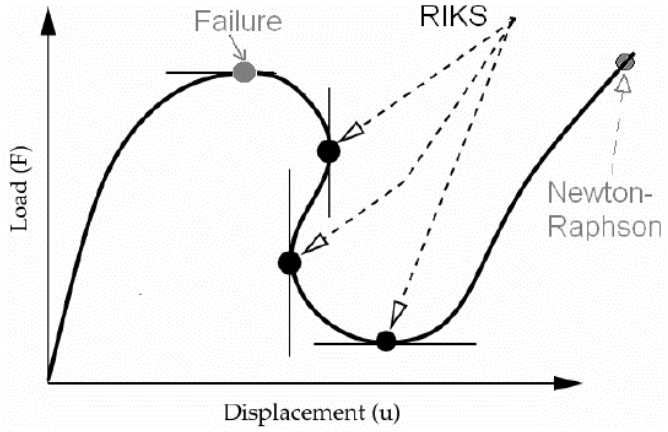

Figure 3.5-2 Riks method [48]

Riks is a suitable method to use in order to solve post-buckling problems with stable or unstable post buckling behaviour. However, due to the discontinuous response at the point of buckling, it is not possible to analyse the problem directly. To enable this analysis, the problem must be turned into a continuous response rather than bifurcation. This can be obtained by including an initial imperfection into the geometry without discontinuities. This way, some response exists in the buckling mode, before reaching the critical load. An alternative is to introduce perturbations in loads or boundary conditions. This creates fictitious loads that trigger the instability. The trigger loads should perturb the structure in expected buckling modes and their magnitudes must be small enough that they do not influence the overall post buckling solution.

3.5.5 Eigenvalue buckling

In an eigenvalue buckling problem one looks for the loads for which the stiffness matrix becomes singular and hence the problem governed by [48]

$$K^{MN} v^{M} = 0 \qquad \textbf{3.5-5}$$

has nontrivial solutions. Note that K^{MN} is the tangent stiffness matrix when the loads are applied, and v^{M} are nontrivial displacement solutions. The loads may include pressures, concentrated forces, displacements, and/or thermal loading.

In general, eigenvalue buckling is used to estimate critical buckling loads of stiff structures. Such structures mainly carry their design loads by axial or membrane action and not by bending. Often, only slight deformations occur before buckling. For instance, the Euler column responds very stiffly to a compressive axial load until a critical load is reached, when it bends suddenly and exhibits a much lower stiffness. However, estimates of collapse mode shapes can be obtained using a general eigenvalue buckling analysis, even in cases when the structural response prior to collapse is not linear.

CHAPTER 4 - CELLULAR COMPOSITE BEAM AT AMBIENT TEMPERATURE

Numerical simulation of cold beams is selected to begin the numerical study of perforated beams. Simulation of beams at ambient temperature involves fewer parameters in comparison to beams at elevated temperatures. Such parameters include temperature dependency of materials or nonlinear thermal boundary conditions. Reduction of number of variables makes it possible to examine the validity of simulations more accurately.

4.1 INTRODUCTION

Six composite cellular beams were tested at the University of Ulster in 2006. Two of these beams were performed at ambient temperature. One of the composite cellular beam [CCB] experiments at the ambient temperature is selected [37] to develop a numerical model for the simulation of beams at ambient temperature. In the experiment a CCB is loaded gradually until failure occurs, at which point the beam deformation is measured under the applied load.

The numerical results including the beam failure mechanisms, failure load, and deformation of the beam are compared against the test results to calibrate the model.

4.2 TEST DETAILS

This section discusses the test setup including the CCB dimensions, material properties, boundary conditions, and applied load.

4.2.1 General arrangements and material properties

The beam selected for this numerical work has a total depth of 575mm and a span of 4500mm and is made of UB 406×140×39 and UB 406×140×39 beams with the S355 steel grade for top and bottom tees, respectively. The beam openings diameter is 375 mm at 500 mm. This beam is referred to as the Ulster Beam A1. Figure 4.2-1 shows the geometry of the beam.

The concrete slab considered in the work is 150 mm thick with a width of 1200mm and is made of normal-weight concrete. The grade of concrete is 35 N/mm^2 which was determined by concrete cube strength tests. The concrete reinforcement comprises of the welded wire mesh reinforcement A142, with a yield strength of 460N/mm^2. 19 mm diameter shear studs with 120 mm height are used to connect the slab to the steel beam. The shear connectors are distributed along the slab and beam with a high density to ensure the full interaction between the slab and the steel beam. A Holorib sheets (HR 51/150) with a thickness of 1.25 mm is used for the steel sheeting.

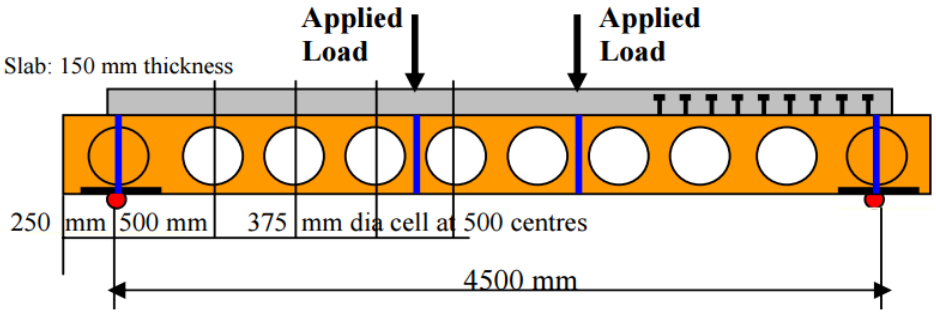

Figure 4.2-1 Symmetrical composite Cellular Beam [37]

4.2.2 Boundary conditions and applied loads

Portal frames with a capacity of 160 Tonnes are utilized to conduct this test. The composite beam specimen is simply supported at the beam ends. The load is applied to the beam using a 600-kN hydraulic jack. The load is applied gradually to the top surface of the

slab using distribution beams located between the hydraulic jack and the slab. Figure 4.2-2 shows the frame and the hydraulic jack.

a) Portal frame

b) Hydraulic jack, distribution beam and LDVT

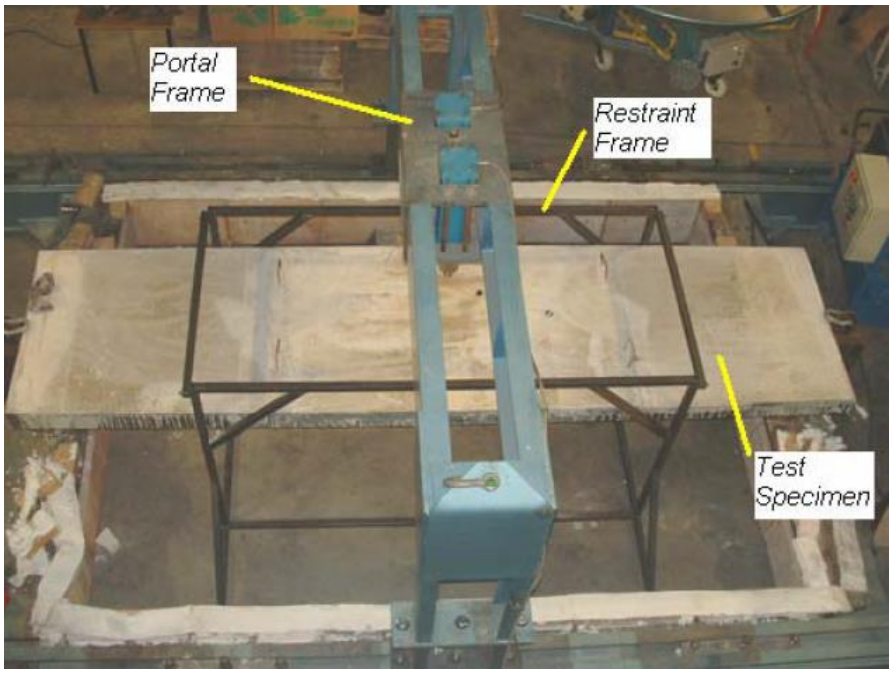

c) Test set up for Beam A1

Figure 4.2-2 The general experiment setup [51]

4.3 SIMULATION METHODLOGY

This section discusses how an FEA model of the composite cellular beam is developed in ABAQUS in this work.

4.3.1 Concrete slab

This section describes the techniques used in the numerical modelling of the concrete deck, reinforcement, shear connection studs, and steel sheeting of the concrete slab

4.3.1.1 Concrete

It is assumed that since the concrete is in compression, no crack appears in the slab due to tension [52]. Therefore, the tension stiffening is ignored for the simulation of the slab. In this method, it is assumed that the concrete loses its strength linearly after reaching its compressive strength.

Shell elements are selected for the modelling of the concrete slab. As mentioned in section 3.4, ABAQUS recommends these elements are used for geometries in which the thickness of the section is relatively smaller than their other dimensions, thus making them a suitable choice for modelling the slab. Moreover, using a composite shell section facilitates the modelling of concrete slab as it makes it possible to define the reinforcement and steel decking within the shell section. Thus, it eliminates the need to create separate parts for the reinforcement and the steel deck. This in turn means that fewer interactions between different parts of the model need to be defined and leads to a high quality structured mesh for the concrete slab. Indeed, the above simplifications of the analysis reduce the simulation time. More specifically, the S4R shell elements are chosen for the mesh. This element type uses reduced integration to prevent shear and membrane locking. S4R is a multi-purpose and robust element which is suitable for a wide range of applications. It is a common practice to use the middle surface offset for shell elements [53], although numerically other types of offsets do not lead to a meaningful difference in results. The middle surface offset is defined for the concrete section.

For discretisation of slab tough its thickness, the Simpson integration rule with nine thickness integration points is used for the concrete. ABAQUS documentation

recommends five integration points is sufficient to model a concrete slab. To obtain more accurate results nine integration points are defined. For the heat transfer analysis, Simpson's rule is the only method available to perform the integrations through the section thickness in ABAQUS [47].

After calibrating and validating the numerical simulation of the beam at ambient temperature, the calibrated model is developed for the simulation of perforated beams at elevated temperatures. The Simpson's rule is used within this research because it is the only available option in ABAQUS which is suitable for both mechanical and heat transfer simulations.

Simpson's is used to numerically to solve definite integrals and requires at least three points. The general form of Simpson's rule is [54]

$$\int_a^b f(x)dx \approx \frac{b-a}{6}\left[f(a) + 4f\left(\frac{a+b}{2}\right) + f(b)\right] \qquad \textbf{4.3-1}$$

The nominal concrete cube strength is 35 N/mm^2. The cylinder strength test leads to closer results to the actual strength of the concrete as the effect of stiffening at the corners of the cube is excluded. Therefore, as recommended by BS EN 206-1 [55], a cylindrical cube strength of 28.3 N/mm^2 is assigned to the concrete slab. The stress-strain relation of concrete under uniaxial compression is taken from Section 3.2.2 of BS EN 1992-1-2:2004 [2]. The relationship between stress and strain at ambient and elevated temperatures can be expressed as [2]

If $e £ e_{c1,}$,

$$\sigma = \frac{3\varepsilon f_{c,\theta}}{\varepsilon_{c1,\theta}\left(2+\left(\frac{\varepsilon}{\varepsilon_{c1,\theta}}\right)^3\right)} \qquad \textbf{4.3-2}$$

where $f_{c,q}$ is the compressive strength and $e_{c1,q}$ is the strain corresponding to $f_{c,q}$. Increasing strain reduces the strength of concrete after compressive strength. Linear and

non-linear descending is permitted by BS EN 1992-1-2:2004 as shown in Figure 4.3-1. Similar to most current studies [35, 37, 40], this research work implements linear decreasing strain.

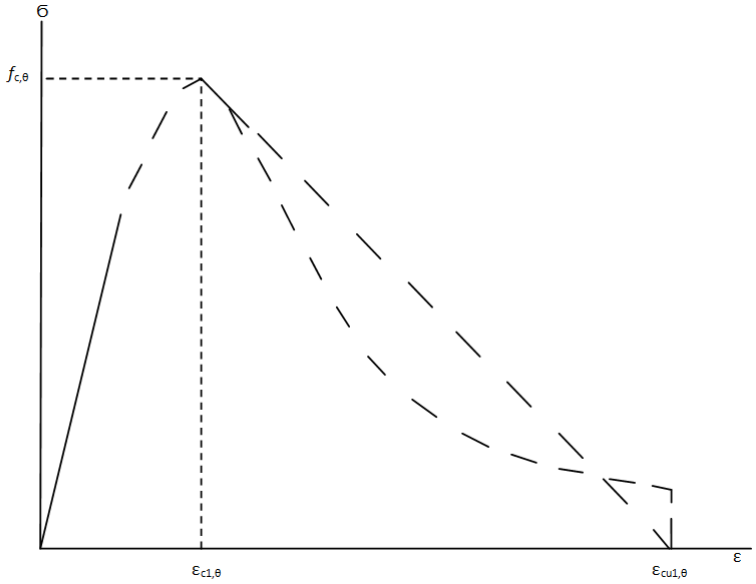

Figure 4.3-1 Stress-strain relationships of concrete [2]

Table 3.1 of BS EN 1992-1-2:2004 [2] for normal weight concrete with siliceous or calcareous aggregates recommends a value of 0.0025 ($e_{c1,q}$) and 0.0200 ($e_{cu,q}$) for compressive strength, strain, and ultimate strain, respectively. These values are selected to define material properties of the concrete.

4.3.1.2 Steel reinforcement

Wire mesh reinforcement A142 with a 460 N/m^2 yield strength is defined as two rebar layers in the shell section. The defined steel reinforcement layers are smeared in the concrete shell element. Plastic properties of the reinforcement layers are calculated in accordance with Section 3.2 of BS EN 1994-1-2:2005 [15].

4.3.1.3 Steel decking

The effect of steel decking on the overall structural performance of the composite beam can be ignored as recommended by SCI [56]. However, for more accuracy of the results,

the steel decking is modelled a lower layer of the composite shell element of the concrete slab.

4.3.1.4 Shear studs

The high-density shear stud distribution provides a full interaction between the concrete slab and the steel beam (Figure 4.3-2). Thus, to simulate the shear studs, a fully restrained interaction i.e. a tie restrain, is defined between the bottom surface of the concrete slab and the top surface of the top steel flange. The defined full interaction ensures that all the forces are transferred between the slabs and beam and the whole model works as a composite beam. Assuming that full interaction between the concrete slab and the steel beam is well justified since no shear stud failed prior to the beam failure.

Figure 4.3-2 High density welded shear studs [51]

4.3.2 Steel beam

The nominal steel grade is S335 for the whole sections. Young's modules, Poisson's ratio and plastic stress of the beam are calculated in accordance with Section 3.2 of BS EN 1994-1-2:2005 [15]. To simplify the model, the shell element S4R is used to model the steel section. The isotropic hardening method is chosen for the steel material.

4.3.3 Analysis type

Predicting the failure mode of the beam, the failure load and the post buckling behaviour of the beam are of interest. Shear forces across the web opening can lead to web-post

buckling or Vierendeel mechanisms. The modelling of these failures include non-linear material (plastic) and geometry (buckling) simulation [57]. The failure of the beam is analysed using two types of analysis: the Riks method and the general static analysis with artificial damping.

This way, the limitations and capabilities of each method is realised and the method that is more suitable for simulation of the beam in fire is selected.

In general, Riks method is more suitable in the prediction of buckling and post-buckling of structures, materials or loading conditions, where linear and eigenvalue methods are no longer sufficient. This can particularly be the case in the presence of material nonlinearity or post-buckling behaviour. In such cases, structures often undergo finite deformations before buckling occurs, which changes the matrices of the governing equations of the problem. As a result, the eigenvalue analysis becomes inaccurate, difficult, or even impossible to perform. [47].

As mentioned in Section 3.5.4, to utilise Riks method, an imperfection in the initial geometry or a trigger load is required. A buckling analysis is performed prior to Riks analysis in order to provide buckling modes of the beam. The buckling modes are then used to define a reasonable imperfection in the geometry. From this analysis it is found that the first three buckling eigenvalues are close together. Deformations of the first and second buckling modes are identical, and happen at the ends of the beam. The second buckling mode is ignored as the failure of the beam happens at one end of the beam. Therefore, the first and third buckling modes are used to define the initial geometry imperfection with scale factors of 10% and 5% of the web thickness for the first and third buckling mode, respectively.

According to the ABAQUS documentation, the Riks method is more suitable for the modelling of post-buckling a snap-through simulation. The method is not ideal for

modelling of localised buckling such as web-post failure in beams. Consequently, here the beam is also modelled using a general static solver with artificial damping. This method is used extensively in previous research works on the performance of perforated and solid beams at ambient and elevated temperature [35, 40, 58, 59]. To minimise the level of damping on the overall response of the beam, the ratio of the energy dissipated by damping to the total strain energy is limited to less than 5%.

4.3.4 Load and boundary condition

In the conducted test, two line loads (spreader beams) were applied to the top of the slab by using the distribution beams as it is shown in Figure 4.2-2. In the simulation, for simplicity, each line load is replaced by two point loads. A total of four point loads are applied at 1/3 of the slab width on the same lines where the test's loads were applied. The beam ends are restrained for vertical and transverse displacements. Additionally, the beam ends are restrained against torsion and out of plane bending.

4.4 RESULTS

Figure 4.4-1 compares FEM model results from Riks analysis against the test results. The vertical axis represents the total load applied to the beam by the hydraulic jack. The horizontal axis represents the displacement of the beam at the middle of the concrete beam. The dotted and solid lines show the results of the general static and Riks analysis, respectively. The dashed line represents the experimental outcome.

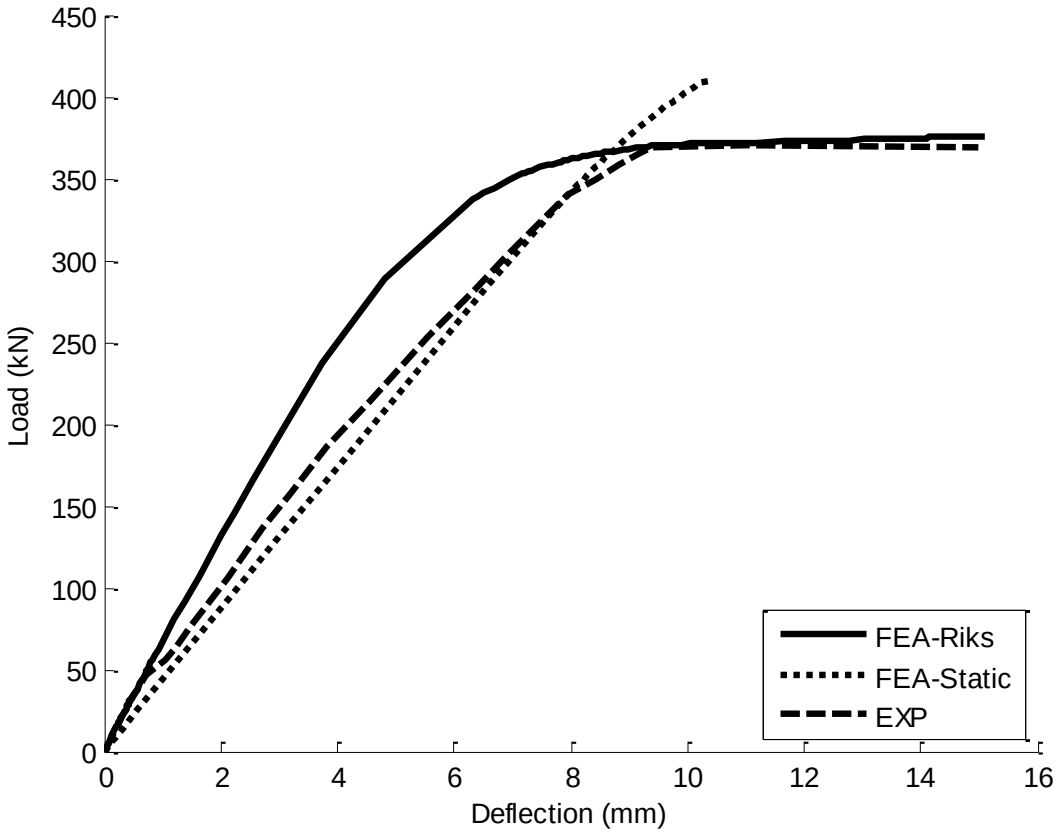

Figure 4.4-1 Comparison between FEA and test results, relation between displacement at the middle of the concrete slab and the total load applied by the hydraulic jack

Figure 4.4-1 shows that the Riks method can model the post buckling behaviour properly and on the other hand, the Static analysis predicts the behaviour of the beam before failure more accurately.

Figure 4.4-2 shows the deformed beam under a 376 kN applied load. The results are extracted from Riks analysis output. Figure 4.4-2 shows that webs between openings are buckled under shear force close to the supports.

a) Deformed shape of beam with excessive failure after deformation - Test

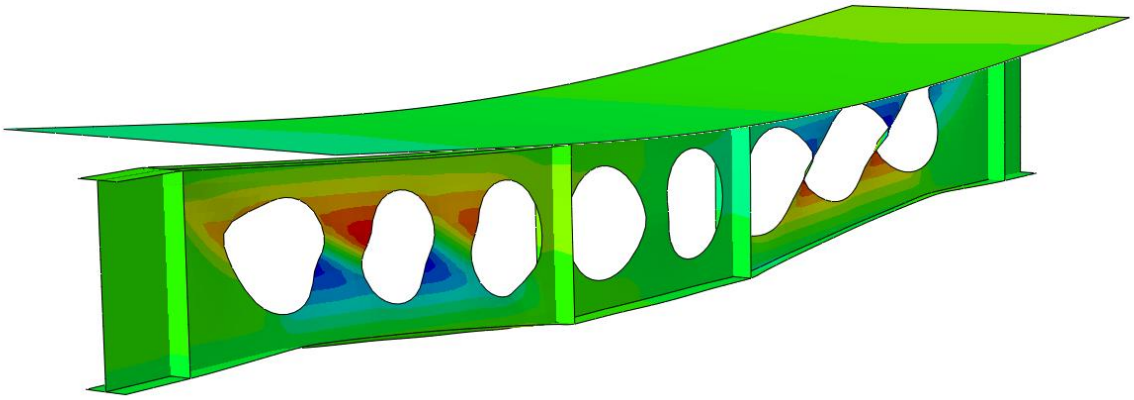

b) Deformed view of beam just before failure- FEA

Figure 4.4-2 Deformed beam under a total 376-kN applied load, Riks analysis, horizontal deformation contour plot

As mentioned in Section 3.5.4, buckling analysis is performed to define a reasonable imperfection in the geometry. Figure 4.4-3 shows the first, second and third mode of buckling from the buckling analysis. The buckling modes are employed to introduce the imperfection in Riks analysis.

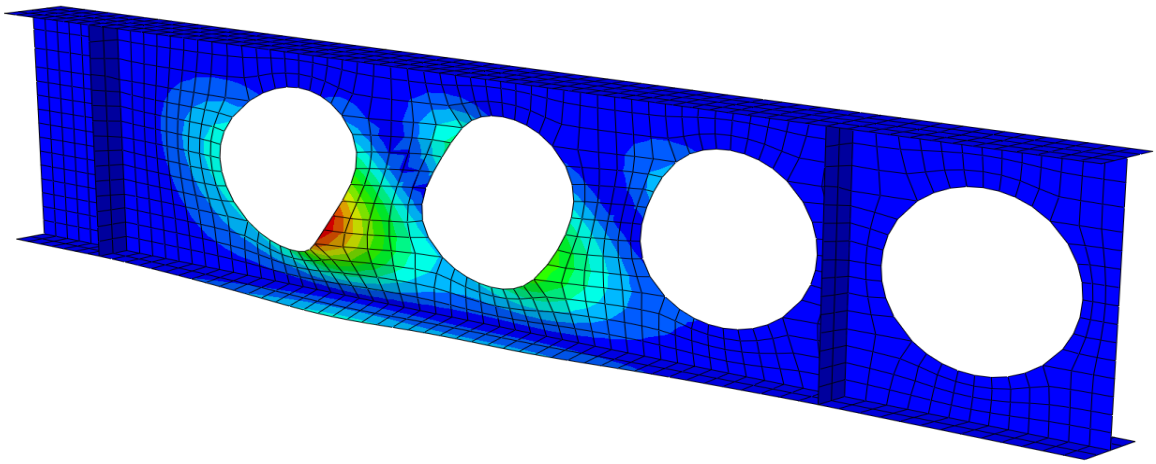

a) First buckling mode

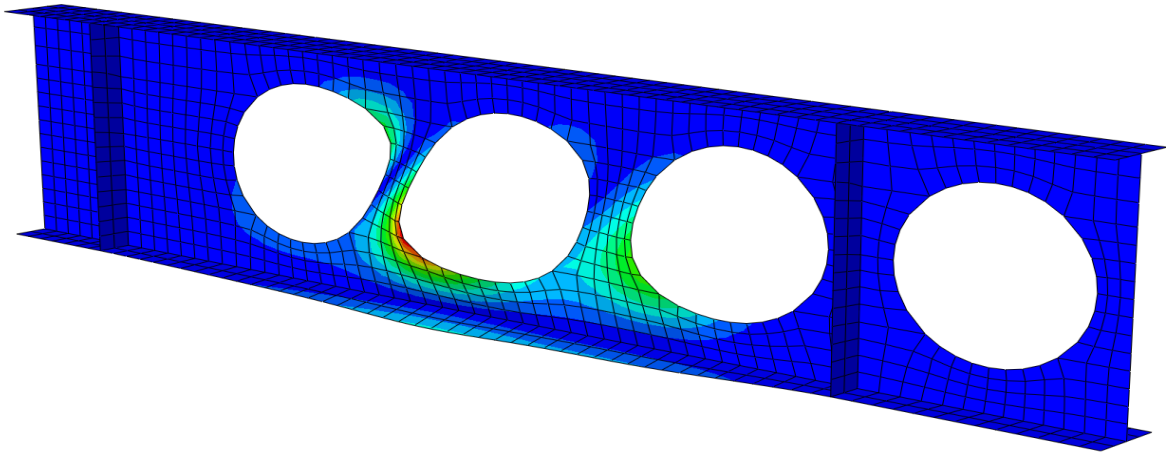

b) Second buckling mode

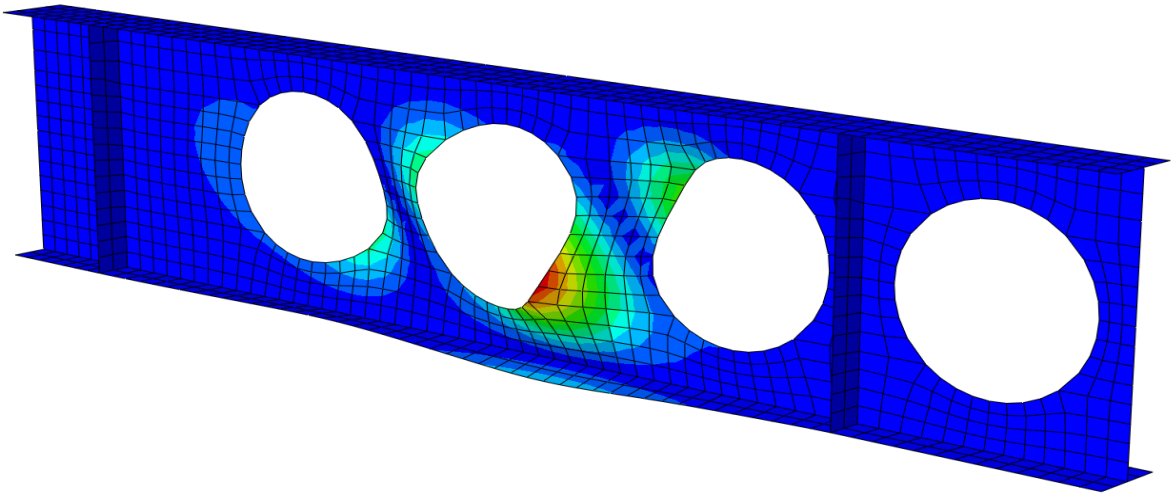

c) Third buckling mode

Figure 4.4-3 Buckling deformation of the beam

Figure 4.4-4 shows the minimum principal stresses (compression) of the beam before web-post deformation.

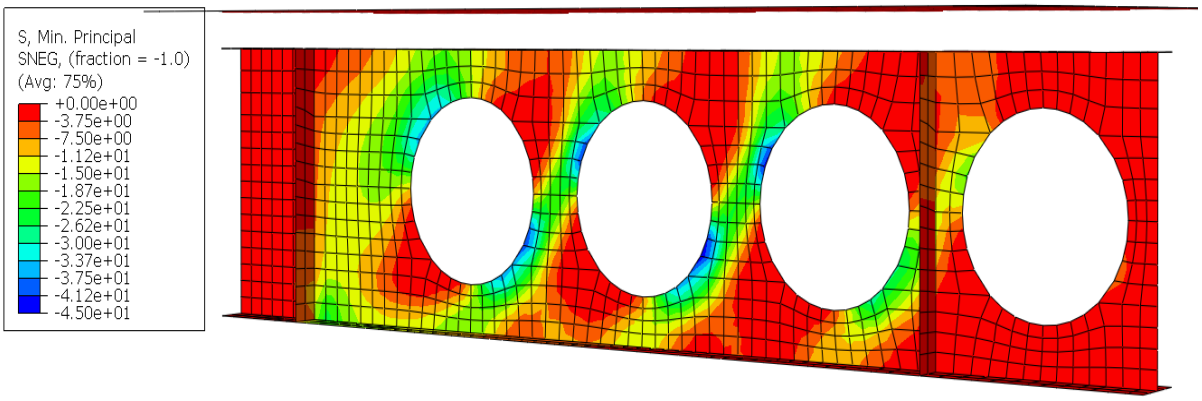

Figure 4.4-4 Compressive stress before buckling

Figure 4.4-5shows the maximum principal stresses (tension) before web-post deformation.

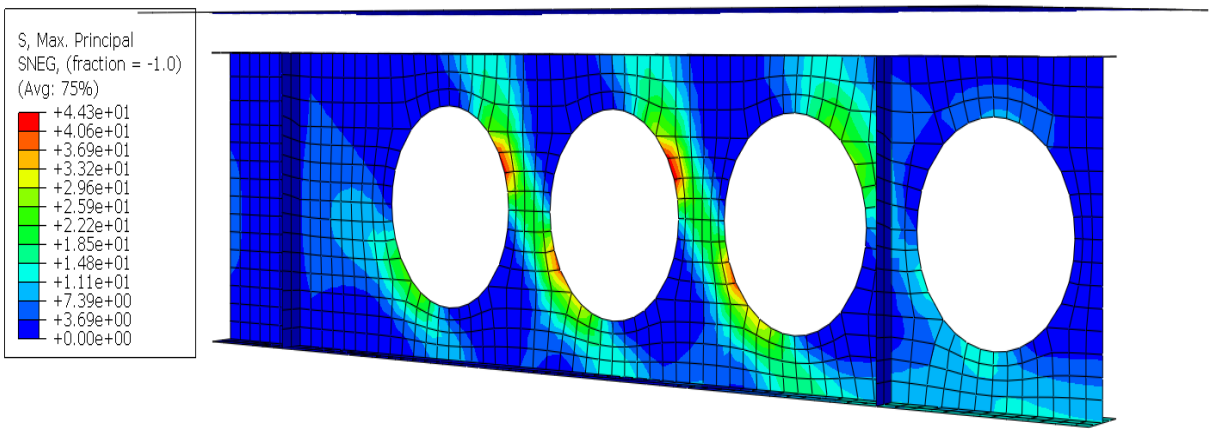

Figure 4.4-5 Tensile stress before buckling

4.5 DISCUSSION

The displacement graph (Figure 4.4-1) shows that the Riks method captures the deformation of the beam correctly and predicts the final displacement similarly to the experiments. The failure mechanisms of the beam are web-post buckling failure. Figure 4.4-2.b shows the numerical predicted failure mechanism of the beam and Figure 4.4-2.a shows the picture of the failed beam in experiments. As shown in Figure 4.4-2.b, the beam fails due to web post buckling and the Riks method predicts the failure mechanisms and load of the beam accurately.

The beam deflection obtained using Riks method is slightly smaller than that of the experiments (Figure 4.4-1). The general static analysis predicts the deformation of the beam against the applied load more accurately than Riks method. However, due to the definition of artificial damping the beam deflects slightly after the real failure point.

Buckling Eigenvalue analysis also is performed to introduce imperfection geometry. The first buckling modes are used to define imperfection for the Riks analysis method. As it is shown in Figure 4.4-3 the buckling failure modes does not reflect the real experimental failure mechanises. This can be explained by two reasons:

1. The base state of the beam in the Buckling analysis is the non-deformed beam. However, in the experiment the beam first is deformed under the loading and then beam buckled. The geometry of the beam is different between deformed and non-deformed beams which leads to different buckling strut length and different stiffness.
2. Eigenvalue buckling analysis uses the elastic properties of the model. However, plastic areas are formed in the deformed beam which leads to different stiffness from the un-deformed beams.

Figure 4.4-4 and

Figure 4.4-5 show the compression and tension of the beam under the deformed shape before the web-post buckling deformation, respectively. These figures show that the tensile and compressive stresses are developed diagonally across the opening. The diagonal tension and compression are developed in opposite directions. This behaviour is similar to truss beams (Figure 4.5-1). However, in the cellular beams the tension and compression diagonals crossed each other in the middle.

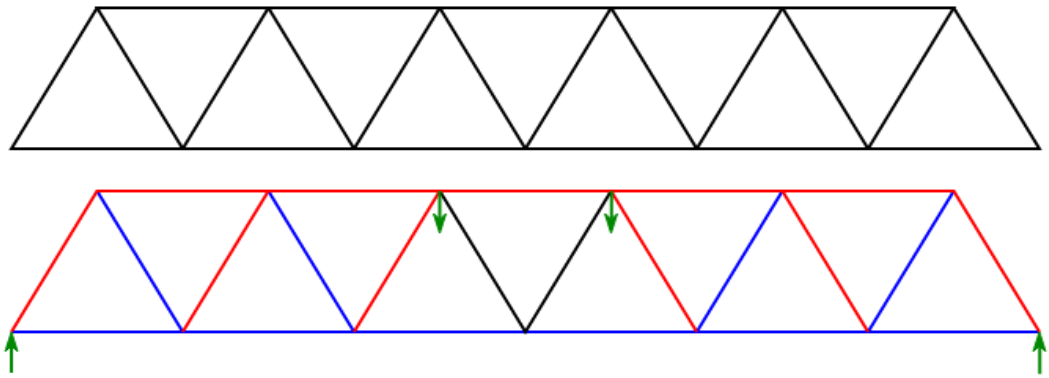

Figure 4.5-1 Warren truss bridge with forces - black for no stress, red is compression, blue is tension

The compression diagonal leads to the web-post buckling and the tension diagonal mitigates the effect of the compression diagonal and acts to delay the buckling. Figure 4.5-2 shows the compression strut, which leads to the web-post buckling and the mitigation effect of the compression strut.

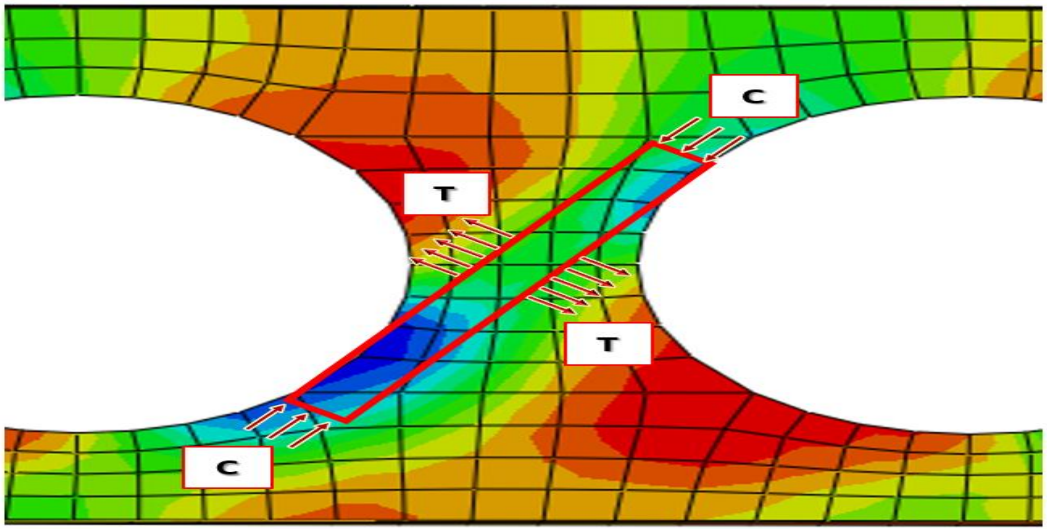

Figure 4.5-2 Compression and tension struts

In most design guides the beneficial effect of the tension strut is ignored, which a conservative approach and the designed webs have more reserve capacity against buckling. The results show that the numerical model is set up such that it predicts the behaviour of cold cellular beam in a precise manner. The employed numerical techniques and assumptions are used and developed in the latter chapters to simulate the performance of the loaded beam in the fire conditions.

4.6 INTERIM SUMMARY

To begin to develop a numerical method to simulate the performance of perforated beams in fire, a simple case was chosen. This involved a composite perforated beam at 20°C with 4.5 m span. Simulation of a beam at room temperature eliminate different factors and parameters in compare to simulation of a beam at elevated temperature such as material degradation due to temperature rise, thermal boundary conditions, etc.

The selected case was an experiment conducted a perforated beam at the University of Ulster [37]. The beam was made of UB 406×140×39 and UB 406×140×39 beams with the S355 steel grade for top and bottom tees, respectively. The concrete slab was 150 mm thick with the width of 1200mm and was made of normal-weight concrete with grade of

35. The beam openings diameter was 375 mm at 500 mm. The perforated beam was loaded gradually during the experiment until the failure of the beam.

A numerical method was used to simulate the behaviour the beam during the test. Riks and general static methods were used to capture the instability of web-post. For the model running with Riks method an imperfection geometry was assigned to the model by using the buckling modes which were achieved from eigenvalue buckling analysis. For the general static model an artificial damping was used to enable the model to capture the local failure of the web. It was shown that the numerical results obtained using both methods were in good agreement with the test outputs. Comparisons of the two methods result indicate that the general static method was more suitable for the simulation of the web-post failure.

CHAPTER 5 - UNLOADED THERMAL PERFORATED BEAM

The temperature profile of a perforated beam is different to that of a solid (non-perforated) but otherwise identical beam. In fact, openings in beams lead to higher web temperatures [37]. Additionally, higher temperatures around the openings of beams lead to the earlier failure of beams in comparison with identical beams without openings. Consequently, perforated beams require more insulation than solid beams, in order to achieve the same performance at the same temperature.

For the design of cellular beams, it is essential to have an insight into the temperature distribution of cellular beams and the influence of intumescent coating on the thermal response of the beams. Design guides use the section factors of solid beams to determine the required thickness of fire insulation coatings. In the earliest revisions of "Fire Protection for Structural Steel in Buildings" which was published by the Association for Specialist Fire Protection (known as the Yellow Book) [28], it was recommended that the thickness of insulation of a perforated beam should be 20% more than the required intumescent thickness for the same beam without openings. However, in the earliest revision (the 5th revision) of the Yellow Book, the 20% rule has been superseded for the usage of the intumescent coatings. This is due to more recent research which has shown that the 20% increase in coating thickness may not be adequate [60].

The present chapter studies the temperature distribution of the beams with and without openings and the effect of the thermal insulation coatings on solid and perforated beams.

ABAQUS is used for the numerical modelling by using test results for calibration and validation of the models.

This chapter investigates the thermal behaviour of perforated beams in fire. More specifically, the thermal response of perforated and solid beams at elevated temperatures is studied numerically and experimentally.

The chapter starts by discussing the study strategy and its aims and objectives in Section 5.1. Section 5.2 explains the experimental setup and the condition of the beams during the experiment. Section 5.3 describes how the material properties of the tested beams are measured and defined. The chapter continues by discussing the numerical modelling and simulation of the experiment with ABAQUS in Section 5.4. This includes how the thermal boundary conditions, meshes, type of analysis, etc are defined. Section 5.5 is allocated to the parametric study of the effect of coating on the thermal behaviour of the beams. Section 5.6 provides the results of the experiment and numerical models and compares them against each other. Section 5.7 discusses the results and findings of the numerical and experimental study of the not-loaded and coated short beams exposed to the ISO fire curve. The chapter concludes with an interim summary in Section 5.8.

5.1 STUDY STRATEGY

A. Nadjai at the University of Ulster tested four asymmetric not-loaded short beams in a furnace. Two of the beams had a solid web whilst the other two contained circular openings. Out of the two solid or perforated beams, one was tested with an intumescent coating with a thickness of 0.8 mm and the other with a thickness of 2.1 mm. The beams were located in the same furnace and hence they were subjected to the same temperatures at their boundaries.

The numerical modelling performed in this chapter is based on the above experiments. In other words, the four beams which were tested experimentally, are numerically modelled

at elevated temperatures. In addition to the four coated beams, a solid and a perforated beam with different any coatings are modelled to further investigate the influence of openings on the thermal behaviour of beams. Table 5.1-1 shows the specification of the six beams modelled.

Table 5.1-1 FEA model specifications

No.	Opening	Intumescent thickness (mm)	Loading	Fire
1	Solid	0.8	Un-loaded	ISO fire curve
2	With opening	0.8	Un-loaded	ISO fire curve
3	Solid	2.1	Un-loaded	ISO fire curve
4	With opening	2.1	Un-loaded	ISO fire curve
5	Solid	None	Un-loaded	ISO fire curve
6	With opening	None	Un-loaded	ISO fire curve

It is important to note that in the numerical modelling the ISO fire curve is applied to the surface of the coatings in order to determine the temperature profile of the beams. In all existing research studies on the effect of intumescent coating on the structural performance of beams, the intumescent coating has not been modelled and the experimental temperatures measurements have been assigned to the steel beam model. In such an approach, the beams are divided into several sections depending on the number of thermocouples (typically between 3 to 12 sectors) and the average recorded temperature of each section is assigned to that section in the numerical model. This approach is not ideal as:

- It assumes that the temperature profile in each section is uniform which is not true; in particularly for web-post sections.

- Any errors in the recording of the temperatures during the experiment is inherited by the numerical simulations.

It is expected that applying the furnace temperature to the beams in this research provides more accurate results and a more reliable validation of the experimental outcomes.
After validation of the numerical results with experimental outcomes and relevant theories, a parametric study is conducted to understand the effect of different coating thicknesses on the thermal response of the perforated beams.

5.2 EXPERIMENTAL SETUP

As mentioned before, four asymmetric not-loaded beams, two with solid web and two with circular openings were tested. One solid and one perforated beam were coated with an 0.8 mm intumescent and the other two beams were coated with a 2.1 mm of the intumescent material. The beams were placed in the same furnace and they are subjected to the same temperatures.
The asymmetric beams were fabricated from a 406 × 178 UB60 beam and a 356 × 406 UC235 beam to form a tee section at the top and bottom of the beam, respectively. This created a section with an overall depth of 500 mm. For the perforated beam, a 300 mm diameter circle and a 300 mm diameter semi-circular opening were cut out. Horizontally, the centre of the circular opening was located 350 mm from one edge of the beam and the web post between the edges of the openings was 120 mm as depicted in Figure 5.2-1. Both the circular and semi-circular openings were positioned at the centre of the beam in the vertical direction. The geometry of the solid and perforated sections is shown in Figure 5.2-1.

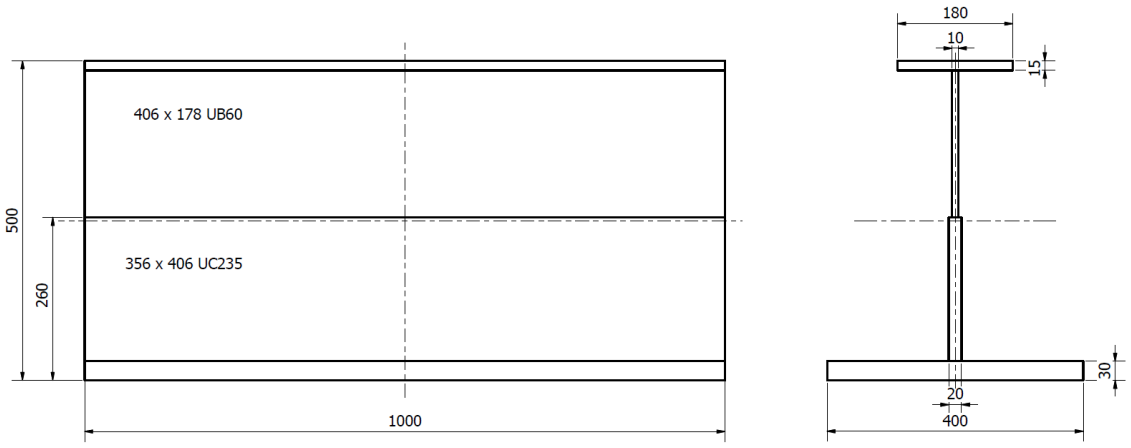

a) Geomtry of solid beams

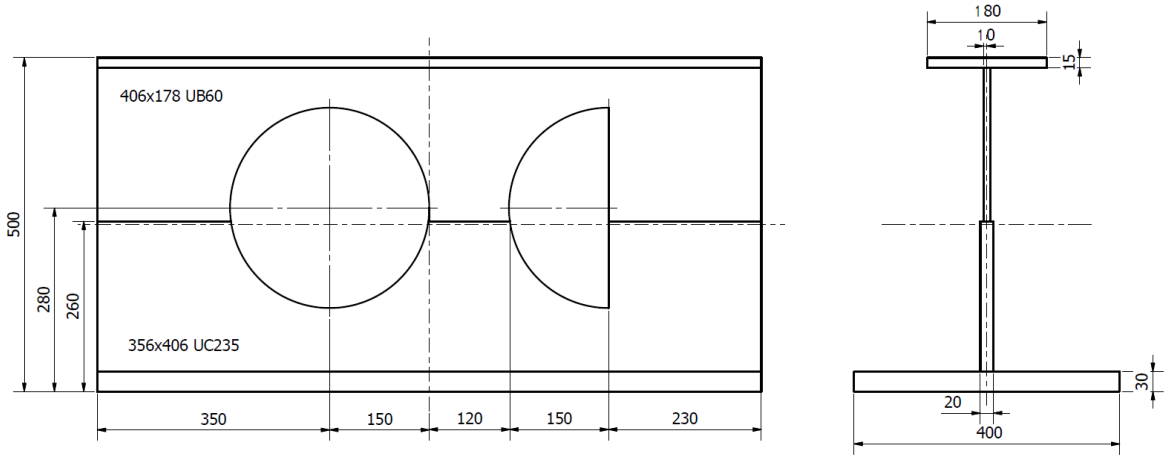

b) Geometry of perforated beams

Figure 5.2-1 Geometry of solid and perforated beams

Four thermocouples were attached to the solid and perforated beams at the positions shown in Figure 5.2-2. This enables the temperatures across the section to be recorded at various time intervals during the test. The beams were attached to the soffit of a combustion chamber by three studs as shown in Figure 5.2-3. The temperature of the furnace was set according to the fire curve provided in BS 476 [61] .

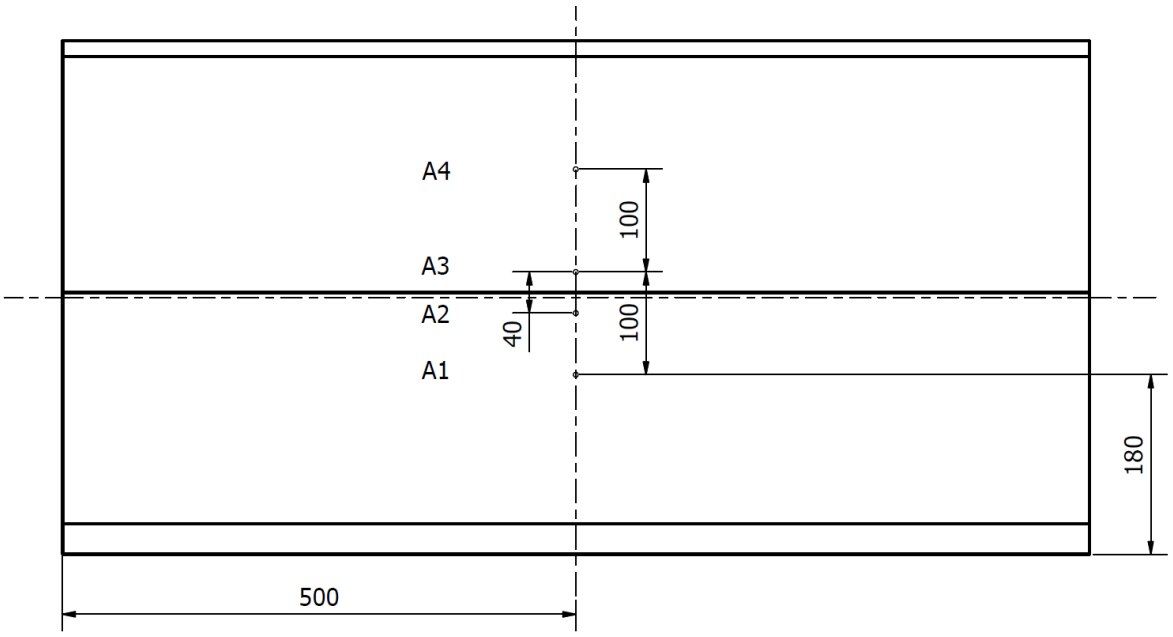

a) Location of thermocouples on the solid beams

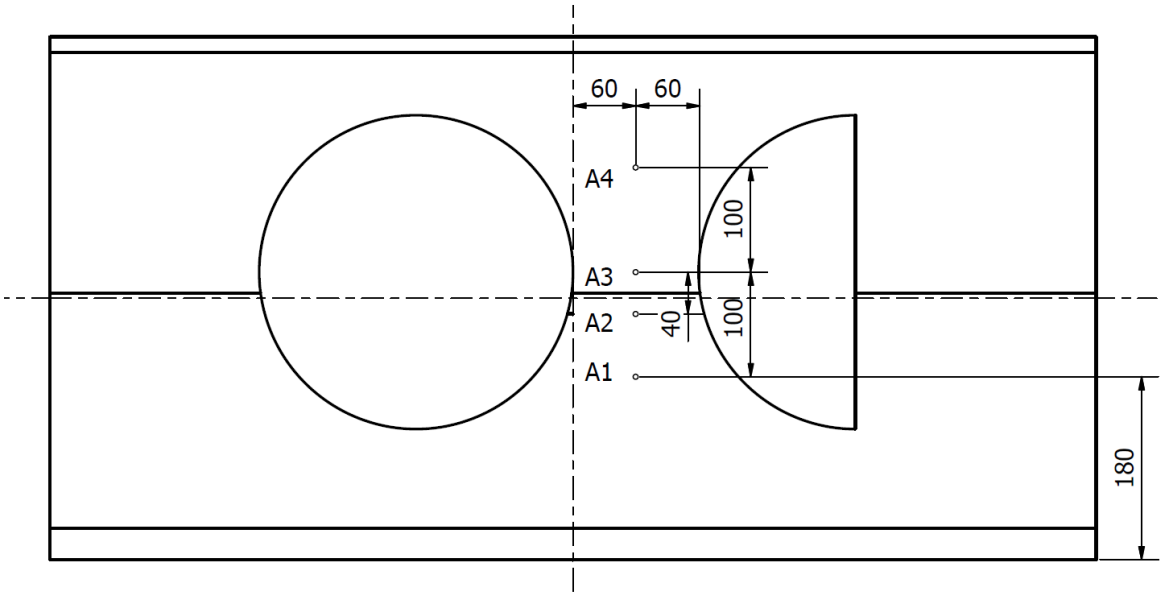

b) Location of thermocouples on the perforated beams

Figure 5.2-2 Location and name of thermocouples

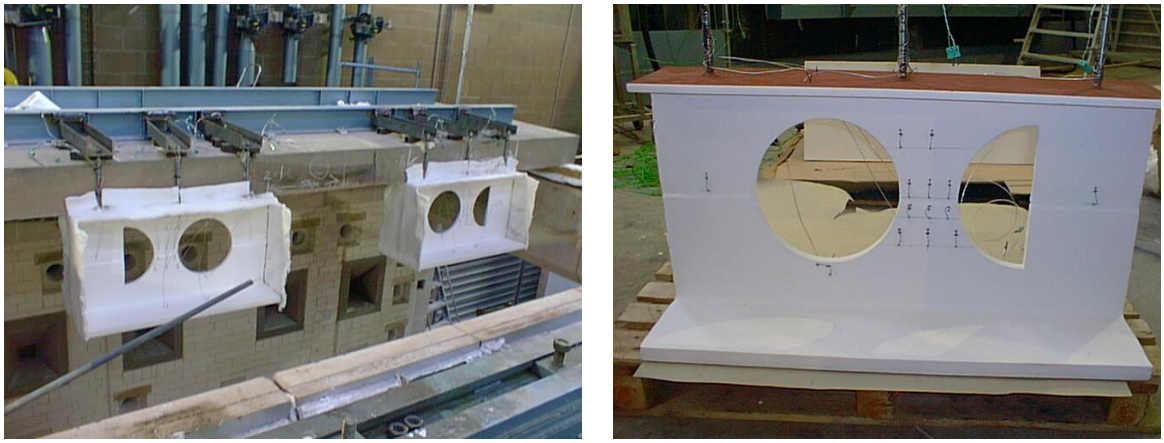

a) Attachment of beams to the soffit of chamber b) General arrangement of thermocouples

Figure 5.2-3 Not-loaded protected perforated beams tested at Ulster University

5.3 MATERIAL PROPERTIES

This section provides a detailed description of the thermal properties used in the numerical modelling of the beams.

5.3.1 Thermal properties of steel

The thermal properties of steel are extracted from BS EN 5959-8-2003 [62]. Figure 5.3-1 and Figure 5.3-2 show the variation of thermal conductivity and specific heat of the steel against temperature, respectively.

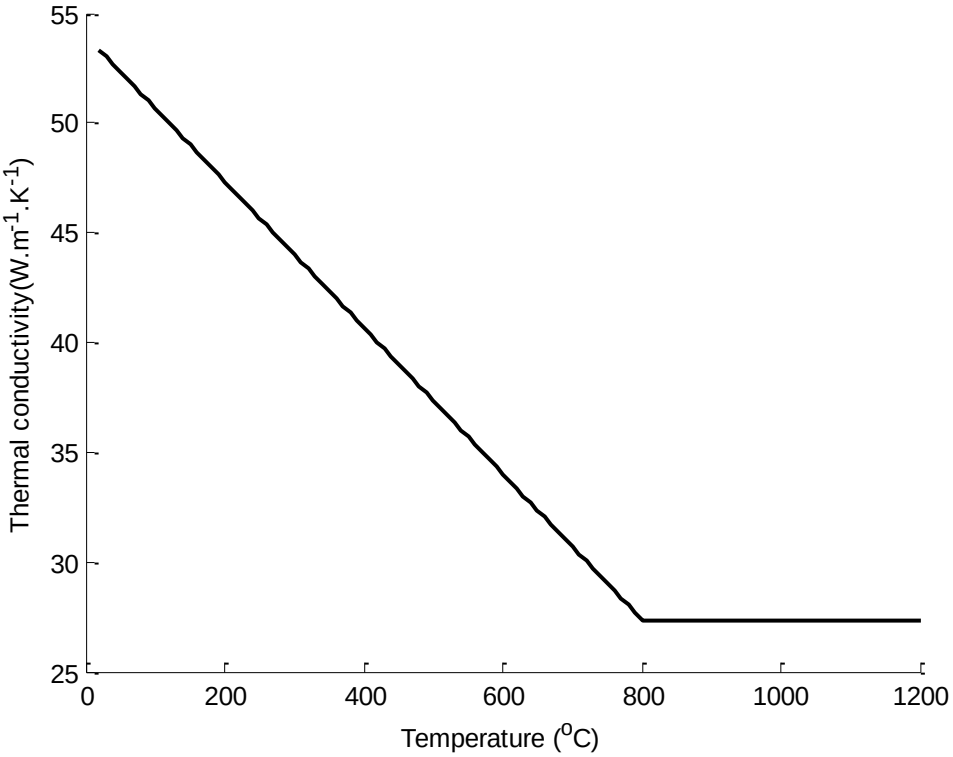

Figure 5.3-1 Thermal conductivity of steel - BS 5950-8

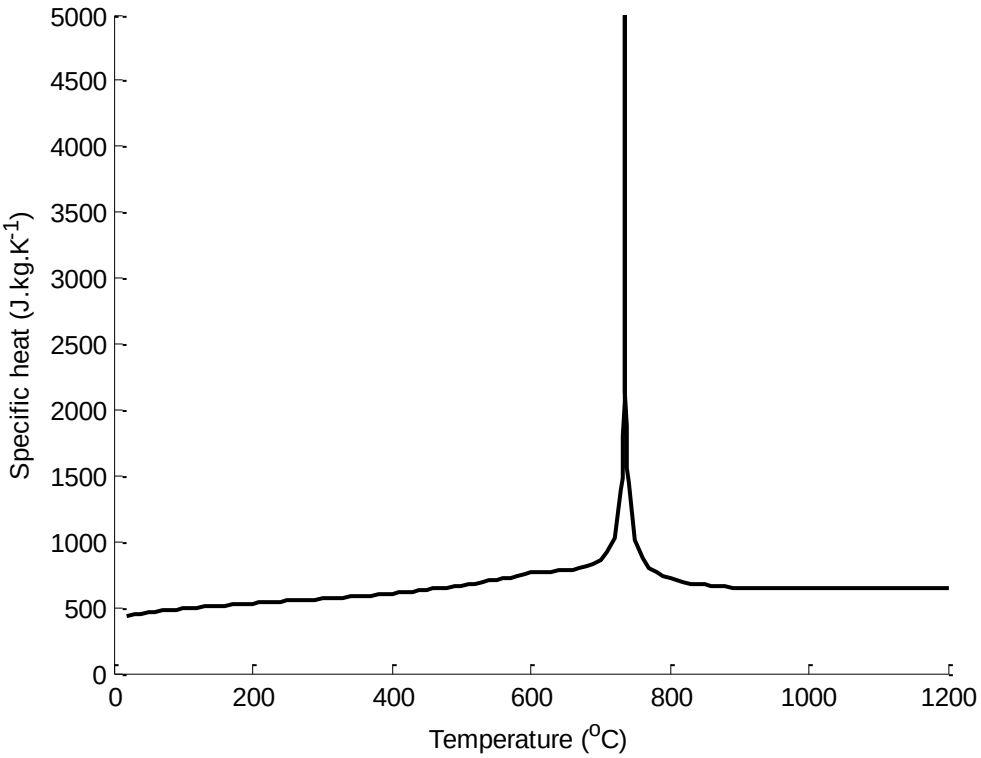

Figure 5.3-2 Specific heat of steel - BS 5950-8

5.3.2 Intumescent coating material properties

Thermal properties of intumescent coatings vary with temperature. However, as it will be discussed in Section 5.3.1, the variation of the specific heat and density of the material do not have a meaningful influence on the thermal profile of the protected beams.

5.3.2.1 Conductivity

The most important parameter which affects the performance of the thermal insulation of intumescent coatings is the conduction heat transfer coefficient. BS EN 13381-8:2013 [33] provides three methods of analysis which can be used to determine the thermal conductivity of reactive coatings such as intumescent. This work adapts the differential formula analysis (DFA) - variable λ approach to estimate the effective thermal conductivity of intumescent coating. This method uses the basic heat transfer differential equation given by

$$\Delta\theta_{a,t} = \frac{\lambda_{p,t}}{d_p} \times \frac{A_p}{V} \times \frac{1}{C_a \times \rho_a} \times (\theta_t - \theta_{a,t}) \times \Delta t \qquad \textbf{5.3-1}$$

where $\Delta\theta \geq 0$ and $\Delta t \leq 30s$.

The experimental results are introduced in the re-arranged form of Equation 5.3-1, expressed as

$$\lambda_{p,t} = d_p \times \frac{V}{A_p} \times C_a \times \rho_a \times \frac{1}{(\theta_t - \theta_{a,t}) \times \Delta t} \times \Delta\theta_{a,t} \qquad 5.3\text{-}2$$

to estimate the effective thermal conductivity of the coating utilised in the experiments. Equation 5.3-2 provides the conductivity of the coating against time.

In the DFA approach, it is assumed that the intumescent coating temperature is equal to the average of the steel temperature and the ambient temperature i.e.

$$\theta_{p,t} = \frac{\frac{\theta_{t-1} + \theta_t}{2} + \frac{\theta_{a,t-1} + \theta_{a,t}}{2}}{2} \qquad 5.3\text{-}3$$

Equation 5.3-3 is used to transfer $\lambda_{p,t}$ (against time t) values to $\lambda_{p,\theta p}$ (against coating temperature) values. Then the mean values of $\lambda_{ave(\theta_p)}$ are calculated for the range of temperatures [θ_p, $\theta_p + 50$] for θ_p from 0 to 1000°C at 50°C intervals; i.e. for 21 ranges [33].

To verify the accuracy of the obtained conductivity, the calculated conductivity $\lambda_{ave}(\theta_p)$ is used to recalculate the steel temperature. The time required to reach the recalculated temperatures are compared with the measured time according to the acceptability criteria, a defined in Section 13.5 of EN 13381-8:2013[63]. Figure 5.3-3 shows the measured temperature and the calculated temperature based on the estimated conductivity value. It is clear from the figure that the results are in a good agreement and that they meet the acceptability criteria of Section 13.5 of EN 13381-8:2013.

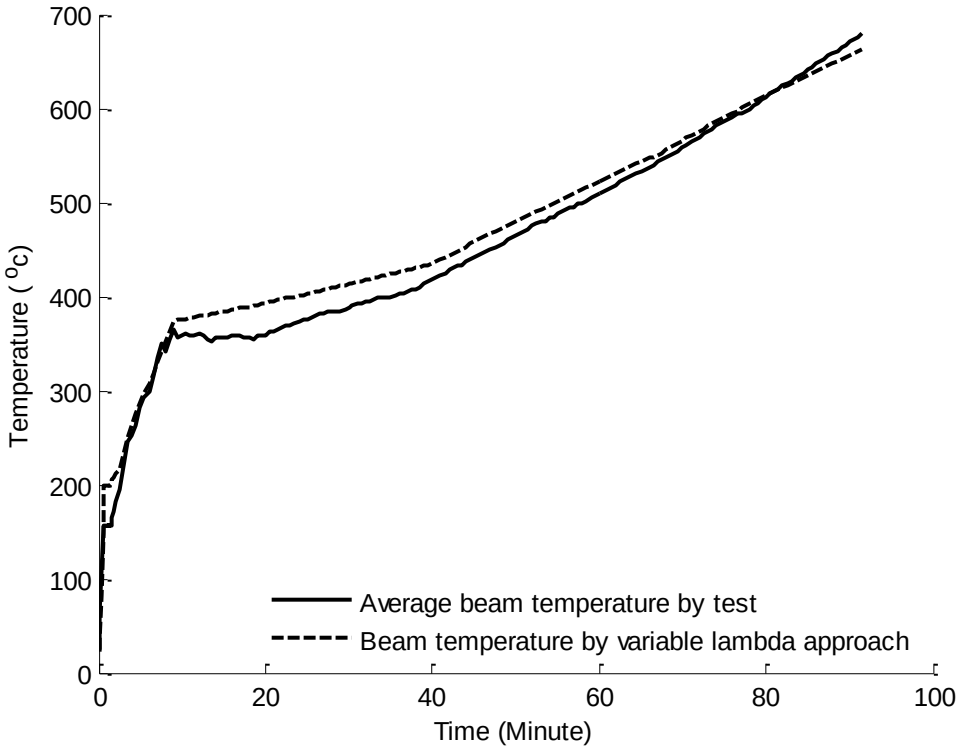

a) 0.8 mm thick solid beam

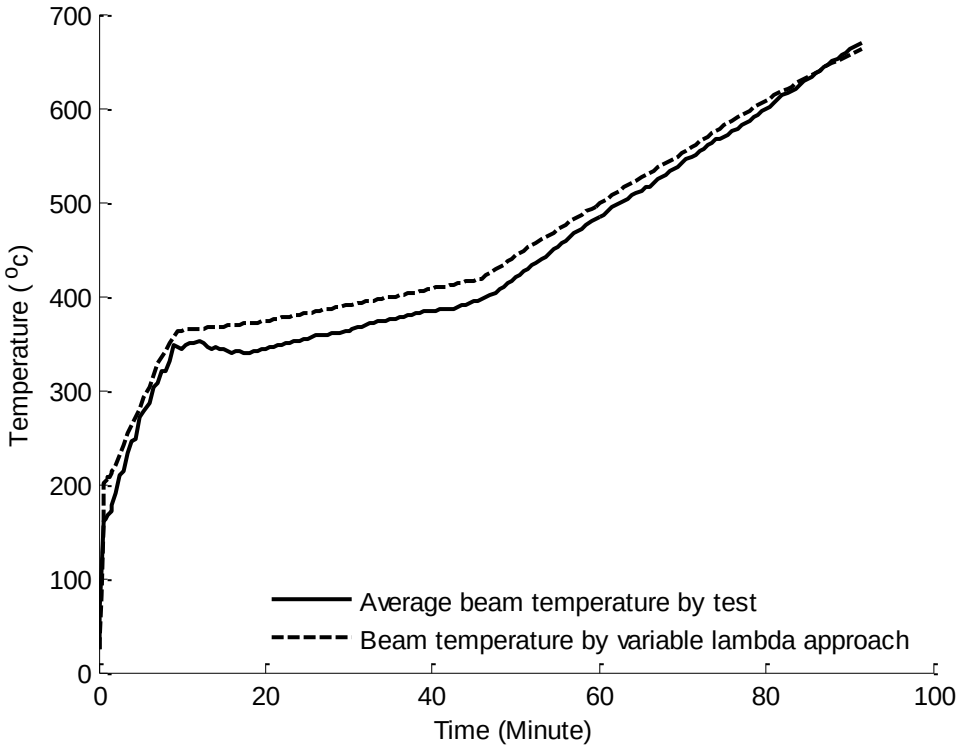

b) 2.1 mm thick solid beam

Figure 5.3-3 Temperature - time curve, predicted by variable λ approach and measured

5.3.2.2 Specific heat and density

Intumescent coatings lose a significant mass during swelling and consequently negligible heat energy is stored inside the intumescent coating. This implies that implementing an accurate temperature dependent specific heat and density in the FEA model does not have a meaningful effect on the outcome. Consequently, the specific heat and the density of the intumescent are defined as temperature independent in the numerical work presented here. Note that using a temperature independent density and specific heat reduces the nonlinearity of the problem and reduces the computation time. The specific heat of intumescent coating is set to 1000 J/kg°C in accordance with Equation E.7 in BS EN 13381-8:2013 [32, 63, 64]. The density of the intumescent coating is set to 100 kg/m^3[32, 64, 65].

5.4 SIMULATION METHODOLOGY

This section provides a detailed description of the techniques used to define an appropriate numerical model to capture the thermal response of the beams described in Section 5.1.

5.4.1 Analysis type

A transient implicit heat transfer analysis is used for the simulation of 5400 seconds. The full Newton method is selected for the solution method. The maximum allowable temperature is set to20°C per time increment.

5.4.2 Mesh type

An 8-node linear heat transfer brick (DC3D8) is used for the spatial discretisation of the beam i.e. the mesh generation. The quality and size of mesh is checked to ensure that the solution analysis is stable and convergent and that the final outcomes would be accurate. Mesh sensitivity study is conducted to determine the optimum size of mesh. The aspect

ratio of all meshes are set to less than 30 and the element angles are not less than 10°C and greater than 160°C. Figure 5.4-1 shows a structured mesh generated for the perforated and solid beams, respectively.

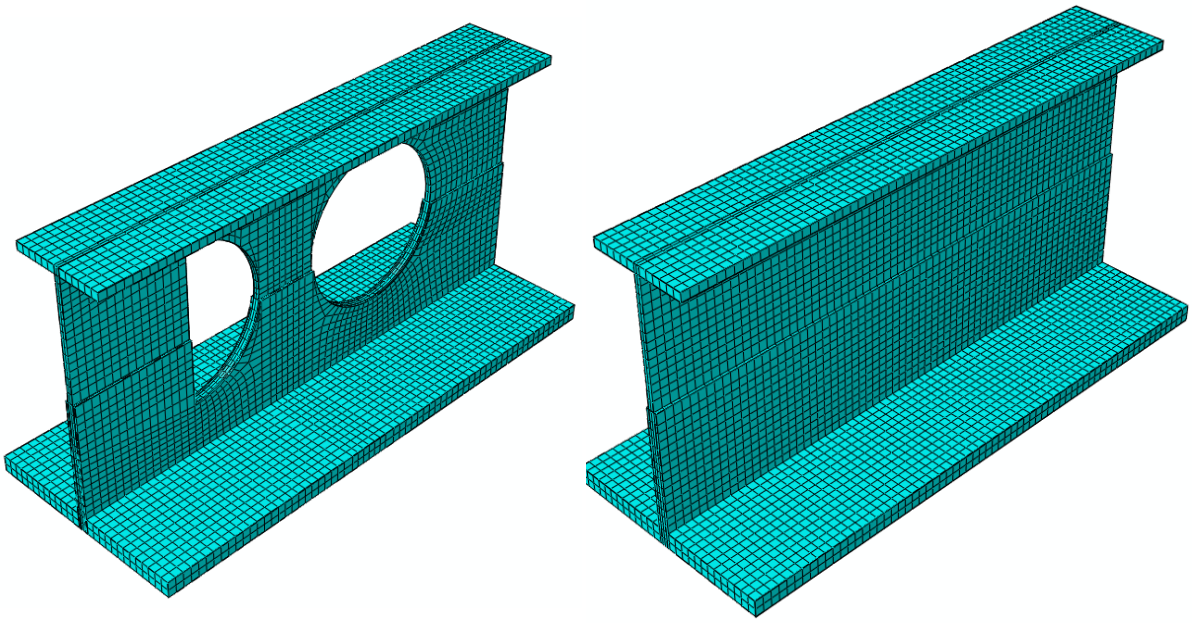

a) Perforated beam b) Solid beam

Figure 5.4-1 Computational mesh

5.4.3 Thermal boundary condition

Section 5.4.3 discusses the interaction between the chamber ambient and the beams as well as the possibility of heat exchange between the inside and outside of the chamber.

5.4.3.1 Chamber conditions

Convection and radiation interactions are used to define heat transfer at the boundaries of each beam. Time-dependent ambient temperature is set to the BS 476 fire curve. The top surface of the beam and the two end edges of the beam are assumed fully insulated. Therefore, no thermal interactions are defined for these surfaces. Figure 5.4-2 shows the thermal boundary of the beams.

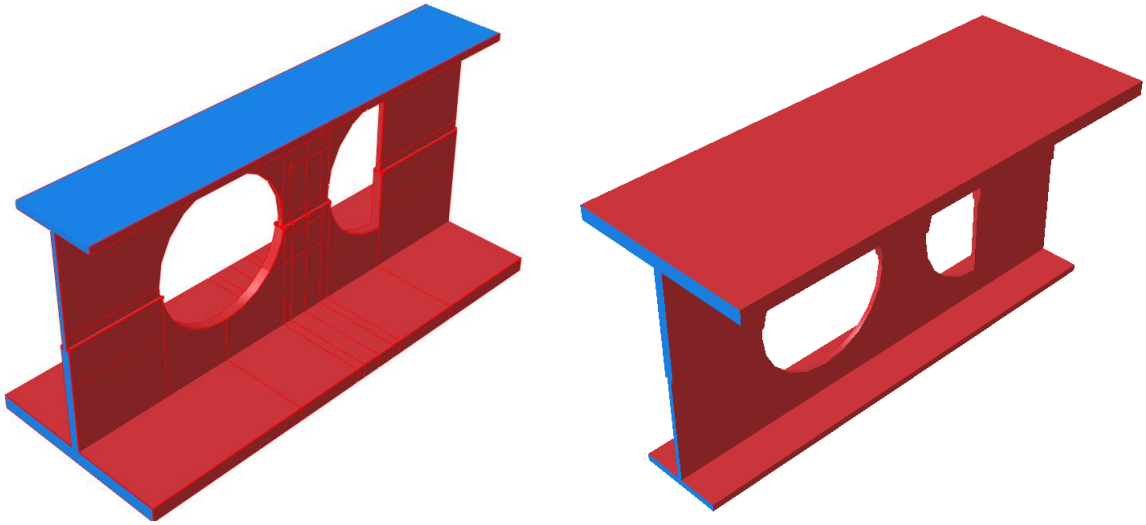

a) Top view b) Bottom view

Figure 5.4-2 Thermal interface surface of the numerical models, blue shows insulated and red shows thermal boundary surfaces

To calculate the amount of heat transferred by convection, the convection coefficient and ambient temperature are required. The governing equation to calculate turbulence flow is:

$$h = \frac{K}{L} 0.037 \,\mathrm{Re}^{\frac{4}{5}} \,\mathrm{Pr}^{\frac{1}{3}}$$

where *K*, *L*, *Re* and *Pr* are conductivity, surface length, Reynolds and Prandtl numbers, respectively. In a standard fire situation, the convection coefficient is assumed to be 25 W/m^2k [13, 66, 67].

The emissivity of the intumescent coating in different literatures are reported to be between 0.7 and 0.95[68]. This work set the intumescent coating emissivity to 0.9 as it was recommended by the intumescent material provider.

It was assumed that all the heat is transferred between the coating and the steel beams. As a result, fully thermal restrained interactions are defined between the intumescent and the steel beams.

5.4.3.2 Heat exchange between inside and outside of the chamber

There is a possibility that heat leakage occurs through the studs that connected the beams to the soffit of the chamber (as shown in Figure 5.2-3 and Figure 5.4-3 a). In order to determine the influence of studs in the numerical model, an FEA model is created which includes a solid beam, slab concrete and the arrangement of studs and steel profiles which are used to fix the beam to the slab (see Figure 5.4-3).

A full interaction is defined between the top of the beam and the bottom of the slab, between the studs and the solid beam, between the studs and the concrete, and between the studs and the channels. Convection and radiation interaction is defined between the top of the slab, studs, channels and the lab ambient. The laboratory ambient is set at up to 20°C.

a) Connections of beams to the chamber using studs

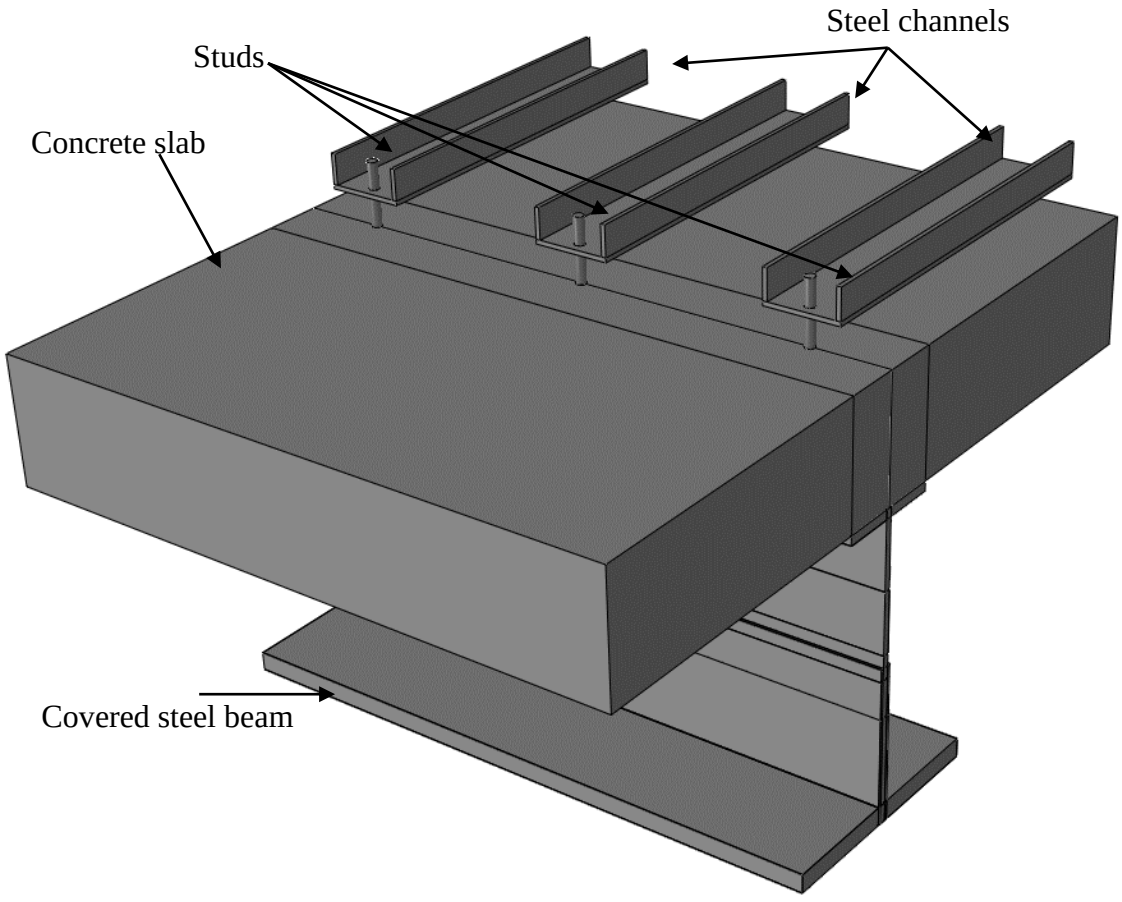

b) The arrangement of the solid beam and the concrete slab in the FEA model

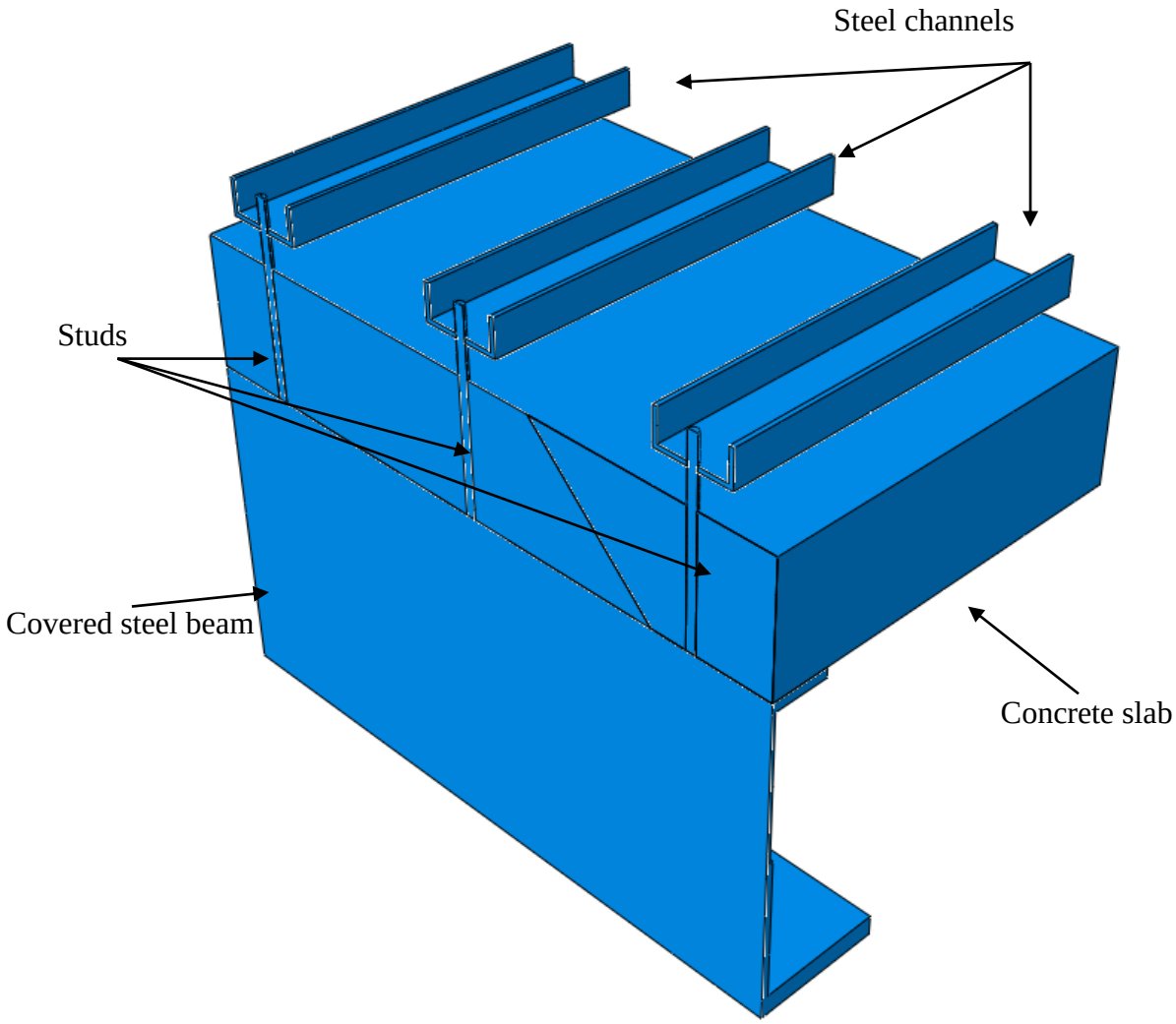

c) A section view of the FEA model

Figure 5.4-3 The arrangement of the connections between concrete slab and the tested beams

The results of this numerical investigation show that there is no meaningful difference between the outcomes of the FEA analysis with or without the concrete slabs and studs (Figure 5.4-3). Consequently, to save the computational time and cost, the concrete slab and studs are not modelled for the numerical study.

5.4.4 Beam and coating interaction

Intumescent coating can be modelled using two general approaches. In the first approach, the intumescent coating and the beam are modelled and meshed separately, and fully restrained interactions are defined between them. As the intumescent and steel are meshed separately in this approach, the nodes at the interface do not coincide (see Figure 5.4-4).

Due to the fully restrained interaction, ABAQUS linearly interpolates the temperature between the nodes on the two sides of the common interface between the beam and the coating to solve the governing equilibrium thermal equations.

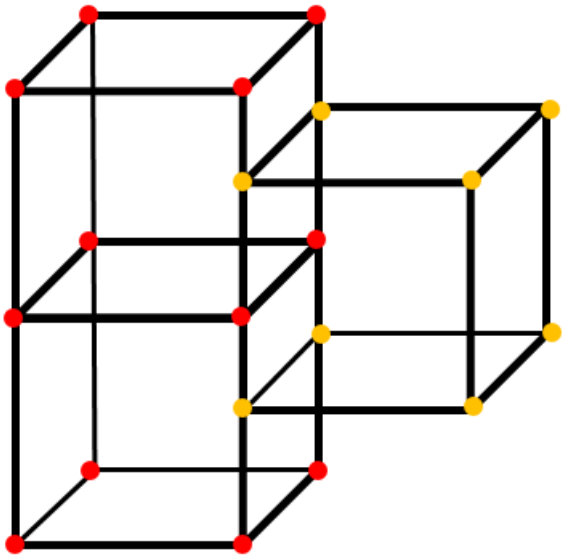

Figure 5.4-4 Schematic arrangement of steel and coating interface mesh and integration nodes, red nodes and orange nodes represent steel and intumescent, respectively

The second approach models steel and intumescent as the same part. In this case, the intumescent coating can be separated via partitioning techniques (see Figure 5.4-5) and subsequent assignment of material properties to the coating and the steel beam.

The second approach enables one to mesh the coating and the steel together. This results in the nodes at the interface between the steel and the intumescent being coincident. This means that is no need for further interpolation between non-matching nodes at the interface between the beam and the coating as in the first approach. This approach could reduce the computing time. As a result, this work uses the second approach.

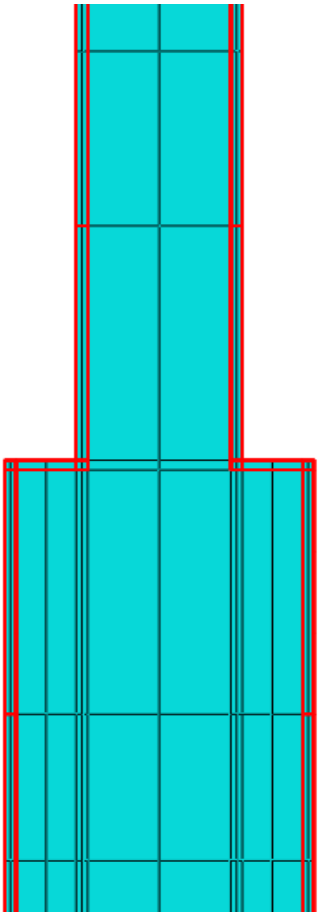

Figure 5.4-5 Part of centre of web coated by intumescent coating, section view, the coating is shown by red lines

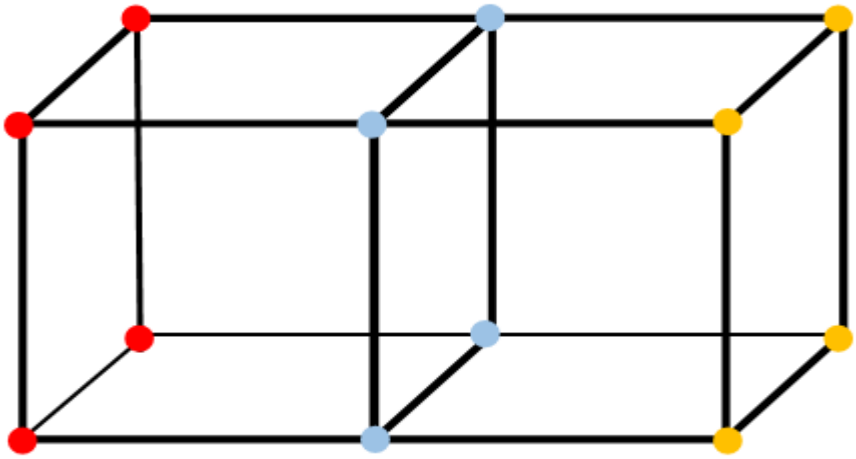

Figure 5.4-6 Schematic arrangement of steel and coating interface mesh and integration nodes. Red nodes, blue nodes and orange nodes represent steel, interface and intumescent, respectively

5.5 PARAMETRIC STUDY

The parametric study is comprised of two sections. The first section studies the influence of different thicknesses of intumescent on the thermal response of the studied beams. The

second part investigates the effect of web-posts on the thermal response of beams by changing the thermal boundary conditions.

5.5.1 Thickness parametric study

A parametric study is conducted to establish the effect of the coating thickness on the thermal response of beams. In this study, the ABAQUS models developed and validated for solid and perforated beams in Section 5.4 are used. Python scripts are developed to streamline the creation of different intumescent coating thickness for this study.

Prior to using the models developed in Section 5.4, an attempt is made to use shell elements to model the intumescent coating instead of using 3D meshes. This makes it possible to use the parametric built in function option in ABAQUS and define the coating thickness as a variable in the composite shell section definitions provided by ABAQUS. However, this method requires considerable computing time as it requires at least three integration points to be defined in each layer of material i.e. at least 9 points in total. The interfaces between the flanges and the web with 9 integration points requires large computational power to perform the interpolations and heat transfer calculations between the flanges and the web. Thus, this work utilised 3D meshes to model the coating in the parametric study. The Python scripts create an identical model for each coating thickness.

The coating thickness is varied between 0.8 mm to 2.2 mm with 0.2 mm increment thickness sizes. This parametric study investigates how the increase in the coating thickness influences the web-post temperature.

5.5.2 Thermal boundary conditions parametric study

A previous test [30] conducted by Bailey on short perforated beams protected with intumescent coatings shows that the web-post temperature is higher than the identical solid beams with the same coating thickness. He justified that by intumescent “pull-back” effect (Figure 2.6-1). To understand the effect of web-post on overall thermal response of the

beam and therefore eliminate the effect of exposing heat flux to the edges of the openings due to the "pull-back" effect, the thermal boundary conditions of the models are changed. In the new thermal boundary conditions, all radiation and convection interactions between beam and furnace are removed. 20 kW heat flux is exposed to the intumescent at the bottom surface of the bottom flange and the top surface of the top flange is set to 20°C (see Figure 5.5-1). For this parametric study, the solid and perforated beams coated with 2.1 mm intumescent are used.

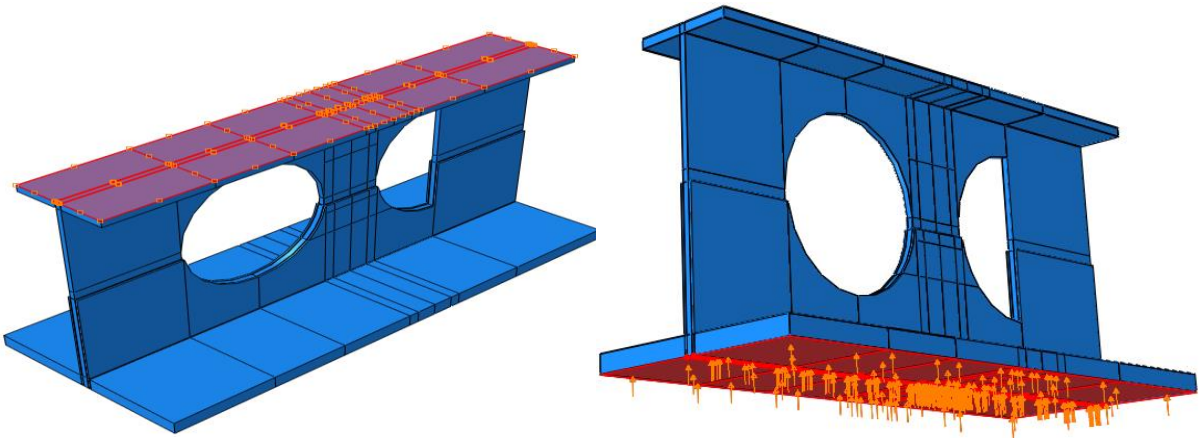

a) Top surface- 20°C boundary b) Bottom heat flux

Figure 5.5-1 Boundary conditions of the parametric study

The new models eliminate the effect of heat exposed to the edge of the openings and amplify the effect of heat conduction from the bottom flange (which is exposed to more heat flux during the experiment) to the concrete surface (i.e the temperature almost remains constant during the experiment).

5.6 RESULTS

In order to make it possible to compare and validate the FEA results, the temperature of the nodes which are located where the thermocouples are positioned in the experiment are extracted from the FEA results.

5.6.1 Unprotected beams

As mentioned in Section 5.1 the unprotected beams are only studied numerically i.e. no experiments were conducted for beams without coating. Therefore, there is no experimental data available for comparison for use in this section (Section 5.6). The results obtained do however provide a generic understanding of the thermal response of beams without any coatings. The location of Nodes 1 to 4 corresponds to the location of A1, A2, A3, and A4 thermocouples.

Figure 5.6-1 and Figure 5.6-2 show the temperature history of the solid and cellular beams without intumescent coating. Figure 5.6-3 and Figure 5.6-4 show the temperature contour plot of the beams after 90 minutes.

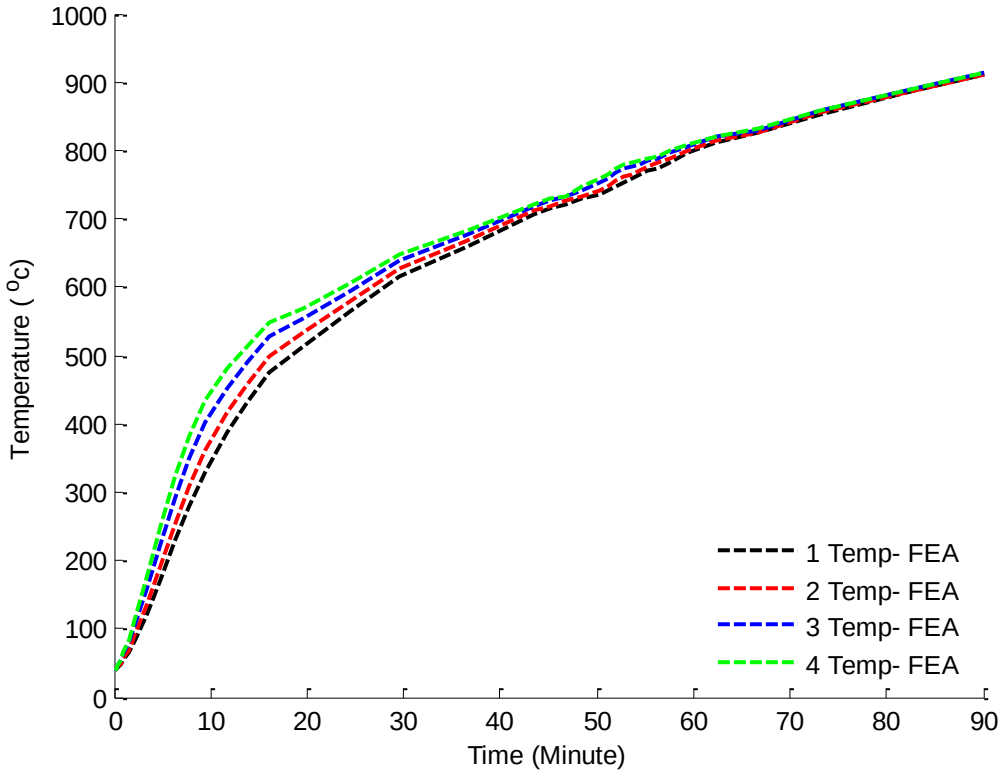

Figure 5.6-1 Temperature history of the solid beam - no coating

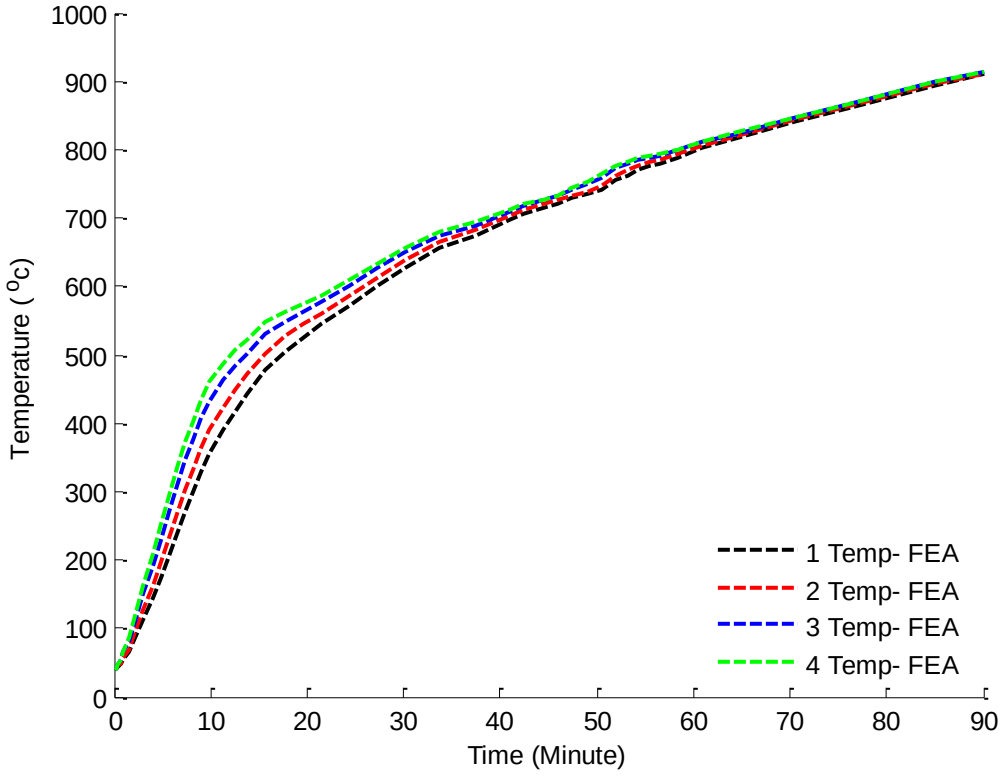

Figure 5.6-2 Temperature history of the cellular beam - no coating

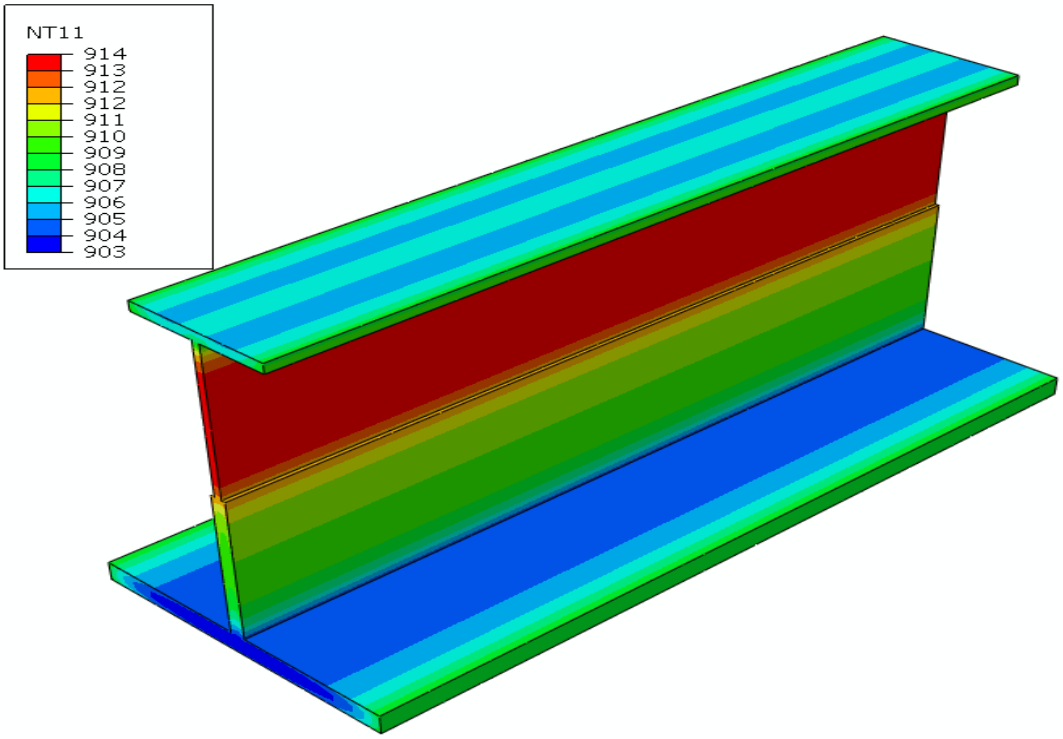

Figure 5.6-3 Temperature contour plot of solid beam - no coating (°C)

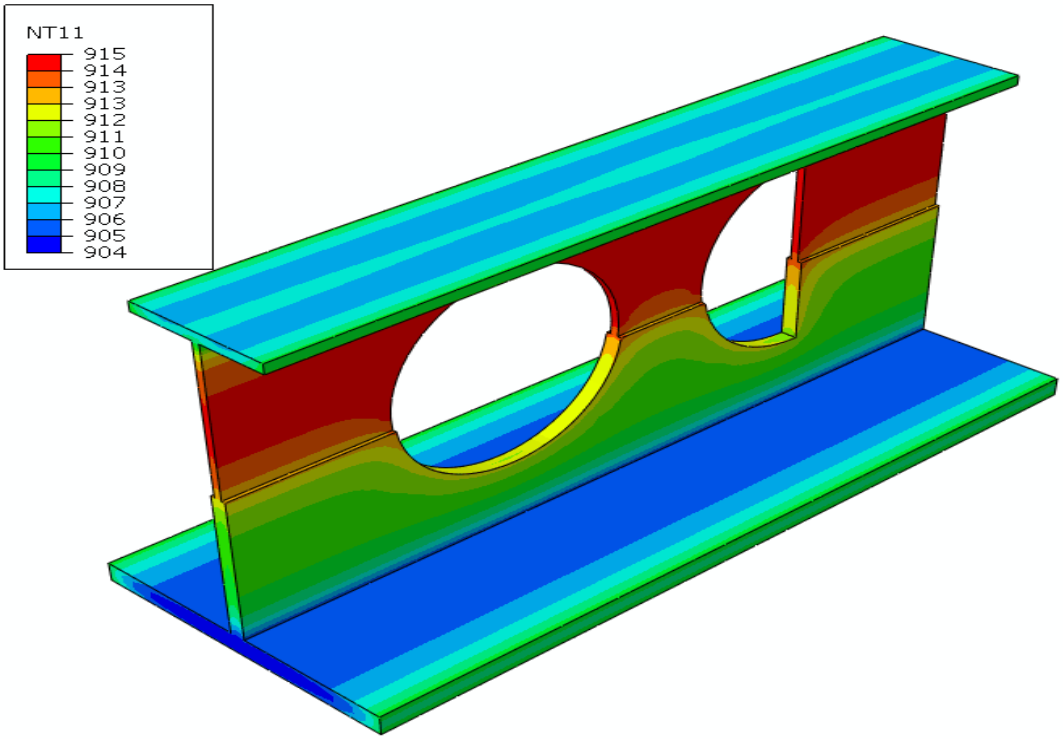

Figure 5.6-4 Temperature contour plot of the cellular beam - no coating (°C)

5.6.2 Beams with 0.8mm coating thickness

This section provides the numerical and experimental results for solid and perforated beams covered with a 0.8 mm thick intumescent insulation. Figure 5.6-5 and Figure 5.6-6 demonstrate the temperature history of the beams. In these figures the numerically obtained temperature profiles of the beams are compared against the temperatures recorded experimentally.

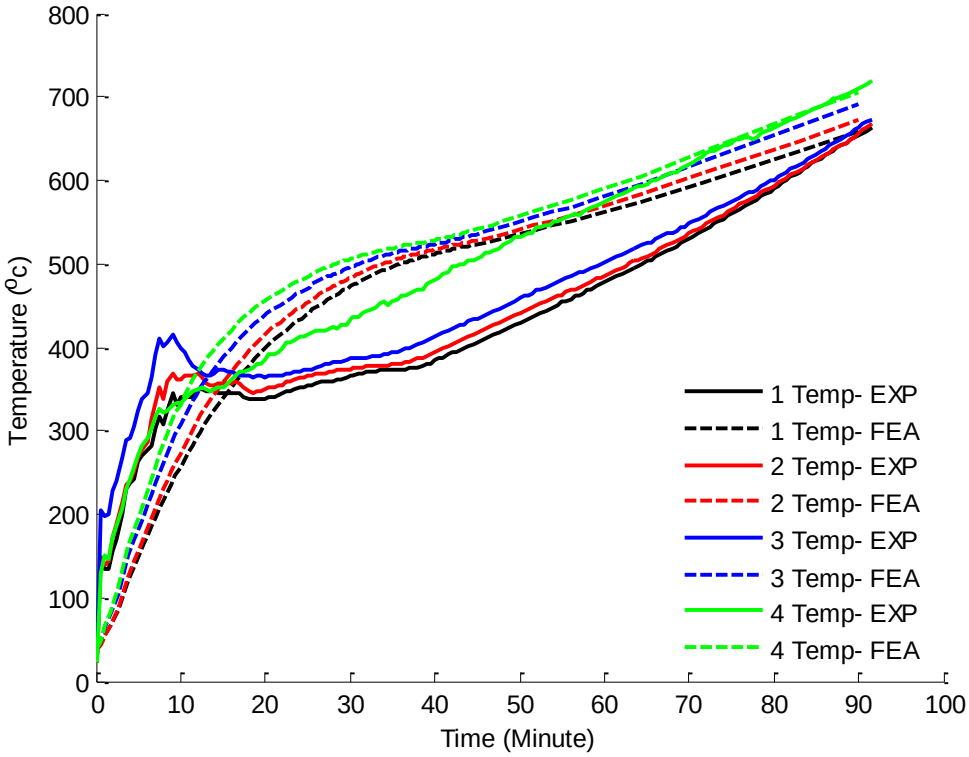

Figure 5.6-5 Temperature history of the solid beam - 0.8 mm coating

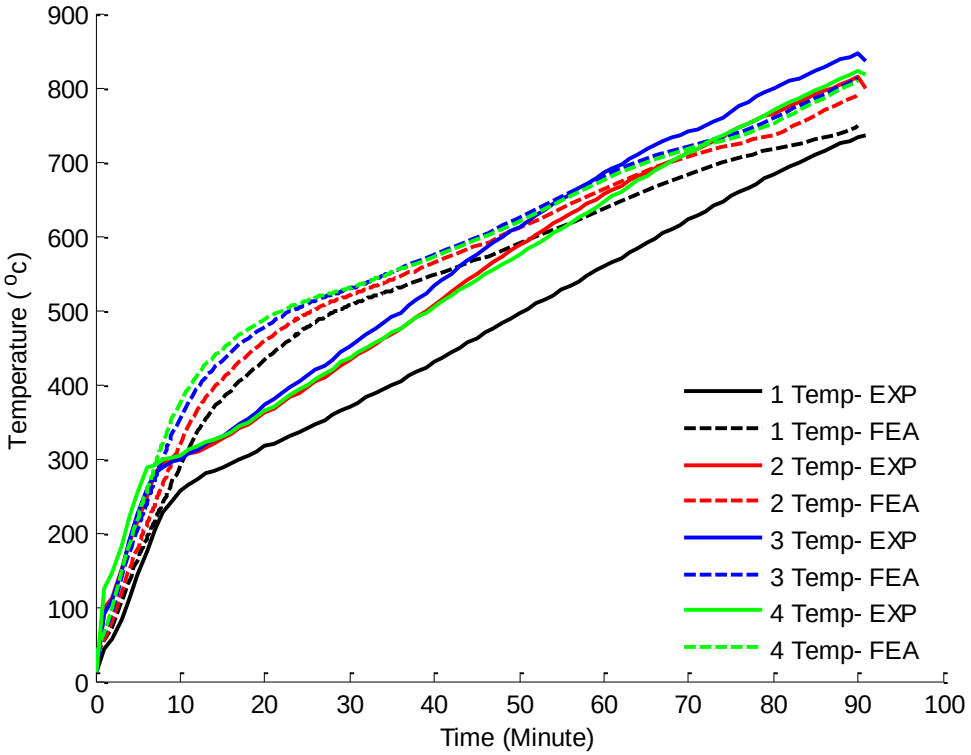

Figure 5.6-6 Temperature history of the cellular beam - 0.8 mm coating

Figure 5.6-7 and Figure 5.6-8 show the numerically obtained temperature contour plot of the beams after 90 minutes. These figures generally show how temperature is distributed in the beams and the overall thermal response of the beams in fire.

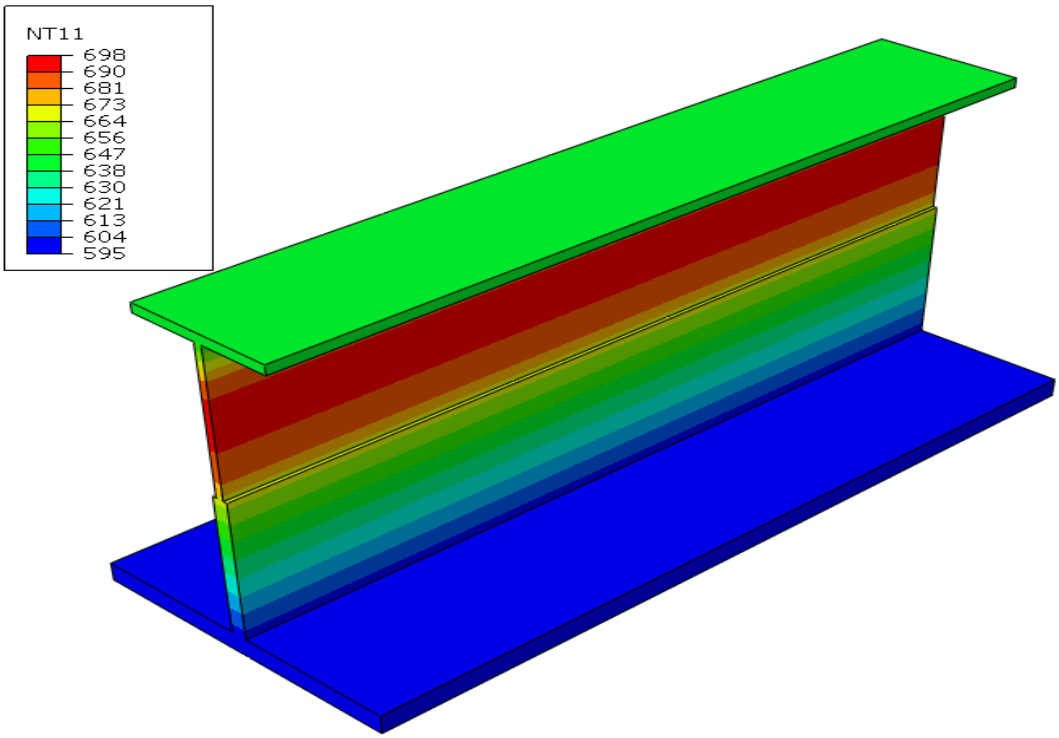

Figure 5.6-7 Temperature contour plot of the solid beam - 0.8 mm coating (°C)

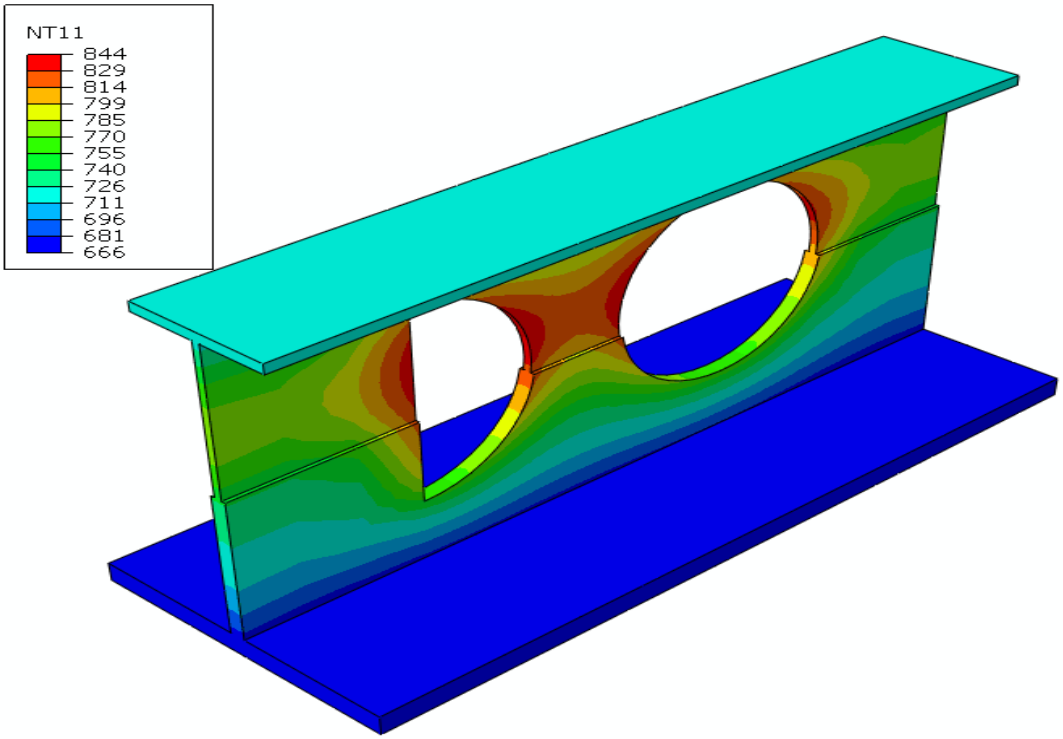

Figure 5.6-8 Temperature contour plot of the cellular beam - 0.8 mm coating (°C)

5.6.3 Beams with 2.1 mm coating thickness

This section shows the numerical and experimental results for the beams covered with a 1.2 mm intumescent coating. Figure 5.6-9 and Figure 5.6-10 show the temperature history of the solid and cellular beams with a 2.1 mm coating.

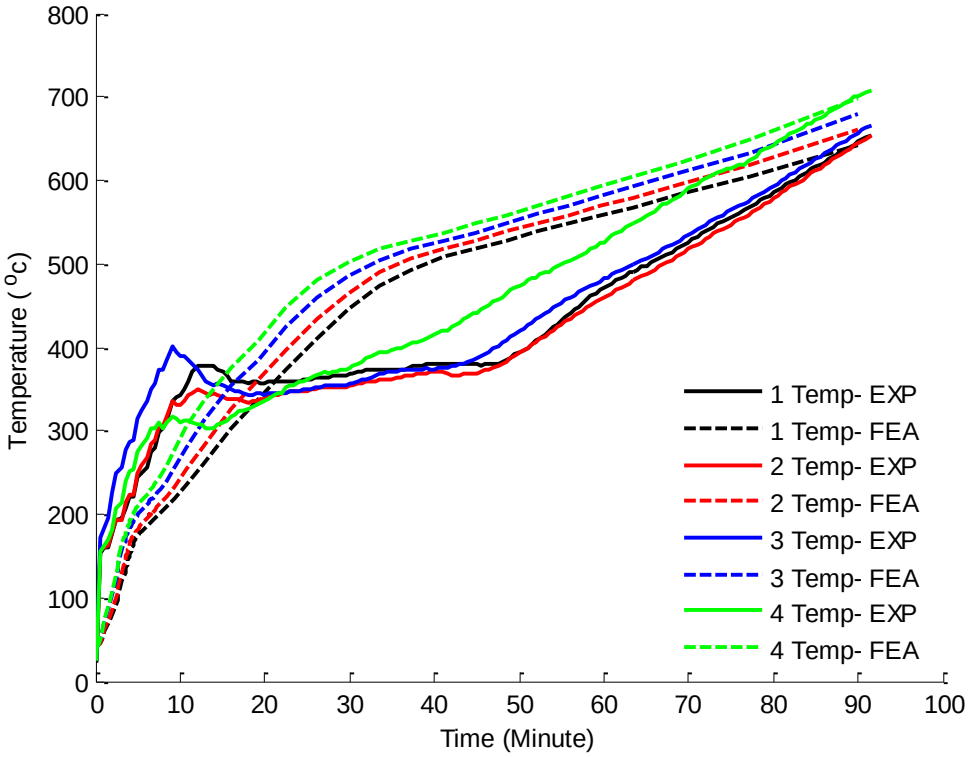

Figure 5.6-9 Temperature history of the solid beam - 2.1 mm coating

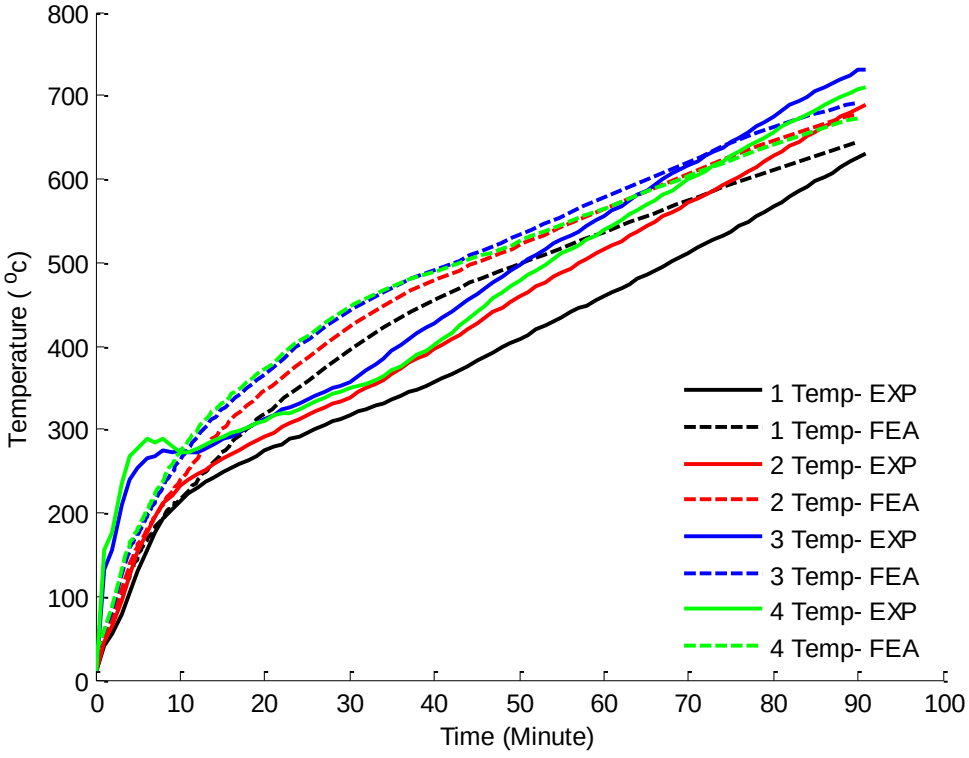

Figure 5.6-10 Temperature history of the cellular beam - 2.1 mm coating

Figure 5.6-11 and Figure 5.6-12 show the temperature contour plot of the beams after 90 minutes.

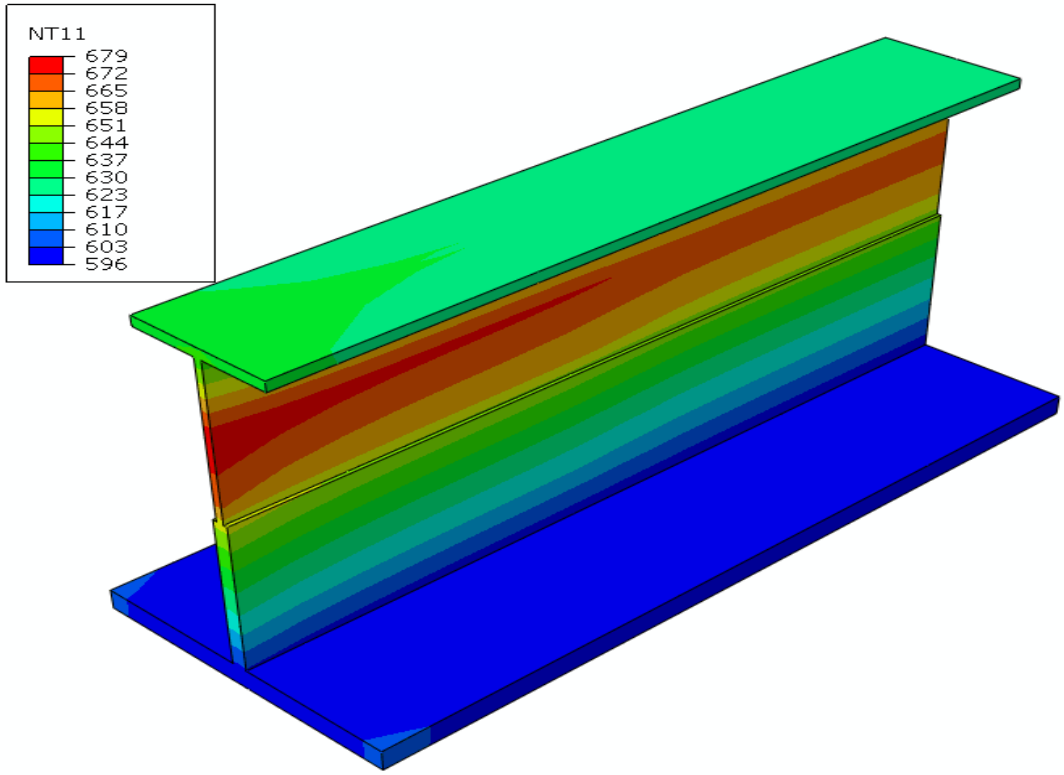

Figure 5.6-11 Temperature contour plot of the solid beam - 2.1 mm coating (°C)

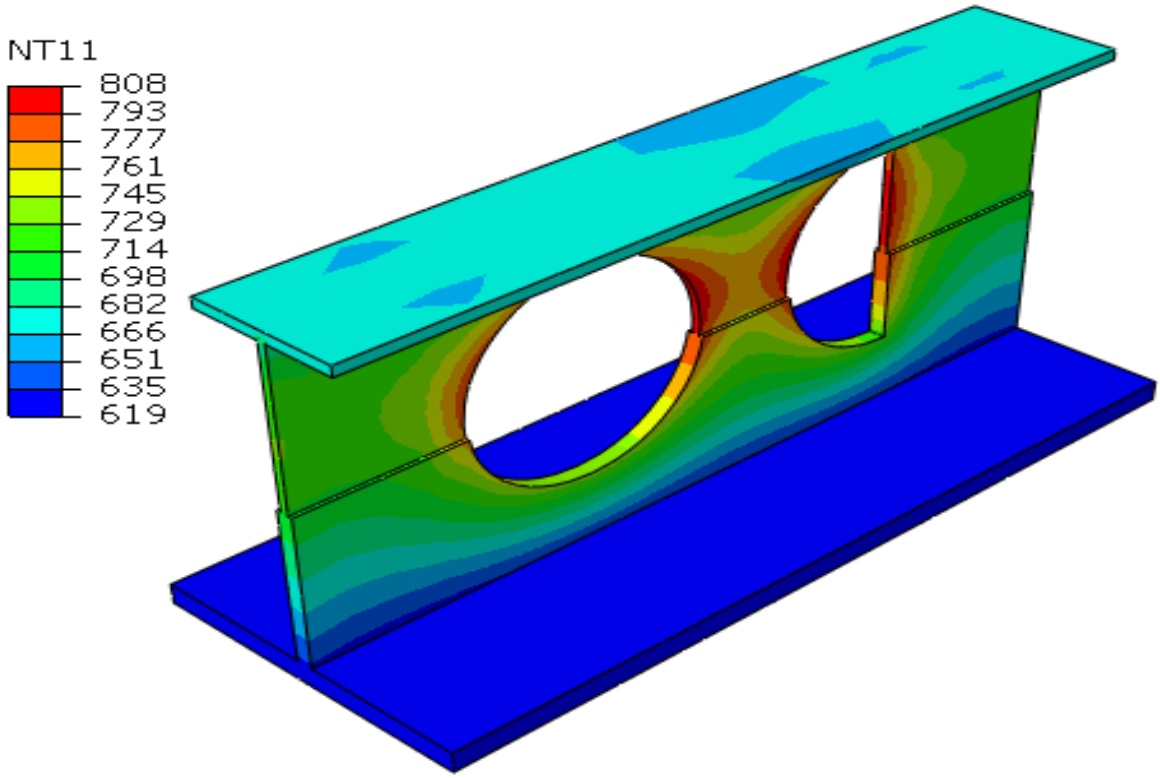

Figure 5.6-12 Temperature contour plot of the cellular beam - 2.1 mm coating (°C)

5.6.4 Parametric study

Figure 5.6-13 shows the nodes with maximum temperatures corresponding to the locations of A2 and A3 thermocouples which are of interest in the parametric study.

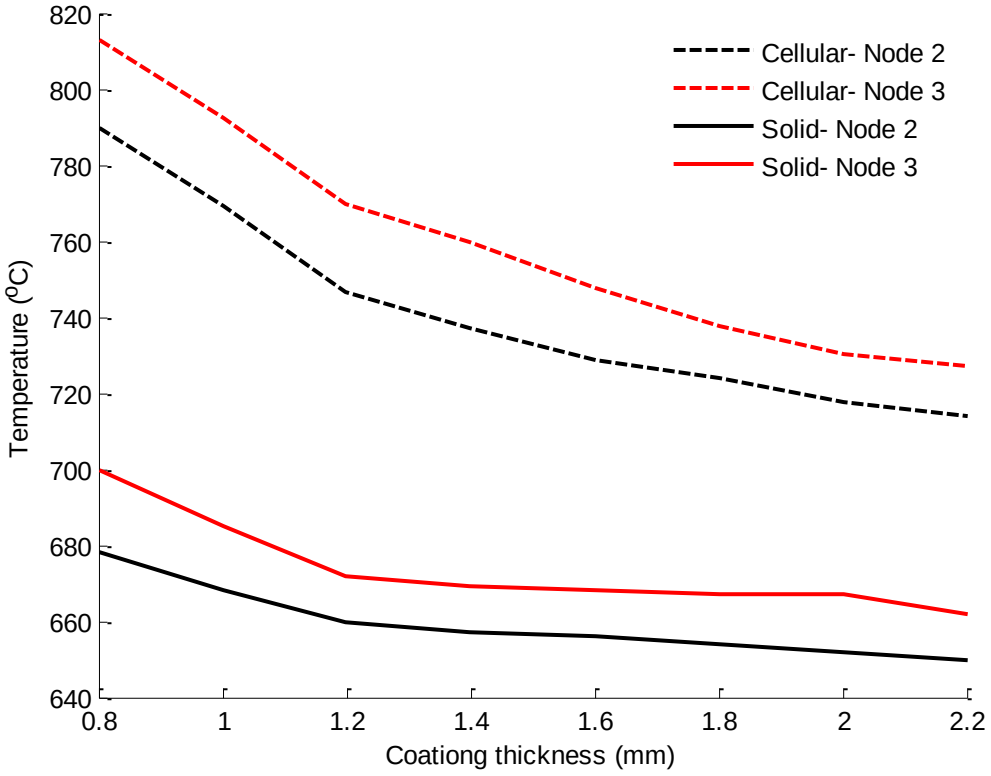

Figure 5.6-13 Maximum temperature of thermocouple nodes with different thicknesses

Figure 5.6-14 shows the temperature history of Node A2 for the solid and perforated beams in which the bottom flanges are directly exposed to a 20 kW/m^2 heat flux.

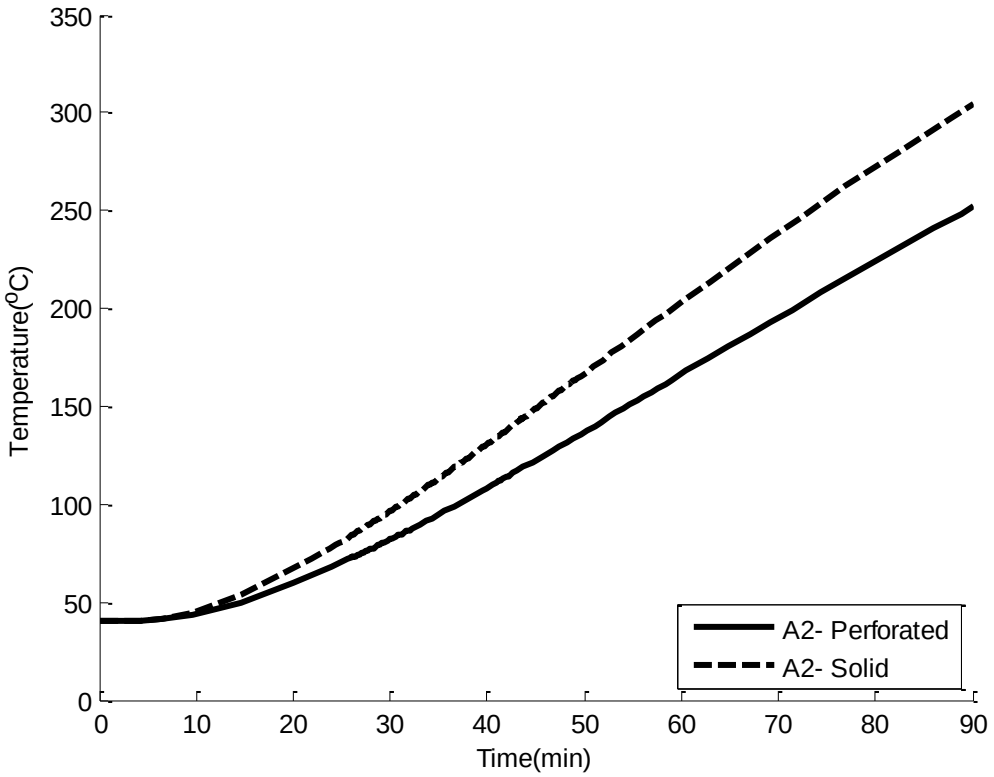

Figure 5.6-14 A2 Temperature, parametric thermal boundary condition study

5.7 DISCUSSION

The temperature profile of webs obtained numerically is in good agreement with the experimental results. The initial rate of temperature increase in the numerical models is less than those obtained in experiments (Figure 5.6-5, Figure 5.6-6, Figure 5.6-9 and Figure 5.6-10). However, the temperature difference between the simulations and the conducted tests decrease after almost 50 minutes for all 4 beams. The temperature of the beams at 90 minutes is of interested in this part of the research as it helps to understand the effect of intumescent coating on the thermal response of the perforated beams for a 90 minutes fire.

This discrepancy between the FEA simulation and experiments may be due to the following reasons:

- The conductivity of intumescent coating is arrived at using the assumption that the temperature of the intumescent coating is uniform through the thickness of the

coating and that it is equal to the average temperature of the furnace and the steel beam.

In reality, the temperature of the intumescent coating is not constant through its thickness. Additionally, the thickness of the coating varies during the activation of the coating at the beginning of experiments. However, as the coating becomes fully activated and the temperature gradient within the intumescent thickness decreases, the estimated conductivity of the coating becomes more realistic. Consequently, the numerical results become closer to the experimental outcomes.

- The effect of latent heat, density loss and endothermic reaction of intumescent coating is ignored in the numerical models. Latent heat is a source of high non-linearity in problems and it does not influence the temperatures of the beams 15 minutes after the initiation of the tests. The temperature of the beams is not increased more than 400°C for the first 15 minutes and the temperature difference due the named parameters does not have any meaningful influence on the overall performance of the beams due to the inherited fire resistance of steel up to 300°C.

The temperature difference between the numerical and the experimental measurements of the beams with a 2.1 mm thick coating is higher than that of the beams with a 0.8 mm coating. The reason is that the temperature of air surrounding the beam with the 2.1 mm coating is not recorded during the experiment. Instead, the temperature of air surrounding the beams with 0.8 mm coating is used in the numerical study of all the beams. This assumed temperature is imposed as a boundary condition in the numerical work and thus influences the results.

Expectedly, the beams with no protection experience higher temperatures. Additionally, due to the high conductivity of steel and the short length of beams, the temperature distribution within the beams is almost uniform. Therefore, there is no

meaningful difference between the temperature profile of the perforated and solid beams.

The comparison between the temperature of the solid and perforated beams at the centre of their webs shows that the temperatures of the web at the centre of the cellular beams are higher than those of the solid beams as shown in Figure 5.7-1 and Figure 5.7-2.

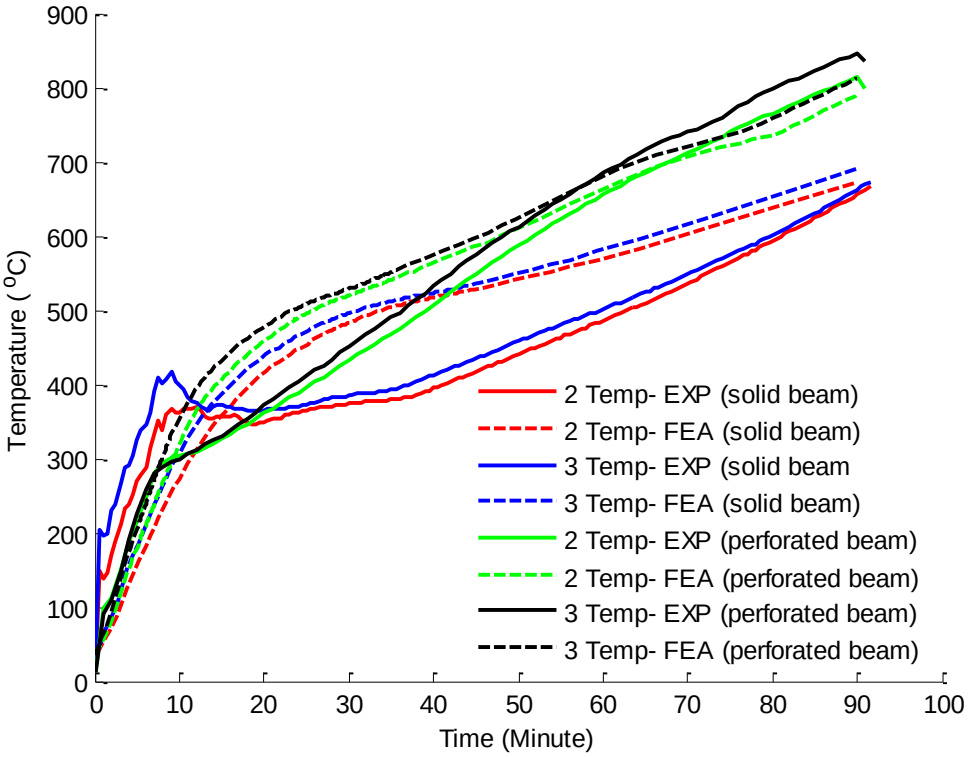

Figure 5.7-1 Temperature of web at the centre area of web, 0.8 mm coating

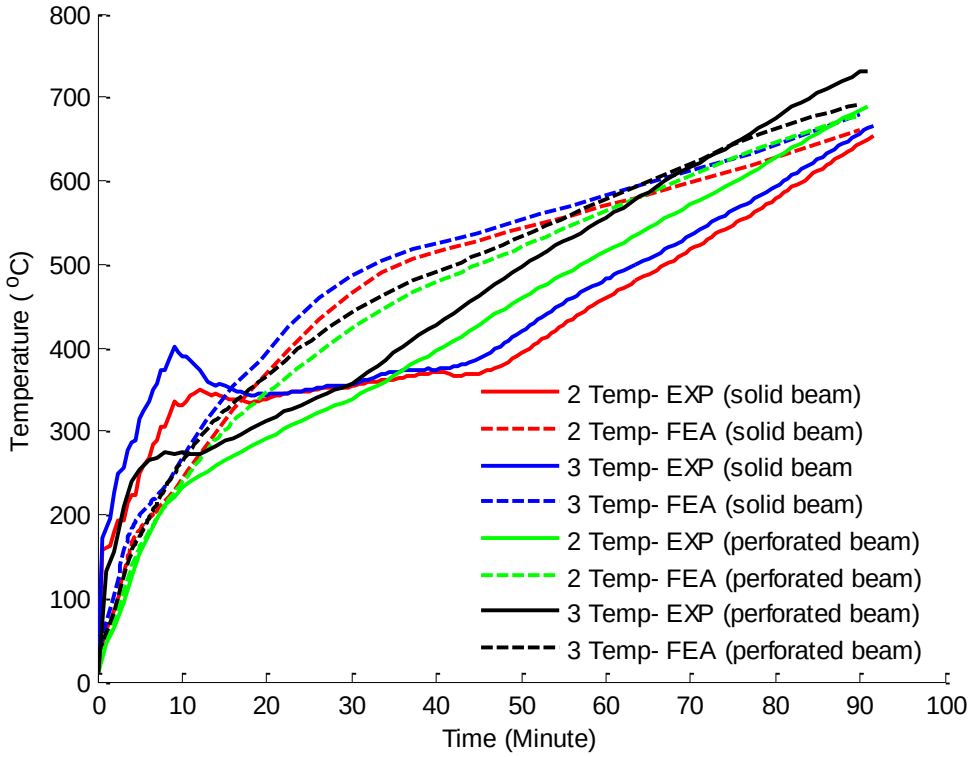

Figure 5.7-2 Temperature of web at the centre area of web, 2.1 mm coating

As shown Figure 5.7-1 and Figure 5.7-2, the temperature difference between the solid and perforated beams with a 0.8 mm thick coating at the centre of their webs are considerably higher than that of the beams with a 2.1 mm thick coating. This temperature difference is about 19%. However, this difference reduces to 8% for the beams with a 2.1 mm thick coating.

At the same time, the results show that the increase in the thickness of the solid beam coating does not have a significant effect on the web temperature of the beams coated with a 2.1 mm and the 0.8 mm thick coating. The web temperature difference between 2.1 mm and 0.8 mm coating for the solid beam is approximately 1.5%.

The parametric study on the thermal boundary conditions show that by solely exposing heat flux directly to the intumescent at the bottom surface of the bottom flange, the web-post temperature is higher the solid web temperature. This implies that the higher

temperature at the web-post is not mainly due to the "pull-back" effect and exposure of the edge openings to the furnace heat. The higher web-post temperatures occur due to heat conduction from the bottom flange which has a higher temperature due to receiving more radiation from the furnace burners. By introducing openings to the web, the cross-sectional area of the web is decreased and consequently the web-post temperature is decreased (see Eq.2.2-1). However, the temperature difference between the web-post and the solid web due to heat conduction is mitigated in the real fire test due to the direct exposure of the web to heat.

5.8 INTERIM SUMMARY

In this chapter, the thermal behaviour of short perforated beams covered with intumescent coating was studied experimentally and numerically. In the experimental study, four asymmetric not-loaded short beams in a furnace were exposed to the standard ISO fire. Two of the beams had a solid web whilst the other two contained circular openings. Out of the two solid or perforated beams, one was tested with an intumescent coating with a thickness of 0.8 mm and the other with a thickness of 2.1 mm. The temperature of the beams was recorded during the experiments.

All the beams mentioned above were modelled numerically. The thermal properties of the coating were extracted from the recorded temperature of the beams during the experiment in accordance with BS EN 13381-8:2013 [33]. Appropriate thermal boundary conditions were defined to simulate the chamber conditions and heat was applied to the surface of the intumescent coating. The numerical solutions were in a good agreement with the experimental results.

The experimental results and the numerical study show that generally the web between the opening has higher temperatures than their identical beams with no openings. These temperature differences are reduced by increasing the thickness.

The numerical techniques used in this chapter to model the thermal behaviour of the coated beams will be used and developed in the next chapters to predict the temperature profile of long loaded beams in a furnace.

CHAPTER 6 - LOADED PROTECTED CELLULAR COMPOSITE BEAM AT ELEVATED TEMPERATURE

Chapter 6 aims to investigate the performance of large scale composite cellular beams at elevated temperatures. The beams investigated in this work are fully protected by intumescent coating. The research is comprised of experimental tests and numerical modelling. The numerical and experimental results are compared against each other for validation purposes to establish the validity of the numerical methods. The methods validated in this chapter are used for further parametric studies and in the modelling and simulation of additional case studies in Chapter 7.

The chapter starts by discussing the study strategy and its aims and objectives in Section 6.1. Section 6.2 explains the experimental setup and the condition of the beams during the experiment. The chapter continues by discussing the numerical modelling and simulation of the experiment in ABAQUS in Section6.3. This includes how the thermal and mechanical boundary conditions, mesh, type of analysis, etc are defined. Section 6.4 presents the experimental and numerical outcomes and provides a comparison between the two. Section 6.5 discusses the results and findings of the numerical and experimental study of the unloaded and coated beams exposed to the ISO fire curve. The chapter concludes with an interim summary in Section 6.6.

6.1 STUDY STRATEGY

Chapter 6 studies the structural performance of CCB at elevated temperatures. Currently, perforated steel beams are the preferred section type for designers as they allow services to pass through and as they are lighter and are made out of less material in comparison to their identical solid beams [69]. However, the lack of precise design guides for perforated beams in the event of fire has emphasised the necessity for further research.

Introducing the opening in the web of beams leads to different failure mechanisms from those of solid beams in fire. The failure is a function of the closeness of openings, the slenderness of web-post sections and the section factor of the beams. Generally, perforated beams fail at lower temperatures than a plan beam with the same geometry. The principal structural failures in perforated beams are web post buckling and Vierendeel failures.

The majority of numerical studies conducted on the performance of perforated beams make use of experimental data to determine the temperature of perforated beams covered with insulation coatings [37, 40-42, 70, 71]. In existing numerical research works, the beams are divided into several sections depending on the number of thermocouples. The average recorded temperature of each section is then assigned to that section in the numerical model. This approach may give rise to inaccuracies as

- It assumes that the temperature profile in each section is uniform which is not true; for web-post sections (for instance see Figure 6.1-2). As it is shown in Chapter 5, the web-post buckling occurs due to formation of compressive struts between openings (see Figure 6.1-1). Inaccurate temperatures in the model lead to inaccurate stiffness values. Consequently, web buckling occurs under loads, which are different to those of the experiment.
- Any errors in the temperatures recorded during the experiment are inherited by the numerical simulations.

In contrast, this research predicts the temperature profile of the beams by exposing the surface of the intumescent coating to heat and simulating the transfer of heat within the coating and the protected steel. This technique is expected to provide an accurate temperature profile of web-post sections. Additionally, predicting web-post temperatures, rather than using an average temperature recorded in an experiment, results in more accurate models of the failure of the beams. The work presented here uses the experimental results for validation purposes.

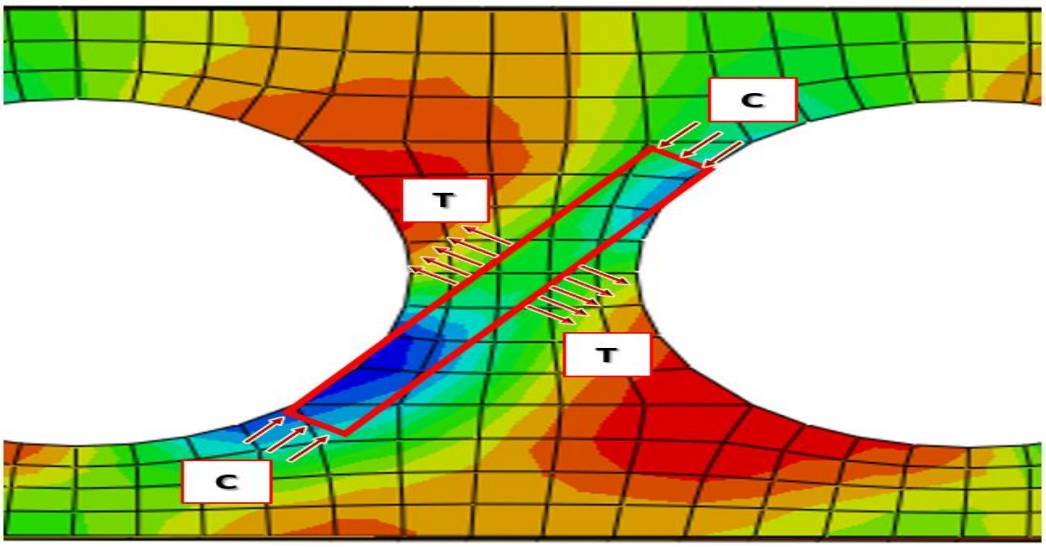

Figure 6.1-1 Compression zone between openings, green and blue regions show compression, red and orange regions show tension

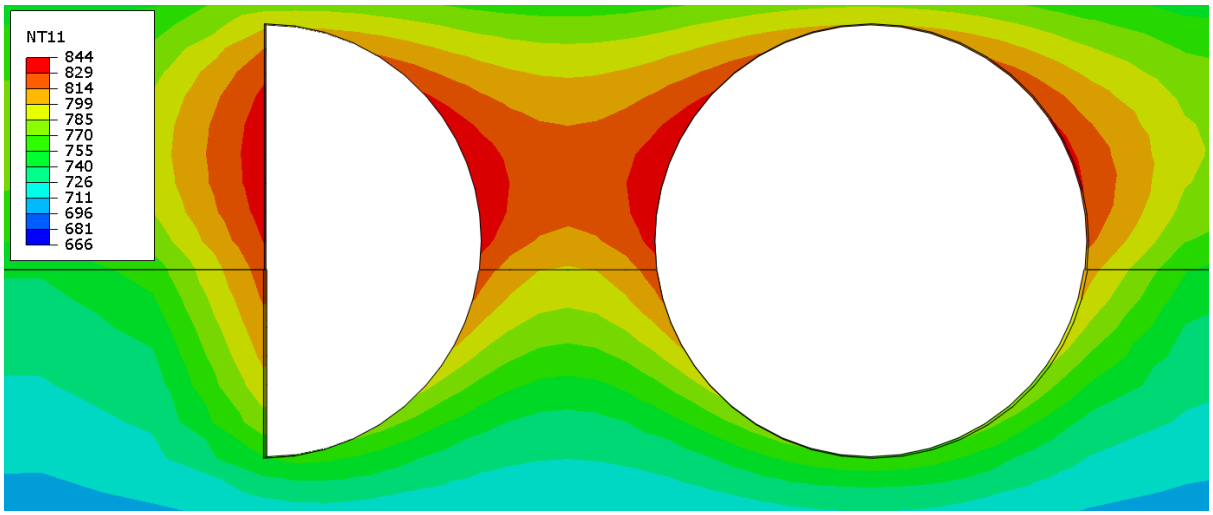

Figure 6.1-2 Temperature profile of the 0.8 mm coated beam after 60 minutes, (°C)

The present chapter utilises the modelling and simulation techniques used in Chapter 4 and 5 (in which the structural and thermal response of coated perforated beams at elevated temperatures are studied respectively) to predict the thermal and mechanical behaviour of the beams.

Three tests were conducted on the loaded CCBs at elevated temperatures at the FireSERT laboratory at Ulster university. The experimental outcomes are used as a base model for the numerical analysis. The temperature and deformation of the beams are measured during the tests. The recorded results are used for the validation of the numerical models.

6.2 TEST SET UP

The present section describes in detail the experiment set up including the geometry of the beams and the thermal and mechanical loads applied. The fire experiments are carried out in a state-of-the-art combustion chamber at the FireSERT laboratory of the University of Ulster. The chamber is 4 m long, 3 m wide, and 3 m high. The furnace is equipped with reaction frames for loading and restraint purposes and is capable of generating a wide range of heating from slow heating curves up to high temperature rapid heating curves (see Figure 6.2-1).

a) Outside view of the chamber

b) Inside view of the chamber

Figure 6.2-1 The combustion chamber in the FireSERT laboratory

6.2.1 Steel beam specifications

Three full-scale CCBs protected by intumescent coating are examined. The length of the beams is 5m and they are fabricated from standard beam sections. The beams are loaded gradually during the experiments with one or two point loads. Figure 6.1-2 demonstrates the configurations of the three beams prior to the tests. Their corresponding geometries are shown in Table 6.2-1.

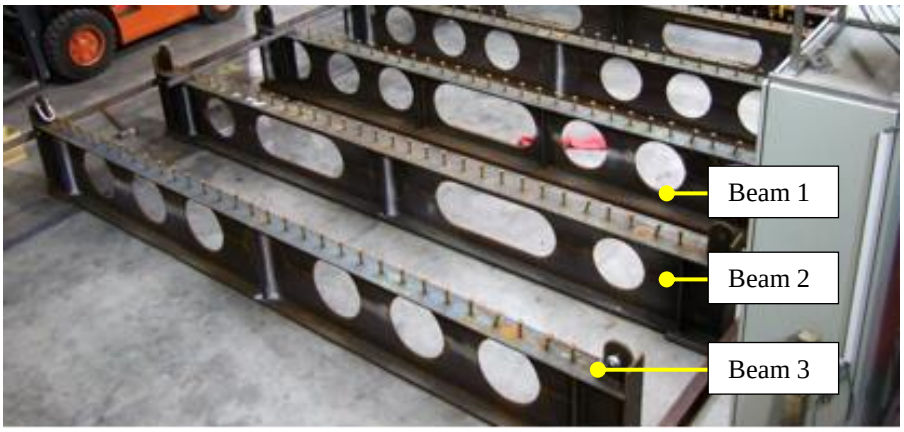

Figure 6.2-2 Configurations of cellular steel beams as they are being prepared for the tests

Table 6.2-1 The geometry of the beams used for FEA simulations

Geometry	Beam 1 (mm)	Beam 2 (mm)	Beam 3 (mm)
Span	4500	4500	4500
Top flange width	172	190	172
Top flange thickness	13	14.5	13
Top tee depth	255	275	255
Bottom flange width	307	190	190
Bottom flange thickness	23.6	14.5	14.5
Bottom tee depth	300	275	300
Web thickness - top	8	9	8
Web thickness - bottom	14	9	9
Overall depth	555	550	555
Cell diameter	375	335	375
Cell spacing	600	600	600

Figure 6.2-3 shows the schematic arrangement of CCBs and the location and magnitude of the applied loads.

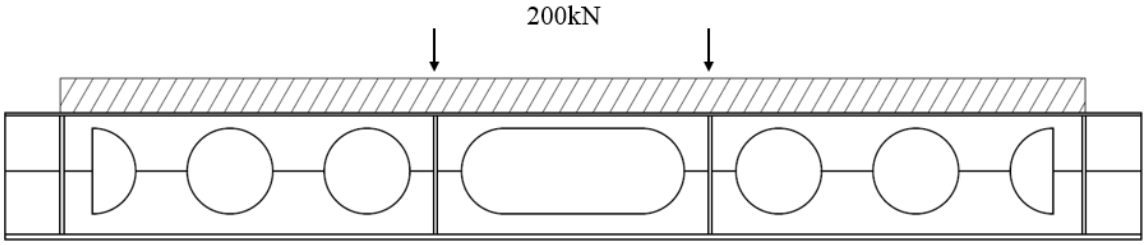

a) Beam 1

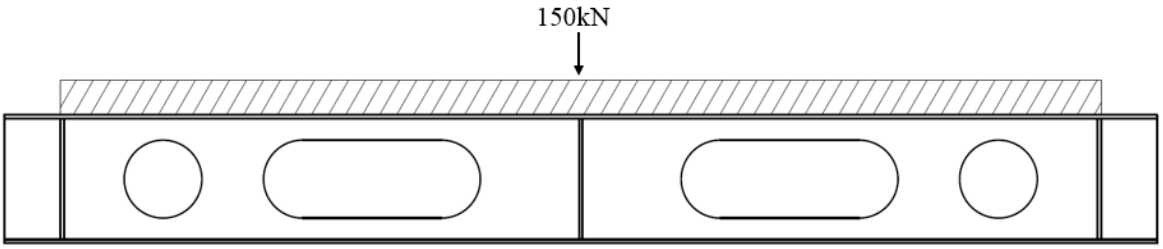

b) Beam 2

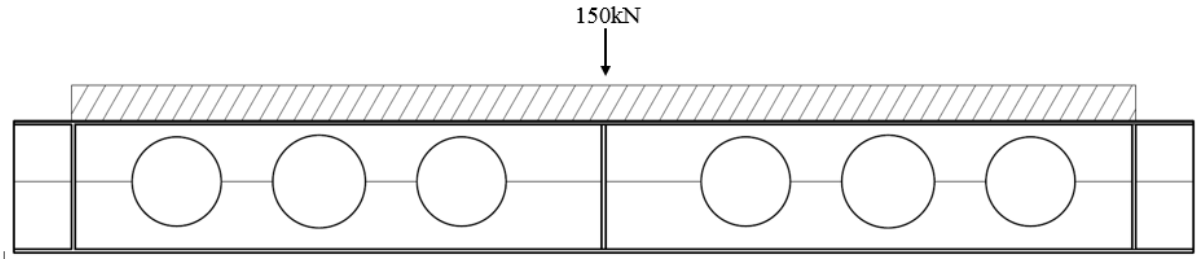

c) Beam 3

Figure 6.2-3 The schematic geometry of beams used for FEA simulations

6.2.2 Concrete slab

Concrete slabs made out of normal-weight concrete (grade 35 N/mm^2) are used in the experiment. The overall thickness of the concrete slab attached to the three beams i.e. from the bottom of the rib of the profiled steel sheeting to the outer face of the concrete slab, is 150 mm. The width of the slab is 1100 mm and its length is 4000 mm.

The compressive strength of the concrete is examined using a compressive strength calibrated machine. The compressive strength is measured on ten cubic samples with a volume of 1000 cm^3. The resistance of the concrete samples to compression are recorded after 1 week, 28 days and on the day of the furnace test. The average value of the measured compressive strength on the day of the test is recorded as 35 N/mm^2.

To prevent the concrete slabs from cracking due to shrinkage, the top surface of the flange of the concrete specimens are kept moist via application of wet burlap for a period of 2 weeks, prior to the furnace test.

The concrete slabs have a 50 mm cover depth and are reinforced using welded A252 Steel mesh with a yield strength of 460 N/mm^2. The mesh is made out of bars of 8 mm diameter forming a 200 mm × 200 mm spacing.

The cellular beams are equipped with headed studs (shear connectors) to ensure a full interaction between the slabs and the cellular beams (Figure 6.4-2). The studs have a 19 mm diameter and a 95 mm height and are located in single rows across the length of the beams. They are equally spaced with a distance of 150 mm between each connector.

6.2.3 Profiled steel sheeting

The steel deck used for all 3 beams is Multideck 50-V2 (Kingspan MD50) with a thickness of 0.9 mm. The steel properties follow BS EN 10143 and BS EN 10147 with a minimum yield strength of 350 N/mm^2 and a minimum total coating mass of 275 g/m^2. Figure 6.2-4 shows a photo of the decking and Figure 6.2-4 provides a diagram of its dimensions.

a) Preparation of steel decking

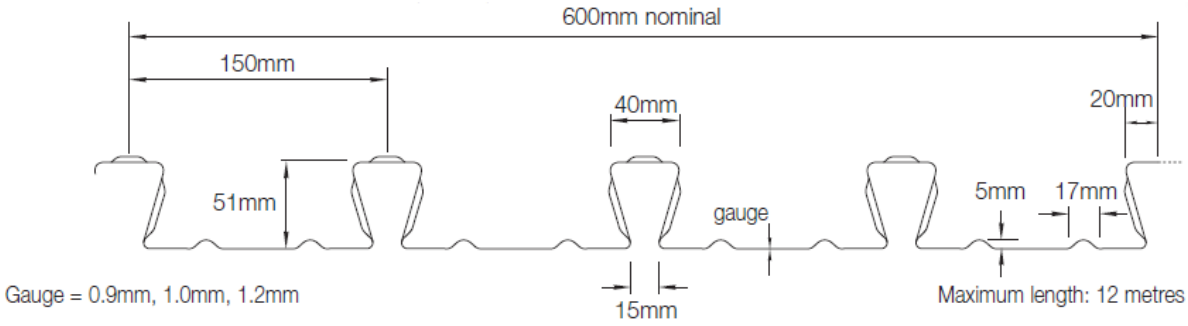

b) Steel decking dimensions [72]

Figure 6.2-4 Steel decking

6.2.4 Intumescent coating

Nullfire S707-60 intumescent coating material is applied to the cellular beams. The intumescent coating is applied in three steps (see Figure 6.2-5). Initially, a primer coating is applied along the openings. This is followed by the application of the primer coating along the full length of the beams. Finally, the intumescent coating is applied. The thicknesses of the applied layers are measured accurately during each step such that the resulting overall thickness meets the thickness that provides a 60-minute fire protection.

The resulting thicknesses of the intumescent coating applied to beams 1, 2, and 3 are 606 µm, 2586 µm and 3637 µm, respectively.

a) Application of primer coating around openings

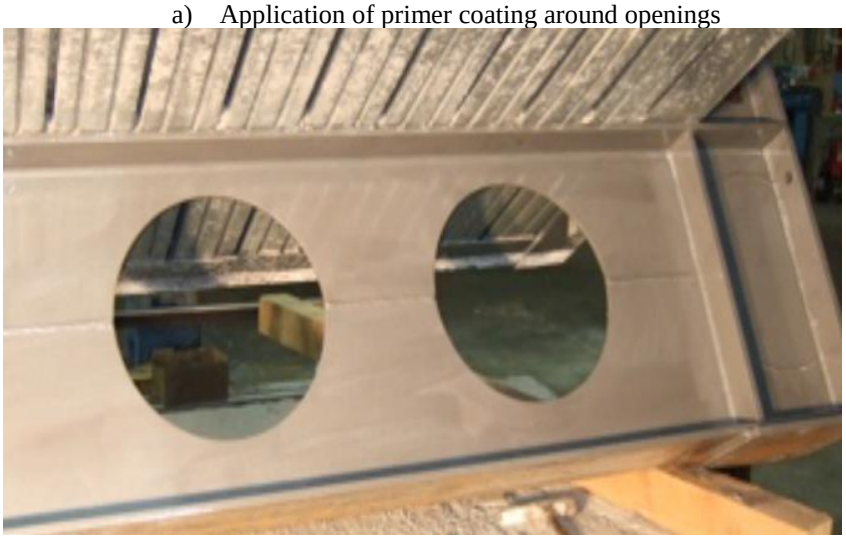

b) Application of primer coating along the beam

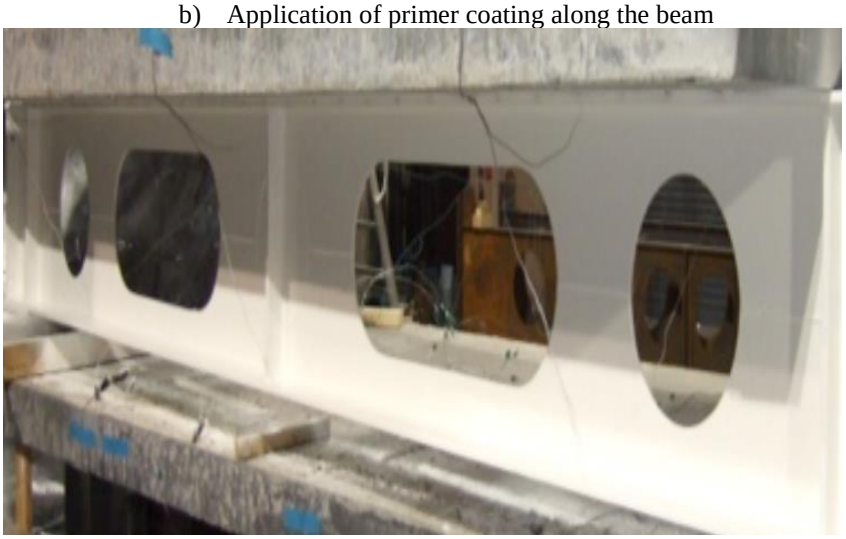

c) Application of intumescent coating along the beam

Figure 6.2-5 Procedure of application of the intumescent coating

6.2.5 Loading

The cellular beams are subjected to concentrated loads, which are symmetric about the mid-spans of the beams. The furnace has four external movable frames, which can be arranged as required across the furnace length. The frames support hydraulic pressure actuators, which can be positioned at any location along the span of the frames. The maximum force exerted by the actuators is 1250 kN. The loading system is self-equilibrating, the chamber walls only need to support the self-weight of the main frame and portals.

The loads applied to beams 1, 2 and 3 are 200 kN and 150 kN, respectively as shown in Figure 6.2-3. The loading is considered to be approximately 30% of the ultimate load found from the design of beams for 20°C and by considering previous tests conducted at the University of Ulster [37].

Once the beams are loaded, the burners of the furnace are turned on. Temperature of the furnace is set to the ISO834 standard fire curve [73], which can be expressed as

$$T = 345\log_{10}(8t + 1) + 20 \qquad 6.2\text{-}1$$

where T denotes the furnace temperature at time t. The units of T and t are degrees Celsius and minutes, respectively.

6.2.6 Temperature measurement

In order to take temperature readings during the tests, *K* Type sheathed thermocouples with 1 mm diameters are used. As shown in Figure 6.2-6, the thermocouples are attached to the 3 beams at various locations. The thermocouples are attached to the beams prior to the application of the coatings (see Figure 6.2-7).

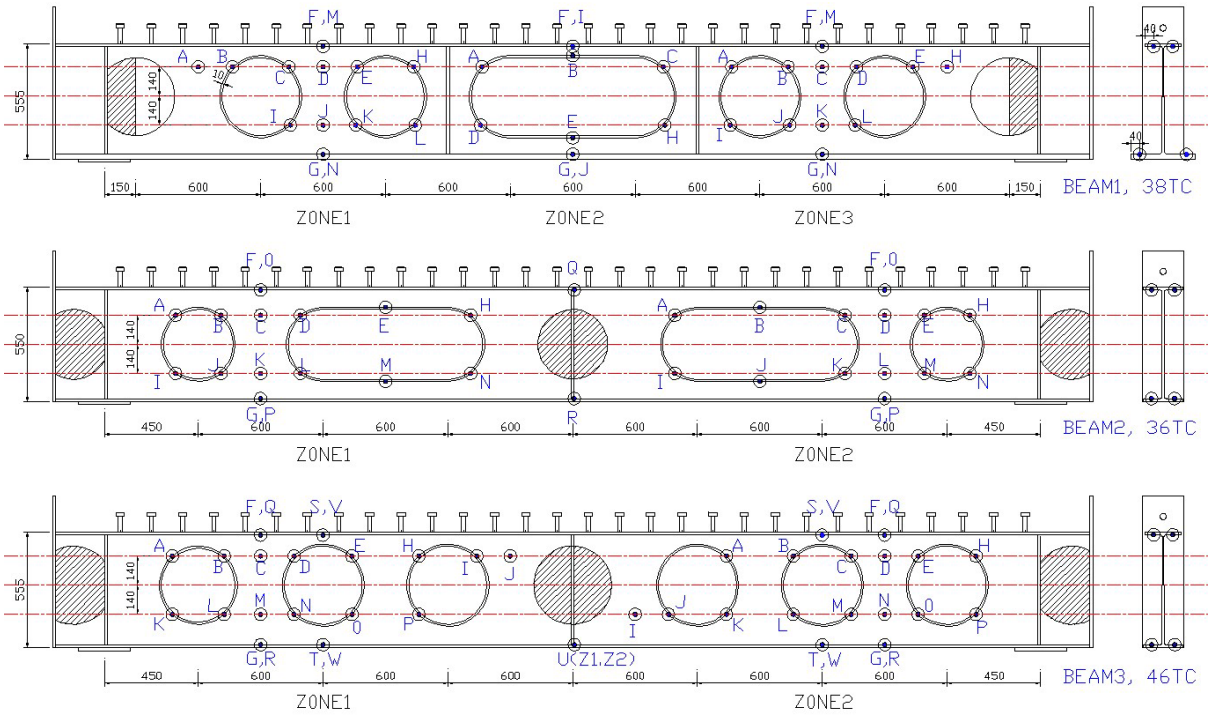

Figure 6.2-6 Location of thermocouples on CCBs

Figure 6.2-7 Thermocouples on protected CCBs

6.2.7 Deformation measurement

Five linear differential transducers (LVDT) are employed to measure the deformations of the beams around the mid-span of the beams during the furnace test. The LVDTs are located at different locations on top of the concrete slabs as shown in Figure 6.2-8.

a) Portal frame b) Hydraulic jack, spreader beam and LDVT

Figure 6.2-8 General arrangements of the jack and LDVTs

6.3 SIMULATION METHODOLOGY

This section discusses the procedure of creating a numerical model to simulate the behaviour of perforated beams at elevated temperatures and under the loadings conditions described in Section 6.2.

6.3.1 Thermal boundary conditions

This section discusses the thermal conditions at the boundaries of the models and the interactions between the beam and its surrounding air. In this section, it is explained how the heat transfer between the furnace ambient and the beams is modelled in such a way that leads to acceptable beam temperature profiles.

Generally, heat is transferred from a gas medium to a solid by radiation and convection. The general heat transfer equation by radiation and convection is given by $h_c(T - T_s) + \varepsilon\sigma(T^4 - T_s^4) = \rho V C_v \frac{dT}{dt}$ **6.3-1**

where T is gas temperature, T_s is solid temperature, h_c, σ and ε is convection coefficient Stefan–Boltzmann constant and emissivity of the exposed surface. ρ, V and C are density, volume and specific heat of the exposed surfaces. It is evident from Eq.6.3-1, that defining an accurate emissivity, convection coefficient, and the surrounding temperature of

the exposed surfaces are the main parameters that define the thermal boundary of the problem. The following sub section explains how these three variables are used in ABAQUS to define the appropriate thermal boundary conditions.

6.3.1.1 Surrounding temperatures

Furnace temperature

The fire load in the experiments is set to the ISO 834 fire curve. During the experiment, the furnace temperature is measured using 8 thermocouples located in various locations around the beams. These recorded temperatures are used in the numerical model to define the boundary condition. Using the recorded temperature instead of the ISO 834 fire curve provides more accurate boundary conditions as the temperature around the beam may not be uniform. In order to calibrate the surrounding temperature, two sets of analysis are carried out for Beam 2 with two different furnace temperatures as follows:

1. **Average furnace temperature**: the temperature of the furnace is assumed to be uniform and equal to the average temperature of the 8 thermocouples. Therefore, the ambient temperature for the convection and radiation function is set to the average temperature of the furnace.
2. **Localized furnace temperatures:** previous tests on composite beams different to the ones used in this research at the University of Ulster shows that shadow effects leads to discrepancies in the temperature measurements between the bottom and top flanges with the same section [74]. As Figure 6.3-1 shows the upper flange is not directly subjected to radiations of the burners below the furnace. This means that the lower flange is receiving more radiation than the rest of the beam and consequently has higher temperatures.

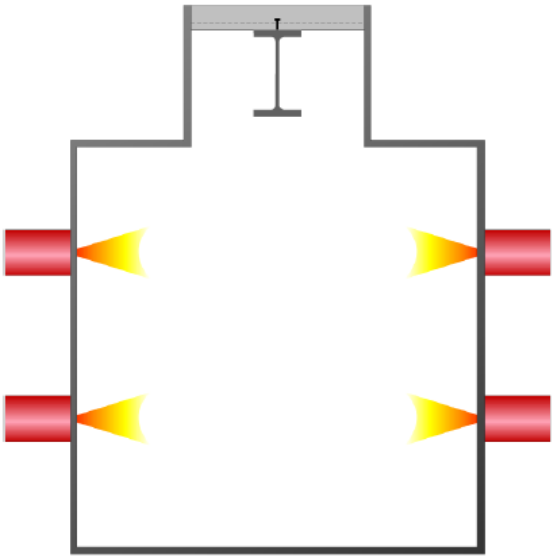

Figure 6.3-1 Schematic burner arrangement [74]

In order to account for the shadow effects on the thermal boundary conditions, three different furnace temperatures are defined for the bottom flange, web and upper flanges. Instead of using the average temperature of all thermocouples as the ambient temperature of the entire beam in the convection and radiation functions of the FEA package, the experimentally measured temperatures around the web, upper and lower flange of the beam are assigned to the relevant part of the beam in the FEA.

As mentioned previously, during the experiments, 8 thermocouples record the temperature of the furnace surrounding the beams. Figure 6.3-2 shows the recorded temperatures of the furnace by each thermocouple. Table 6.3-1 shows the temperature of which thermocouples are assigned to which part of the beam.

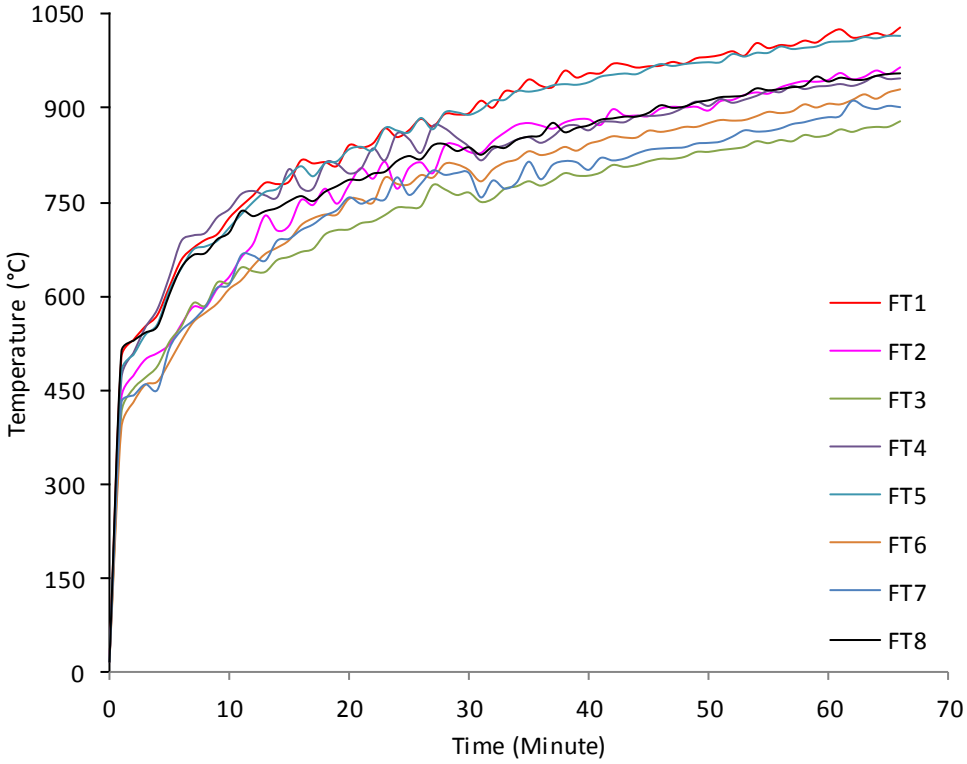

Figure 6.3-2 Furnace temperature

Table 6.3-1 Furnace thermocouples location

Thermocouple No.	Location
FT 1	Lower Flange
FT 5	Lower Flange
FT 2	Web
FT 4	Web
FT 6	Web
FT 7	Web
FT 8	Web
FT 3	Upper Flange

Laboratory ambient temperature

The laboratory temperature is recorded during the experiment. The upper side of the concrete slab is directly surrounded by the air in the laboratory. Hence, the recorded

laboratory ambient temperature is assigned to the upper surface of the slab in the FEA model.

6.3.1.2 Interactions

Convection and radiation interactions are defined between the furnace and the intumescent coating and between the furnace and the bottom surface of the concrete slab (steel deck), and between the top surface of the concrete slab and the lab ambient.

To calculate the heat transferred by convection, the convection coefficient and ambient temperatures are required. The governing equation to calculate the convection coefficient *h* in a turbulent flow is

$$h = \frac{K}{L} 0.037 \mathrm{Re}^{\frac{4}{5}} \mathrm{Pr}^{\frac{1}{3}}, \qquad 6.3\text{-}2$$

where *K*, *L*, *Re* and *Pr* are conductivity, surface length, Reynolds and Prandtl numbers, respectively. In a standard fire, the convection coefficient is assumed to be 25 W/m^{2}k [2, 13, 66, 67, 75]. This value is adopted in the work presented here.

The emissivity of the intumescent coating in different publications is reported between 0.7 and 0.95 [67, 68, 76]. This research work sets the intumescent coating emissivity to 0.9 as this is the recommended value by the intumescent material provider.

The emissivity of the steel deck is set to 0.4 [77]. This is discussed in more detail in Section 6.3.2.3. The convection coefficient of the furnace and emissivity of the intumescent are used previously in the modelling of the unloaded short beam presented in Chapter 5. As mentioned in this chapter, the numerical results of the short beams were in good agreement with the experimental results.

The emissivity of the upper surface of the concrete slab is set to 0.8 [78] and its convection coefficient is set to 20 W/m^{2}K. Table 6.3-2 shows a summary of the values of emissivity and convection coefficients used throughout the experiment.

Table 6.3-2 Interaction properties

Item	Emissivity	Convection coefficient
Upper surface of concrete	0.8	20 W/m^{2}K
Steel deck	0.4	25 W/m^{2}K
Intumescent	0.9	25 W/m^{2}K

It is assumed that there are no air pockets between beam and coating after the coating activation and consequently all the heat is transferred between the coating and the steel beams. Therefore, fully thermal restrained interactions are defined between the intumescent and the steel beams.

6.3.2 Thermal properties

6.3.2Section 6.3.2 discusses how appropriate material properties are defined and assigned to the models.

6.3.2.1 Concrete

The thermal properties of concrete are taken from Section 6.1.2 of BS EN 5950-8-2003 [62]. Figure 6.3-3 and Figure 6.3-4 depict the variation of thermal conductivity and specific heat of concrete against temperature, respectively.

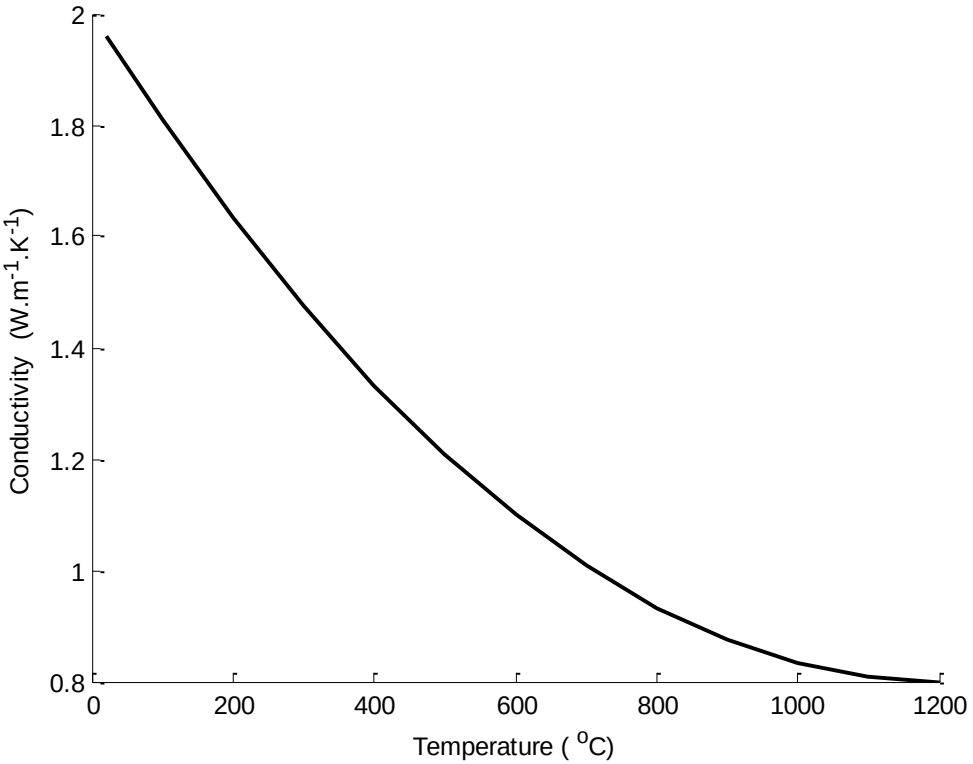

Figure 6.3-3 Thermal conductivity of concrete - BS 5950-8

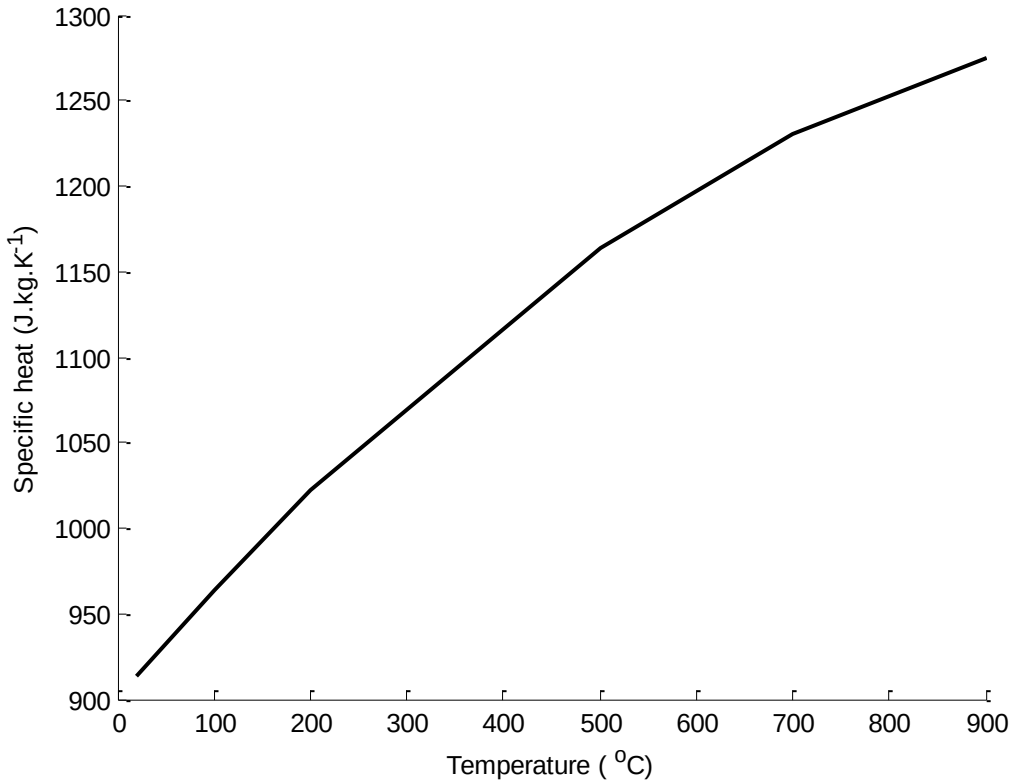

Figure 6.3-4 Specific heat of concrete - BS 5950-8

6.3.2.2 Steel thermal properties

The thermal properties of steel are extracted from BS EN 5950-8-2003 [62]. Figure 6.3-5 and Figure 6.3-6 show the variation of thermal conductivity and specific heat of steel with temperature, respectively.

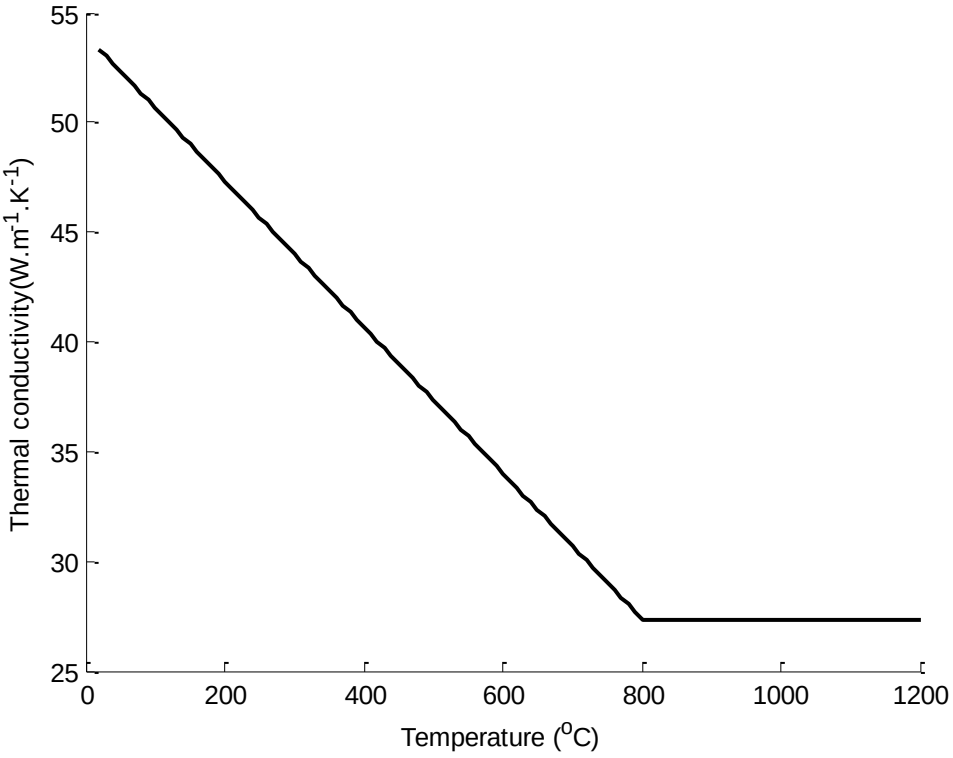

Figure 6.3-5 Thermal conductivity of steel - BS 5950-8

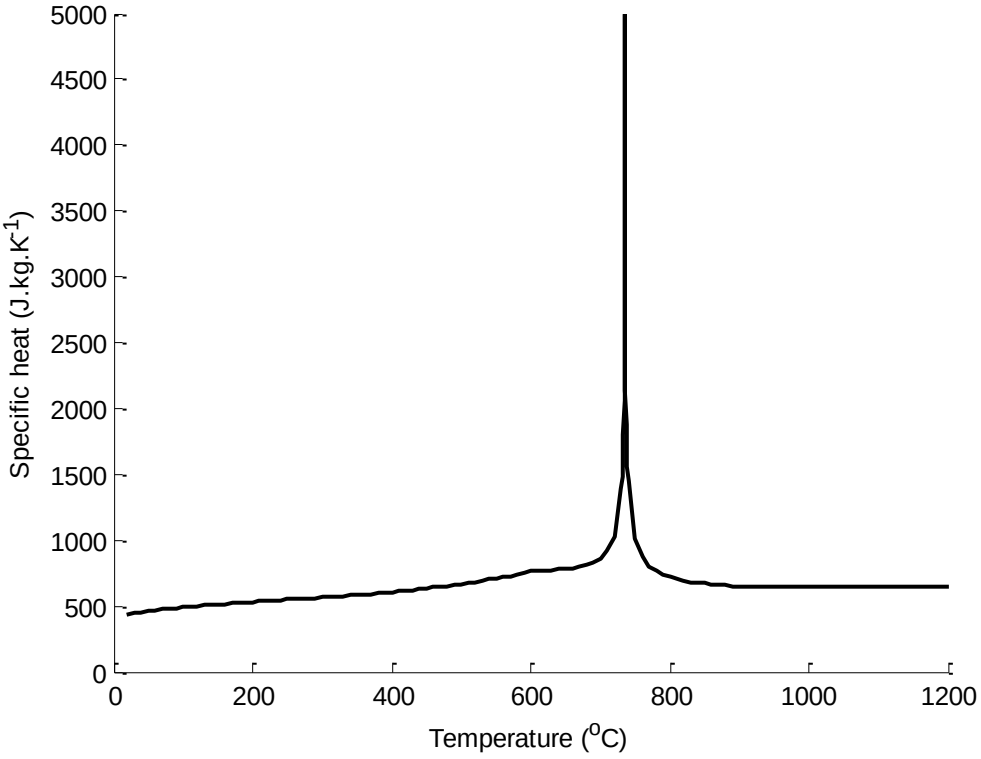

Figure 6.3-6 Specific heat of steel - BS 5950-8

6.3.2.3 Steel deck

The steel deck is modelled as part of a composite layer within the concrete slab. Therefore, it is not added as an independent part in the FEA models. The temperature gradient within the steel deck due to the high conductivity of steel and the small thickness of the steel deck can be neglected. Therefore, adding the steel deck as a separate part to the FEA model does not have any influence on the FEA results. This is explained in further detail in Section 6.3.5.4.

However, in the experiment the steel deck was exposed to radiation from the furnace during the test and the rate of radiation absorption by the steel deck has a meaningful effect on the thermal behaviour of the model. The Steel Construction Institute conducted a research on the emissivity of the steel deck and recommends an emissivity of 0.4 [77]. As the steel deck is not included in the model, the emissivity of 0.4 is assigned to the lower surface of the slab to account for the radiation absorbed by the steel deck during the test.

6.3.3 Specific heat and density of intumescent coating

Intumescent coatings lose a significant amount of mass during swelling. This implies that a negligible amount of heat energy is stored inside the intumescent coating. As a result, implementing an accurate temperature dependent specific heat and density in the FEA model does not have a meaningful effect on the final outcome. Hence, the specific heat and density of the intumescent are set as temperature independent. Using a temperature independent density and specific heat, reduces the nonlinearity of the problem and reduces the simulation time. The specific heat of the intumescent coating is set to 1000 J/kg$^{\circ}$C in accordance with Equation E.7 of BS EN 13381-8:2013 [33]. The density of the intumescent coating is set to 1000 kg/m^3 [65].

6.3.4 Thermal conductivity of intumescent

Due to the fragile nature of the intumescent coating, it is impossible to measure the surface temperature of the activated coatings. Therefore, the definitive effective thermal properties of the coating used in the experiment are unknown. Additionally, as the beams used in the experiment are cellular rather than solid, the methods recommended by BS EN 13381[33] to predict the thermal conductivity of the coatings based on the experimental results are not valid. Annex D of BS EN 13381-8 provides a correction (stickability correction) factor. This factor is applied to the thermal properties of coatings, which are extracted from short and unloaded beam tests to alter the thermal properties of the coatings for their application on long and loaded beams. However, according to Table D.1, the correction factor is not applicable for perforated beams.

Here, the thermal conductivity value estimated from the previous tests presented in Chapter 5. However, the thickness of the coating used in the experiments presented in this chapter is slightly higher than those used in the unloaded solid beams experiment. The thicker layer leads to a lower conductivity. Figure 6.3-7 shows that the temperature difference between the results obtained from FEA of beam 2 (loaded CCB) using the conductivity of the unloaded solid beam test and the test outcomes of beam 2.

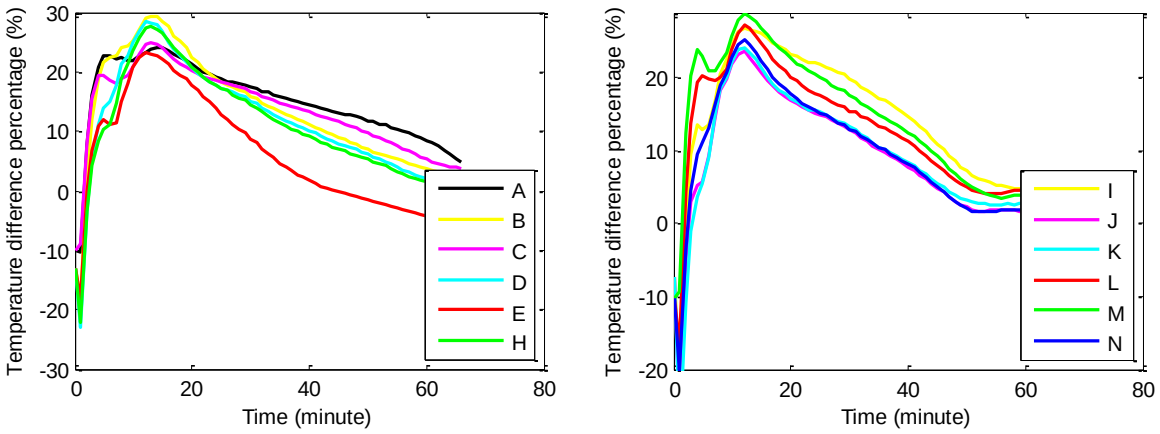

a) Thermocouples A to H

b) Thermocouples I to N

Figure 6.3-7 Temperature difference between FEA and test results

Figure 6.3-7 shows that as expected due to the implementation of a lower conductivity the FEA temperature results are higher than the experimental results.

As discussed in Section 6.3.3, the density and the specific heat do not have any meaningful influence on the thermal behaviour of the coating. In fact, conductivity is the main variable that affects the temperature of the beam. Therefore, a sensitivity study was carried out to calibrate the thermal conductivity of the intumescent coating for this test.

Figure 6.3-7 shows that the temperature differences between the FEA and the test results increase up to 30% in the first 12 minutes and then they are drop at a slower rate. In the FEA models, temperature dependent thermal conductivity is used. This means that the FEA temperatures are higher than the measured temperatures. Therefore, it can be concluded that the implemented thermal conductivity of the coating in the first 10 minutes (considering a 2-minute time lag for transferring heat within the coating) is higher than the real conductivity value of the coating. It is assumed that the average temperature of the intumescent coating along its thickness is equal to the average temperature of the furnace. The average temperature of the furnace after 10 minutes is approximately 650°C. Therefore, for the sensitivity study the conductivity of the coating for temperatures above

650°C is kept the same as the initial conductivity used. Three different batches of conductivity values are studied as shown in Table 6.3-3. Figure 6.3-8 shows the result of the sensitivity study.

Table 6.3-3 Conductivity sensitivity study

	Batch 1	**Batch 2**	**Batch 3**
Ratio of the batch conductivity to the conductivity extracted from the solid unloaded beam test (see Chapter 5)	0.5	0.25	0.125

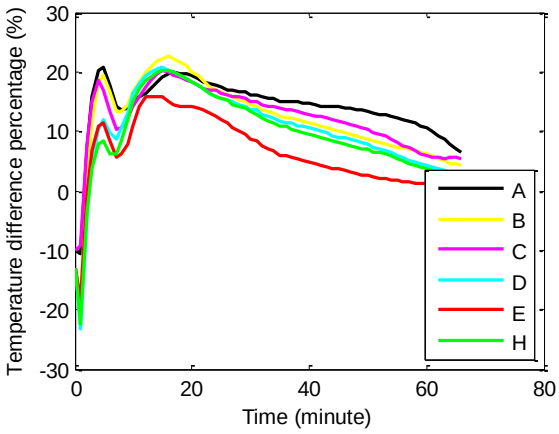

a. Batch 1, thermocouple A to H

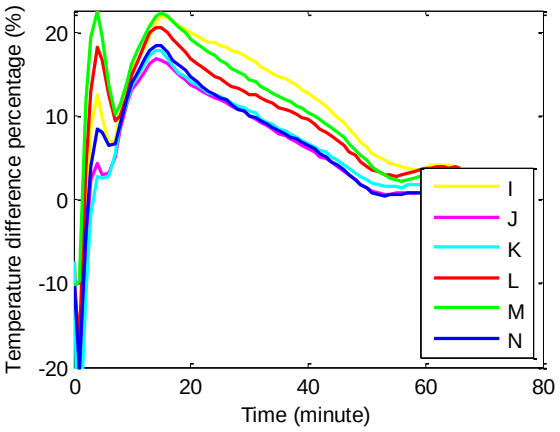

b. Batch 1, thermocouple I-N

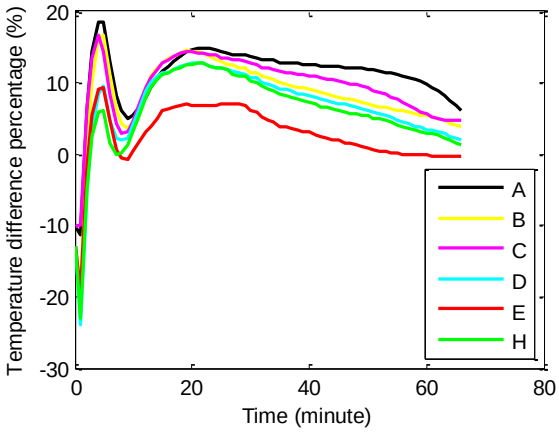

c. Batch 2, thermocouple A to H

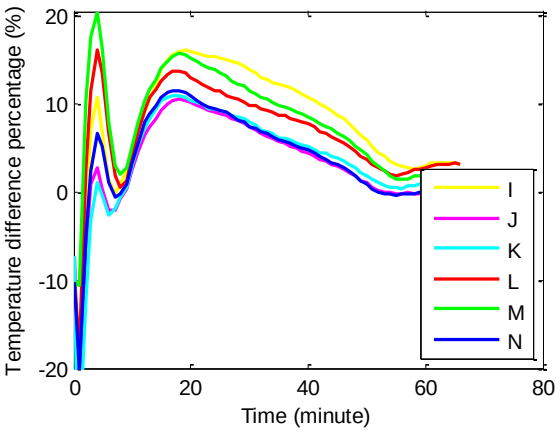

d. Batch 2, thermocouple I-N

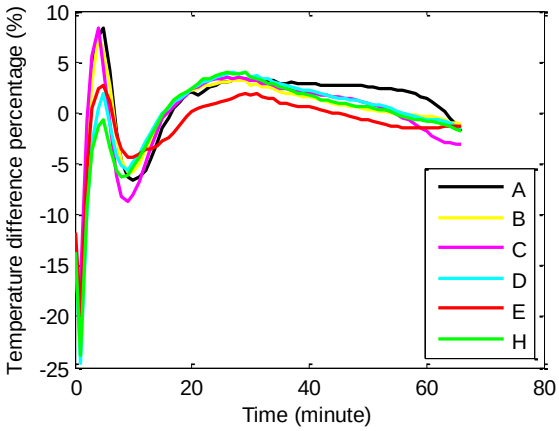

e. Batch 3, thermocouple A-H

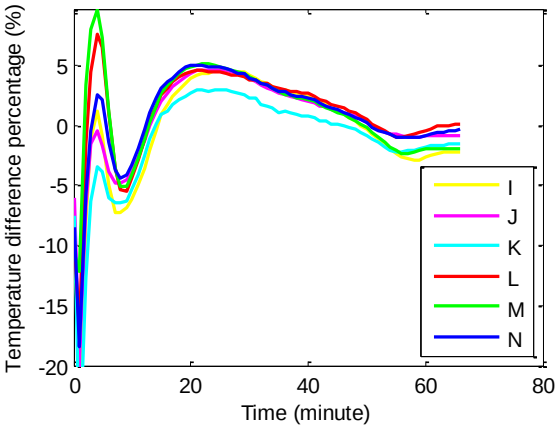

f. Batch 3, thermocouple I-N

Figure 6.3-8 Conductivity sensitivity study

As show in Figure 6.3-8, the temperature differences obtained for batch 3 is smaller than those obtained using the other two batches. For batch 3, the temperature difference after 12 minutes is less than 5%. The maximum temperature discrepancy for the first 5 minutes of the test is about 20°C, which does not have a meaningful influence on the structural performance of the beam. Therefore, conductivity values of batch 3 are chosen for the numerical studies of the Beams.

6.3.5 Mechanical properties

This section discusses the mechanical properties of the materials used in the numerical simulation work presented here.

6.3.5.1 Concrete slab

Two approaches are employed in this part of the research to model the concrete material. In the first method, the Concrete Smeared cracking method is used to consider the effect of cracks in concrete due to tension. In this approach, the yield stress of concrete is taken as 40% of the mean value of the compressive strength of concrete as is recommended by Figure 3.2 of BS EN 1992-1-1:2004 [79]. The strain value of concrete is taken from Table 3.3 of BS EN 1994-1-2:2005 [15]. The plastic strain at yield stress (0.4 of compressive strength) is set to zero and the plastic strain of compressive strength is set to the difference between the yield strain and the ultimate strain. The ultimate strain of concrete is given in Table 3.3 of BS EN 1994-1-2:2005 for different temperatures.

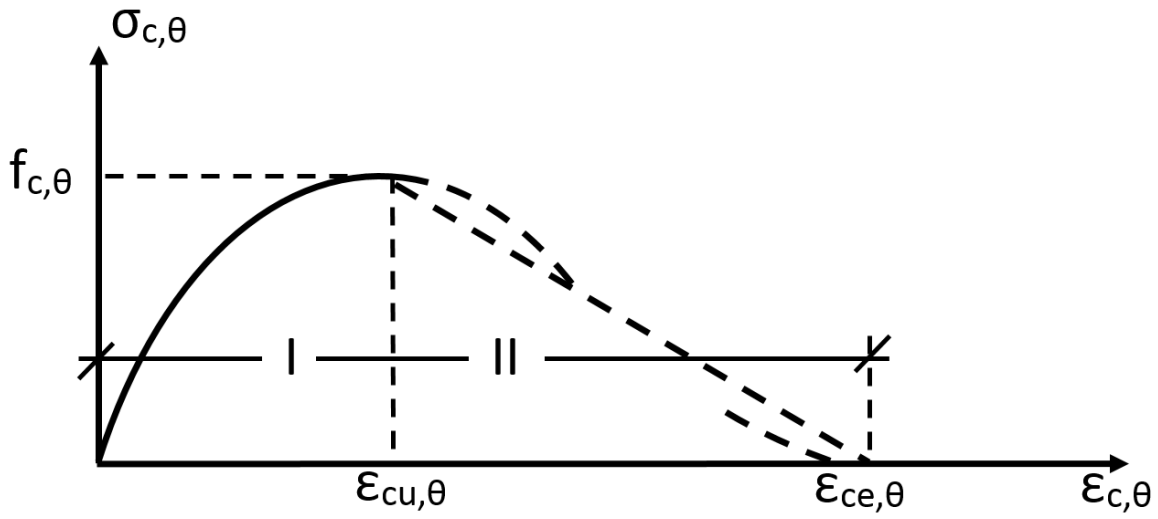

Figure 6.3-9 Stress strain relation of concrete [2]

In the second approach, it is assumed that since the concrete is in compression, no crack appears in the slab due to tension. Therefore, the tension stiffening is ignored in this approach. In this method, it is also assumed that concrete loses its strength linearly after reaching the compressive strength. This approach was also used in the other research on composite beams [80].

Concrete is not truly elastic and hence the relationship between its strain and stress is not constant. In general, three Young's modulus conventions are defined in the design guides (see Figure 6.3-10):

1. secant modulus;
2. tangent modulus;
3. initial tangent modulus.

The above are all measurements of the static modulus. The former is approximately equal to the dynamic modulus and can only be used at very low stress levels. The secant modulus is recommended by BS EN 1992-1-1 [79] for design purposes.

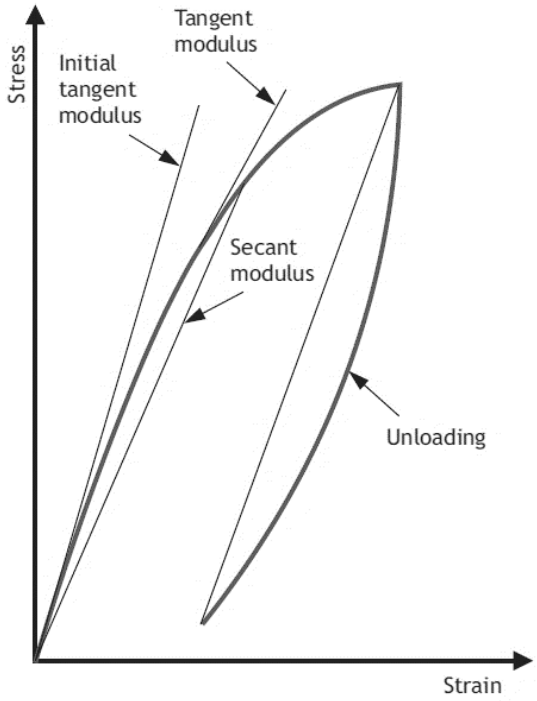

Figure 6.3-10 Diagrammatic stress–strain relationships for concrete

Moreover, since ABAQUS does not provide dependence of the tangent modulus on field variables, it is implemented using an elastic material with the equivalent secant modulus [81].

In design, the secant modulus, E_{cm} (in *GPa*), is derived from the mean compressive strength of a concrete cylinder f_{cm} (in *MPa*) [2]

$$E_{cm} = 22[f_{cm}/10]^{0.3} GPa \qquad \textbf{6.3-3}$$

Beam 2 is modelled and analysed using both the Concrete Smeared cracking method and the one which ignored the tension stiffening. No meaningful difference is found between the results obtained using the two approaches. Using the Smeared Cracking method is considerably more time consuming due to its highly nonlinear behaviour. Therefore, only the second approach is used to simulate the other two beams.

6.3.5.2 Steel

Steel properties and steel temperature derating factors are extracted from Table 3.3 of BS EN 1994-1-2:2005 [15]. Steel loses its strength and stiffness with increasing temperature.

Table 3.1 of EN 1993-1-2 or Table 3.2 of BS EN 1994-1-2 [15] provides the reduction factor for the strength and the elastic modulus of steel at elevated temperatures. Figure 6.3-11 depicts the variation of the reduction factors against temperature.

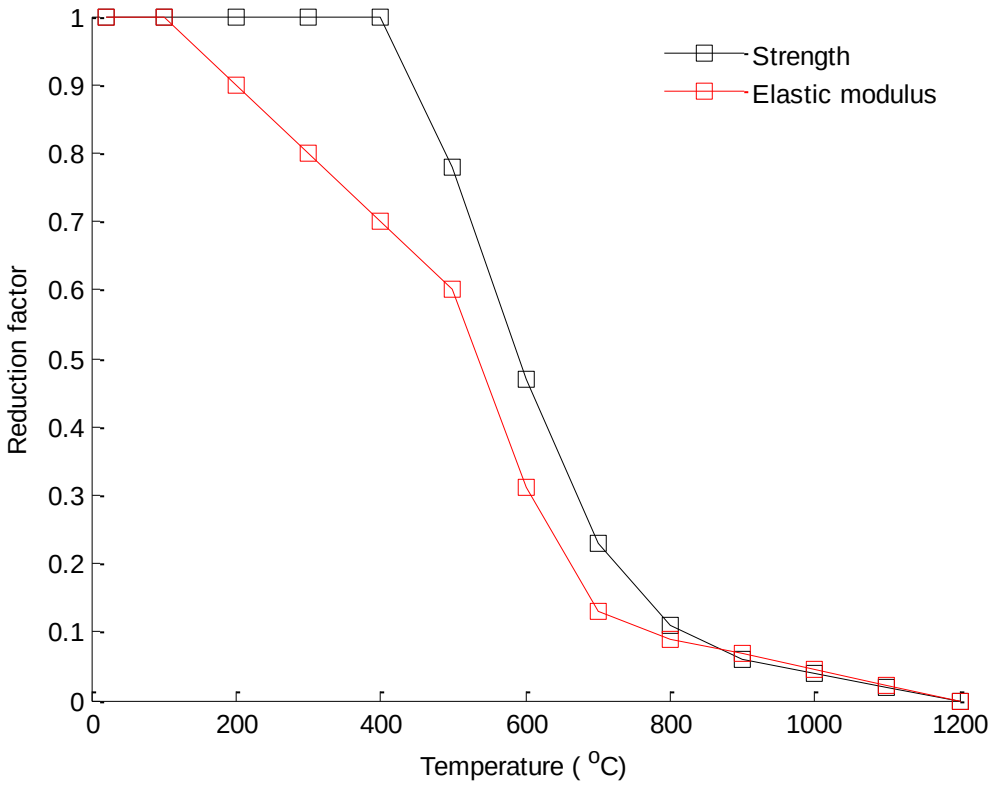

Figure 6.3-11 Variation of yield strength and elastic modulus against temperature

6.3.5.3 Steel reinforcement

As mentioned in section 6.2.2, in the test the concrete slabs are reinforced with A142 mesh reinforcement with yield strength of 460 N/mm^2. This is accounted for in the numerical model by assigning steel bars to the concrete shell as a reinforcement layer option.

6.3.5.4 Steel deck

The steel deck was Multideck 50-V2 (Kingspan MD50) for the test beams 1, 2 and 3 with the strength of 350 N/mm^2. The thickness of steel deck Multideck 50-V2 is 0.9 mm with the yield strength of 350 N/mm^2, and a minimum total coating mass of 275 g/m^2. In the

numerical model the steel deck section is defined as a layer at the bottom of the composite shell element.

6.3.6 Mesh

A shell element is used for the modelling of the concrete slab and a solid element is used for the rest of the beam. The steel deck and reinforcement bars are defined as composite layers within the shell composite section. For the heat transfer analysis, 4-node heat transfer quadrilateral shell elements and 8-node linear heat transfer bricks are used for the concrete slab and coated beams, respectively. For the static analysis, 4-node doubly curved thin or thick shell elements and 8-node linear brick elements are used for the concrete slab and the steel beam, respectively (see Figure 6.3-12). The types of mesh used are explained in more detail in Chapters 3 and 4.

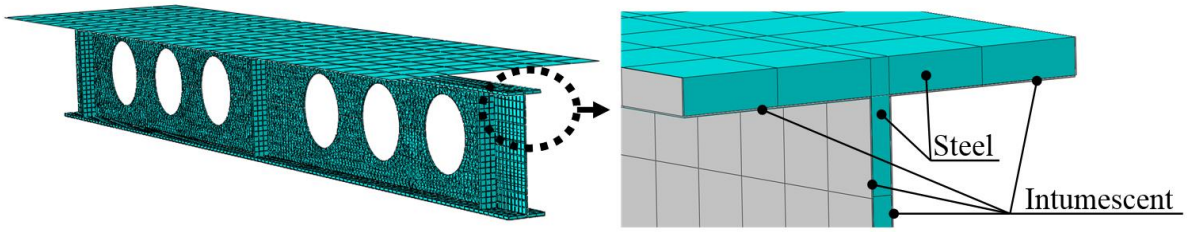

Figure 6.3-12 Computational mesh of Beam 3

6.3.7 Analysis type

Two sets of analyses are conducted to simulate the loaded CCBs in a furnace (see Figure 6.3-13). The first analysis is a heat transfer analysis in which the thermal load and thermal interactions are applied to the CCBs. The temperature history of each node of the models is saved in an output file for use in a second type of analysis which has three stages.

The first stage is a static analysis in which the mechanical load and the boundary conditions are applied to the beam. During this stage, the temperature of the CCB is set to the lab ambient temperature. The beams deform under the loading applied in this stage.

Essentially, this stage simulates the behaviour of the beam prior to the furnace burners being turned on during the experiment.

A static analysis is chosen for the second stage of the second set of analysis. Temperature dependent material properties are defined for the model. The second stage starts at the end of the first stage. The initial geometry of the model in the second stage is the deformed shape of the beam at the end of the first stage. The applied load remains steady and equal to the load at the end of the first stage. The temperature history of all the nodes from the first set of the analysis (heat transfer analysis) is assigned to the nodes in the second stage. By increasing the temperature of the nodes in the second stage, the CCBs begin losing their strength and stiffness and consequently the beam becomes more deflected under the applied load from the first stage. An artificial damping is introduced into the general static method to enable the model to simulate the local failure of the web-post. The ratio of the dissipated energy by damping to the total strain energy is limited to the 2.5%.

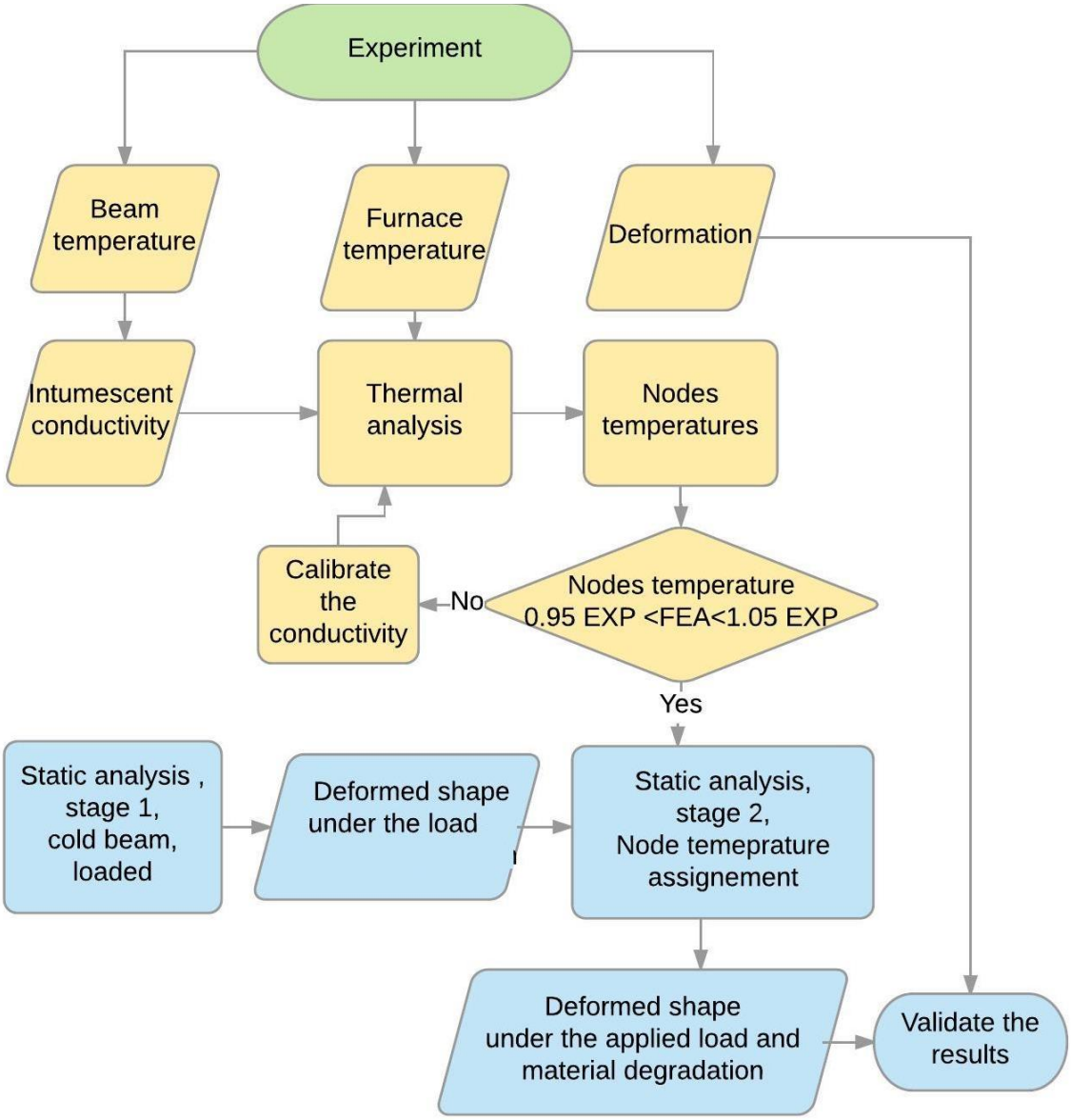

Figure 6.3-13 Flowchart of the analysis process

6.4 RESULTS

This section includes thermal, deflection and buckling results. To enable a comparison and validation of the FEA results, the nodes at which the FEA results are extracted from are identical to the location of the thermocouples in the experiment.

6.4.1 Thermal analysis results

6.4.1.1 Beam 1

Figure 6.4-1 depicts the temperature history of the beams at locations where the 15 thermocouples (see Figure 6.2-6) are attached to the beam.

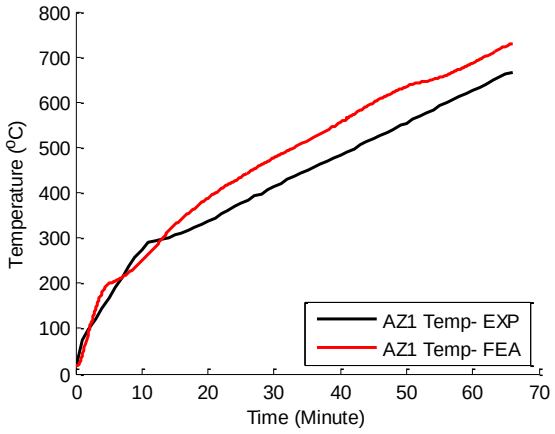

a) Temperature history of thermocouple A-Z1

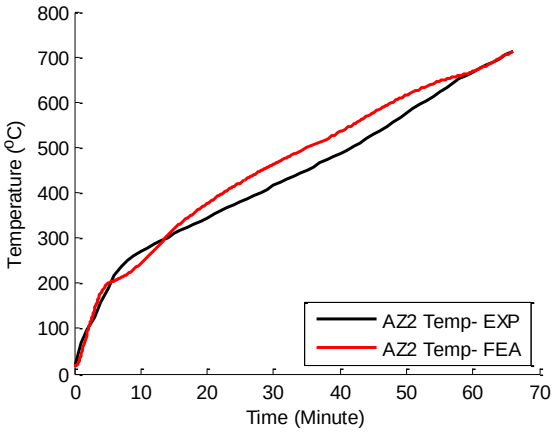

b) Temperature history of thermocouple A-Z2

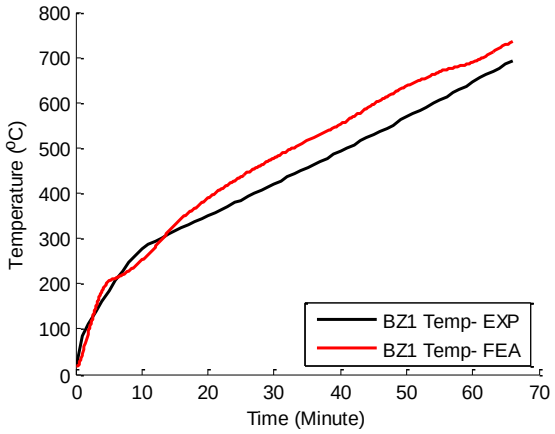

c) Temperature history of thermocouple B-Z1

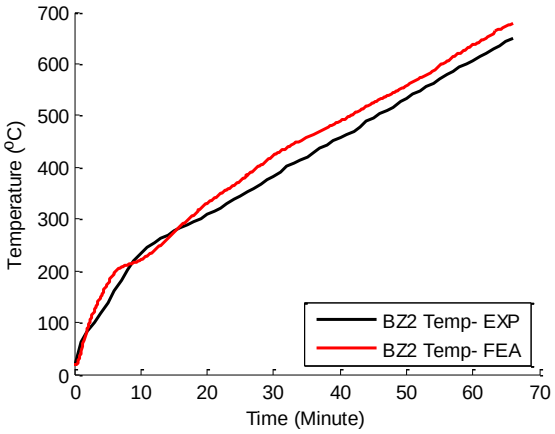

d) Temperature history of thermocouple B-Z2

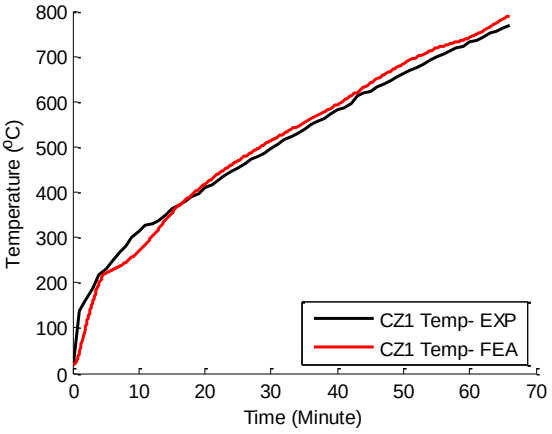

e) Temperature history of thermocouple C-Z1

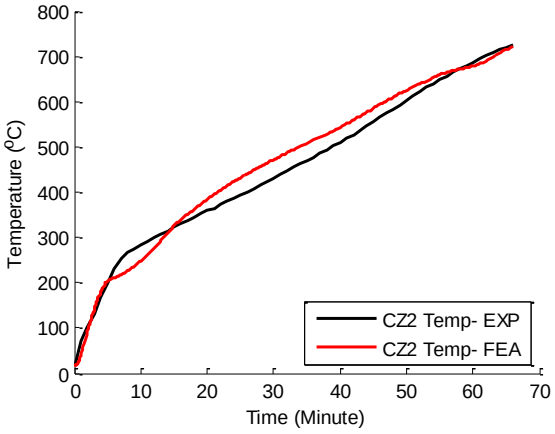

f) Temperature history of thermocouple C-Z2

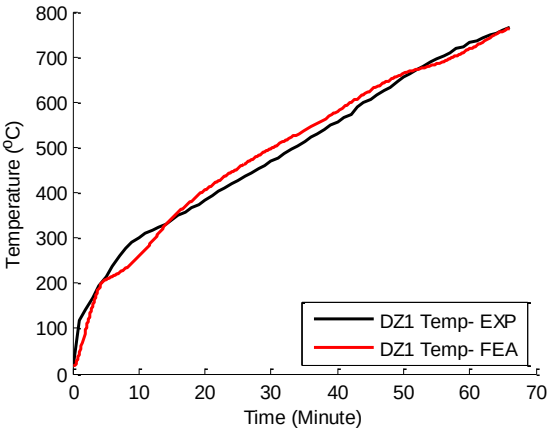

g) Temperature history of thermocouple D-Z1

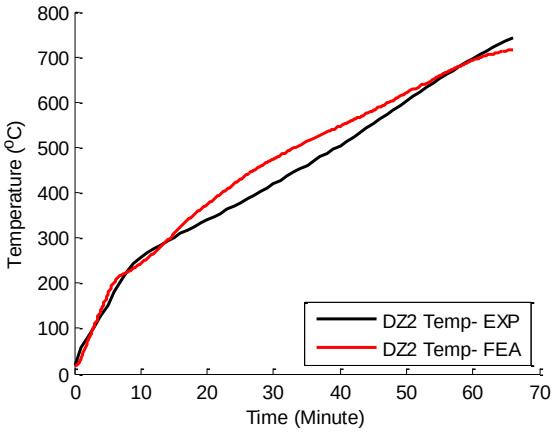

h) Temperature history of thermocouple D-Z2

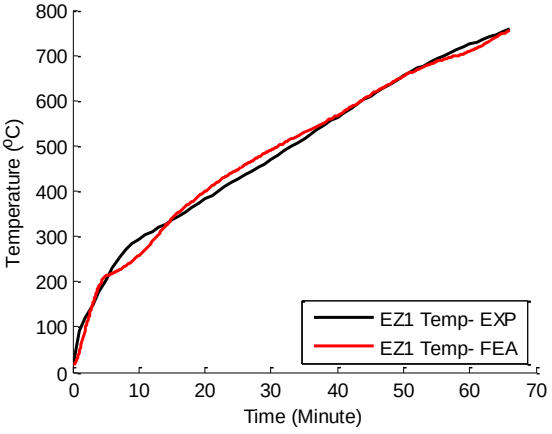

i) Temperature history of thermocouple E-Z1

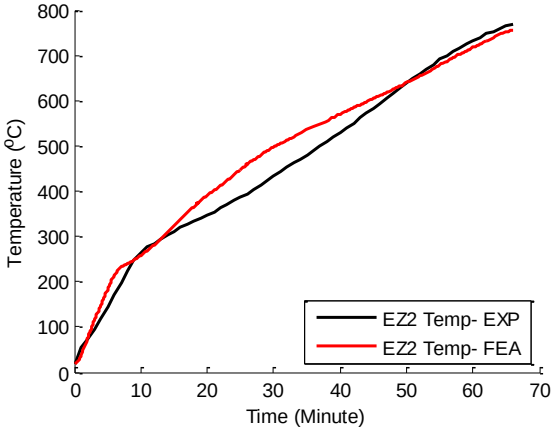

j) Temperature history of thermocouple E-Z2

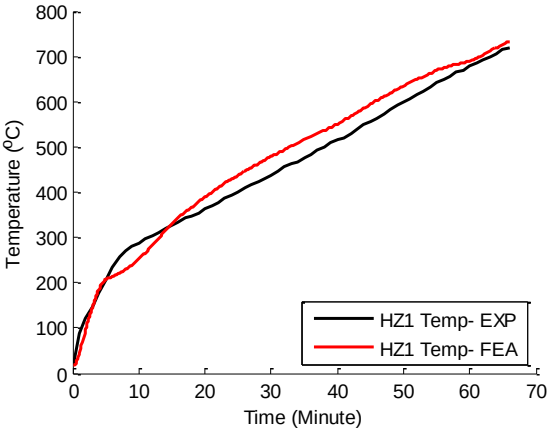

k) Temperature history of thermocouple H-Z1

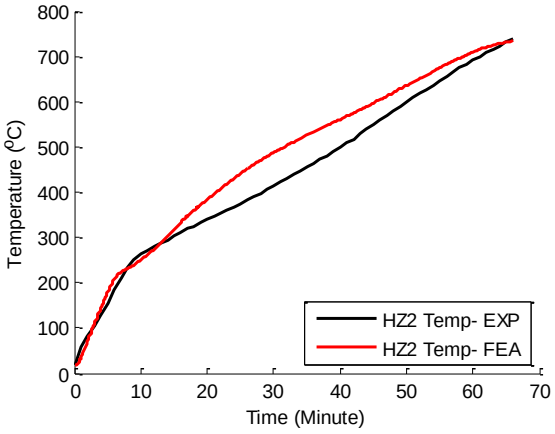

l) Temperature history of thermocouple H-Z2

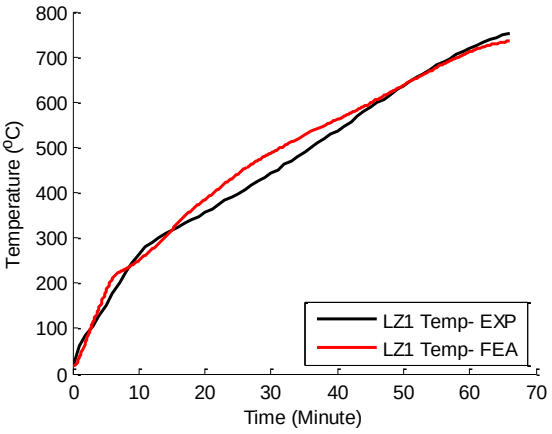

m) Temperature history of thermocouple L-Z1

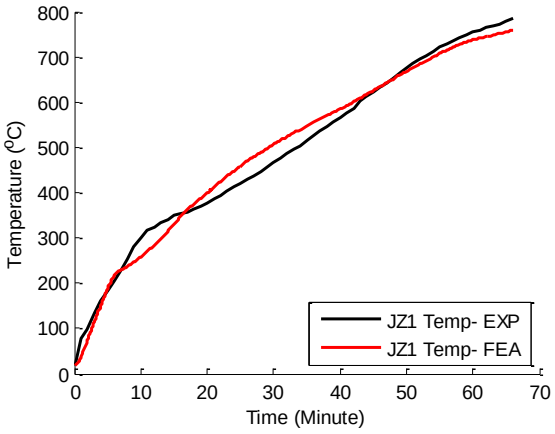

n) Temperature history of thermocouple J-Z1

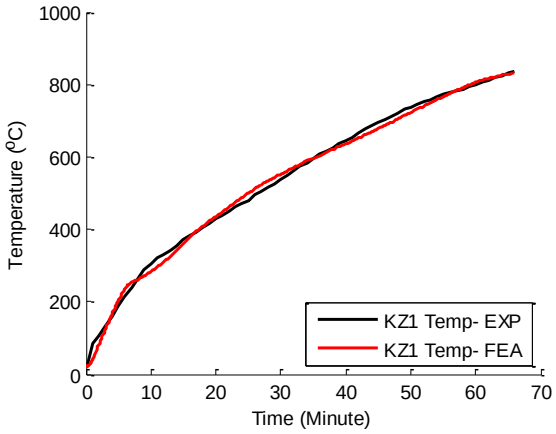

o) Temperature history of thermocouple K-Z1

Figure 6.4-1 Temperature history of Beam 1, FEA and experiment results

Figure 6.4-2 shows the temperature contour plot of the steel section of Beam 1 at the end of the test (i.e. after 66 minutes).

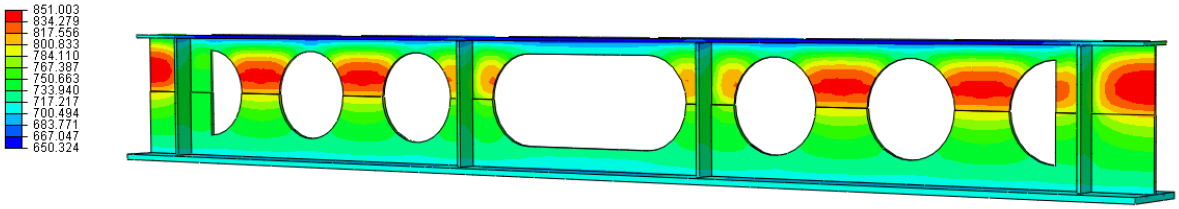

Figure 6.4-2 Temperature contour plot of the steel part of Beam 1 (°C)

6.4.1.2 Beam 2

Similar to thermal results of Beam 1, Figure 6.4-3 depicts the temperature history of the Beam 2 at locations where thermocouples (see Figure 6.2-7) are attached to the beam.

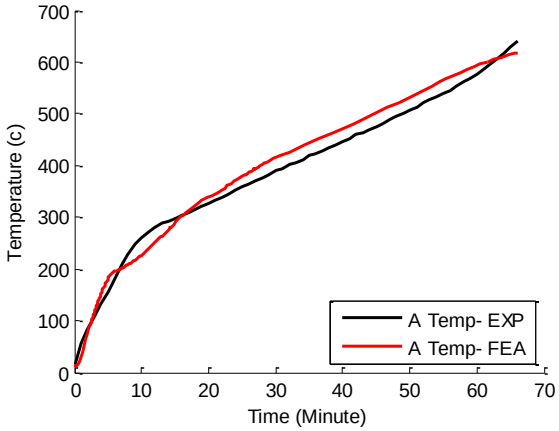

a) Temperature history of thermocouple A

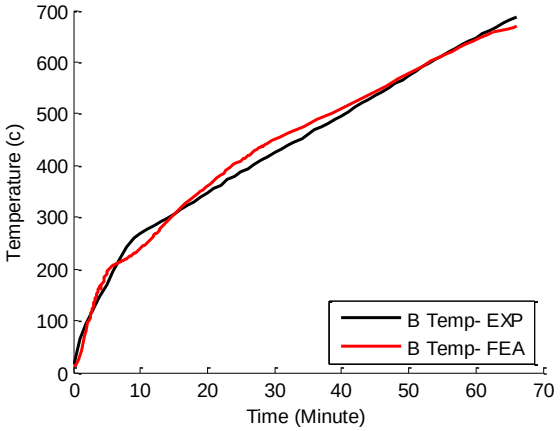

b) Temperature history of thermocouple B

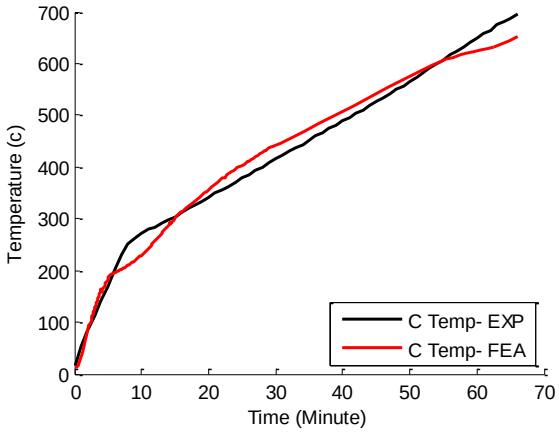

c) Temperature history of thermocouple C

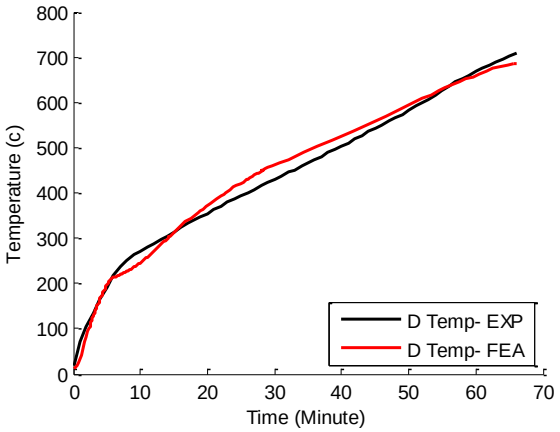

d) Temperature history of thermocouple D

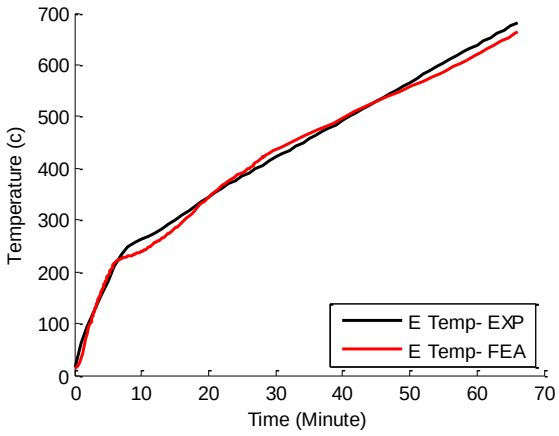

e) Temperature history of thermocouple E

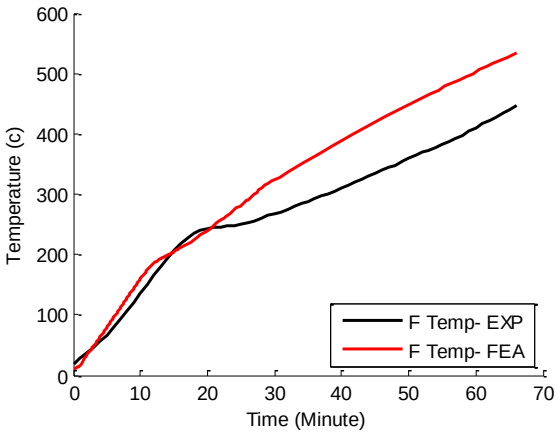

f) Temperature history of thermocouple F

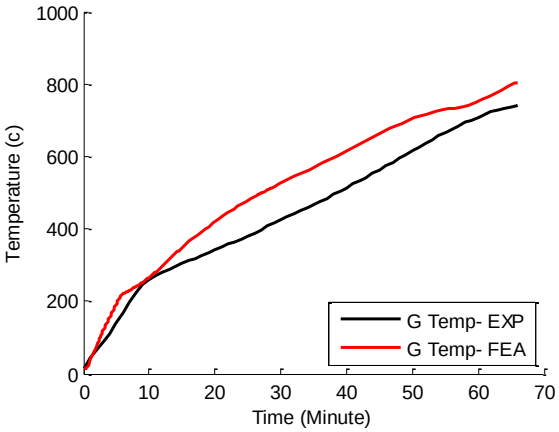

g) Temperature history of thermocouple G

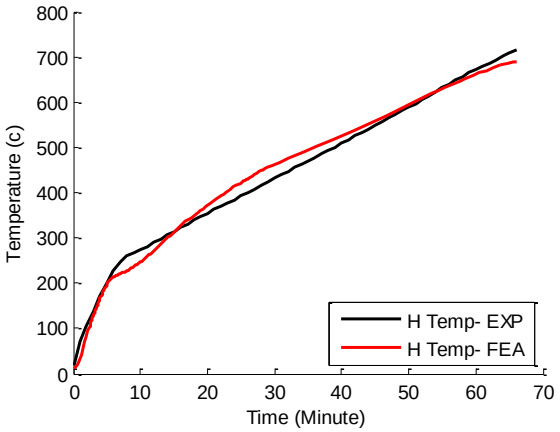

h) Temperature history of thermocouple H

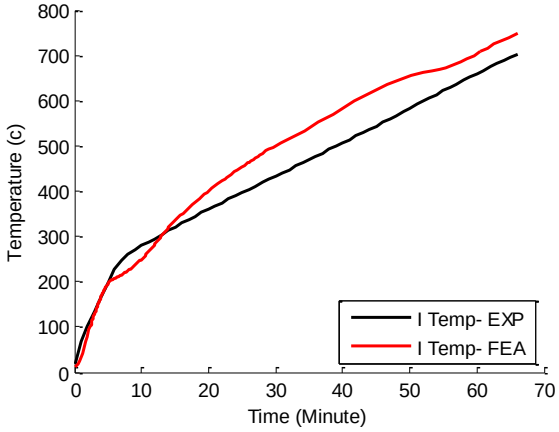

i) Temperature history of thermocouple G

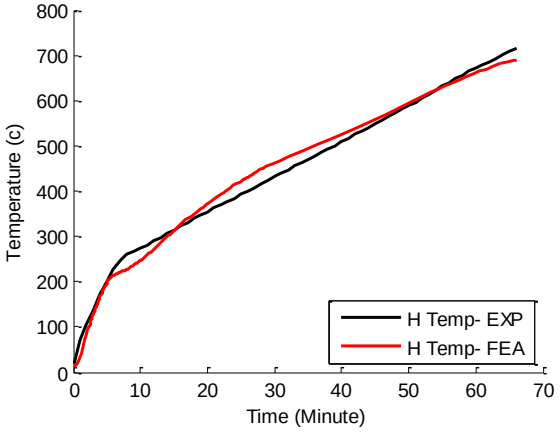

j) Temperature history of thermocouple H

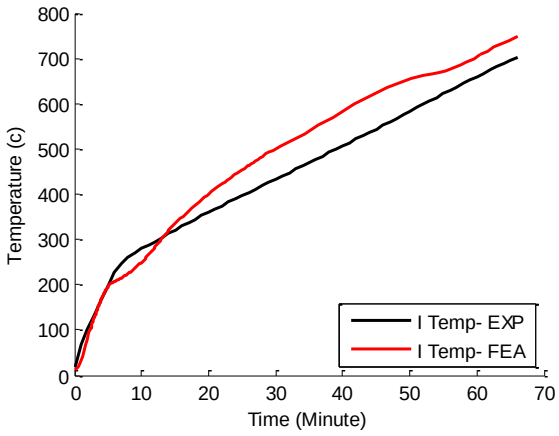

k) Temperature history of thermocouple I

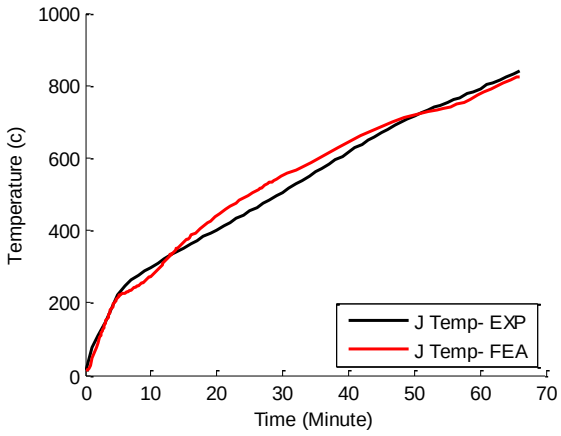

l) Temperature history of thermocouple J

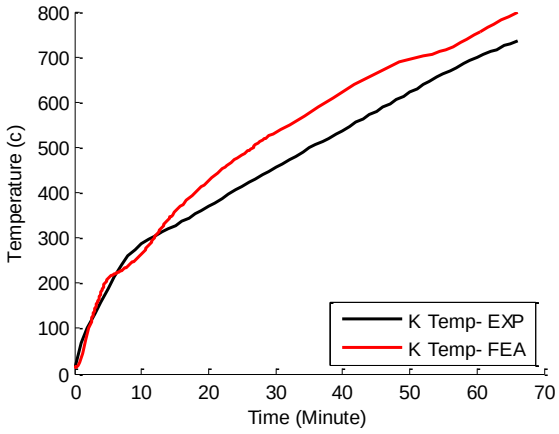

m) Temperature history of thermocouple K

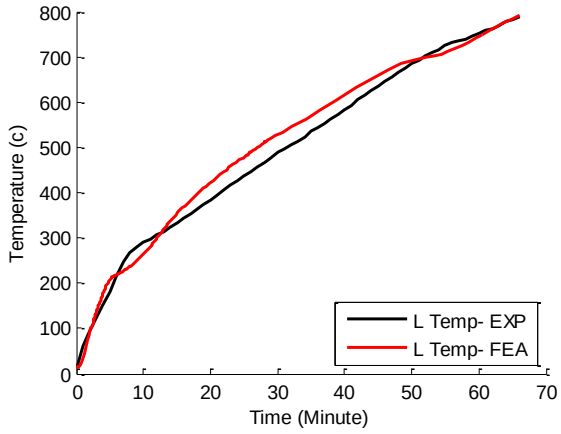

n) Temperature history of thermocouple L

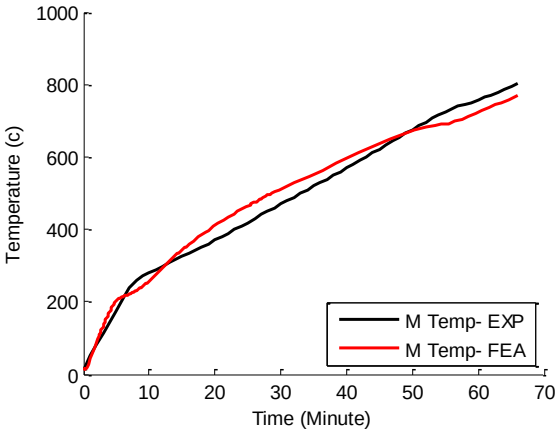

o) Temperature history of thermocouple M

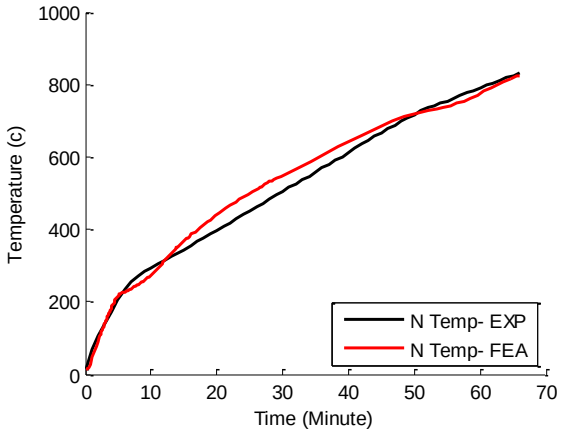

p) Temperature history of thermocouple N

Figure 6.4-3 Temperature history of Beam 2, FEE and experiment results

Figure 6.4-4 shows the temperature contour plot of the steel section of Beam 2 at the end of the test (after 66 minutes).

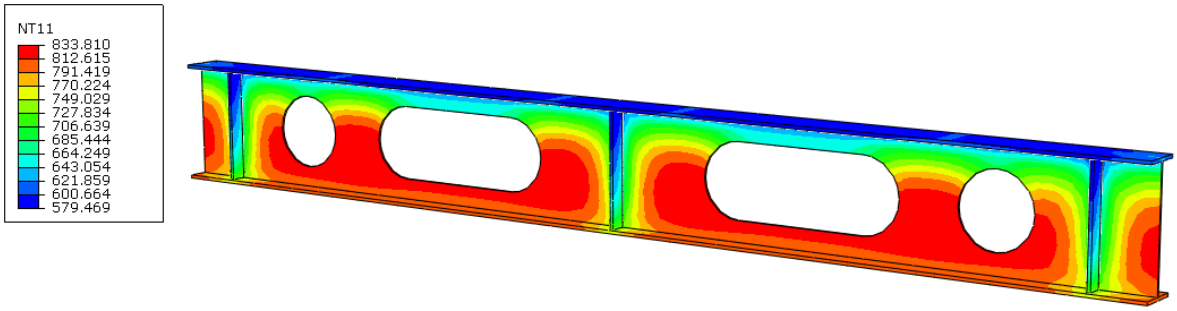

Figure 6.4-4 Temperature contour plot of the steel section of Beam2 (°C)

6.4.1.3 Beam 3

Similarly, Figure 6.4-5 depicts the temperature history of the Beam 3 at locations where the 15 thermocouples (see Figure 6.2-7) are attached to the beam.

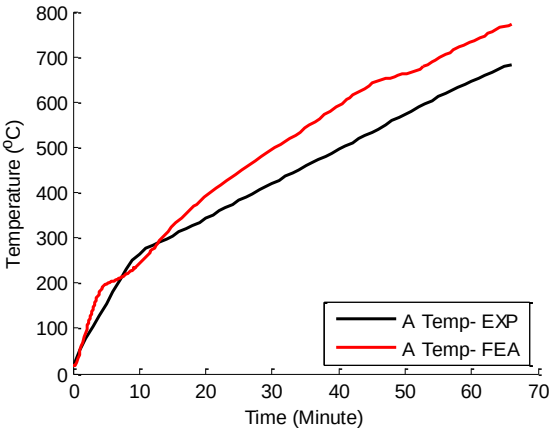

a) Temperature history of thermocouple A

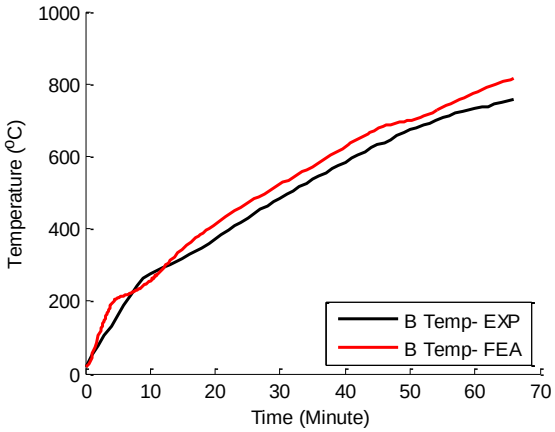

b) Temperature history of thermocouple B

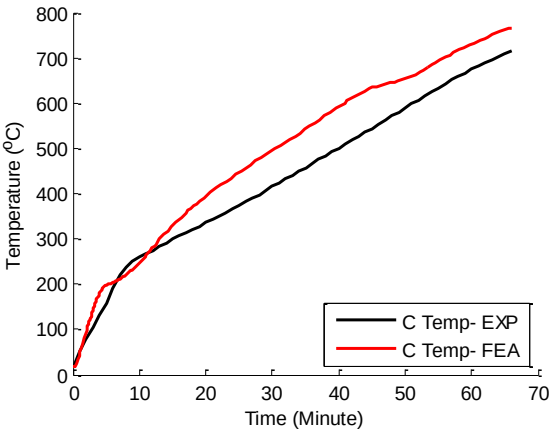

c) Temperature history of thermocouple C

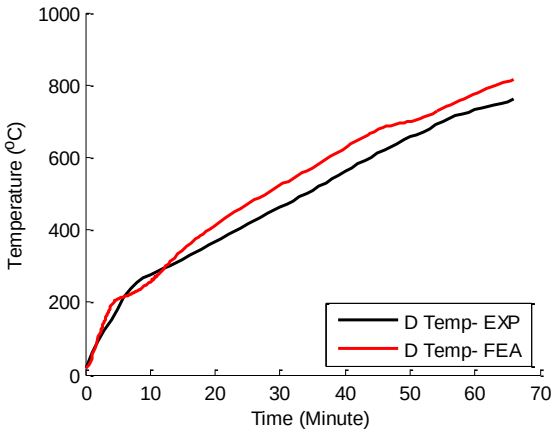

d) Temperature history of thermocouple D

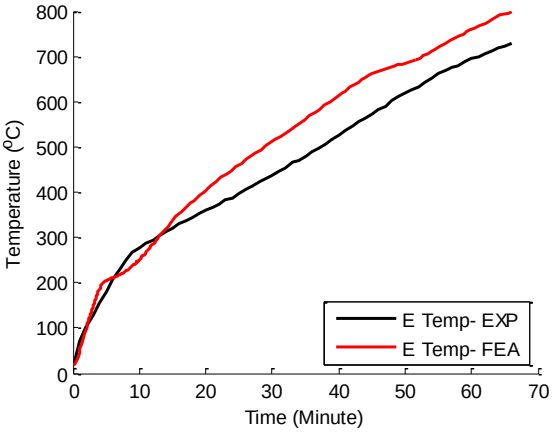

e) Temperature history of thermocouple E

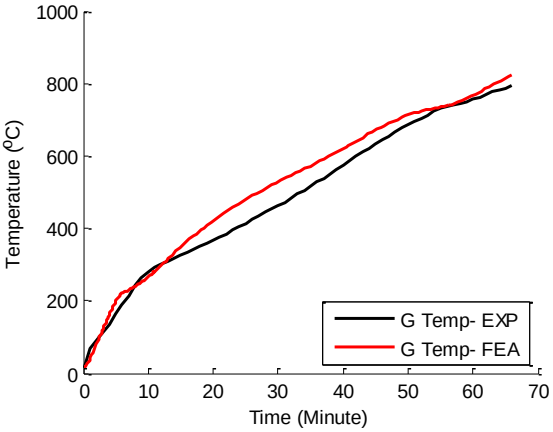

f) Temperature history of thermocouple G

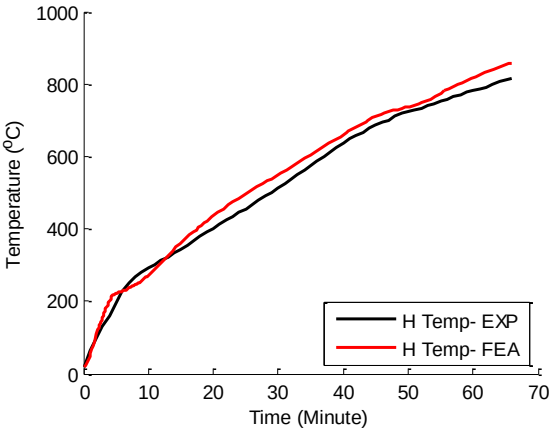

g) Temperature history of thermocouple H

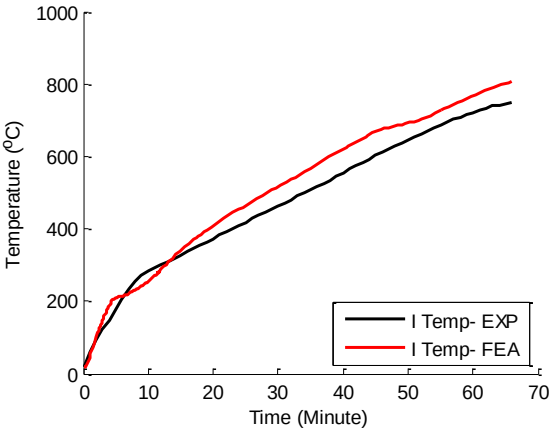

h) Temperature history of thermocouple I

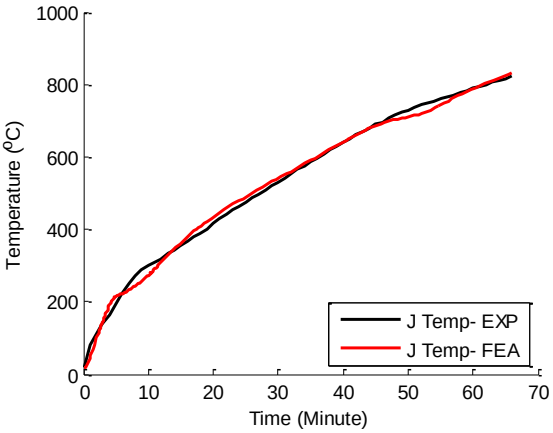

i) Temperature history of thermocouple J

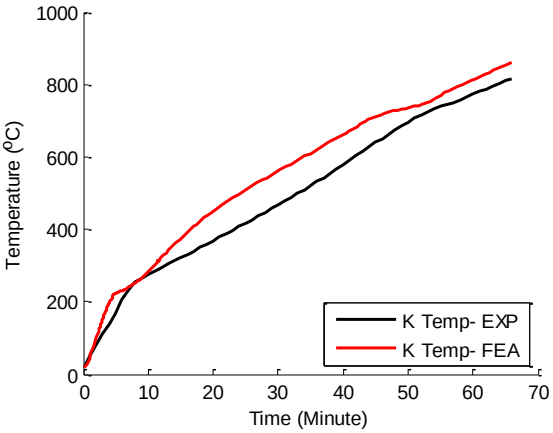

j) Temperature history of thermocouple K

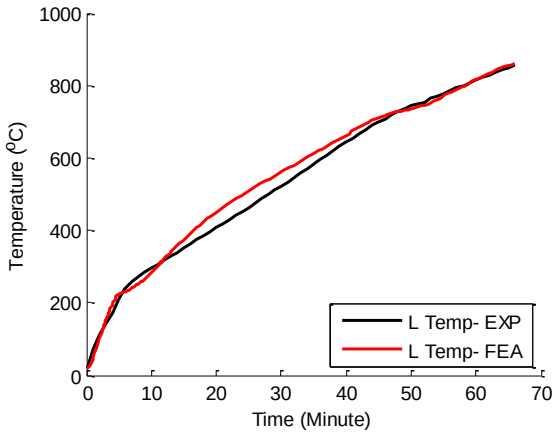

k) Temperature history of thermocouple L

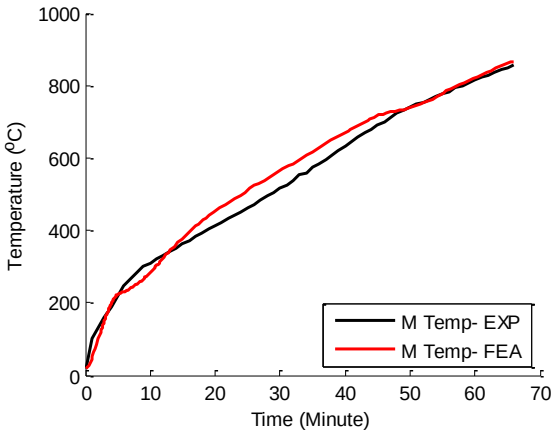

l) Temperature history of thermocouple M

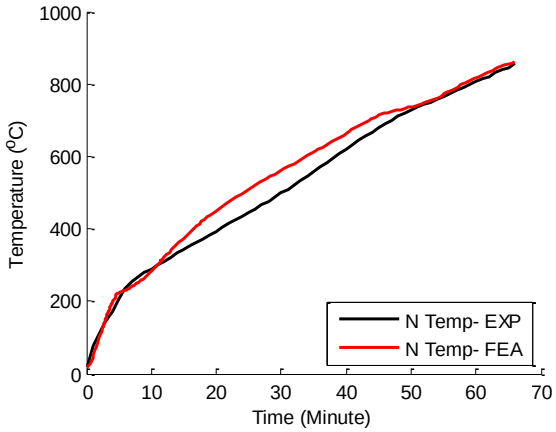

m) Temperature history of thermocouple N

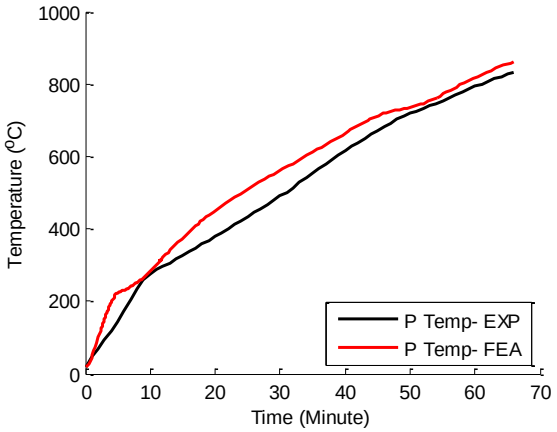

n) Temperature history of thermocouple P

Figure 6.4-5 Temperature history of Beam 3, FEE and experiment results

Figure 6.4-6 shows the temperature contour plot of the steel section of the beam at the end of the test (after 66minutes).

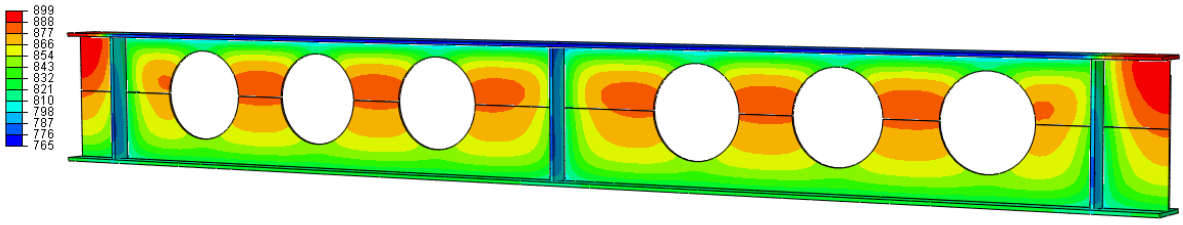

Figure 6.4-6 Temperature contour plot of the steel section of Beam 3 (°C)

6.4.2 Beam deflection

6.4.2.1 Beam 1

Figure 6.4-7 shows the deformation of the beam during the experiment. The deformed geometry of the beam after 66 minutes (end of the tests).

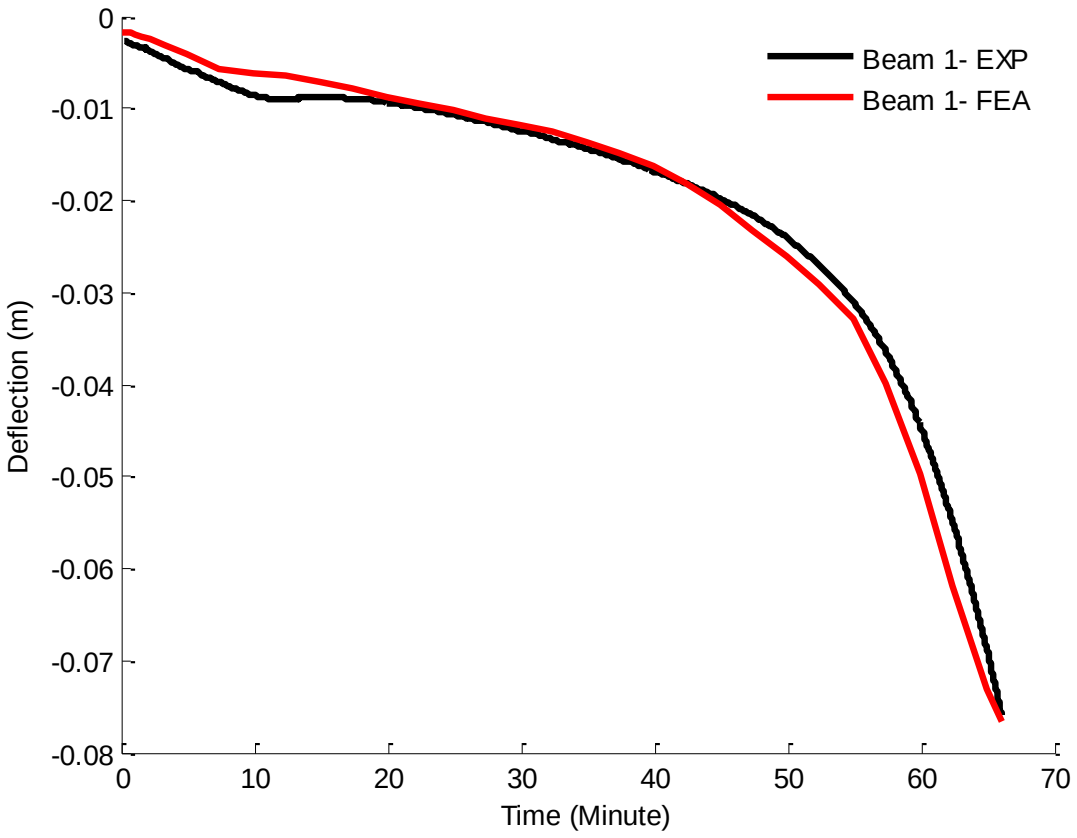

Figure 6.4-7 Deformation of the mid span of Beam 1, FEA and experiment results

a) Deformed Beam 1, experiment

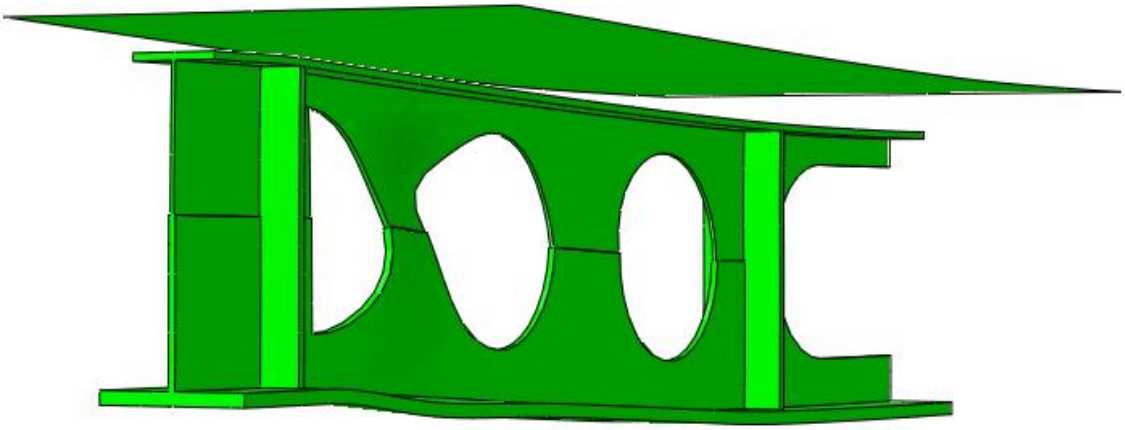

b) Deformed Beam 1, FEA

c) Deformed Beam 1, FEA and experiment

Figure 6.4-8 Vertical deformation of Beam 1 at time of 66 minutes

6.4.2.2 Beam 2

Figure 6.4-9 shows the deformation of the Beam 2 under the applied load. Figure 6.4-10 depicts the deformed geometry of the beam after 66 minutes.

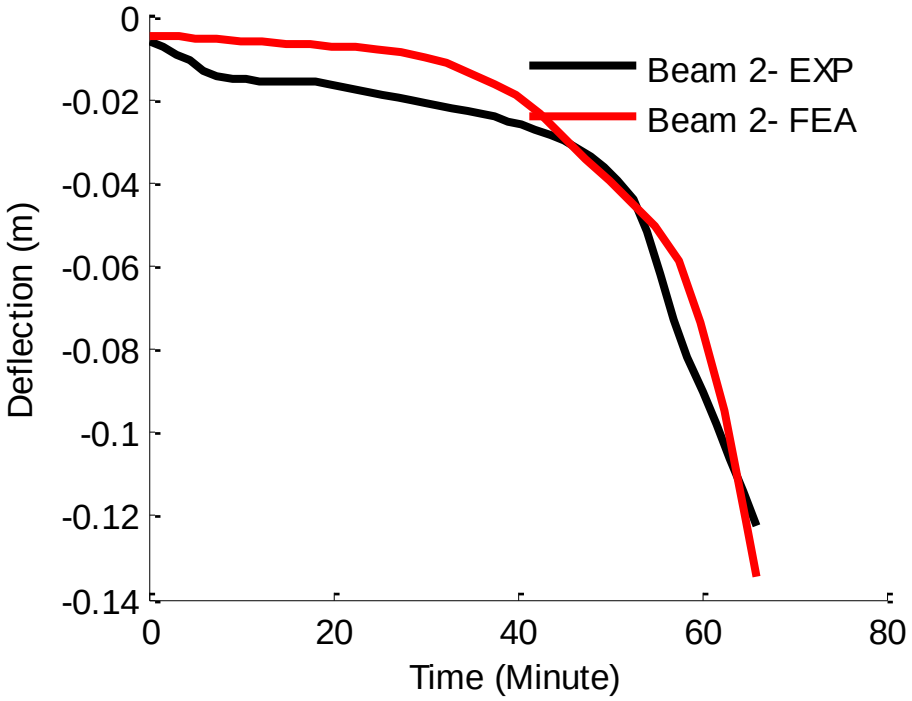

Figure 6.4-9 Deformation of the mid span of Beam 2, FEA and experiment results

a) Deformed beam 2, experiment

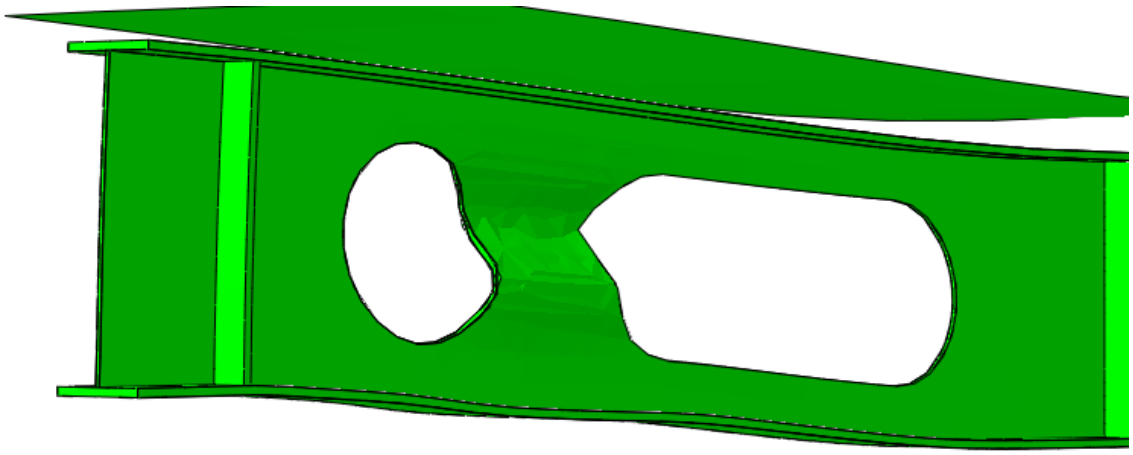

b) Deformed beam 2, FEA

Figure 6.4-10 Deformation of Beam 2 at time of 66 minutes

6.4.2.3 Beam 3

Figure 6.4-11 shows the deformation of the beam under the applied load. Figure 6.4-12 shows the deformed geometry of the beam after 66 minutes (end of the test).

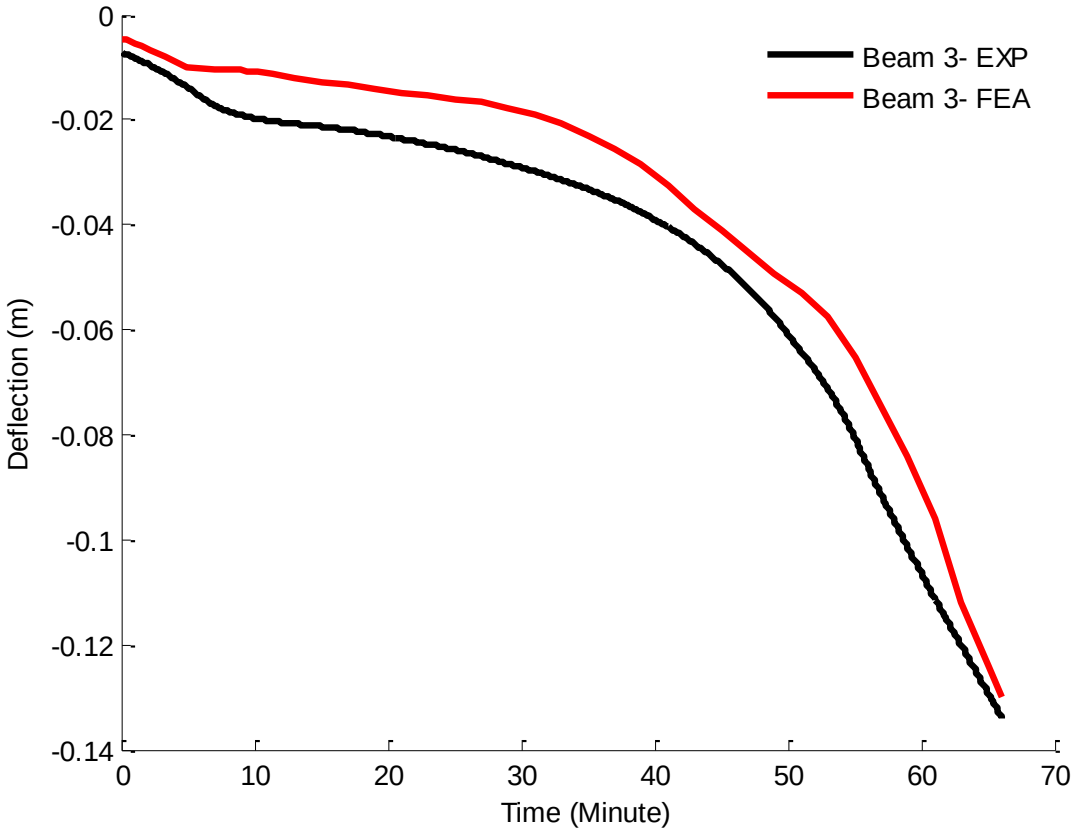

Figure 6.4-11 Deformation of the mid span of Beam 3, FEA and experiment results

a) Deformed Beam 3, experiment

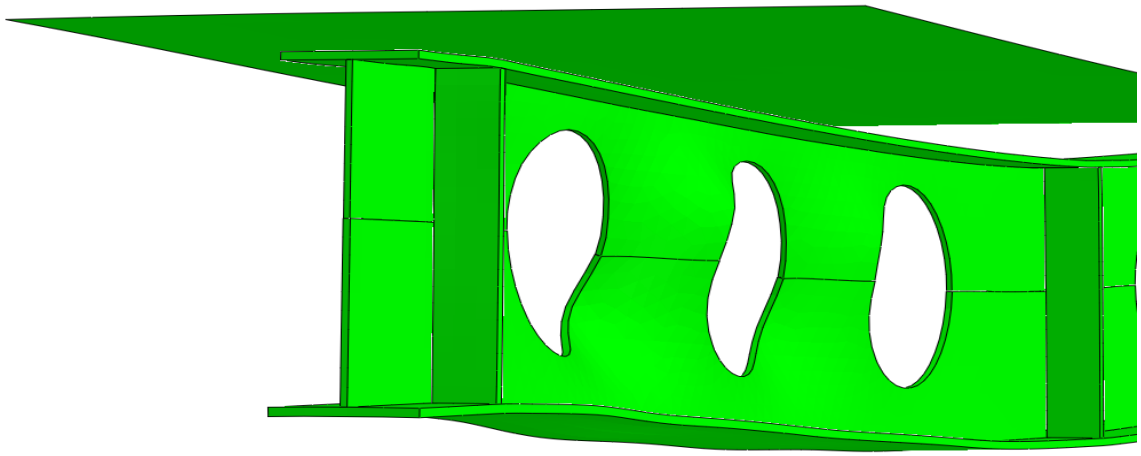

b) Deformed beam 3, FEA

Figure 6.4-12 Deformation of Beam 3 at time of 66 minutes

6.5 DISCUSSION

Generally, the numerically estimated temperature profiles of all three beams are in good agreement with experimental results. The temperature contour plots of the beams clearly show that the upper web temperature is higher than the bottom web temperature in Beam 1 and Beam 3. This is due to fact that Beam 1 and 3 have thinner upper sections and the thickness of the web for beam 2 is the same through the web.

Both the experimental and numerically obtained temperatures show that the temperature of the beams raise in faster rates in the first 10 minutes. After that, the temperature increases in slower rates. Figure 6.4-1, Figure 6.4-3, and Figure 6.4-5 show that the numerical

temperature history of the beams follows the same pattern as the experimental outcomes. Figure 6.4-7, Figure 6.4-9, and Figure 6.4-11 show that the numerically predicted deformation of the beams follow the same deformation pattern and has the same final deformed profile as the experimental results.

Additionally, the experimental results show that beam 1 fails between the two openings close to the end of the beam (see Figure 6.4-8 a). The failure is similar to the Vierendeel bending failure and web-post buckling. However, it is more likely that the Vierendeel failure happens first and after that the web buckles due to loss of stiffness. The numerical results demonstrate that the failure mode of beam 1 is the Vierendeel mechanism (see Figure 6.4-8 b). The failure occurs in the first web opening where the shear force is at its maximum.

Figure 6.4-10 and Figure 6.4-12 show the deformed configurations of beam 2 and 3, respectively. Evidently, the experimental and numerical outcomes are in agreement. It is also clear from the figures that the beams fail due to web-post buckling failure as web-post deformations are in S shape.

In general, it is found that the failure of beams occurs at the high shear zone areas, which are not stiffened with web stiffener. It can be expected that if the webs above the supports are not stiffened, the beams fail prematurely as they experience excessive shear loads at the supports.

To determine the time at which the rate of beam deformation increases and consequently leads to beam failure, the deformation graph is rotated such that the start and end deformations are located on the X axis (see Figure 6.5-1). The correspondence time for the maximum displacement is then determined numerically and projected on the original coordinate system. The determined time from the rotated graph is considered as the point

in time after which deformations begin to occur at considerably faster rates. This point in time can be referred to as the “critical time”.

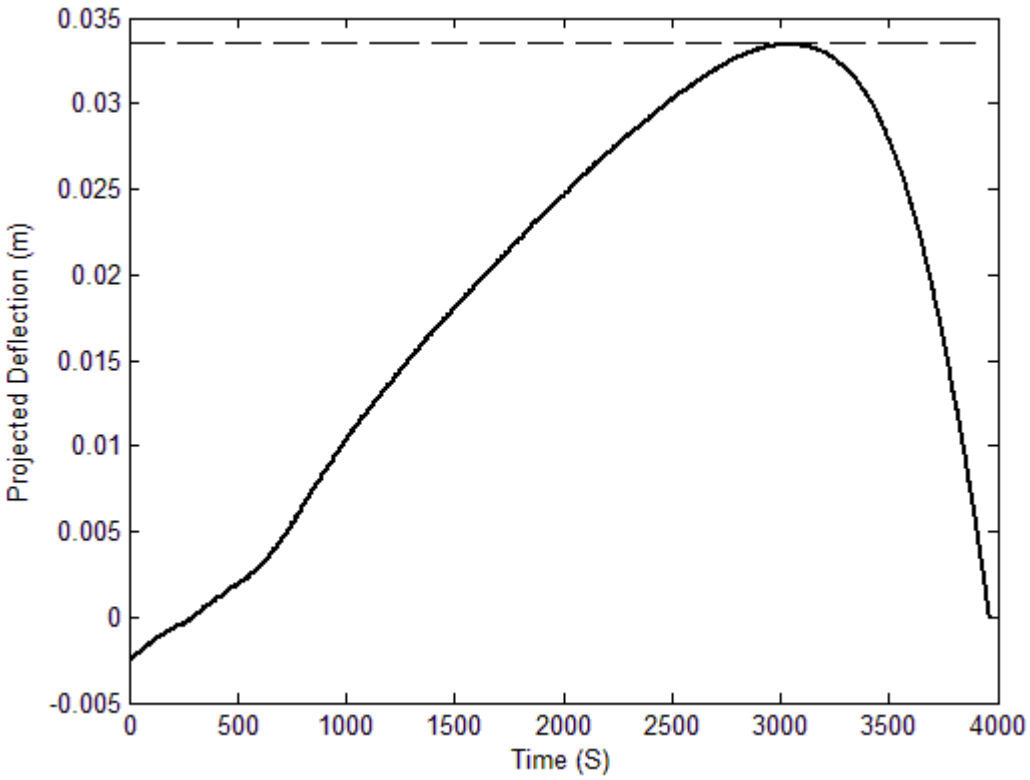

Figure 6.5-1 Rotated deformation graph of beam 1 - dashed line shows the maximum Y axis value

Similarly, the rotated deformation graph approach is applied to beams 2 and 3 to find the critical time. Figure 6.5-2 shows the graph of deflections beams 1, 2 and 3 found using the rotated deformation approach. The vertical dashed lines indicate the critical time values.

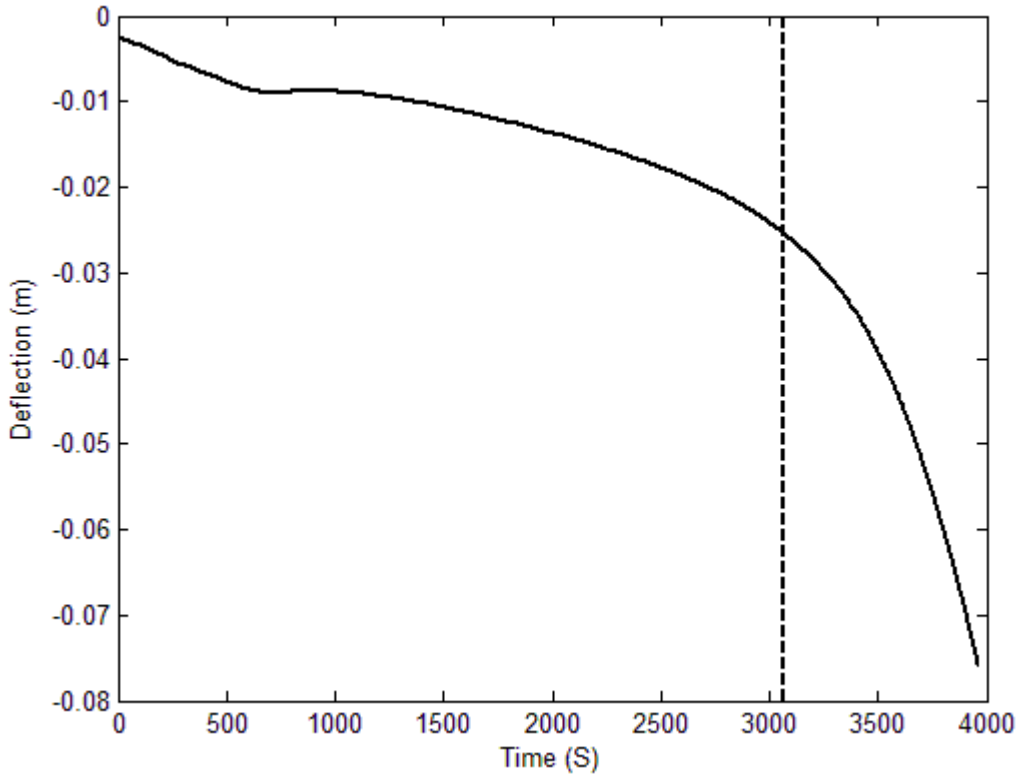

a) Beam 1

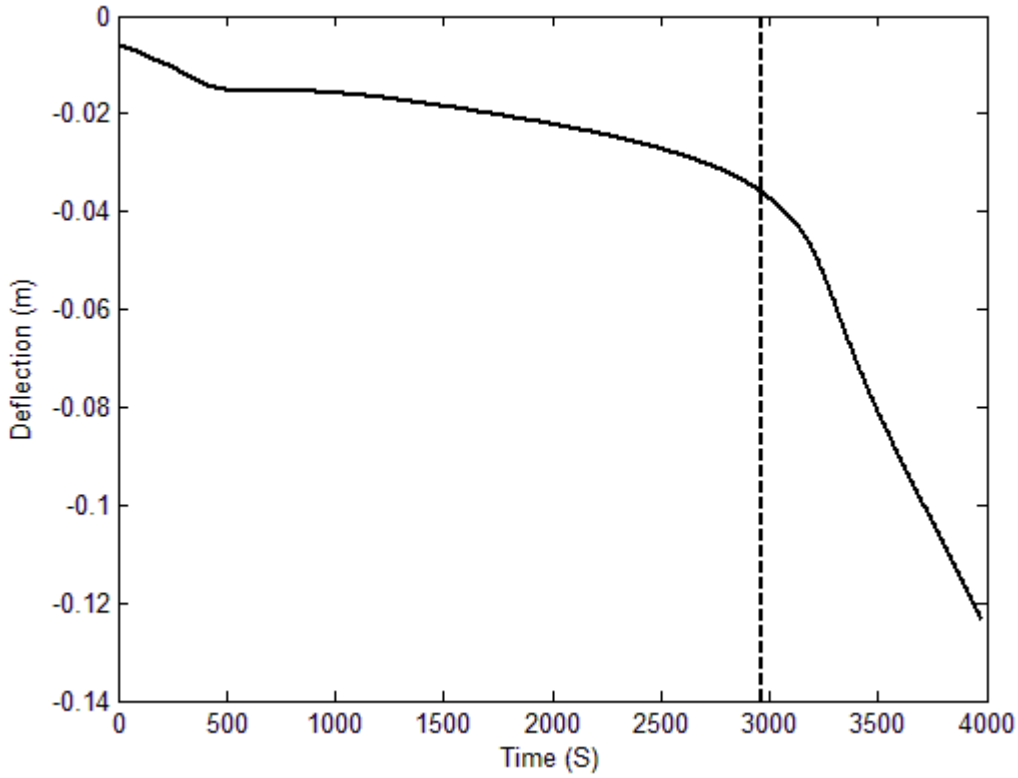

b) Beam 2

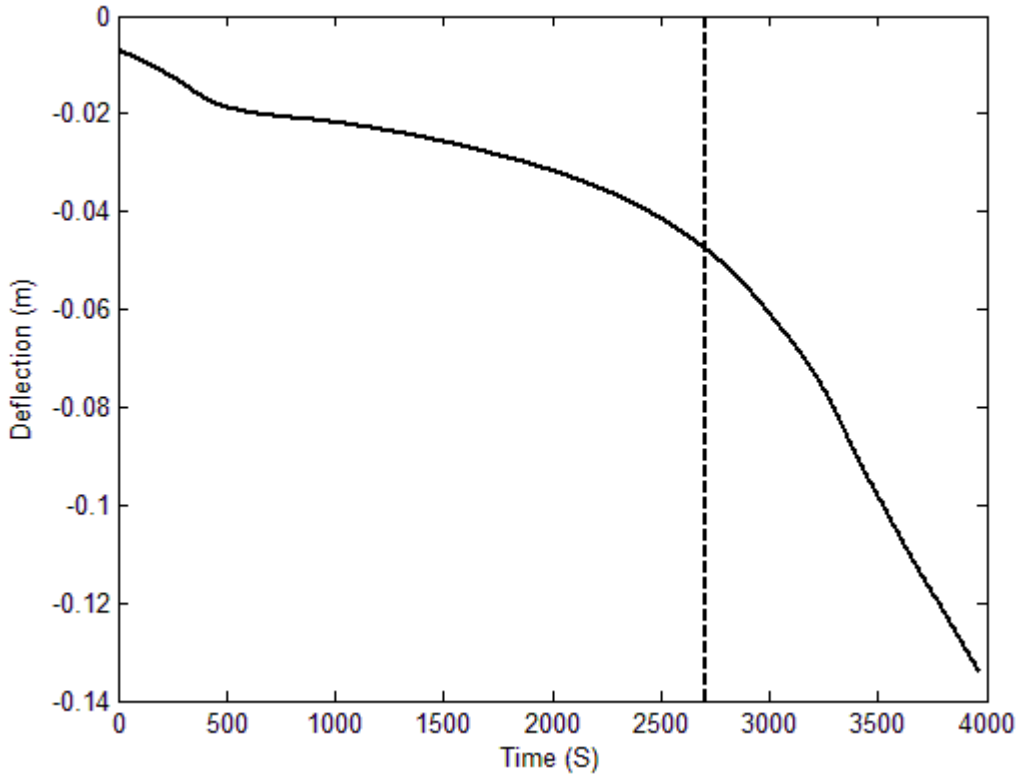

C) Beam 3

Figure 6.5-2 Beam deformations – the dashed lines show the critical times

Figure 6.5-2 shows the critical times for beams 1, 2 and 3 are 51, 49, and 45 minutes after turning on the chamber, respectively. Figure 6.5-3 shows the temperature of the beams at the critical times demonstrated in Figure 6.5-2. This temperature profile can be referred to as the “critical temperature” profile.

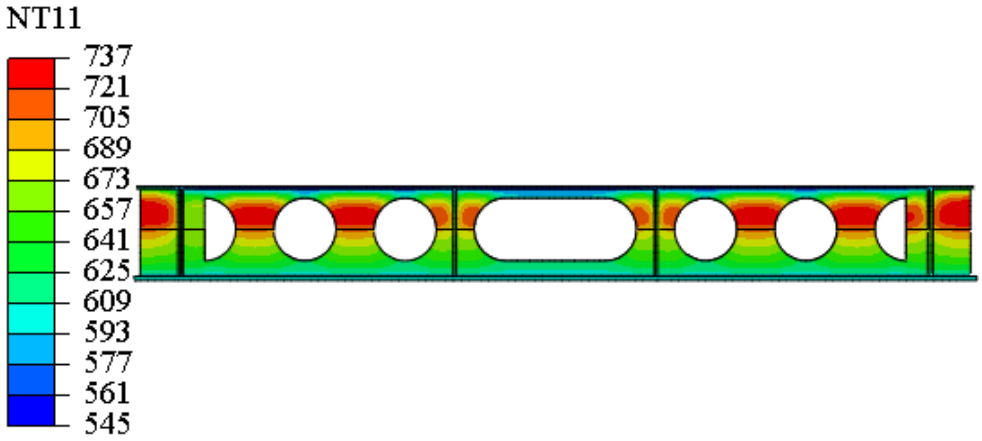

a) Beam1 – temperature (°C) at 51 minutes

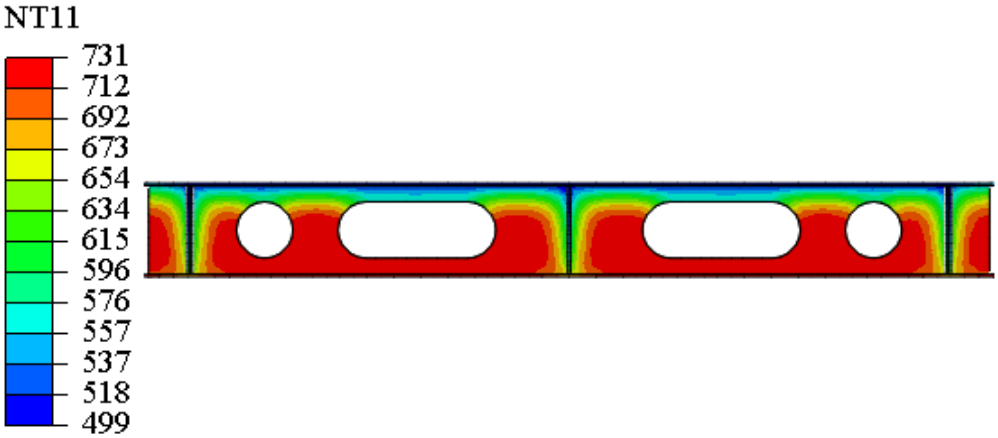

b) Beam 2 – temperature (°C) at 49 minutes

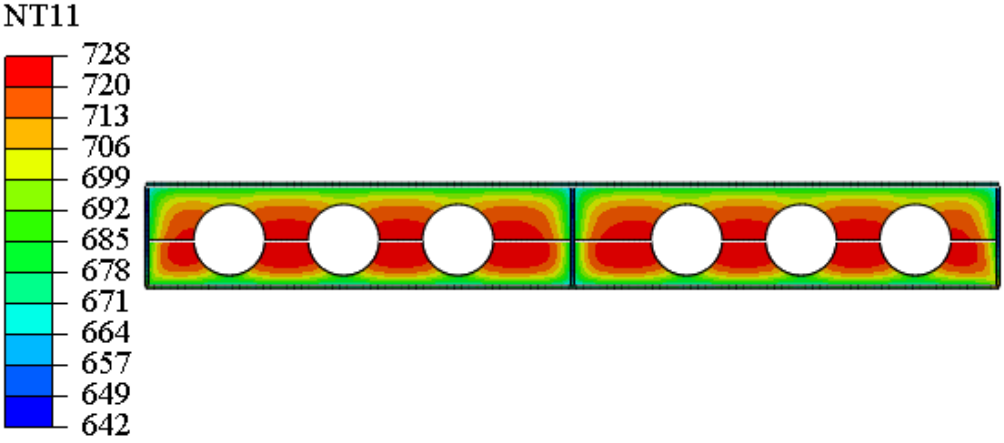

c) Beam 3 – temperature (°C) at 45 minutes

Figure 6.5-3 Critical temperature profiles

Figure 6.5-3 shows that the temperatures at the failed openings at the critical time vary between 728°C to 737°C. This shows that when the temperature around the openings

reaches 730°C, the beams lose their load bearing capacity. Figure 5.6-5 shows the compression contour plots of the three beams at the critical time.

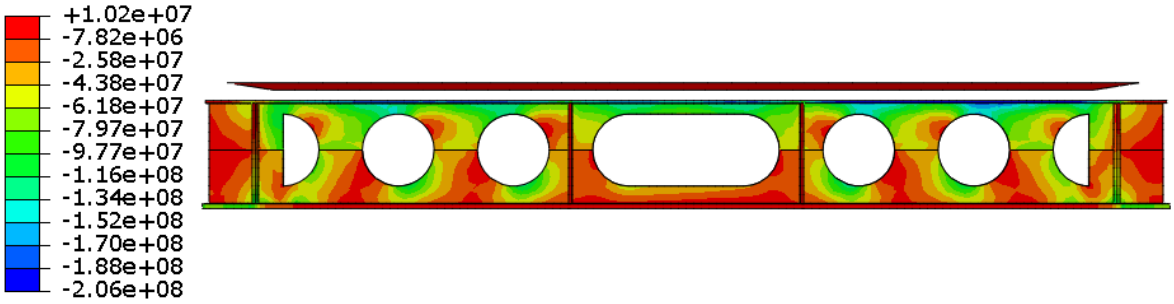

Beam 1

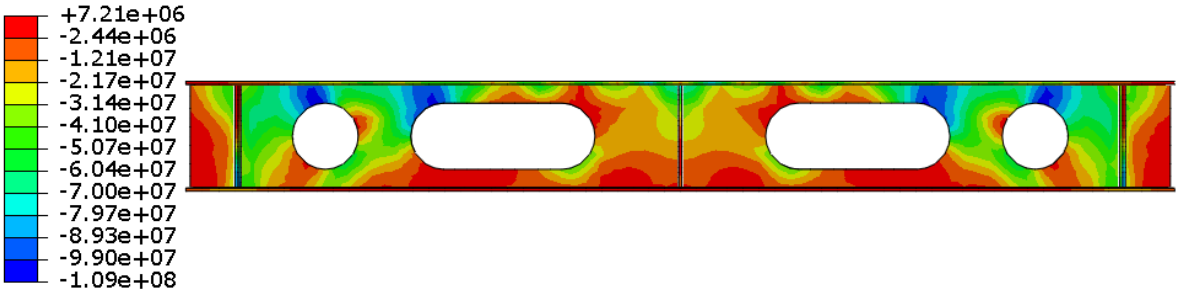

Beam2

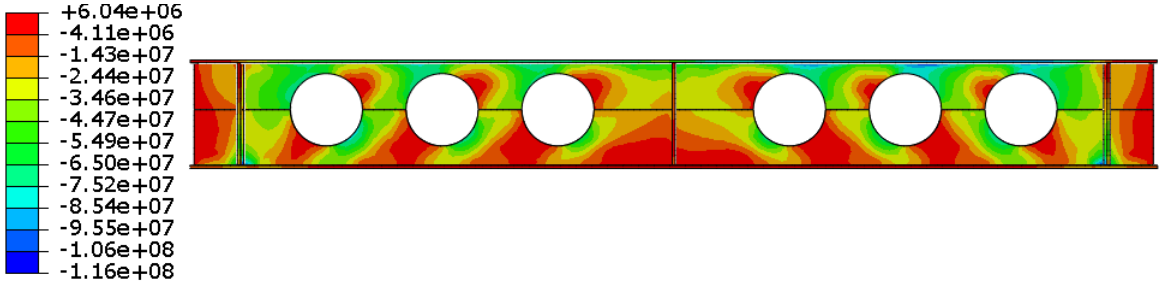

Beam 3

Figure 6.5-4 Compression of the beams at the critical time, N/m^2

As shown in Figure 6.5-4, the compressive stress at the webs and between the openings (at which web failure occurs) is at around 40 MPa. The stress distribution at this temperature has significantly changed from the stress distribution at 20°C (see Figure 6.5-5) as the stress at this temperature is influenced by the plastic zones and changes in the geometry of the beams. For instance, the top of the web at the critical time is fully under compression. Figure 6.5-5 shows that, similar to the truss structures as shown in Figure 4.5-1, the compression of the struts occur diagonally between the openings. However, as discussed

above, the stress distributions are changed due to plastic areas, different stiffnesses and strengths, and changes in the beam geometries at higher temperatures. Figure 6.5-4.

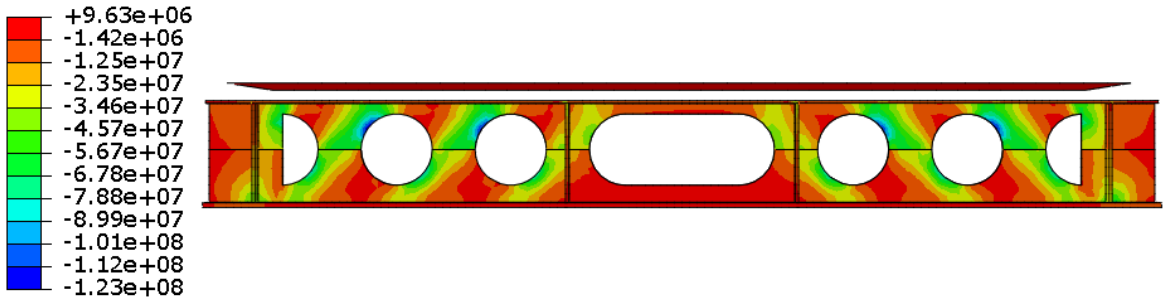

a) Beam 1

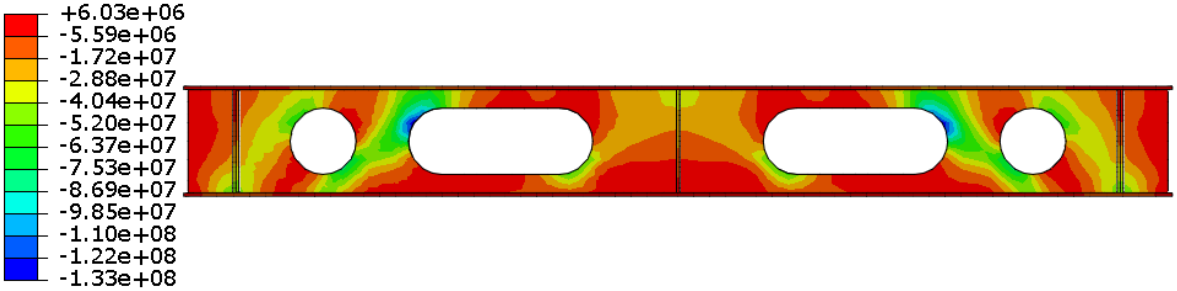

b) Beam 2

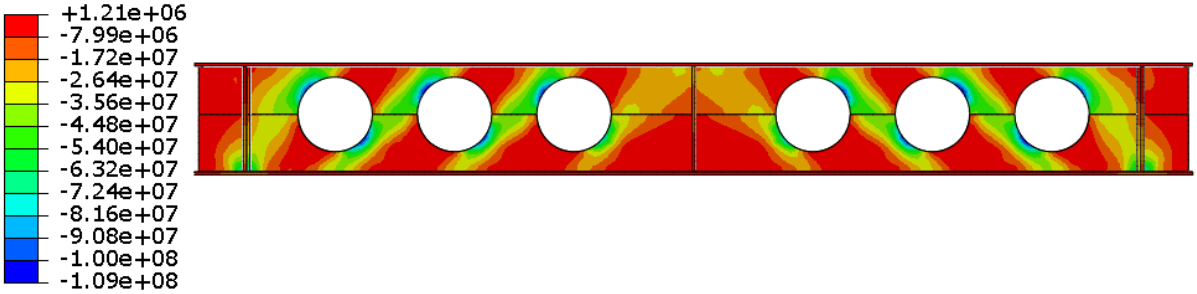

c) Beam 3

Figure 6.5-5 Compression contour plots of beams at 20°C, (N/m^2)

Figure 6.5-6 shows the stress variation of a node located between the two openings at which the web failures occur.

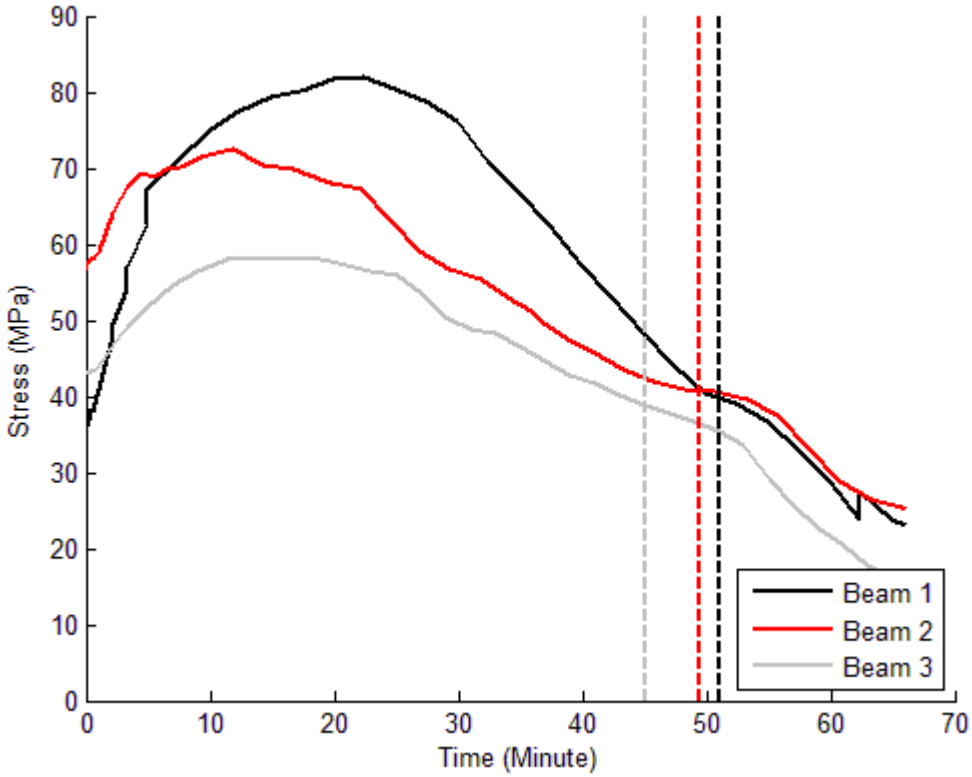

Figure 6.5-6 Compression stress at the web and between the two openings which failure occurs

Figure 6.5-6 shows that at the critical temperature the compression stress is about 40 MPa. The stress patterns show initially the stress increases by losing stiffness but after 20 minutes the overall temperature of the beams reaches 400°C (Figure 6.4-1, Figure 6.4-3, Figure 6.4-5) after which point the strength of the beams reduces rapidly (Figure 6.3-11). This leads to formation of plastic areas within the beams and consequently the redistribution of stresses and reduction in compressive stresses. The reduction factor of steel at 600°C and 700°C is 0.31 and 0.13, respectively. When the web-posts reach the 700°C temperature, they lose most of their stiffness and become susceptible to buckling failures.

6.6 INTERIM SUMMERY

Three perforated composite beams were studied experimentally and numerically in this chapter. The beams were coated with intumescent and located in a fire test chamber at the Ulster University. The beams were first loaded to 30% of their load bearing capacity at room temperature. The load bearing capacity of the beams were determined from previous tests carried out at the Ulster University [37]. Once the loads were fully applied using a hydraulic jack and the beams were deformed under the applied loads, the furnace burners were turned on. The applied loads remain constant during the test. The temperature of the furnace was set to the ISO 834 standard fire curve [73]. The beams lose their stiffness and strength due to the temperature increase and deform more at higher temperatures under the load. By increasing the furnace temperature, the beams were deformed at a faster rate and finally fail due to web-post failure. The two beams fail due to web-post buckling and one beam fails due to Vierendeel failure.

The three beams were also modelled numerically in order to understand the thermal and structural response of composite perforated beams in fire. The simulation was comprised of three steps. The first step was the heat transfer analysis which was carried out to predict the temperature profile of the beam. In this analysis, the composite cellular beams were modelled with intumescent coating and the furnace heat was applied to the surface of the coating. The temperature profile obtained numerically were in good agreement with the experimental results. The temperature profile of each node was stored in an output file for use in the steps which follow.

In the second step the hydraulic jack load was applied. A static model of the beam was created, Temperature dependent material properties were defined for the model and the load applied to the beam. The temperature of the beam was set as room temperature. In the next step the load was kept the same and the transient temperature profile of the heat

transfer analysis was assigned to the beams. The beams lose their stiffness and strength by increasing the temperature due to the definition of the temperature dependent material properties. The deformation and failure mechanisms of the beams were compared against the experimental results and the findings were in a good agreement.

Numerical results show that when the temperature of web-posts reaches to 730°C and simultaneously the compressive stress between the opening (at critical locations with highest sheer forces) reaches 40 MPa, the beams lose their load bearing functionality.

CHAPTER 7 - PARAMETRICAL STUDY

PERFORATED BEAMS

This chapter implements the numerical models developed in Chapter 6 to conduct two parametric studies. The studies address two areas in design standards which are currently insufficient in providing guidelines specific to perforated beams.

The limiting temperature i.e. the temperature at which solid beams become unstable under different ratios of maximum load utilised by a beam during fire to the load utilised by the same beam at 20°C is provided in Table 8 of BS 5950-8 [67]. However, this table is not valid for perforated beams. Consequently, the first part of the present chapter aims to investigate the effect of different load ratios on the performance of composite cellular beams and to determine the temperatures at which beams become unstable under different load ratios.

Additionally, a clear gap exists in codes regarding the structural performance of composite perforated beams exposed to hydrocarbon fires. Hydrocarbon fires may occur onshore and in residential, industrial or commercial buildings such as car parks, aircraft warehouses, industrial buildings with fuel storage vessels, train stations, coach stations, ports, etc. However, they mostly occur in the oil and gas industry and particularly the offshore sector. The high risk of hydrocarbon fire is the offshore sector is due to the existence of high temperature and high pressure crude oil and gas pipes and vessels and the dense distribution of instruments in limited space of platforms [82].

In terms of the specification of limiting temperatures, offshore standards tend to refer to a single limiting temperature for all members. ISO 13702 [83] clearly suggests 400°C as the

limiting temperature of structural steelwork for offshore facilities. The standard only provides a number. It does not provide a table (similar to Table 8 of BS 5950-8). API standards do not categorise limiting temperatures as per load ratios. For instance API 2218 [84] for refineries, uses a failure temperature of 1000°F (538°C) as per the standard fire test (UL 1709) [85]. The Health and Safety Executive (HSE) [86] also set the limiting temperature of steel elements for accommodation area and helideck structure of offshore facilities to 400°C. DNV-OS-D301[87] gives a limiting temperature of 400°C to 450°C for steel members.

The second part of this chapter explores the influence of hydrocarbon fires on the structural performance of perforated beams and aims to provide a strategy and guidelines which narrow this particular gap in the standards.

The chapter starts by discussing the research strategy implemented in this chapter. Section 7.25.6 explains how numerical models are developed for the parametric studies. Section 7.3 and 7.4 provides the results obtained using the numerical models of the load ratio and hydrocarbon fire studies, respectively. Section 7.5 discusses the results and findings of the numerical study of the of protected perforated beams. The chapter concludes with an interim summary in Section 5.8.

7.1 STUDY STRATEGY

The numerical models and methods developed and validated in Chapter 6 provide a suitable tool in performing the two parametric studies presented in this chapter: 1) the influence of load ratio on the structural performance of perforated beams and identifying the limiting temperatures, 2) the behaviour of perforated beams in hydrocarbon fires.

The 3 long perforated coated composite beams examined in Chapter 6 and their numerical models are used in both parametric studies (see Section 6.2 – 6.3 for details).

To carry out the first study, different load magnitudes are applied to the beams. The resulting deformation of the beams are then compared and analysed to find the points in time at which the beams fail to function (critical time). This leads to the determination of the limiting or critical temperature i.e. the maximum temperature at the critical time which leads to the beam failure. Note that this is the maximum temperature at bottom flange and not the maximum temperature of the entire beam.

Regarding the second study, note that even though in Chapter 6 the beams are exposed to a standard fire curve (cellulose) and validated via comparison with experimental data, the numerical methods are independent of the fire curves and hence experimental hydrocarbon data is not required. In the FEA models, the temperature of the furnace is changed from a cellulose fire to hydrocarbon fire. Time vs deformation plots are then produced and analysed to determine the critical temperature of the beams.

The models of Beams 1, 2 and 3 from the previous chapter (Figure 7.1-1) are used for the parametric studies. The geometry of the beams is given in Table 6.2-1.

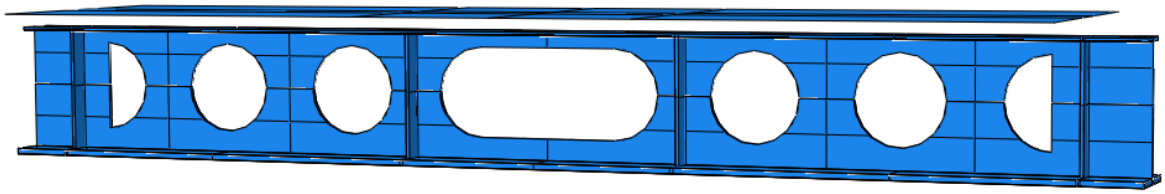

a) Beam 1

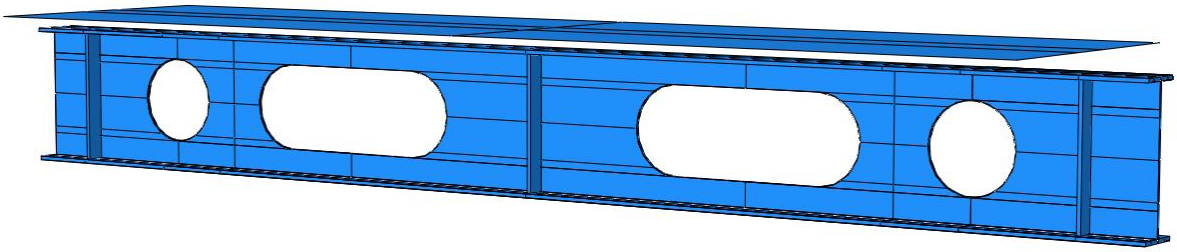

b) Beam 2

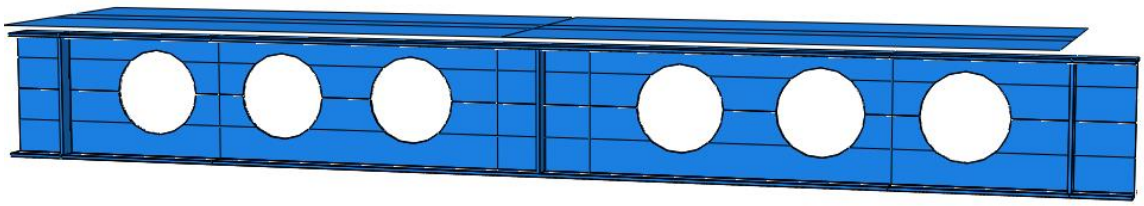

c) Beam3

Figure 7.1-1 FEA models of beams

7.2 PARAMETRIC STUDY

This section discusses the numerical methods used for the parametric studies and processing of the FE simulation results.

7.2.1 Load ratio study

For the parametric study of the effect of load ratios on the performance of perforated beams, the temperature distribution of coated beams rather uncoated beams is used. This is because steel has a high thermal conductivity and a relatively low thermal capacity. Therefore, the time lag between the temperatures of the steel reaching the furnace temperature is small. This leads to a more uniform temperature distribution in a non-protected beam in comparison with a protected beam. Different temperature distribution profiles may lead to different stability limits in beams. EN 1993-1-2 (clause 4.2.3.3) uses

an empirical adoption factor to capture the effect of non-uniform temperature distribution. Here protected beam temperature distributions are used for the parametric study and therefore, there is no need for any adoption factors.

The applied loads on the beam during the experiment are set to up to 30% of the ultimate load of the beam at room temperature. The ultimate loads of the beam are estimated from previous tests conducted by Nadjai at the Ulster University [37]. The loads are varied from 85% of ultimate load to 15% of the ultimate load in l0kN load increments. For beam 1 with the ultimate load of 670kN, 71 load cases are defined and for beams 2 and 3 with the ultimate load of 500kN, 54 loads cases are defined. In total, ABAQUS is run for 179 cases. In order to decrease the computational time and avoid the user error due to large number of required simulation runs, scripts are written in Python to automate pre-processing, processing and post-processing of the parametric study.

Buckling phenomena is a numerically unstable condition. As it was discussed in Chapter 3, in general to model web-post failure three methods (Riks method, general static and eigenvalue buckling methods) are available in ABAQUS. The Riks method is not applicable for a thermal transient condition because time is not a numerical parameter in this technique and therefore temperature variations of the beams cannot be defined. The general static and eigenvalue buckling methods are more suitable for simulation of loaded beams with transient temperatures. The latter has to be used in combination with the general static method in order to take into account the deformed geometry of the beam before buckling. In other words, first the static analysis is run and the deformed geometry resulting from the static analysis becomes the initial model for the buckling analysis. The limitation of this technique is that the buckling analysis uses underrated properties (material properties at 20°C). This means that the Eigenvalue method uses stiffer material properties. This leads to inaccurate results as buckling strength is a function of stiffness.

Overall, the static analysis method is more suitable for the simulation of beams at fire conditions.

In the static analysis method, an artificial damping is introduced to stabilise the solution. The damping factor for the simulation is selected with extra care so that the artificial damping does not lead to inaccurate results. The ratio of energy dissipated by damping to the total strain energy is limited to the less than 5% to minimise the damping on the overall response of the beam to the applied load. The artificial damping is explained in detail in Chapter 3.

Using the numerical stabilise method allows the model to deform after failure for a limited time. However, since the damping factor for the simulation is selected with extra care and the ratio of dissipated energy by damping to the total strain energy is limited to less than 5%, the deformation of the beam after failure load is limited as the model becomes unstable. Determining the exact time of the beams failure is difficult due to introduction of the artificial damping.

To define the limiting temperature, it is required to identify the exact failure load in the parametric study. However, as it is explained in the above paragraphs due to numerical limitation it is not possible to determine those exact failure loads. In order to compare the performance of the beams under different load ratios, two types of failure indicators are defined. The first type of indicator assumes that the beams are not functional after deforming more than a certain limit. BS 476 [61, 88] uses a limit of span over 20 and span over 30 as the maximum allowable deformation in fire condition. Building Research Establishment [BRE] [89] identified span over 40 as the maximum deformation of coated steel beams. The rate of beam deformation is the other indication of the failure of the beams. BS 476 sets the maximum rate of beam deformation to

$$V = \frac{L^2}{9000d}, \qquad \textbf{7.2-1}$$

where V is the rate of deformation in *mm/min*, *L* is span of beam in *mm* and *d* is the distance from the top of the beam to the bottom of the beam in *mm* [42, 61, 71, 88].

The deformation and the rate of deformation indicators are used to determine the failure time of the beam. The maximum temperature of the bottom flanges against time are extracted separately from the FEA models. The bottom flange temperature for each load ratio is then determined from the failure time.

7.2.2 Hydrocarbon fire

As mentioned in Section 7.1, the second parametric study looks at the failure of the 3 beams studied in Chapter 6 exposed to the hydrocarbon fire curve and compares the structural and thermal performance of the beams between hydrocarbon and celluloses fire. As shown in Figure 7.2-1, the hydrocarbon temperature rises faster and reaches a steady state temperature of 1100°C after 10 minutes. The temperature in the standard fire curve (cellulose fire) increases to 600°C in the first 10 minutes and in the 80 minutes after that it gradually rises to 1005°C.

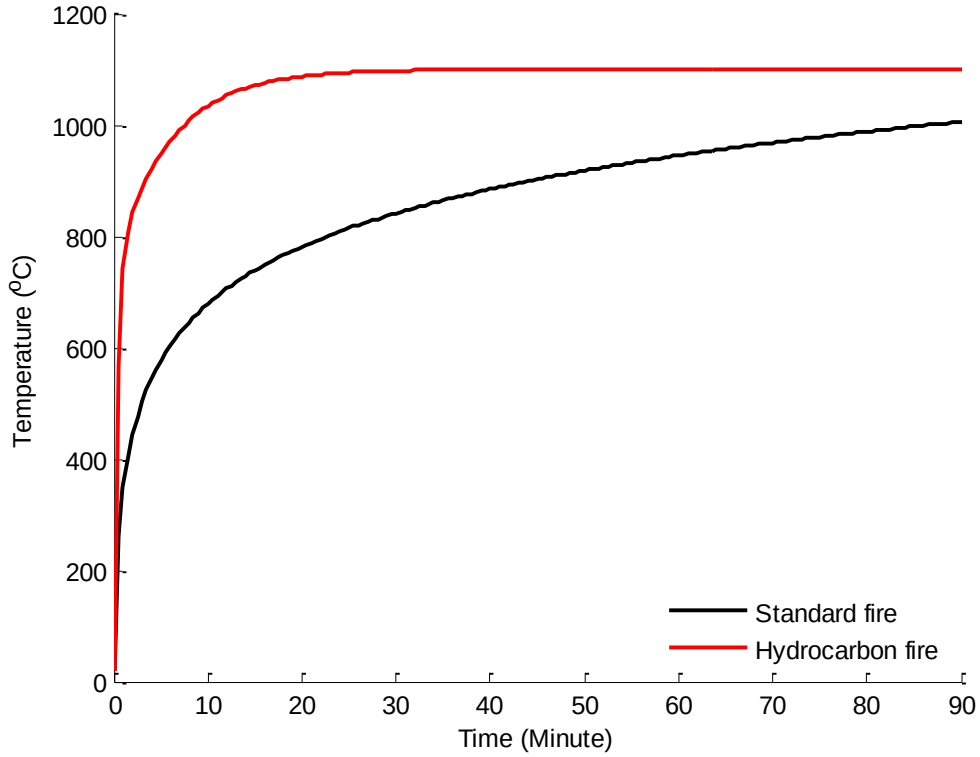

Figure 7.2-1 Hydrocarbon and standard fire curves

The fast rate of increase in heat and higher temperatures can lead to different structural performances of the beams as the stiffness and strength of the perforated beams decrease almost at the same percentage after 10 minutes.

As explained in Chapter 6, due to shadow effects during the tests, the lower flanges are exposed to more heat by radiation compared to the rest of the beam. Therefore, in Chapter 6 to cover the heat exposed variation different furnace temperatures around the beams are used. During the experiment, 8 thermocouples are used to measure the temperature of the ambient around the beams. To capture the different heat exposed, instead of defining a uniform temperature around the beams, the recorded gas temperatures around the beams are used as the beams ambient temperatures. This approach can be referred to as the localised furnace temperatures.

For the hydrocarbon numerical study, there is no fire test experiment available. Therefore, the percentage difference between the recorded temperature during the experiments

(Section 6 of Chapter 6) and the standard fire ISO curve is calculated. This percentage difference is then applied to the hydrocarbon fire curve, in order to localise the ambient temperature around the beams. The localised temperature is used for the definition of radiation and convection functions. This approach causes more heat to be exposed to the bottom flange compared to the rest of the beam.

7.3 RESULTS OF THE LOAD RATIO PARAMETRIC STUDY

Figure 7.3-1 shows the rate of deformation of beam 1 for every other five load ratios. The red line in the figure shows that the displacement of the beams increases at a faster rate after the displacement rate of the beam reaches 1.5 mm/minute. The deformation rate of 3.96 mm/minute is then taken as an indicator that the beams lose their load bearing capacity after this point and start to deform at faster rates. This time is referred to as the "critical time".

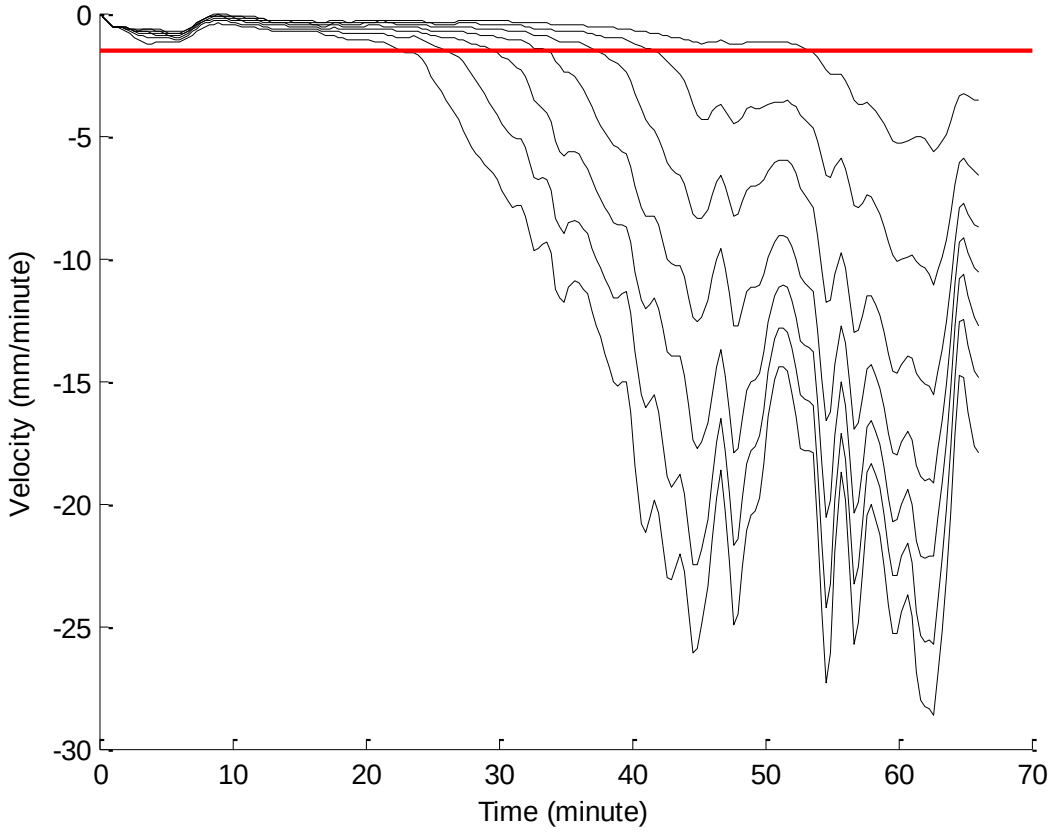

Figure 7.3-1 Velocity of beam deflection, for every other five load ratio velocities

Figure 7.3-2 shows the maximum bottom flange of beams temperature against the different load ratios at the failure time. The failure time is set to the limit of deformation and the rate of defamation which are specified in the BS 476 and the BRE publication [61, 89].

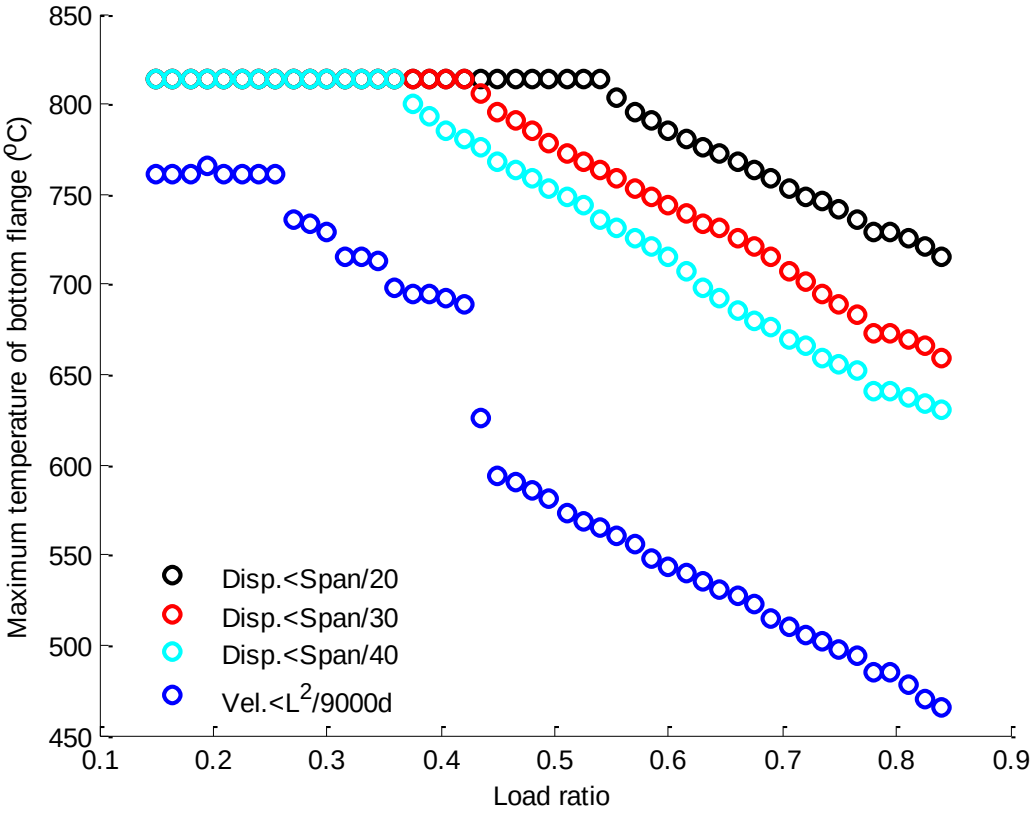

a) Beam 1

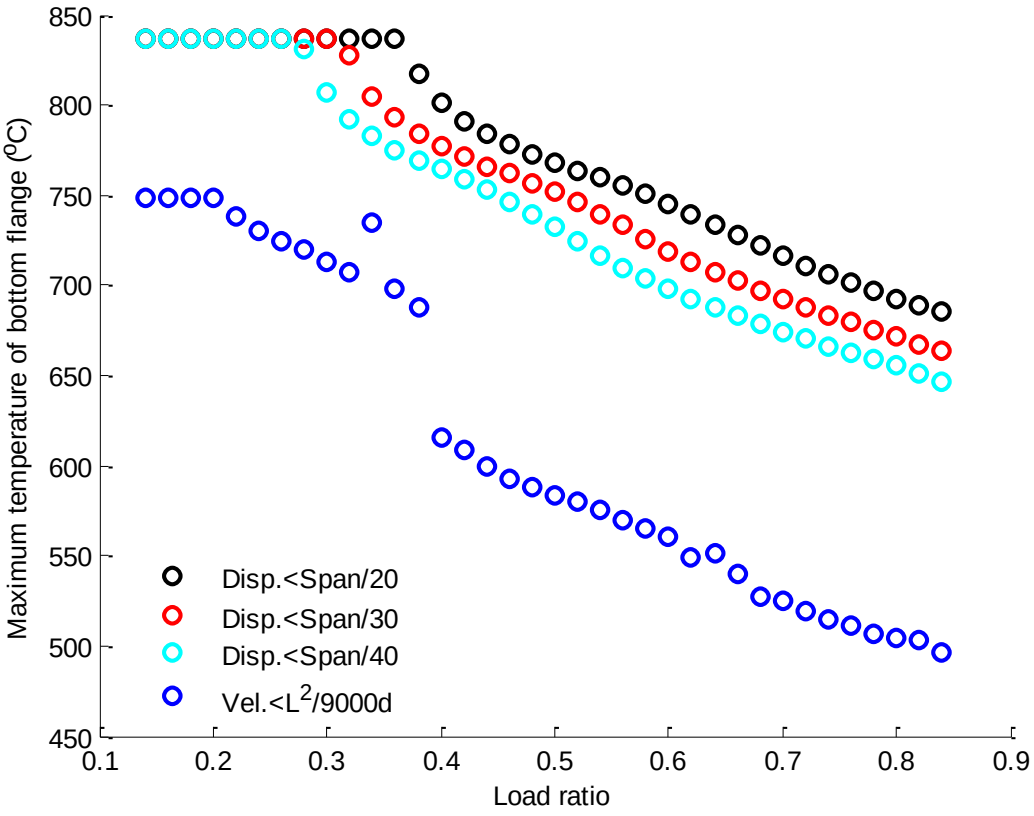

b) Beam 2

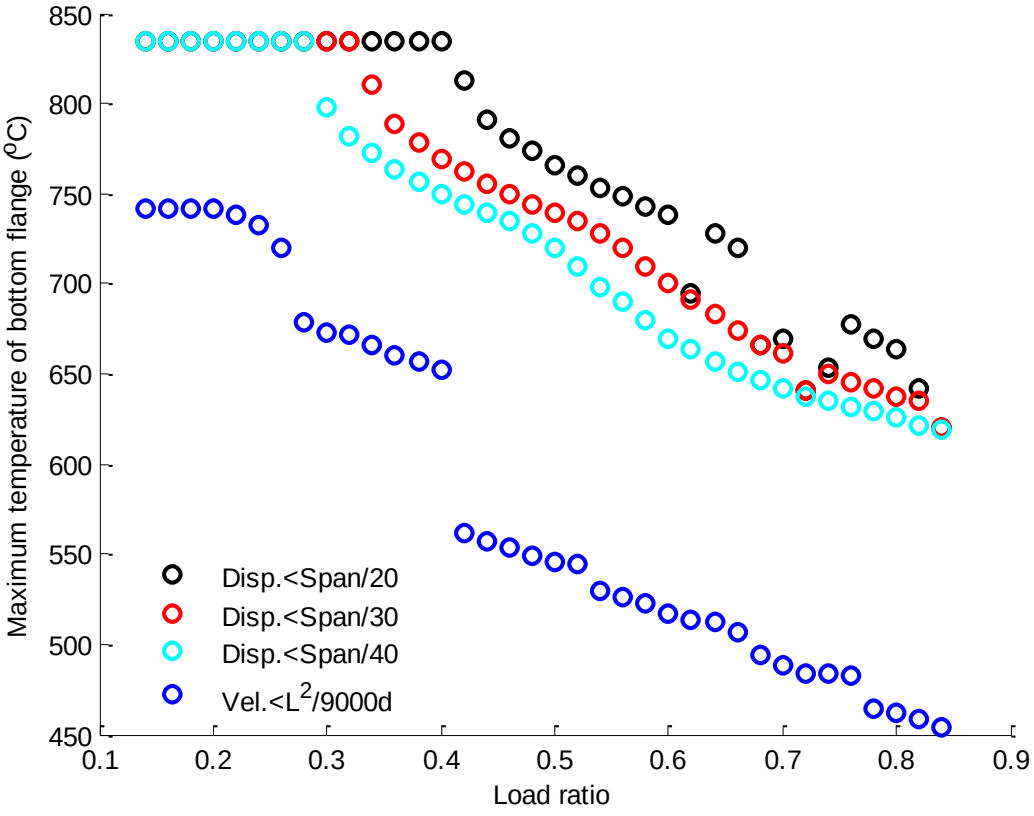

c) Beam 3

Figure 7.3-2 Maximum bottom flange temperature at failure time versus load ratios

7.4 RESULTS OF THE HYDROCARBON FIRE LOAD

7.4.1 Thermal analysis results

This section presents the temperature profiles of perforated beams exposed to hydrocarbon fire.

7.4.1.1 Beam 1

Figure 7.4-1 shows the temperature history of the beam at the nodes which represent the location of the thermocouples in the test.

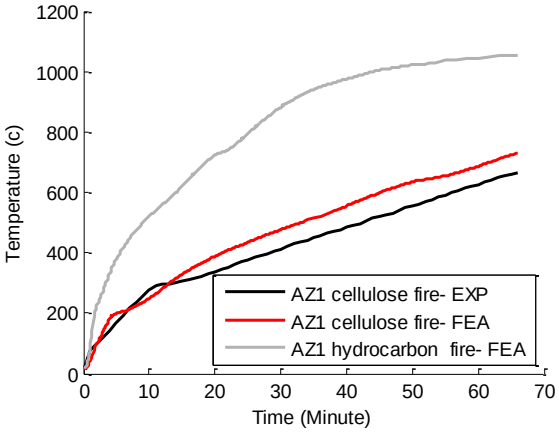

a) Temperature history of thermocouple A-Z1

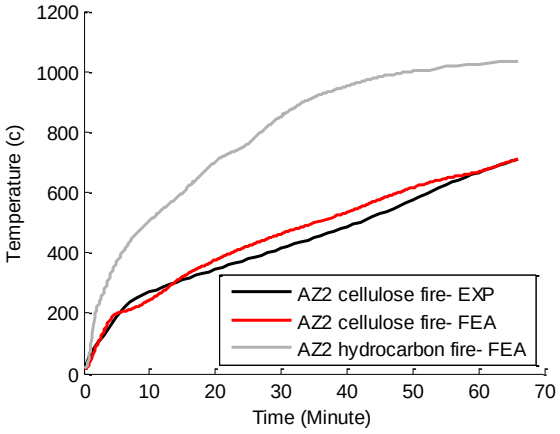

b) Temperature history of thermocouple A-Z2

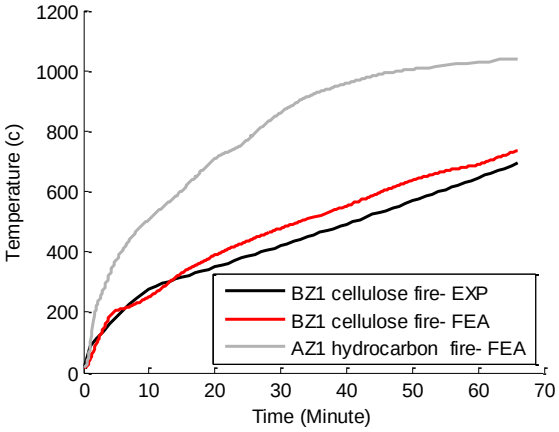

c) Temperature history of thermocouple B-Z1

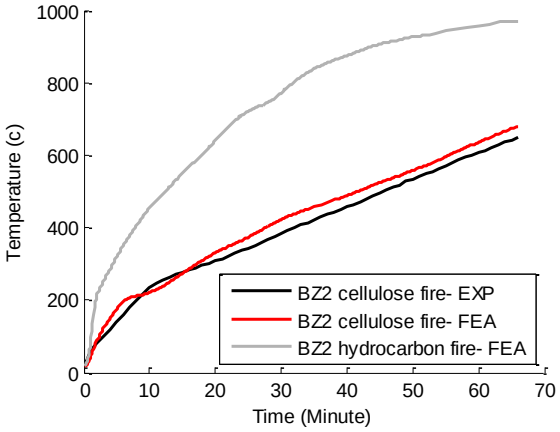

d) Temperature history of thermocouple B-Z2

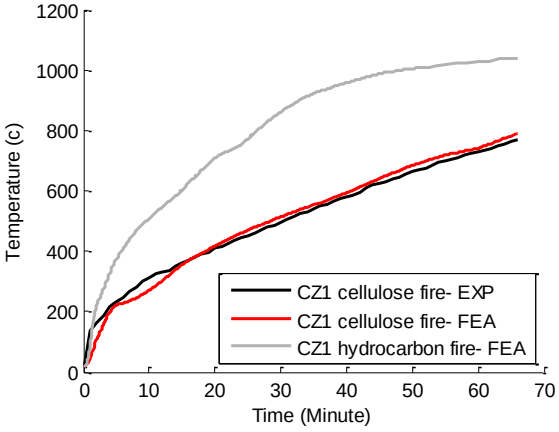

e) Temperature history of thermocouple C-Z1

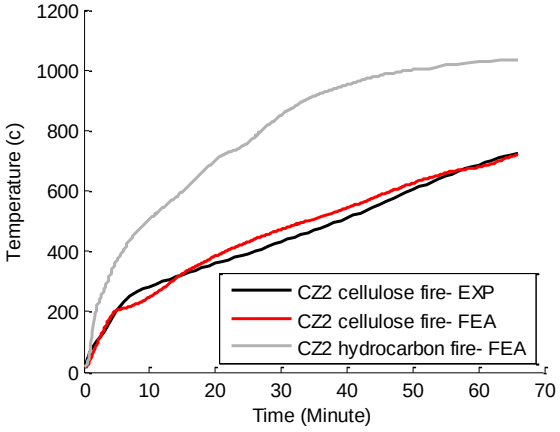

f) Temperature history of thermocouple C-Z2

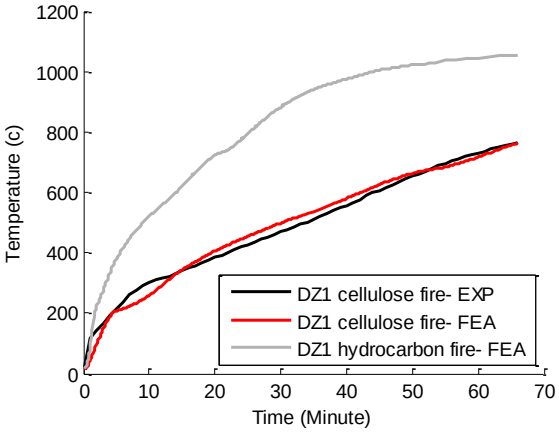

g) Temperature history of thermocouple D-Z1

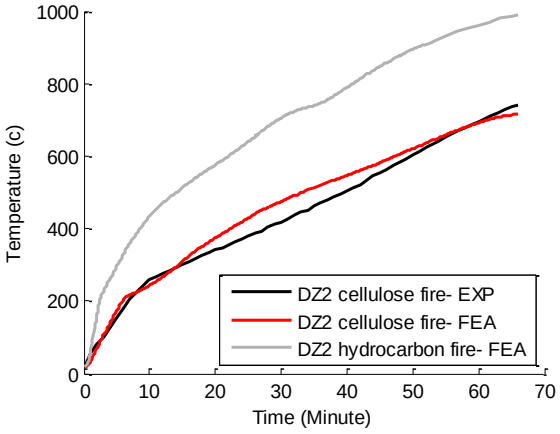

h) Temperature history of thermocouple D-Z2

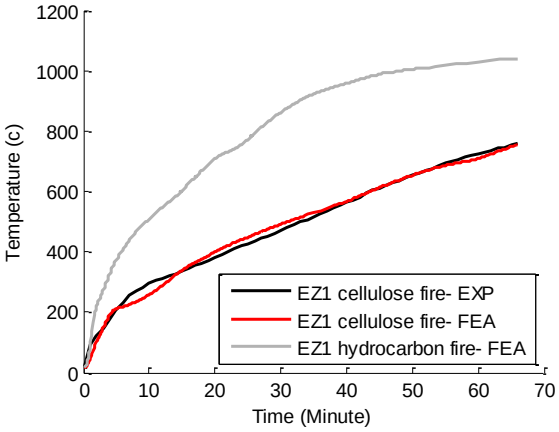

i) Temperature history of thermocouple E-Z1

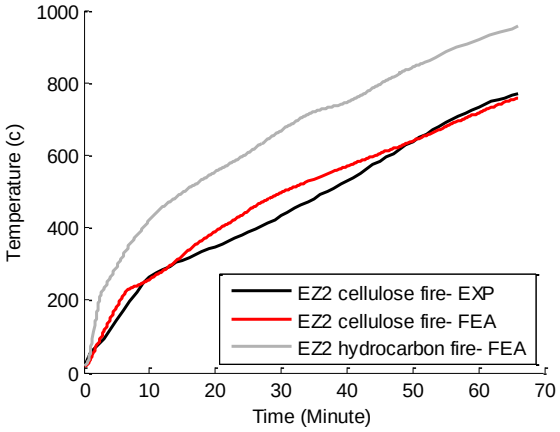

j) Temperature history of thermocouple E-Z2

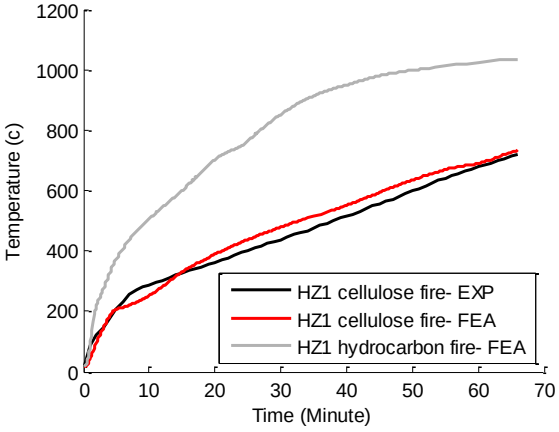

k) Temperature history of thermocouple H-Z1

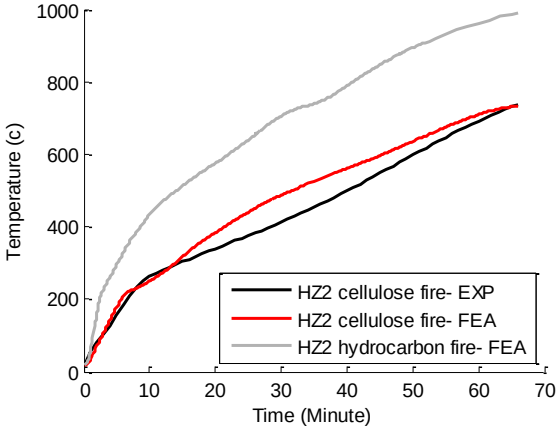

l) Temperature history of thermocouple H-Z2

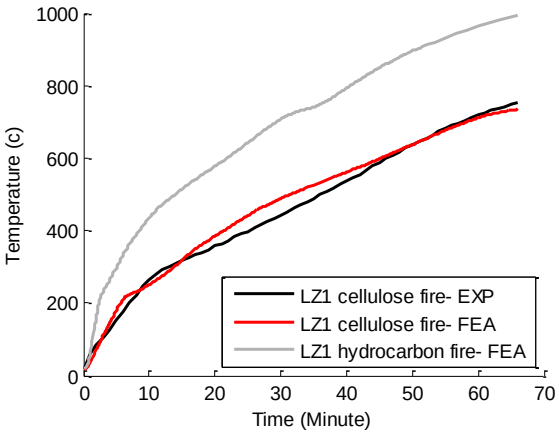

m) Temperature history of thermocouple L-Z1

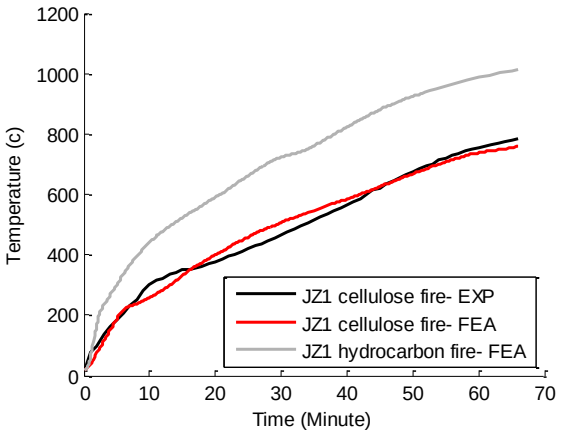

n) Temperature history of thermocouple J-Z1

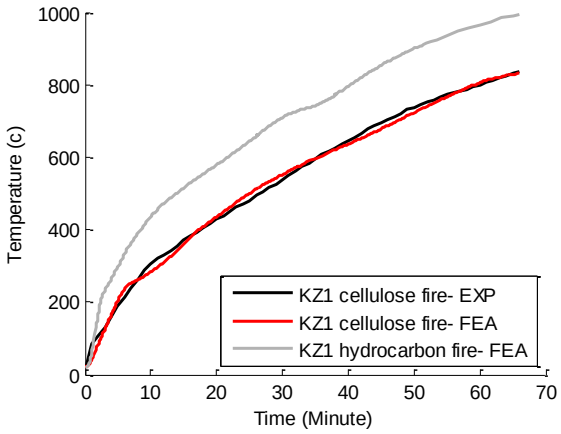

o) Temperature history of thermocouple K-Z1

Figure 7.4-1 Temperature history of beam 1, FEE and test results

Figure 7.4-2 shows the temperature contour plot of the steel section of beam 1 at the end of the test.

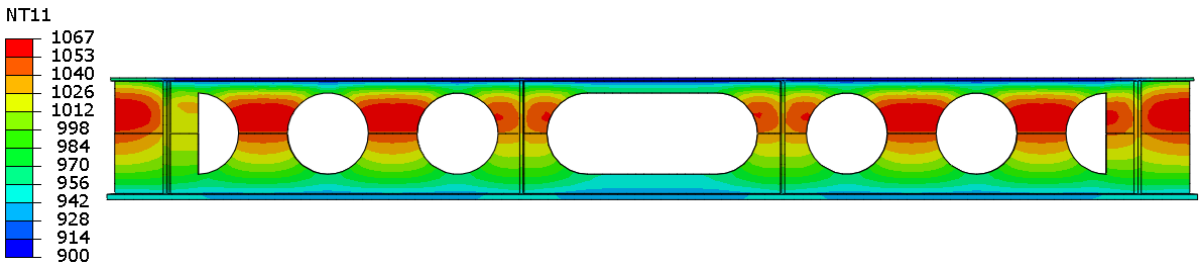

Figure 7.4-2 Temperature contour plot of the steel part of the beam 1 (°C)

7.4.1.2 Beam 2

Figure 7.4-3 shows the temperature history of the nodes at the locations of the thermocouples in the test.

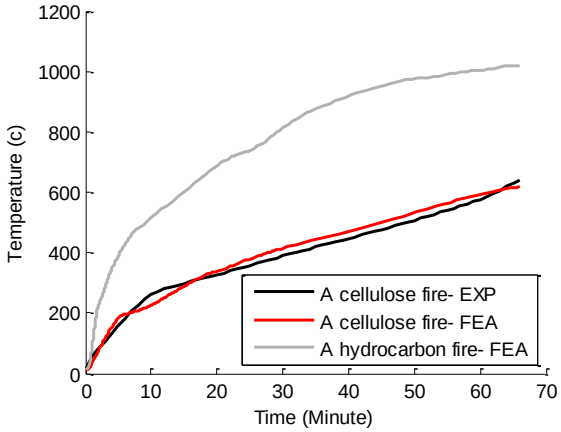

a) Temperature history of thermocouple A

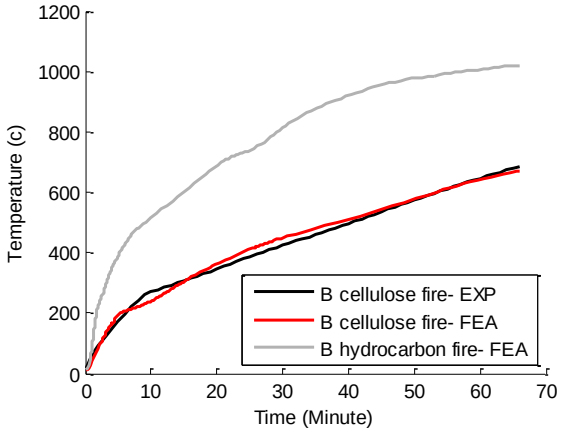

b) Temperature history of thermocouple B

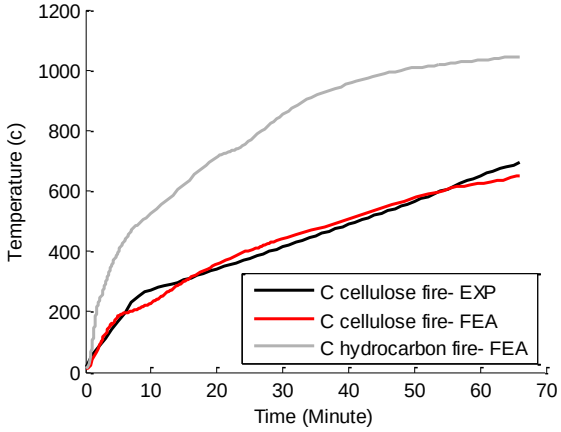

c) Temperature history of thermocouple C

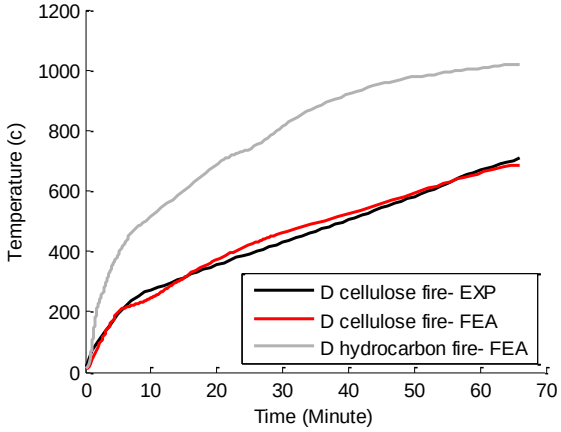

d) Temperature history of thermocouple D

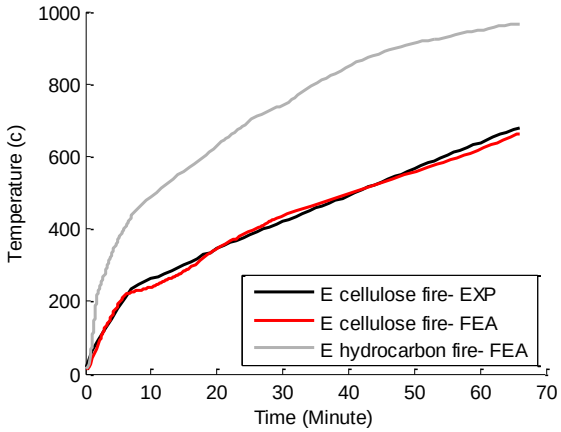

e) Temperature history of thermocouple E

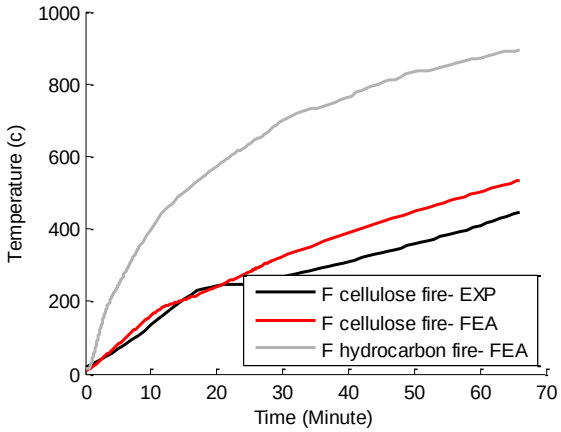

f) Temperature history of thermocouple F

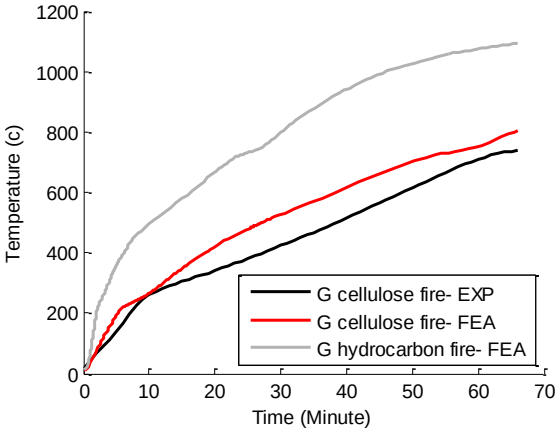

g) Temperature history of thermocouple G

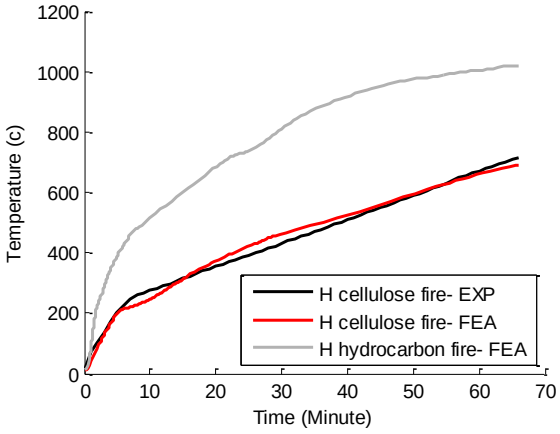

h) Temperature history of thermocouple H

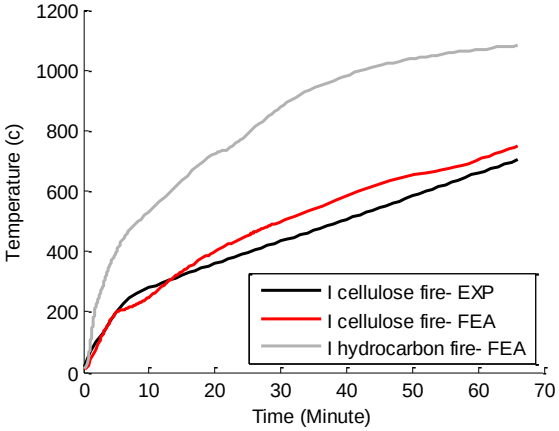

i) Temperature history of thermocouple I

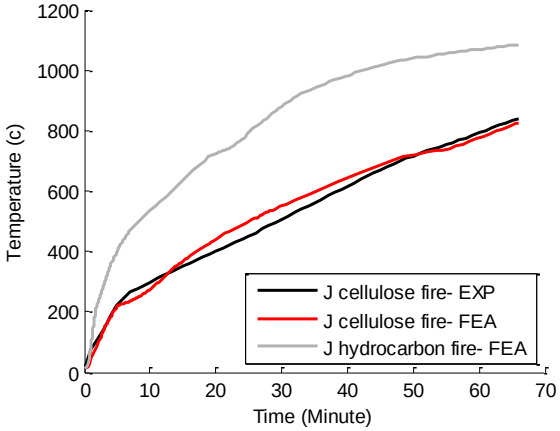

j) Temperature history of thermocouple J

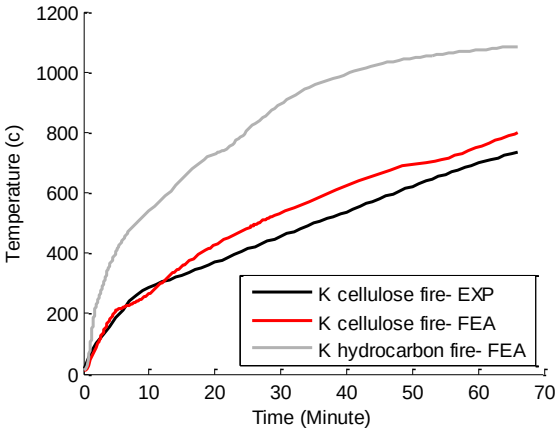

k) Temperature history of thermocouple K

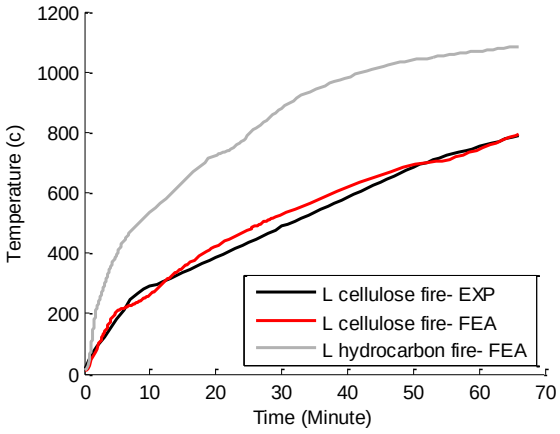

l) Temperature history of thermocouple L

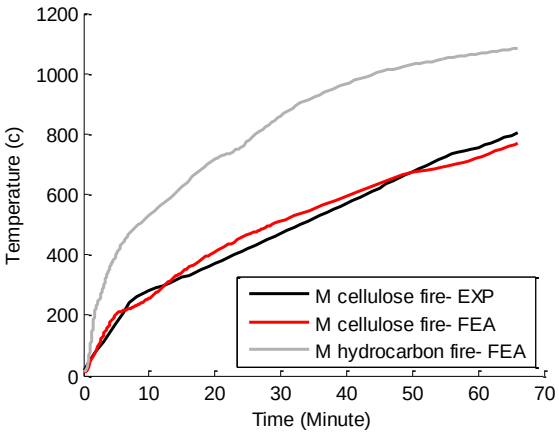

m) Temperature history of thermocouple M

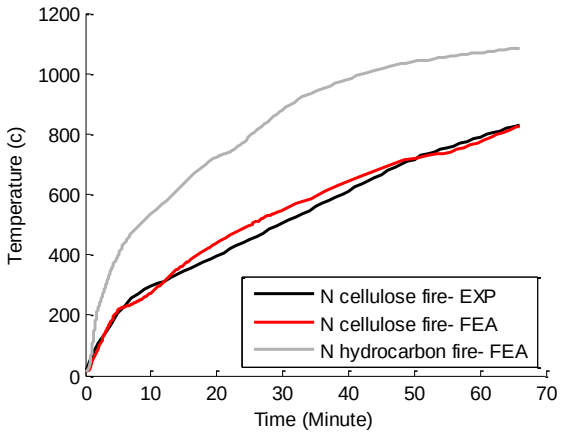

n) Temperature history of thermocouple N

Figure 7.4-3 Temperature history of beam2, FEE and test results

Figure 7.4-4 shows the temperature contour plot of the steel material of beam 2 at the end of the test.

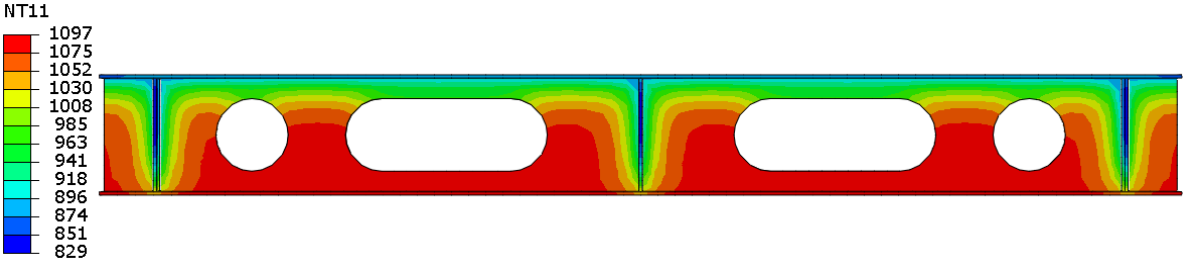

Figure 7.4-4 Temperature contour plot of the steel part of beam 2 (°C)

7.4.1.3 Beam 3

Figure 6.4-5 shows the temperature history of the nodes at the locations of the thermocouples in the test.

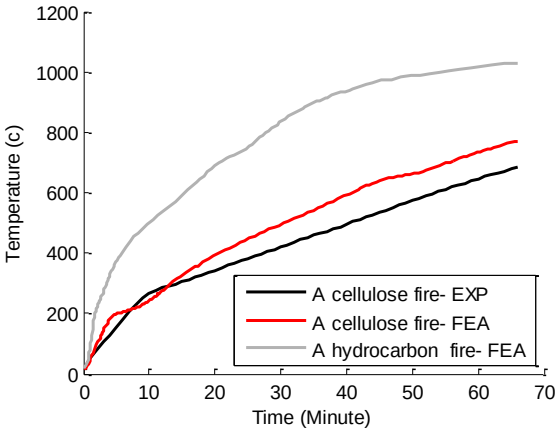

a) Temperature history of thermocouple A

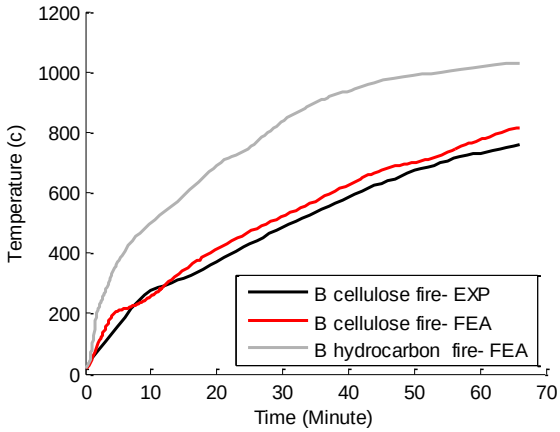

b) Temperature history of thermocouple B

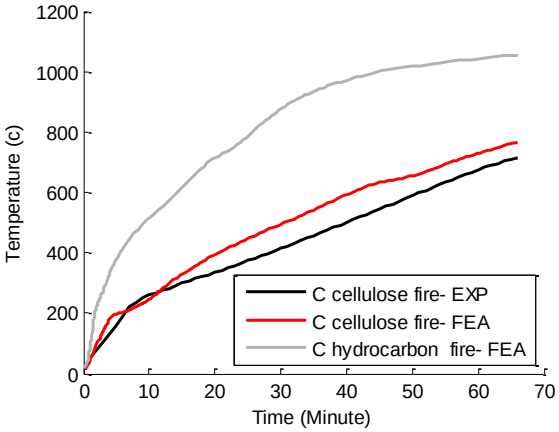

c) Temperature history of thermocouple C

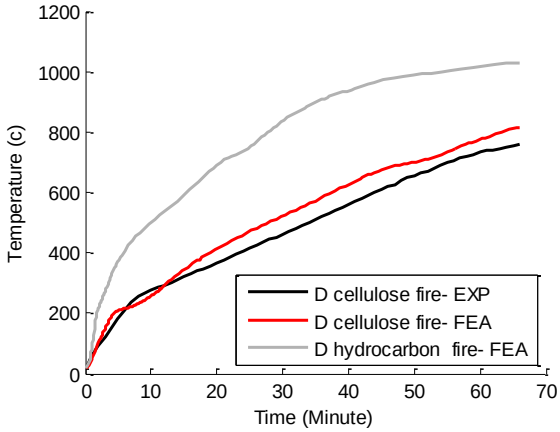

d) Temperature history of thermocouple D

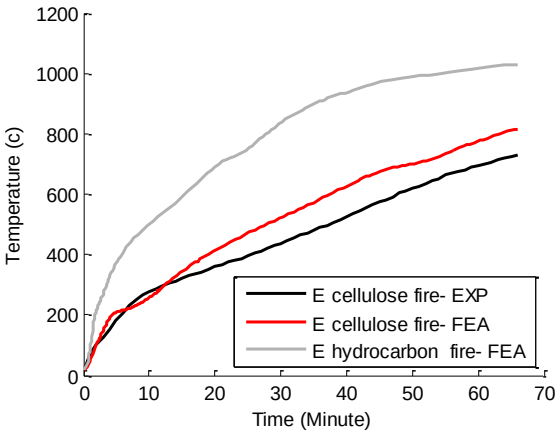

e) Temperature history of thermocouple E

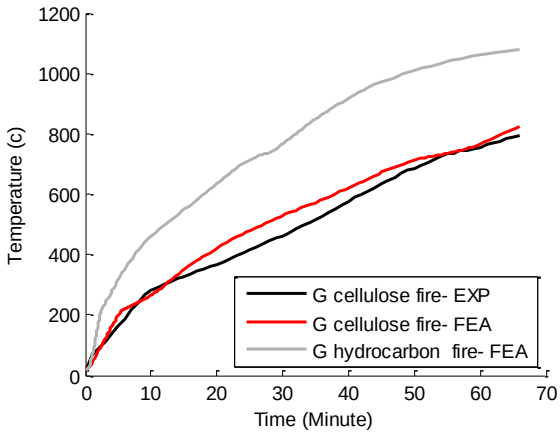

f) Temperature history of thermocouple G

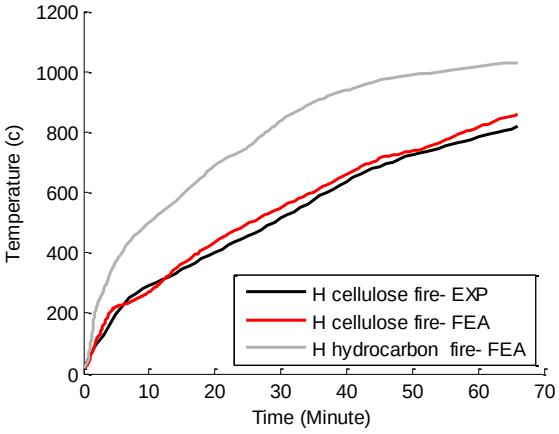

g) Temperature history of thermocouple H

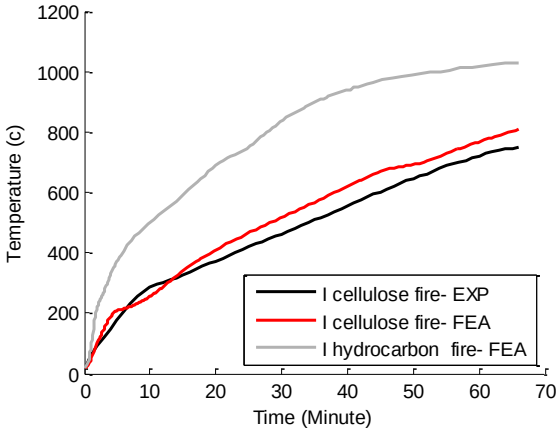

h) Temperature history of thermocouple I

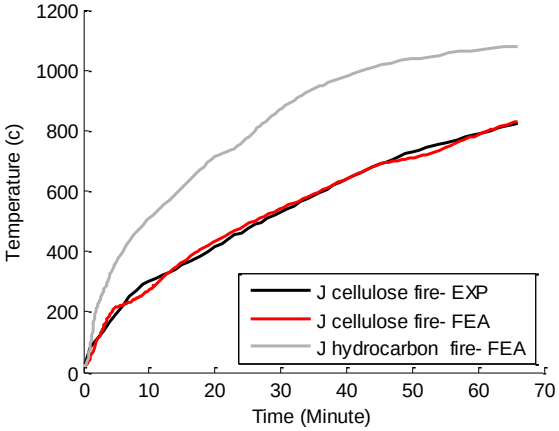

i) Temperature history of thermocouple J

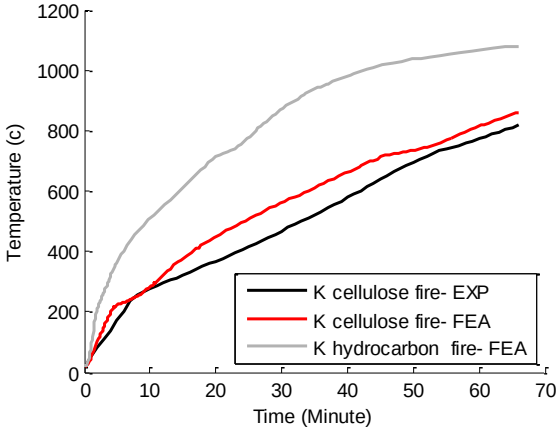

j) Temperature history of thermocouple K

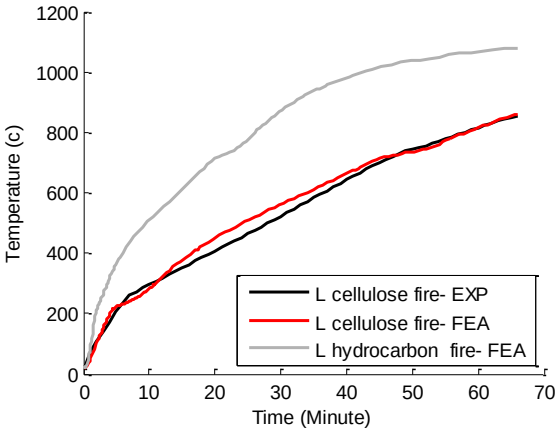

k) Temperature history of thermocouple L

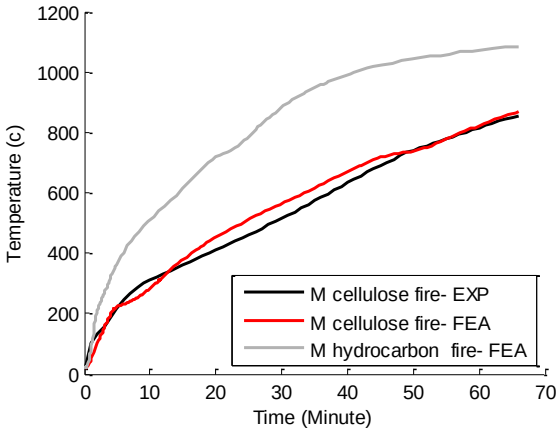

l) Temperature history of thermocouple M

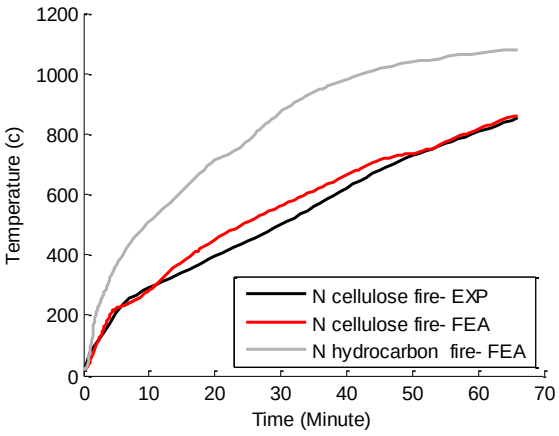

m) Temperature history of thermocouple N

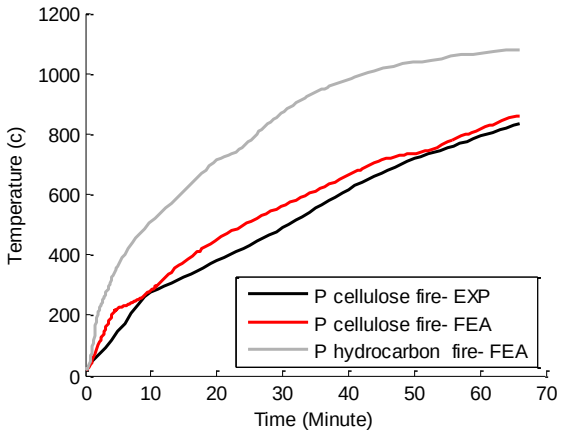

n) Temperature history of thermocouple P

Figure 7.4-5 Temperature history of beam 3 - FEA and test results

Figure 7.4-6 shows the temperature contour plot of the steel part of the beam at the end of the test.

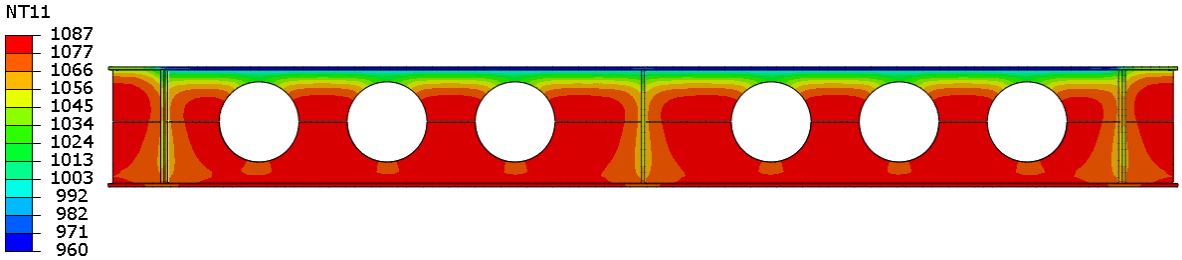

Figure 7.4-6 Temperature contour plot of the steel part of beam 3 (°C)

7.4.2 Beam deflection

7.4.2.1 Beam 1

Figure 7.4-7 depicts the deformation of the beam under loading. The deformation graph shows that beam 1 loses its load bearing capacity after 23 minutes.

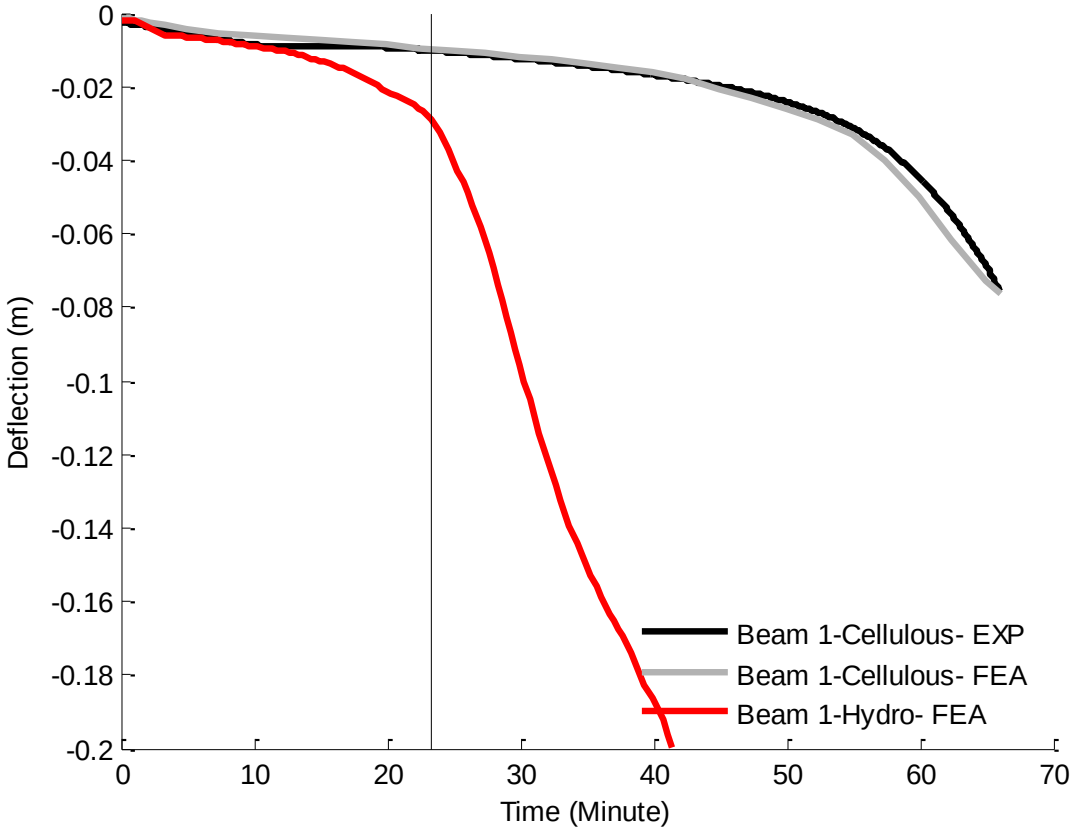

Figure 7.4-7 Deformation of the mid span obtained using FEA and experiment- beam 1

Figure 7.4-7 shows the deformed geometry of beam 1 after 40 and 66 minutes for hydrocarbon and celluloses fire, respectively.

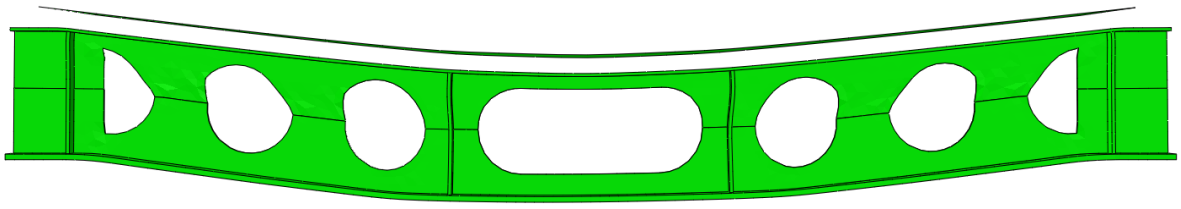

a) Deformed beam 1, hydrocarbon after 40 minutes

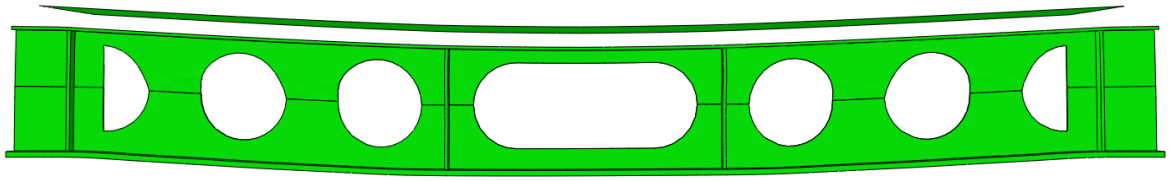

b) Deformed beam 1, celluloses fire after 66 minutes

Figure 7.4-8 Predicted beam deformation in beam1 under celluloses and hydrocarbon fires

7.4.2.2 Beam 2

Figure 7.4-9 shows the deformation of beam 2 under loading. Beam 2 loses its load bearing capacity after 22 minutes under hydrocarbon fire temperatures.

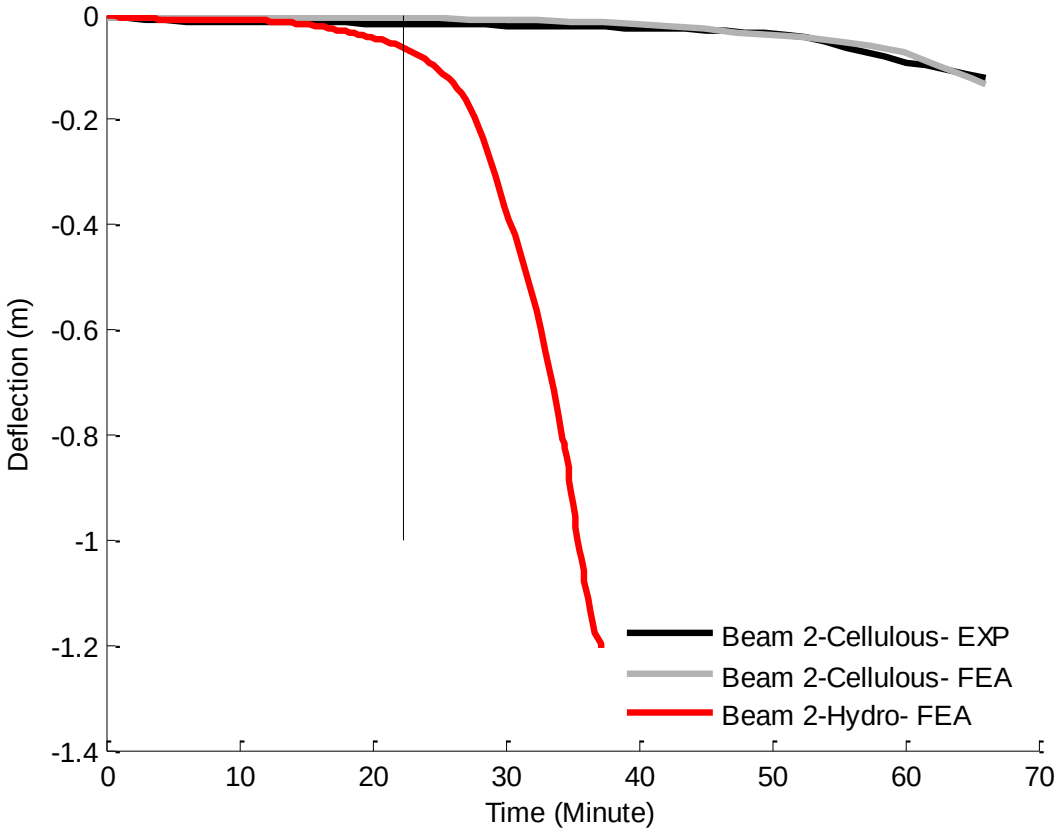

Figure 7.4-9 Beam 2 FEA and experiment deformation of the mid. span under the applied load

Figure 7.4-10 shows the deformed geometry of beam 2 after 30 and 66 minutes.

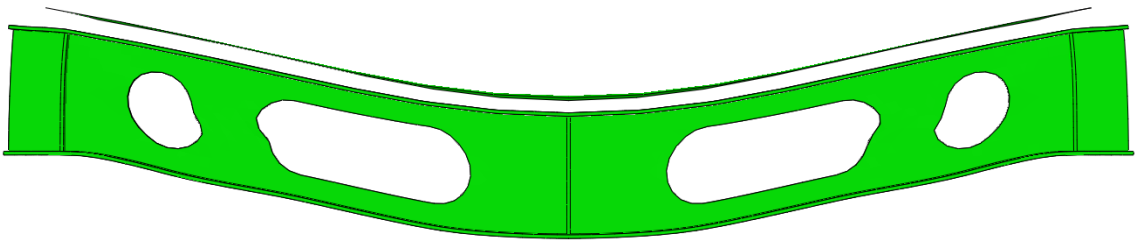

a) Deformed beam 2, hydrocarbon fire after 30 minutes

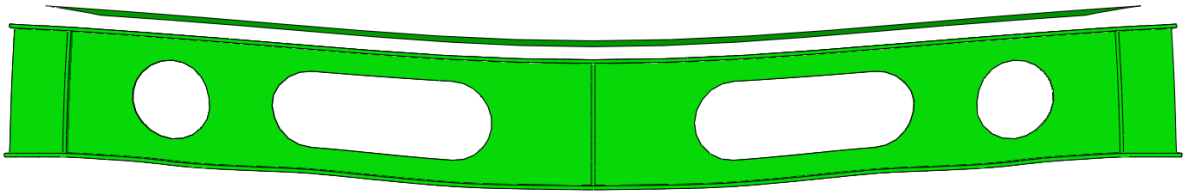

b) Deformed beam 2, celluloses fire after 66 minutes

Figure 7.4-10 Predicted beam deformation in beam 2 under celluloses and hydrocarbon fires

7.4.2.3 Beam 3

Figure 7.4-11 shows the deformation of the beam under loading. Beam 3 loses its capacity after 21 minutes under hydrocarbon fire temperature.

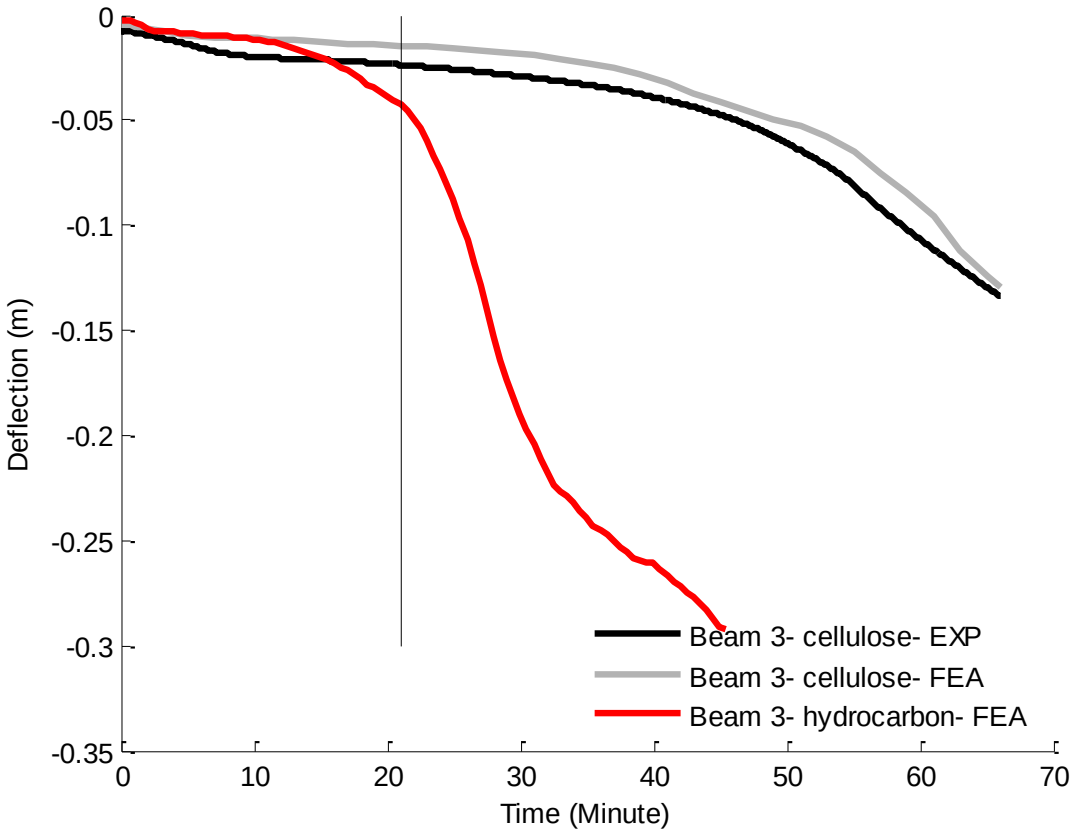

Figure 7.4-11 FEA and experiment deformation of the mid span, Beam 3

Figure 7.4-12 shows the deformed geometry of the beam after 66 minutes and 21 minutes for hydrocarbon and celluloses fire, respectively.

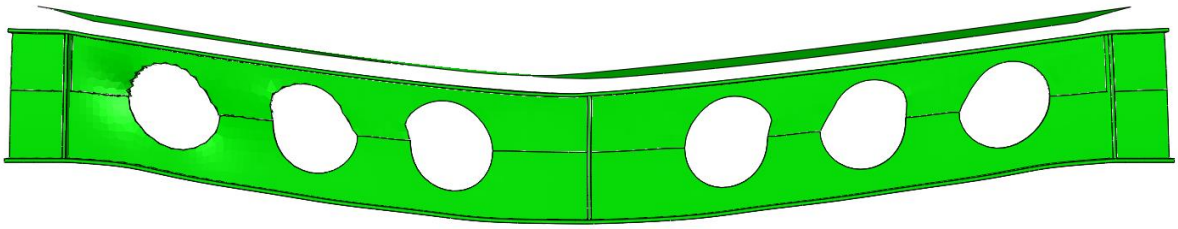

a) Deformed beam 3, hydrocarbon fire after 40

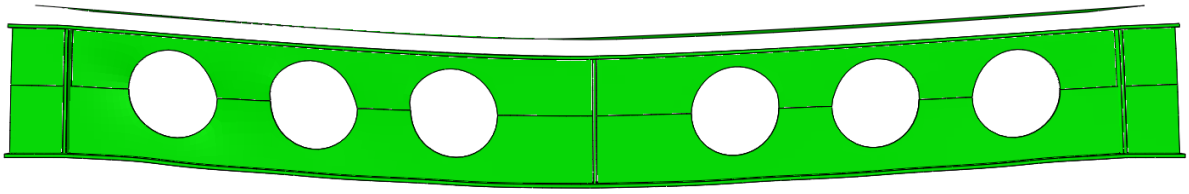

b) Deformed beam 3, celluloses fire after 66 minutes

Figure 7.4-12 Predicted beam deformation in beam 3 under celluloses and hydrocarbon fires

7.5 DISCUSSION

7.5.1 Load ratio study

As shown in Figure 7.3-1 the three beams deform at a faster rate after their deformations reach 1.5 mm/minute. According to BS 476, the critical deformation rate is 3.91 mm/minutes. This discrepancy is because the rate of deformation increases after it reaches 1.5 mm/minute but the steel beams are still functional at this time and they can carry the applied loads. A deformation rate of 1.5 mm/minute is an indication that failure will occur after this point but not earlier. The 3.91 mm/minutes is the criteria that the beams are not able to carry the applied loads.

Figure 7.3-2 shows the bottom flange temperature against the failure criteria defined in BS 476 [88] and BRE [89]. According to BRE, the displacement at which composite beam failure occurs is span/40. Comparison between the rate of deformation and maximum deformations criteria shows that the beams first reach the maximum rate of deformations.

This means that the beams with different load ratios first begin to deform at a faster rate due to loss of their stiffness and then they reach the maximum deformation.

Figure 7.3-2 shows that for lower load ratios (i.e. load ratios below 30%) the critical temperature (which is determined from the rate of deformation) is the same. This means that due to lower loads beams do not reach the defined failure criteria.

BS 476 and other standards define the deflection rate failure criteria for both steel and composite beams. Concrete has better fire resistance properties than steel and therefore the composite beams have deformed less than the steel beams with the same section modules and under the same loading. Therefore, it can be concluded that to be on the safe side, the rate of failure criteria in these standards is set for the steel beam deflections which are deflated more and faster than composite beams.

Hence, using one failure criterion for both steel and composite beams leads to the composite beams having higher temperatures than steel beams with the same section modulus and loading. The higher temperature and consequently lower stiffness makes web-posts of composite perforated beams susceptible to web-post buckling. This means that CCB may fail before reaching the deformation limits set by BS476.

As explained previously, the deformation rate limit is more conservative and also the current BS 1363-1 [90] states that after the first 10 minutes of test is applicable. Therefore, the deformation rate limit is used to compare the behaviour of the beams under different load ratios.

The limiting temperature of all beams with load ratios equal or less than 30% is about 750°C. By increasing the load ratio to 85%, the limiting temperature reduces to 500°C. The parametric study shows that there is a sudden reduction in limiting temperature with load ratio of about 40%. However, the reduction in the limiting temperature for the maximum displacement limits are consistent and there no such jumps exist.

7.5.2 Hydrocarbon fire load

The numerical results show that beams 1, 2 and 3 lose their load bearing capacity at 23, 22, and 21 minutes, respectively under hydrocarbon fire load. Figure 7.5-1 shows the temperature of the beams at these critical times.

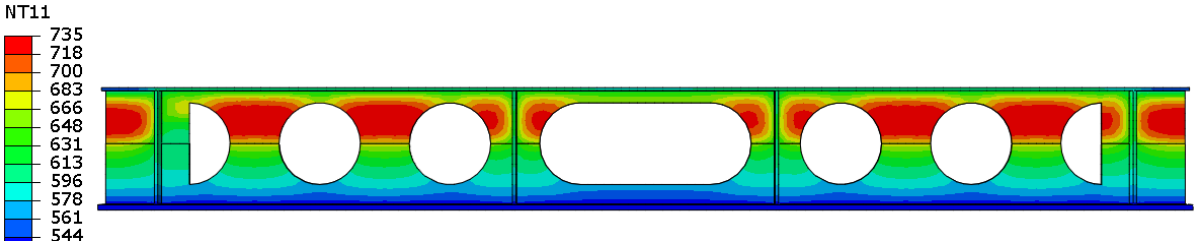

a) Beam1, time: 21 min

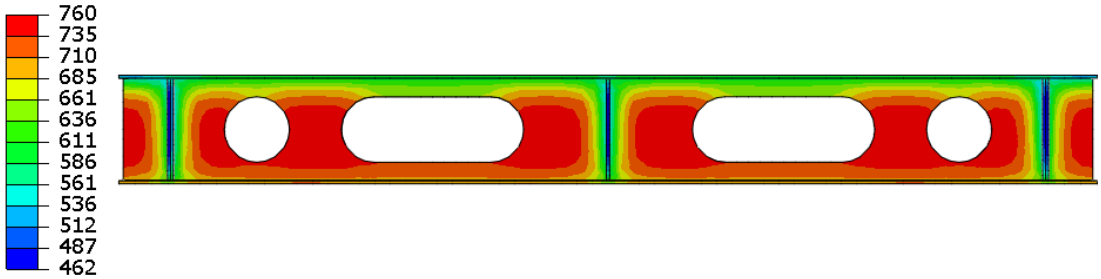

b) Beam 2, time: 22 min

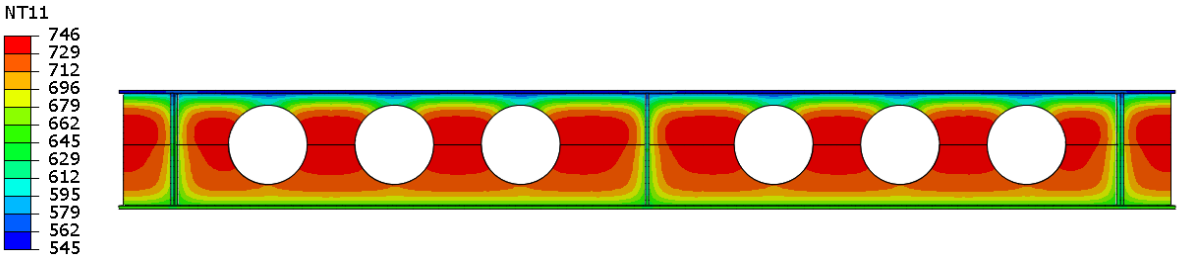

c) Beam 3, time 21 min

Figure 7.5-1 temperature of beam at the time the rate of deformation is increases, °C

Another indicator that shows the beam failure is the deformation of the beams. It is assumed that the maximum deflection of the beam is about span/40 [89]. Beams 1, 2 and 3 reach their maximum span/40 deformation at 32, 27 and 28 minutes. Figure 7.5-2 shows the temperature of the beams at these times.

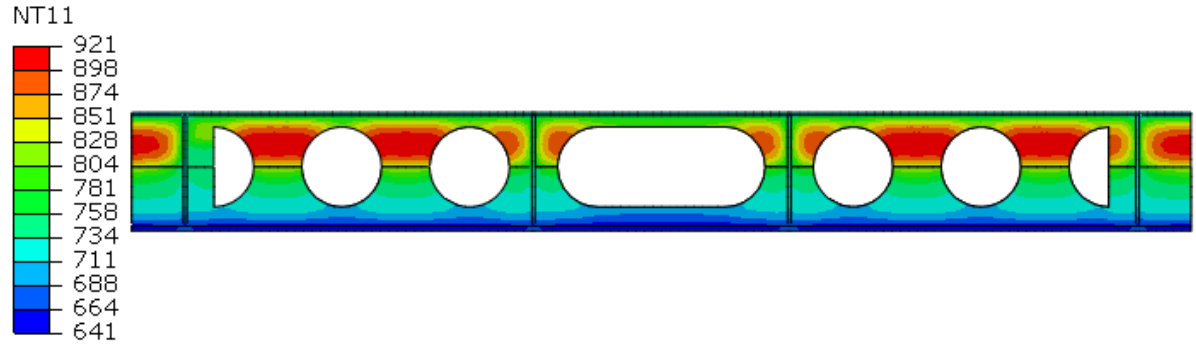

a) Beam1, time: 32 min

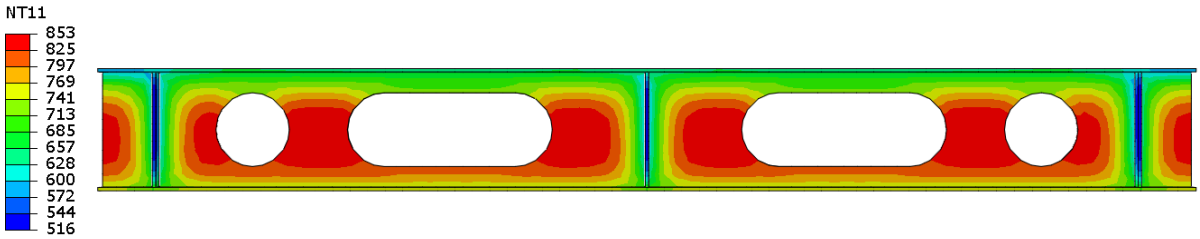

b) Beam 2, time: 27 min

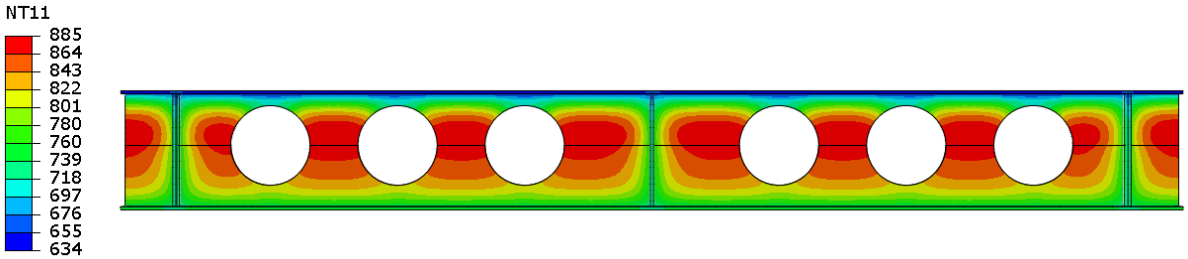

c) Beam 3, time 28 min

Figure 7.5-2 temperature of beam at when the beam deformations reaches span/40, °C

The compressive stress of node α (Figure 7.5-1) is extracted from the results. Figure 7.5-4 shows the compression stress of node α at this time.

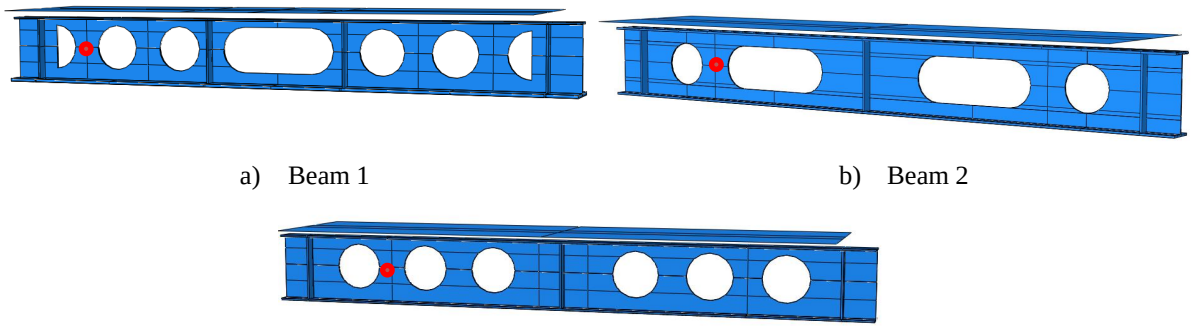

a) Beam 1 b) Beam 2

c) Beam 3

Figure 7.5-3 Location of node α (red dot)

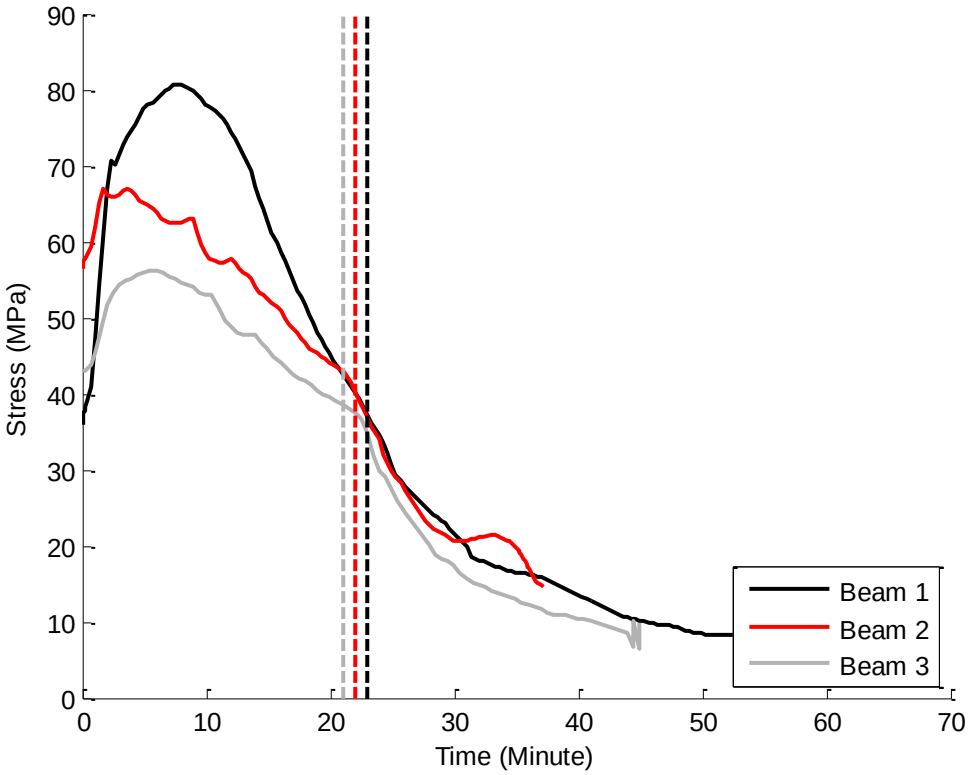

Figure 7.5-4 Compressive stress of node α

As shown in Figure 7.5-4, the stress at node α increases in the first 10 minutes at which the overall temperature of the beams is less than 400°C (see Figure 7.4-1, Figure 7.4-3, and Figure 7.4-5). By increasing the temperature of steel from room temperature to 400°C, the stiffness of the beams is decreased but the strength of the steel remains constant as shown in Figure 6.3-11 per BS EN 1994-12[15].

The reduction of the stiffness of the beams leads to higher deflections on the beams. The deflected geometry of the beams introduces extra bending on the beams, which leads to more deformation. The rate of deformation is faster than the rate of stiffness reduction. When the beam reaches 400°C, the strength of the beams begins to reduce and it leads to the formation of the plastic areas. This means that the force distribution pattern is changed in the beams and that the compression stresses reduce by increasing the temperature. As shown in Figure 7.5-4 when the stress of the node α reaches 40 MPa, the temperature of the beams reaches the critical temperature (see Figure 7.4-7, Figure 7.4-9 and Figure 7.4-11).

7.6 INTERIM SUMMARY

Three perforated composite beams were studied experimentally and numerically in Chapter 5. The beams were coated with intumescent coating and are located in a fire test chamber at the Ulster University. The beams were first loaded to 30% of their load bearing capacity at room temperature. In Chapter 5, numerical models were developed based on these experiments. The validity of the models was established by showing that experimental and numerical results were in close agreement. The validated models were used for further numerical study of the perforated beams. Chapter 7 was comprised of two parts, the first part investigated the effect of load ratios on the performance of CCBs and the second part studied the general behaviour of the beams under hydrocarbon fire load.

This Chapter studied the effect of load ratios on the general performance of composite perforated beams via application of 10% to 85% of the ultimate load at cold conditions with the beams exposed to the standard fire curve. Due to limitations of the numerical methods, the exact failure point of the beams was not clear. Therefore, the failure criteria of BS 476 were adopted as failure indications. The numerical output was screened against the criteria. The rate of deformation was the most onerous criteria. Therefore, it was selected to compare the effect of different load ratios on the performance of the beams. The numerical results showed that the maximum bottom temperatures for load ratios below 30% was about 750°C and it reduced to 450°C by increasing the load ratio to 85%.

The second part of this chapter studied the thermal and structural response of the composite cellular beams in the event of hydrocarbon fire. The study began with a brief review of all oil and gas standards and concluding that there was no limiting temperature table available for hydrocarbon fire besides, no additional information is available for perforated beams. The weighted hydrocarbon fire curve temperature was assigned to the ambient temperature of the beams in order to capture the shadow effect (discussed in Section 6.3.1 of Chapter 6). The numerical results show that the beams lose their functionality after about 20 minutes of the experiments. The maximum web-post temperate at the critical time varies between 732°C to 746°C which was slightly higher than the web-post temperature (730°C) for standard fire curve. The compression at the middle of the failed web post at the critical time was about 40MPa which was the same as the standard fire curve.

CHAPTER 8 - CONCLUSION

Unprotected perforated beams in fire mainly fail due to failure of web-posts under design loads for room temperature. To delay this failure, beams are protected with various insulation materials such as intumescent coatings. Designers are required to specify the type and thickness of the coatings that are sufficient to maintain the stability of the structure for specific time periods. Currently, designers are able to determine these parameters for solid beams based on limiting temperatures of the beams provided in standards. However, no such standards exist for coated perforated beams in buildings or extreme fire, as their behaviours in such conditions is not fully understood. The key focus of this research is therefore to fully analyse the thermal and structural behaviour of perforated beams protected with intumescent coatings in building and extreme fires. Both numerical modelling and experiments are utilised for this purpose.

The numerical modelling of beams at room temperature eliminates fire condition parameters such as thermal degradation; making it less complex and more accurate to validate and establish analysis types and modelling methods. Consequently, in Chapter 4 composite perforated beams at room temperature were studied. A composite perforated beam was loaded gradually until it fails due to web-post buckling. Two different types of analysis (the Riks method and the general static with artificial damping factor) were used for the simulation of the beam. It was shown that the former predicts the failure load and displacement of the beam very accurately. However, the beam displacement before failure was predicted to be less that of experimental results by a maximum of 11%. Additionally, it was illustrated that the general static analysis predicts the beam displacement with a higher accuracy (less than 5% difference between experimental and numerical outcomes).

However, due to the introduction of an artificial damping the numerical model remains stable for a short period of the time after the time at which the beam fail in the experiment. The comparison of the two methods implies that that general static analysis is more accurate than the Riks method in modelling the local failure of beams. This method was therefore used in the modelling of the beams in subsequent chapters.

The temperature profile of a perforated beam is different to that of non-perforated but otherwise identical beams. In fact, opening in beams lead to higher web temperatures and higher temperatures around the openings is one of the main parameters for their earlier failure. Consequently, perforated beams require more insulation than solid beams in order to obtain the same performance at the same temperature. Chapter 5 presents a comparison of the thermal behaviour of unloaded perforated and solid beams with different intumescent coating thicknesses in fire. Four asymmetric unloaded short beams (two with solid webs and two with cellular webs) were tested in a furnace. Out of the two solid or perforated beams, one was covered with a 0.8 mm thick coating and the other with a 2.1 mm thick coating. All four beams were modelled numerically. Additionally, the solid and perforated beams were modelled without any coating. The numerical model consists of a heat transfer analysis in which the surface of the coatings (or the steel in case of the unprotected beams) was exposed to furnace temperatures. The thermal conductivity of intumescent coatings was calculated from recorded experimental temperatures in accordance with BS EN 13381-8:2013 [33]. It was shown that the numerical results were in good agreement with experiment outcomes. This investigation demonstrates that:

- The beams with no protection experienced higher temperatures. Additionally, due to the high conductivity of steel and the short length of the beams, the temperature distribution within the beams was almost uniform. Thus, there was no meaningful

difference between the temperature profile of the unprotected perforated and solid beams.

The temperatures between openings in the perforated webs were higher than those of the solid webs. The temperature difference between the solid and perforated beams with a 0.8 mm thick coating at the centre of their webs were considerably higher than that of the beams with a 2.1 mm thick coating. This temperature difference was about 19%. However, this difference reduced to 8% for the beams with a 2.1 mm thick coating.

- The increase in the thickness of the solid beam coatings did not have a significant effect on the web temperature of the beams. The web temperature difference between the 2.1 mm and 0.8 mm coating for the solid beam was approximately 1.5%.
- The heat transfer modelling strategy developed here was valid and can be used in subsequent chapters.

Bailey [30] suggests that the higher web-post temperatures is due to the "pull-back" effect which leads to the direct exposure of the opening edges to furnace heat. Therefore, Chapter 5 presents a numerical test case, which examined the credibility of this suggestion. In this test case, the furnace thermal boundary condition of the 2.1 mm protected cellular and solid beams was removed and the coating at the bottom surface of the beam was exposed to a 20 kW/m^2 heat flux. The results showed that the web-post temperature was higher than the solid web temperature. The higher web-post temperature occurred due to the heat conduction from the bottom flange, which had a higher temperature due to receiving more radiation from the furnace burners at the bottom of the beams. By introducing openings to the web, the cross-section area of the web decreased and consequently the web-post temperature increased. However, the temperature difference due to heat conduction between the web-post and the solid web is mitigated in the real fire test due to the direct

exposure of the web to heat. This illustrates that the higher temperature at the web-post is not mainly because of the "pull-back" effect or exposure of the furnace heat to the edge of openings.

The numerical strategies developed in Chapters 4 and 5 were implemented in Chapter 6 to simulate loaded protected composite cellular beams with various geometries at elevated temperatures. The beams were exposed to a standard fire in a furnace and were loaded to 30% of their capacity at room temperature. It was demonstrated that the numerical results were in close agreement with experimental outcomes. The analysis shows that:

- The maximum web-post temperature was around 730°C at failure.
- The maximum compressive stress between the two openings at the section where failure occurs was 40 MPa.
- Increasing the beam temperature changed stress distribution patterns due to formation of plastic areas and changes in the geometry of the beams.
- The methodology developed here is valid and independent from furnace test conditions. Consequently, it provides a suitable tool for the study of the behaviour of coated composite perforated beams in condition, which are different from the conditions of the experiment described in Chapter 5.

BS 5950-8 [5] provides a limiting temperature table for steel structural members for different load ratios. However, this table is only valid for solid beams and there is no such limiting temperature table available for the design of coated perforated composite beams. Consequently, Chapter 7 presents a numerical parametric investigation of the effect of different load ratios on the performance of perforated beams in fire. Load ratios from 10% to 85% of the ultimate load (in 10 kN increments) were applied to the three beams studied in Chapter 6. The results showed that the limiting temperature of all beams with load

ratios equal or less than 30% was around 750°C. By increasing the load ratio to 85%, the limiting temperature reduced to 450°C.

Currently, no regulations or publications exist on the design of perforated beams exposed to hydrocarbon fires. Hydrocarbon fires reach steady temperature faster than standard (cellulose fire) and their steady temperature is higher than that of cellulose fire. This causes the behaviour of perforated beams under hydrocarbon fire loads to differ from their behaviour in standard fire. Consequently, a parametric study of the performance of coated composite perforated beams exposed to hydrocarbon fire is presented in Chapter 7. The thermal boundary conditions of the perforated beams were changed from standard fire curve to hydrocarbon fire. The results showed that:

- The web-post reached its maximum (failure) temperature of around 740°C after 20 minutes.
- The beam failed 50 minutes earlier than standard fire and the limiting temperature was around 10°C higher than that of standard fire. The reason for this failure is suggested for future investigation.
- Currently, in the offshore industry limiting temperatures is set to a single value of 400°C for all steel members. However, the findings in this research showed that the limiting temperature of perforated beams was considerably higher for hydrocarbon fire. This means that the size of the steel section and the thickness of the protection for hydrocarbon fire can be reduced due to increases in the limiting temperature. This can reduce the weight of offshore structures, which is a crucial parameter. It also reduces steel and insulation cost, and CO_2 emission.

8.1 LIMITATION AND FUTURE WORKS

Several commercial products of intumescent are available in the market. In this research, one commercial intumescent coating was used for the fire coating of the beams as it is not practical to examine and study all available products in the market. The difference in thermal properties of intumescent coating leads to different rates of temperature increase of the protected beams. However, as it is evident from the finding of this research the rate of temperature increase, which is the function of the thermal properties of the coatings, has a secondary effect on the performance composite of perforated beams in fire as well as their limiting temperature and could therefore be neglected.

Further investigation which could be carried out to improve the finding of this research as follows.

- It is currently more common to use longer spans to save interior spaces. The behaviour of long perforated span in fire might be slightly different due to shear deformation and different expansion magnitude of concrete and steel material. It is recommended to carry out further experimental and numerical studies on the performance of large span composite beams.
- This research concentrated on simply supported composite beams in which the concrete part slab is under compression. However, in beams with moment connections, the concrete part close to the connection is under tension. This could lead to a different performance of the beams, particularly in fire. It is recommended that the effect of the different boundary conditions on the overall performance of composite cellular beams in fire is studied.
- It is also recommended that an experimental study is conducted on the performance of perforated beams in hydrocarbon fire to provide more understating on the overall performance of perforated beams in hydrocarbon fire. Additionally, in

offshore platforms aluminium perforated beams are commonly used to reduce the weight of the platform. However, there is no guidance or code available for design of perforated aluminium beams in fire. It is recommended that experimental and numerical investigations are conducted on performance of perforated aluminium beams in hydrocarbon fire.

REFERENCES

1. Government, G.B.D.f.C.L., *The Building Regulations 2010 : approved document B. Vol. 1, Vol. 1*. 2013, NBS: [Newcastle upon Tyne].
2. BSI, *BS EN 1992-1-2: 2004 Eurocode 2: Design of concrete structures*, in *Part 1-2: General rules — Structural fire design*. 2008. p. 1992-2.
3. Horacek, H. and R. Grabner, *Advantages of flame retardants based on nitrogen compounds.* Polymer Degradation and Stability, 1996. **54**(2): p. 205-215.
4. Jimenez, M., S. Duquesne, and S. Bourbigot, *Kinetic analysis of the thermal degradation of an epoxy-based intumescent coating.* Polymer Degradation and Stability, 2009. **94**(3): p. 404-409.
5. BSI, *BS 5950-8: 2003 Structural use of steelwork in building*, in *Part 8: Code of practice for fire resistant design*. 2003.
6. Duthinh, D., *Structural Design for Fire: A Survey of Building Codes and Standards*. 2014, NIST.
7. Beck, V., *Performance-based fire engineering design and its application in Australia.* Fire Safety Science, 1997. **5**: p. 23-40.
8. Bailey, C., *One Stop Shop in Structural Fire Engineering*. University of Manchester.
9. Wang, Y., et al., *Performance-based fire engineering of structures*. 2012: CRC Press.
10. Incropera, F.P., et al., *Fundamentals of heat and mass transfer*. 2011: Wiley.
11. Holman, J., *Heat transfer, 1997.* and. **360**(362): p. 333-352.
12. Lienhard, J.H. and R. Eichhorn, *A heat transfer textbook.* 1987: Prentice-Hall.
13. Milke, J.A., *Analytical methods for determining fire resistance of steel members*, in *SFPE handbook of fire protection engineering*. 1995, Springer. p. 1909-1948.
14. Pettersson, O., S.E. Magnusson, and J. Thor, *Fire engineering design of steel structures*. 1976: Stålbyggnadsinstitutet.
15. BSI, *BS EN 1994-1-2:2005 Eurocode 4–Design of composite steel and concrete structures*, in *Part 1-2: General rules–Structural fire design*. 2014.
16. Mills, A.F., *Basic heat and mass transfer*. 1999: Pearson College Div.
17. *Gateway to UK fire protection*. 2009 Feb 2017]; Available from: http://pfpf.org/pfpf_objectives.htm
18. Raveglia, E. and M. Fontana, *FIRE RESISTANCE OF STRUCTURAL MEMBER PROTECTED BY INTUMESCENT SURFACE SYSTEM*, in *6th International PhD Symposium in Civil Engineering*. 2006: Zurich.
19. Griffin, G., *The modeling of heat transfer across intumescent polymer coatings.* Journal of fire sciences, 2010. **28**(3): p. 249-277.
20. ArcelorMittal, *ArcelorMittal_ACB Cellular Beams*, ArcelorMittal, Editor. 2017.
21. Hajirasouliha, I. and K. Pilakoutas, *General seismic load distribution for optimum performance-based design of shear-buildings.* Journal of Earthquake Engineering, 2012. **16**(4): p. 443-462.
22. Arnold, C., *EARTHQUAKE EFFECTS ON BUILDINGS 4.* Designing for Earthquakes: A Manual for Architects. Fema 454/December 2006.(Risk Management Series), 2006.

23. Lawson, R. and S. Hicks, *Design of composite beams with large web openings.* The Steel Construction Institute, Publication No. SCI P355, 2011.
24. *SteelConstruction.info*. 2017 [cited 2017 Feb 2017]; Available from: http://www.steelconstruction.info/.
25. Sherbourne, A. and J. Van Oostrom, *Plastic analysis of castellated beams—I interaction of moment, shear and axial force.* Computers & Structures, 1972. **2**(1-2): p. 79-109.
26. SIMMS, I., *Fire protection of beams with web openings.* New steel construction, 2007. **15**(1).
27. Allen, B., *PROTECTING STRUCTURAL CELLULAR BEAMS FROM FIRE.* FIRE SAFETY ENGINEERING, 2004. **11**(3): p. 20-22.
28. Association of Specialist Fire Protection, *Fire protection for structural steel in buildings*. 2004, Aldershot: Association of Specialist Fire Protection Contractors and Manufacturers in conjunction with Fire Test Study Group and Steel Construction Institute.
29. Liu, T.C. and K. Liew. *Behaviour of cellular steel beams in fire*. in *Proceedings of the tenth international conference Interflam*. 2004.
30. Bailey, C., *Indicative fire tests to investigate the behaviour of cellular beams protected with intumescent coatings.* Fire Safety Journal, 2004. **39**(8): p. 689-709.
31. Wong, V.B., I.W. Burgess, and R.J. Plank. *Experimental and analytical investigations of the behaviour of protected composite floor beams with web openings in fire*. in *Proc. Structures in Fire Conference, East Lansing, Michigan*. 2010.
32. Dai, X., Y. Wang, and C. Bailey, *A Simple Method to Predict Temperatures in Steel Joints with Partial Intumescent Coating Fire Protection.* Fire Technology, 2009. **46**(1): p. 19-35.
33. BSI, *BS EN 13381-8, Test Methods for Determining the Contribution to the Fire Resistance of Structural Members*, in *Part 8: Applied reactive protection to steel members*. 2010, BSI: London.
34. BSI, *EN 1993-1-1: Eurocode 3: Design of Steel Structures.* , in *Part 1-1: General Rules and Rules for Buildings*. 2005, Comité Europeo de Normalización.
35. Krishnamoorthy, R.R., *The Analysis Of Partial And Damaged Fire Protection On Structural Steel At Elevated Temperature*. 2011.
36. Li, G.-Q., et al., *Assess the fire resistance of intumescent coatings by equivalent constant thermal resistance.* Fire technology, 2012. **48**(2): p. 529-546.
37. Nadjai, A., et al., *Performance of cellular composite floor beams at elevated temperatures.* Fire safety journal, 2007. **42**(6): p. 489-497.
38. Vassart, O., et al., *Fire resistance of long span cellular beam made of hot rolled profiles (FICEB).* RFCS Publishable Report, 2011.
39. Nadjai, A., et al., *Analysis of composite floor cellular steel beams in fire.* Journal of Structural Fire Engineering, 2010. **1**(3): p. 161-175.
40. Bake Mohamadi, S., *Behaviour of cellular beams and cellular composite floors at ambient and elevated temperatures.* 2010.
41. Naili, E., et al. *Experimental and Numerical Modelling of Cellular Beams with Elongations Openings at Elevated Temperature*. in *Structures in Fire: Proceeding of the 6th International Conference*. 2010. DES tech Publications, Inc.
42. Nadjai, A., et al., *Performance of unprotected and protected cellular beams in fire conditions.* Construction and Building Materials, 2016. **105**: p. 579-588.

43. Gilat, A., *Numerical Methods for Engineers and Scientists: An Introduction with Applications Using Matlab 1st Edition with Matlab 3rd Edition Set*. 2008: John Wiley & Sons Canada, Limited.
44. Çengel, Y.A., *Heat Transfer: A Practical Approach*. 2003: McGraw-Hill Companies.
45. Rathore, M.M. and R.R.A. Kapuno, *Engineering Heat Transfer*. 2011: Jones & Bartlett Learning.
46. Systèmes, D., *WHITE PAPER Understanding Nonlinear Analysis*. 2010: Dassault Systèmes.
47. Hibbit, K., *ABAQUS Theory and User Manuals Version 6.9*. USA: ABAQUS Inc. 2009.
48. Hibbitt, H., B. Karlsson, and P. Sorensen, *Abaqus v6. 12 documentation—ABAQUS analysis user's manual.* Providence (RI): Dassault Systèmes Simulia, 2012.
49. Kobayashi, T., Y. Mihara, and F. Fujii, *Path-tracing analysis for post-buckling process of elastic cylindrical shells under axial compression.* Thin-Walled Structures, 2012. **61**: p. 180-187.
50. Zhao, M. *On Nonlinear Buckling and Collapse Analysis using Riks Method*. in *Proceedings of Abaqus users conference*. 2008.
51. Nadjai, A., *TEST REPORT FOR WESTOK Ltd- Behaviour of Composite Floor Cellular Steel Beams at Elevated Temperatures*. 2007: Belfast.
52. Lawson, R., et al., *Design of composite asymmetric cellular beams and beams with large web openings.* Journal of Constructional Steel Research, 2006. **62**(6): p. 614-629.
53. DnV, R., *C203.* Fatigue design of offshore steel structures, 2010.
54. Kwon, G.U., *Strengthening existing steel bridge girders by the use of post-installed shear connectors*. 2008: ProQuest.
55. EN, B., *206-1: 2000: Concrete. Specification, performance, production and conformity.* British Standards Institution, London, 2000.
56. *Fire design of composite beams with rectangular and circular web opening*, in *RT1356*. July 2013, SCI: Berkahire, UK. p. 202.
57. Tsavdaridis, K.D. and C. D'Mello, *Web buckling study of the behaviour and strength of perforated steel beams with different novel web opening shapes.* Journal of Constructional Steel Research, 2011. **67**(10): p. 1605-1620.
58. Dai, X., Y. Wang, and C. Bailey, *Numerical modelling of structural fire behaviour of restrained steel beam–column assemblies using typical joint types.* Engineering Structures, 2010. **32**(8): p. 2337-2351.
59. Chen, L. and Y. Wang, *Efficient modelling of large deflection behaviour of restrained steel structures with realistic endplate beam/column connections in fire.* Engineering Structures, 2012. **43**: p. 194-209.
60. Vassart, O., et al. *Parametrical study on the behaviour of steel and composite cellular beams under fire conditions*. DEStech Publications, Inc.
61. BSI, *BS 476-20: Fire tests on building materials and structures*, in *Method for determination of the fire resistance of elements of construction (general principles)*. 1987, London.
62. BSI, *BS 5950-8:2003 Structural use of steelwork in building*, in *Part 8: Code of practice for fire resistant design*. 2003.
63. EN, B., *13381-8:2013.* BSI Standards Publication Test Methods For Determining The Contribution To The Fire Resistance Of Structural Members Part 8: Applied reactive protection to steel members.

64. Yong, W. and O. Alaa. *A model for prediction of temperature in steel structure protected by intumescent coating, based on tests in the Cone Calorimeter*. in *8th symposium*. 2005. IAFSS.
65. Wang, Y., et al. *A model for prediction of temperature in steel structure protected by intumescent coating, based on tests in the Cone Calorimeter*. in *IAFSS 8th Symposium on Fire Safety Science*. 2005. IAFSS.
66. Drysdale, D., *An introduction to fire dynamics*. 2011: John Wiley & Sons.
67. Lawson, R. and G. Newman, *Fire Resistant Design of Steel Structures: A Handbook to BS 5950*. 1990: Steel Construction Institute.
68. Bartholmai, M., R. Schriever, and B. Schartel, *Influence of external heat flux and coating thickness on the thermal insulation properties of two different intumescent coatings using cone calorimeter and numerical analysis.* Fire and materials, 2003. **27**(4): p. 151-162.
69. Owens, G.W. and P.R. Knowles, *Steel designers manual*. 1992.
70. Vassart, E.-I.O., *Full-scale fire test on a composite floor slab incorporating long span cellular steel beams.* Structural Engineer, 2011. **89**(21): p. 21.
71. Nadjai, A., et al., *BEHAVIOUR OF UNPROTECTED AND PROTECTED CELLULAR BEAMS HAVING DIFFERENT OPENING SHAPES IN FIRE CONDITIONS.*
72. *Technical Handbook*, in *P364*, Kingspan, Editor. 2011, Kingspan.
73. ISO, *ISO 834-1:1999: Fire resistance tests- elements of building construction. Part 1: General requirements*. 1999.
74. Vassart, O., *Analytical model for cellular beams made of hot rolled sections in case of fire*. 2009, Université Blaise Pascal-Clermont-Ferrand II.
75. BSI-main, *BS EN 1992-1-2: 2004 Eurocode 2: Design of concrete structures*, in *Part 1-2: General rules — Structural fire design*. 1992. p. 1992-2.
76. Wang, P., et al., *Web-post buckling of fully and partially protected cellular steel beams at elevated temperatures in a fire.* Thin-Walled Structures, 2016. **98**: p. 29-38.
77. Cashell, K. *Structural applications of ferritic stainless steels*. in *The 4th International Experts Seminar on Stainless Steel in Structures*. 2012.
78. Mago, N. and S.J. Hicks, *Fire behaviour of slender, highly utilized, eccentrically loaded concrete filled tubular columns.* Journal of Constructional Steel Research, 2016. **119**: p. 123-132.
79. BSI, *EN 1992-1-1: 2004 Eurocode 2: Design of Concrete Structures*, in *Part 1-1: General rules and rules for buildings*. 2014.
80. Feldmann, M., et al., *Large web openings for service integration in composite floors.* Contract No: RFS-CT-2005-00037, 2006.
81. Hibbitt, K., *ABAQUS version 6. 7: theory manual, users' manual, verification man ual and example problems manual*. 2007, Hibbitt, Karlson and Sorenson Inc.
82. FABIG, *Design Guidance for Hydrocarbon Fires : (FABIG Technical Note 13)*. 2014, Steel Construction Institute (SCI): [Place of publication not identified].
83. ISO, *ISO 13702: Petroleum and natural gas industries*, in *Control and mitigation of fires and explosions on offshore production installations -- Requirements and guidelines*. 2015.
84. API, *RP I 2218: Fireproofing Practises In Petroleum and Petrochemical Processing Plants*. 2013.
85. UL, *UL 1709: Standard for Rapid Rise Fire Tests of Protection Materials for Structural Steel*. 2011.

86. HSE, *Fire and explosion structural integrity assessment*, in *Appendix 2 - Technical background note*. 2017.
87. DNV, *DNV-OS-D301, Fire Protection*. 2013.
88. BSI, *BS 476-10: Fire tests on building materials and structures.* Part 10: Guide to the principles, selection, role and application of fire testing and their outputs, 2009.
89. Establishment, B.B.R., *Integrity of Compartmentation in Buildings During a Fire*. 2004.
90. BSE, *BS EN 1363-1:2012- Fire resistance tests*, in *Part 1: General Requirements*. 2012.
91. Cengel, Y.A., S. Klein, and W. Beckman, *Heat transfer: a practical approach*. 1998: WBC McGraw-Hill Boston.
92. Sucec, J., *Heat transfer*. 1985: W.C. Brown.
93. Gebhart, B., *Surface temperature calculations in radiant surroundings of arbitrary complexity—for gray, diffuse radiation.* International Journal of Heat and Mass Transfer, 1961. **3**(4): p. 341-346.

APPENDIX A - VALIDATION OF ABAQUS HEAT TRANSFER FUNCTIONS

A.1 INTRODUCTION

This part of the research aims to study the heat transfer functions in ABAQUS and evaluate their accuracy. A benchmark model is defined to study the heat transfer functions in ABAQUS. The model is a square plate with a void which can be thought of as a simplified opening in a web of a perforated beam. A constant temperature is applied to the bottom surface of the model and the top surface is in contact with ambient room temperature. Second order nonlinear and nonhomogeneous differential equations are eliminated by assuming that heat is only transferred to the ambient by convection.

The benchmark problem is modelled and simulated in ABAQUS which uses FEM and by using a code written in MATLAB based on FDM. The FEM and FDM results are compared to evaluate the accuracy of the ABAQUS predictions and provide an understanding of the heat transfer parameters in a perforated beam.

A.2 BENCHMARCK MODEL

A well-known finite difference problem [44] is proposed to define the benchmark model presented here. The geometry of the model is modified in order to resemble an opening in a web (see **Error! Reference source not found.**).

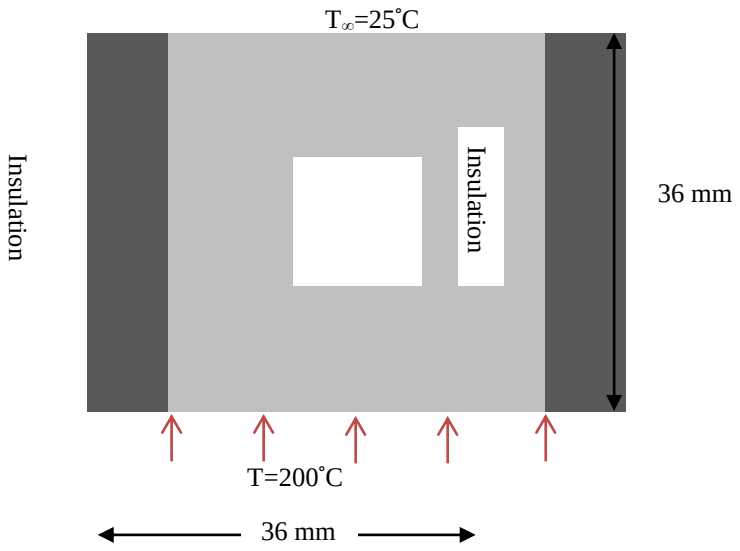

Figure A.2-1 Square benchmark model

The dimension of the plate is $36mm \times 36mm$ with a $12mm \acute{} 12mm$ square void at the centre. The top edge of the plate is exposed to room temperature (25°C). A 200°C constant temperature is applied to the bottom edge of the plate. **Error! Reference source not found.** shows the thermal properties of the solid plate and the enclosed air.

Table A.2-1 Thermal properties of the problem

Material	**Air**	**Solid plate**
Conductivity	-	$15 W/m.°C$
Convection Coefficient, inside the void	$1.5\ W/m^2$	-
Convection Coefficient, top edge	$80\ W/m^2$	-
Density	$1.205\ kg/m^3$	-
Specific heat	$1.005\ kJ/kg.K$	-
Thermal diffusivity	-	$3.2 \times 10^6\ m^2/s$

A.1 HEAT TRANSFER ANALYSIS

In this section, the coupled effect of radiation and convection inside the benchmark's void is numerically studied. FDM and FEM are used for the numerical investigations and the results are compared. To estimate the amount of heat exchanged between enclosed air and the solid section by convection, the gas temperature is assumed to be uniform and the convection coefficient is kept constant.

A.1.1 Finite Difference Method

In the benchmark model, heat is transferred by conduction within the solid part of the plate, radiation within the void, and convection through its top edge. The square plate is divided into nine equal squares (see **Error! Reference source not found.**). The plate consists of 16 nodes and is fully insulated on the left and right sides. Since the model is symmetric about a centreline, the temperature variation within the plate is symmetrically distributed with respect to the vertical centreline. Hence, the temperatures of the nodes appearing on the left side of the plane of symmetry are estimated, and the temperatures of the nodes on the right are set equal to those of their corresponding nodes on left hand side of the plane. This is carried out to simplify the coding of the problem and avoid errors.

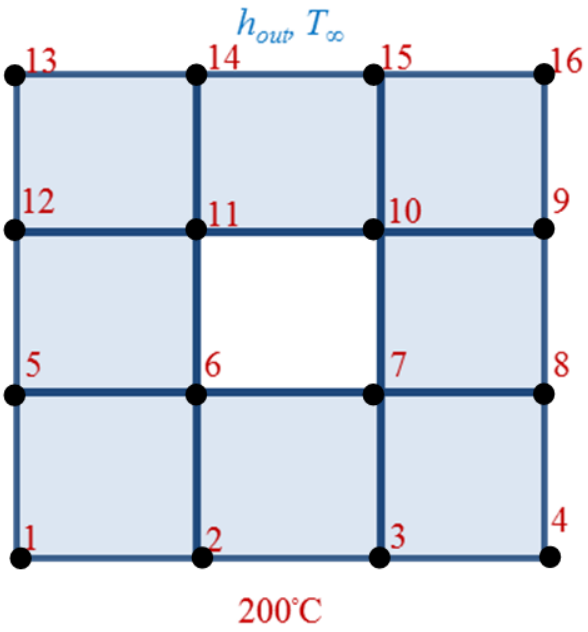

Figure A.1-1 Discretisation of the square plate to nine identical squares

Heat transfer within the solid part

The explicit finite difference equations are determined on the basis of the energy balance equation for the transient case, expressed as

$$\sum_{All.sides} \dot{Q}^{i} = \rho VC \frac{\Delta T}{\Delta t} \qquad \text{A.1-1}$$

where $\dot{Q}$ is rate of heat transfer. The heat transfer mechanisms (and thus transfer rate) for interior nodes consist of conduction, for the nodes beside the void, conduction and radiation, and for the top edge, conduction and convection are the methods of heat transfer. The RHS of Eq. **Error! Reference source not found.** represents the changes in the energy contents of the control volume of a node during a given time interval (see **Error! Reference source not found.**).

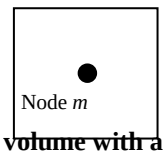

Figure A.1-2 A control volume with a node in the centre

To further simplify the codes, the energy balance expression is simplified by using the definition of thermal diffusivity $\alpha = k/\rho C$ and a dimensionless mesh Fourier number, $\tau = \alpha \Delta t / l^2$, where the control volume length $l = \Delta x = \Delta y$.

The steps carried out in the development of the FDM equations for each node, to predict the benchmark model temperatures, as are follows:

(a) At the boundaries, nodes 1 and 2 are subjected to a 200°C constant temperature as shown in **Error! Reference source not found.**. Therefore, $T_1^i = T_2^i = 200^o\mathrm{C}$.

(b) Node 5 is on the insulated boundary and can be treated as an interior node. (see **Error! Reference source not found.**). Note that $T_1^i = 200^o\mathrm{C}$. The temperature at the interior node can be calculated using [91]

$$T_{node}^{i+1} = (1-4\tau)T_{node}^i + \tau(T_{left}^i + T_{right}^i + T_{top}^i + T_{bottom}^i) \qquad \textbf{A.1-2}$$

Hence the temperature at Node 5 is:

$$T_5^{i+1} = (1-4\tau)T_5^i + \tau(T_{12}^i + 2T_6^i + 200) \qquad \textbf{A.1-3}$$

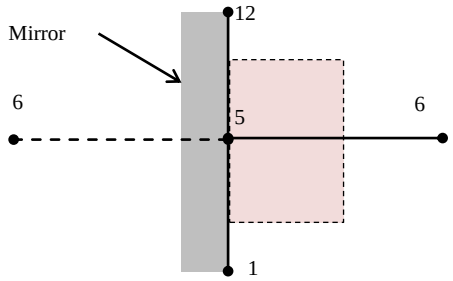

Figure A.1-3 Schematic for energy balance - control volume of node 5

(c) Node 6 is a boundary node subjected to radiation on two surfaces (see **Error! Reference source not found.**).

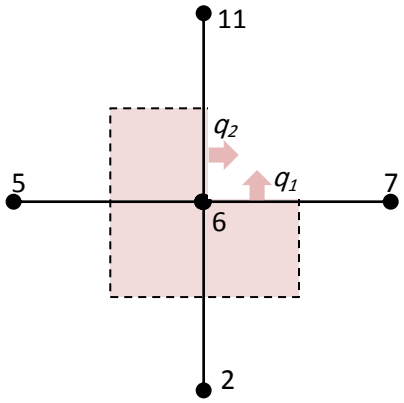

Figure A.1-4 Schematic for energy balance - control volume of node 6

Note that q_1 and q_2 are the net energy leaving the void surfaces by radiation. The energy balance equation of Node 6 is given by

$$h_{in}(\frac{\Delta x}{2}+\frac{\Delta y}{2})(T_g^i-T_6^i)+q_1\frac{\Delta x}{2}+k\frac{\Delta y}{2}\frac{(T_7^i-T_6^i)}{\Delta x}+k\Delta x\frac{(T_2^i-T_6^i)}{\Delta y}+k\Delta y\frac{(T_5^i-T_6^i)}{\Delta x}$$
$$+q_2\frac{\Delta y}{2}+k\frac{\Delta x}{2}\frac{(T_{11}^i-T_6^i)}{\Delta y}=\rho\frac{3\Delta x\Delta y}{4}C\frac{T_6^{i+1}-T_6^i}{\Delta t} \quad \text{A.1-4}$$

Dividing the two sides of Eq. **Error! Reference source not found.** by 3k/4, simplifying and solving for T_6^{i+1} gives

$$T_6^{i+1}=(1-4\tau-\frac{4}{3}\tau-\frac{h_{in}l}{k})T_6^i+\tau/3(4T_2^i+4T_5^i+2T_7^i+2T_{11}^i+2\frac{q_1}{k}l+2\frac{q_2}{k}l+$$
$$4\frac{h_{in}l}{k}T_g) \quad \text{A.1-5}$$

where, T_g is the gas temperature.

(d) Node 12 is identical to Node 5. The finite difference formulation of this node can be obtained in a similar manner to that of Node 5 (see **Error! Reference source not found.**).

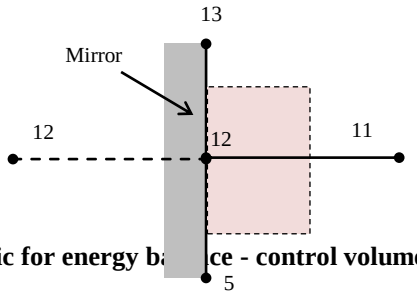

Figure A.1-5 Schematic for energy ba ce - control volume of node 12

The energy balance equation for Node 12 can be expressed as

$$T_{12}^{i+1} = (1-4\tau)T_{12}^{i} + \tau(T_{13}^{i} + 2T_{11}^{i} + T_{5}^{i}) \qquad \textbf{A.1-6}$$

(e) Node 11 is identical to Node 6, and the finite difference formulation of this node can be obtained in a similar manner to that of Node 6 (see **Error! Reference source not found.**). This gives

$$T_{6}^{i+1} = (1-4\tau-\frac{4}{3}\tau-\frac{h_{in}l}{k})T_{11}^{i} + \tau/3(4T_{14}^{i} + 4T_{12}^{i} + 2T_{6}^{i} + 2T_{10}^{i} + 2\frac{q_1}{k}l + 2\frac{q_2}{k}l + 4\frac{h_{in}l}{k}T_{g}) \qquad \textbf{A.1-7}$$

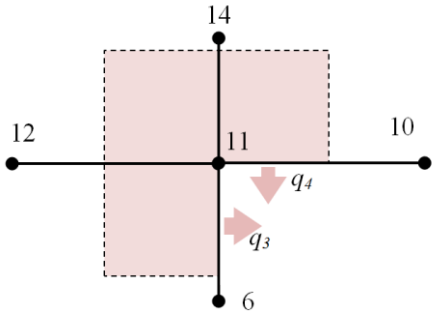

Figure A.1-6 Schematic for energy balance - control volume of node 11

(f) Node 13 is a boundary node subjected to convection and insulation (see **Error! Reference source not found.**)

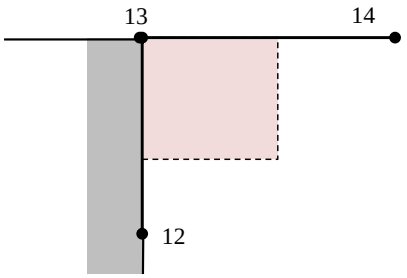

Figure A.1-7 Schematic for energy balance - control volume of node 13

The finite difference energy balance equation for node 12 is given by

$$h(\frac{\Delta x}{2})(T_{\infty}^{i} - T_{13}^{i}) + k\frac{\Delta y}{2}\frac{(T_{14}^{i} - T_{13}^{i})}{\Delta x} + k\Delta x\frac{(T_{12}^{i} - T_{13}^{i})}{\Delta y} = \rho\frac{\Delta x \Delta y}{4}C\frac{T_{13}^{i+1} - T_{13}^{i}}{\Delta t} \qquad \textbf{A.1-8}$$

Dividing Eq. **Error! Reference source not found.** by *k/4*, simplifying and solving for T_{13}^{i+1} gives

$$T_{13}^{i+1} = (1-4\tau-2\tau\frac{hl}{k})T_1^i + 2\tau(T_{14}^i + T_{12}^i + \frac{hl}{k}T_\infty) \quad \text{A.1-9}$$

(g) Node 14 is a boundary node subjected to convection as shown in **Error! Reference source not found.**.

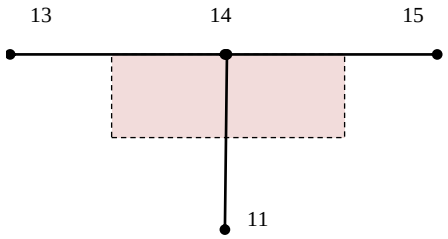

Figure A.1-8 Schematic for energy balance - control volume of node 14

The energy balance equation for node 14 can be expressed as

$$h_{out}\Delta x(T_\infty^i - T_{14}^i) + k\frac{\Delta y}{2}\frac{(T_{15}^i - T_{14}^i)}{\Delta x} + k\Delta x\frac{(T_{11}^i - T_{14}^i)}{\Delta y} + k\frac{\Delta y}{2}\frac{(T_{13}^i - T_{14}^i)}{\Delta x} = \rho\Delta x\frac{\Delta y}{2}C\frac{T_{14}^{i+1} - T_{14}^i}{\Delta t} \quad \text{A.1-10}$$

Dividing equations Eq. **Error! Reference source not found.** by *k/2*, simplifying, and solving for T_{14}^{i+1} gives

$$T_{14}^{i+1} = (1-4\tau-2\tau\frac{h_{out}l}{k})T_{14}^i + \tau(T_{13}^i + T_{15}^i + 2T_{11}^i + 2\frac{h_{out}l}{k}T_\infty) \quad \text{A.1-11}$$

(h) Enclosed air temperature is represented by a single control volume as shown in **Error! Reference source not found.**.

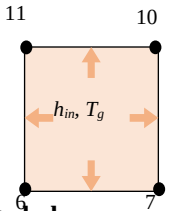

Figure A.1-9 Schematic for energy balance on control volume of enclosed air

The energy balance equation for the enclosed air temperature is given by

$$h_{in}(\frac{\Delta x}{2}+\frac{\Delta y}{2})[(T_{11}^{i}-T_{g}^{i})+(T_{6}^{i}-T_{g}^{i})+(T_{10}^{i}-T_{g}^{i})+(T_{7}^{i}-T_{g}^{i})]$$
$$=\rho_{air}(\Delta x\Delta y)c_{air}\frac{T_{g}^{i+1}-T_{g}^{i}}{\Delta t},$$
$$\beta=\frac{2h_{in}\Delta t}{\rho lc},$$
$$T_{g}^{i+1}=\beta(T_{6}^{i}+T_{11}^{i})+(1-2\beta)T_{g}^{i}$$

A.1-12

The above complete the finite difference formulation of the problem. The next step is defining the upper limit of the time step Δt from the stability criterion, which requires the coefficients of T_g^i and the solid node temperatures T_m^i , to be greater than or equal to zero. For $\Delta t = 1$ all T_g^i and T_m^i values are greater than zero. Finite difference equations of the model are coded using MATLAB and a solution is obtained for a total time of 600s.

Heat transfer within the void

The net heat exchange in an enclosure is a function of geometry and surface temperature of the void. Several methods are available to predict the net radiant heat loss from each surface of an enclosure. An example is the electronic network method. However, such methods are impractical for the cases whereby the enclosure surfaces have more than four faces [91, 92].

In this study the absorption factor method is used to predict the radiative heat loss from each surface. As it is shown in **Error! Reference source not found. Error! Reference source not found.** the net radiation leaving surface *i* is

$$\begin{pmatrix}\text{Net radiation}\\ \text{leaving the surface } i\\ q_i\end{pmatrix}=\begin{pmatrix}\text{Rate at which the Surface } i\\ \text{emits radiative energy}\\ (w_i A_i)\end{pmatrix}-\begin{pmatrix}\text{Rate at which Surface } i\\ \text{absorbs radiant energy}\\ \text{from other surface}\end{pmatrix}$$

The incident radiations to surface 1 includes a combination of emitted heat by other surfaces and the reflected radiations.

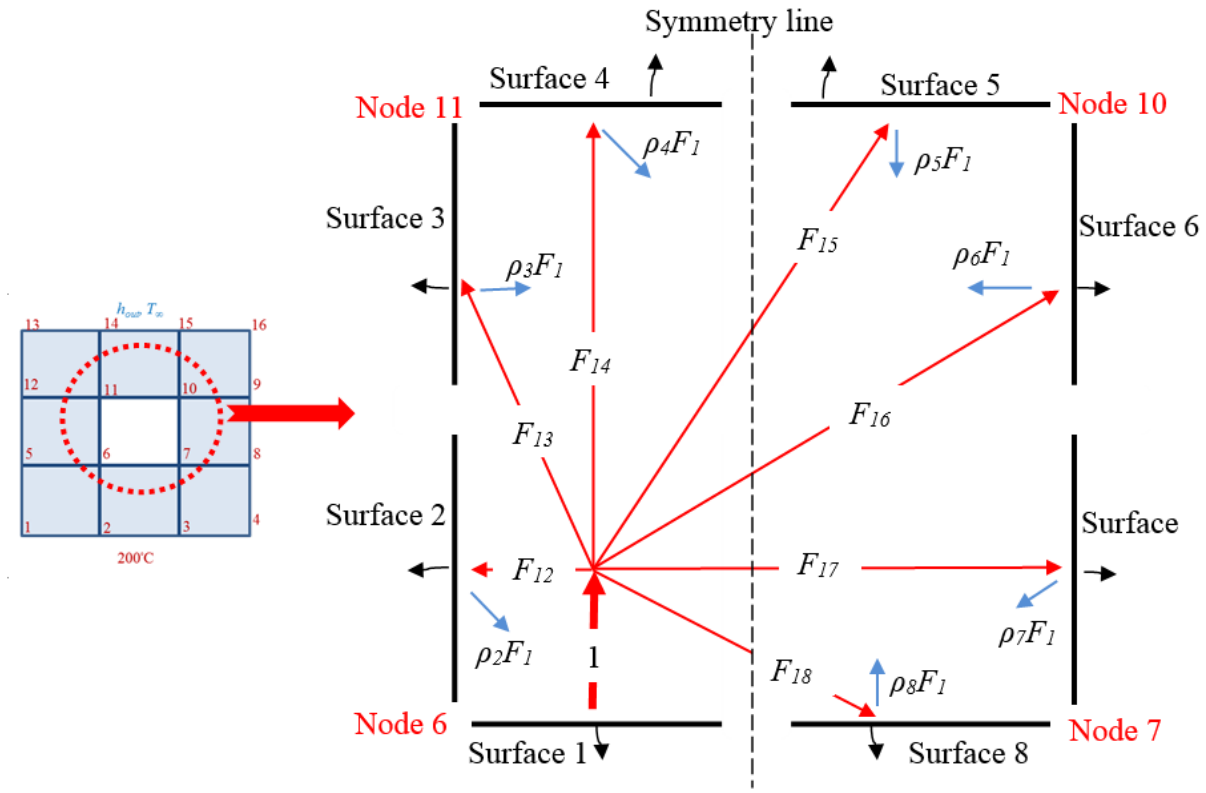

Figure A.1-10 Schematic for radiation heat exchange inside the benchmark void

Gebhart defined the absorption factor B_{ij} as the fraction of the energy emitted by the *i*th surface which is eventually absorbed by the *j*th surface after a complex reflection pattern [92, 93]. Hence, the net radiation that leaves surface *i* is

$$q_i = w_i A_i - B_{1i} w_1 A_1 - B_{2i} w_2 A_2 - \ldots - B_{ji} w_j A_j \qquad \textbf{A.1-13}$$

According to the definition of the Gebhart factor, the expression for B_{ij} is

$$B_{ij} = \varepsilon_j F_{ij} + B_{1j} F_{i1} \rho_1 + B_{2j} F_{i2} \rho_2 + \ldots + B_{ij} F_{ij} \rho_j \qquad \textbf{A.1-14}$$

where ε, ρ and F are emissivity, absorption factor and view factor, respectively. $F_{ij}\rho_j$ appears in almost every term. Therefore, to make the equation simple to program, $F_{ij}\rho_j$ is replaced by K_{ij}.

In order to solve the finite difference equation for nodes 6 and 11 (Eq.**Error! Reference source not found.** and Eq. **Error! Reference source not found.**), it is essential to calculate the heat radiation (q_i) leaving or striking the void surfaces. Hence, to find the net

radiation (q_i), Eq. **Error! Reference source not found.** is rearranged for surfaces 1 to 4 (**Error! Reference source not found.**). The rearranged equations for these surfaces are

$$\begin{aligned}
q_1 / A &= w_1 - B_{11}w_1 - B_{21}w_2 - B_{31}w_3 - B_{41}w_4 - B_{51}w_5 - B_{61}w_6 - B_{71}w_7 - B_{81}w_8 \\
q_2 / A &= w_2 - B_{22}w_2 - B_{12}w_1 - B_{32}w_3 - B_{42}w_4 - B_{52}w_5 - B_{26}w_6 - B_{72}w_7 - B_{82}w_8 \\
q_3 / A &= w_3 - B_{13}w_1 - B_{23}w_2 - B_{33}w_3 - B_{43}w_3 - B_{53}w_5 - B_{63}w_6 - B_{73}w_7 - B_{83}w_8 \\
q_4 / A &= w_4 - B_{14}w_1 - B_{24}w_2 - B_{34}w_3 - B_{44}w_4 - B_{54}w_5 - B_{64}w_6 - B_{74}w_7 - B_{84}w_8
\end{aligned} \qquad \textbf{A.1-15}$$

To solve the system of equations (Eq. **Error! Reference source not found.**), values of absorption factor (B_{ij}) and the emitted radiation (w_i) need to be determined. To calculate B_{ij}, Eq. **Error! Reference source not found.** is rearranged for Surface 1. The rearranged equations give a linear system of equations with eight unknowns which are expressed as

$$\begin{aligned}
(K_{11}-1)B_{11} + K_{12}B_{21} + K_{13}B_{31} + K_{14}B_{41} + K_{15}B_{51} + K_{16}B_{61} + K_{17}B_{71} + K_{18}B_{81} &= -\varepsilon_1 F_{11} \\
K_{21}B_{11} + (K_{22}-1)B_{21} + K_{23}B_{31} + K_{24}B_{41} + K_{25}B_{51} + K_{26}B_{61} + K_{27}B_{71} + K_{28}B_{81} &= -\varepsilon_2 F_{21} \\
K_{31}B_{11} + K_{32}B_{21} + (K_{33}-1)B_{31} + K_{34}B_{41} + K_{35}B_{51} + K_{36}B_{61} + K_{37}B_{71} + K_{38}B_{81} &= -\varepsilon_3 F_{31} \\
K_{41}B_{11} + K_{42}B_{21} + K_{43}B_{31} + (K_{44}-1)B_{41} + K_{45}B_{51} + K_{46}B_{61} + K_{47}B_{71} + K_{48}B_{81} &= -\varepsilon_4 F_{41} \\
K_{51}B_{11} + K_{52}B_{21} + K_{53}B_{31} + K_{54}B_{41} + (K_{55}-1)B_{51} + K_{56}B_{61} + K_{57}B_{71} + K_{58}B_{81} &= -\varepsilon_5 F_{51} \\
K_{61}B_{11} + K_{62}B_{21} + K_{63}B_{31} + K_{64}B_{41} + K_{65}B_{51} + (K_{66}-1)B_{61} + K_{67}B_{71} + K_{68}B_{81} &= -\varepsilon_6 F_{61} \\
K_{71}B_{11} + K_{72}B_{21} + K_{73}B_{31} + K_{74}B_{41} + K_{75}B_{51} + K_{76}B_{61} + (K_{77}-1)B_{71} + K_{78}B_{81} &= -\varepsilon_7 F_{71} \\
K_{81}B_{11} + K_{82}B_{21} + K_{83}B_{31} + K_{84}B_{41} + K_{85}B_{51} + K_{86}B_{61} + K_{87}B_{71} + (K_{88}-1)B_{81} &= -\varepsilon_8 F_{81}
\end{aligned} \qquad \textbf{A.1-16}$$

The above system of equations (Eq. **Error! Reference source not found.**) is coded in MATLAB and solved monolithically. The emitted radiation (w_i) in Equation **Error! Reference source not found.** is the net radiation emitted by each surface and it can be calculated using

$$w_i = \varepsilon\sigma T_i^4 \qquad \textbf{A.1-17}$$

where T_i is the average temperature of the *i*th void surface. The above equations for surfaces 1 to 4 are coded in MATLAB. The magnitude of q in Eq. **Error! Reference source not found.** is updated in each time increment.

A.1.1 Finite Element Method

As mentioned previously, the benchmark problem is also simulated in ABAQUS which uses FEM. The software has a built-in solver for cavity radiation, which can deal with coupled transient radiation-conduction problems. **Error! Reference source not found.** is used for the geometry of the simulation and the thermal properties of the model are taken from **Error! Reference source not found.**. A constant temperature of 200°C is applied to the bottom surface of the model. A Surface Film interaction (convection boundary) is assigned to the top surface of the model. The Sink (ambient) temperature and Film (convection) coefficient are set to 25°C and 80 W/m^2, respectively.

The heat transfer within the intumescent coating is a nonlinear problem because the material properties are temperature dependent and the boundary conditions (radiation and convection) are functions of surface temperature. ABAQUS uses an iterative scheme to solve nonlinear heat transfer problems. The scheme uses the Newton's method with some modifications to improve stability of the iteration process [47]. The time period for the simulation is set to 600s. The time increment size is fixed to 1s which is equal to the time increment size in the FDM study. The maximum allowable temperature change per increment is 10°C. A 4-node linear heat transfer quadrilateral element is used for the simulation. The mesh size is set to be the same as the mesh size in the FDM study (12mm). To consider the combined effect of convection, a Film (convection) interaction is assigned to the void surfaces. The Film interaction definition requires two parameters to simulate heat transfer by convection, the Film (convention) coefficient and the Sink (ambient) temperature.

A.1.2 FORTRAN Subroutine

ABAQUS is not capable of predicting the enclosed air temperature based on the void surface temperature. Therefore, a FORTRAN subroutine is developed and linked to

ABAQUS to estimate the gas temperature based on the void surface to enable ABAQUS to simulate convection within the void. Eq. **Error! Reference source not found.** is used to predict the enclosed air temperature.

The FORTRAN subroutine consists of two parts. The initial part introduces the relevant theories used for estimating the gas temperature. The latter part illustrates the techniques used to code the subroutine. An energy equation balance is set for the node's void surface (see **Error! Reference source not found.**). This equation reads

$$hA(T_1^i - T_g^i) + hA(T_2^i - T_g^i) + hA(T_3^i - T_g^i) + hA(T_4^i - T_g^i) = \rho Vc \frac{T_g^{i+1} - T_g^i}{\Delta t}, \qquad \text{A.1-18}$$

$$hA(\sum T_m^i - 4T_g^i) = \rho Vc \frac{T_g^{i+1} - T_g^i}{\Delta t}$$

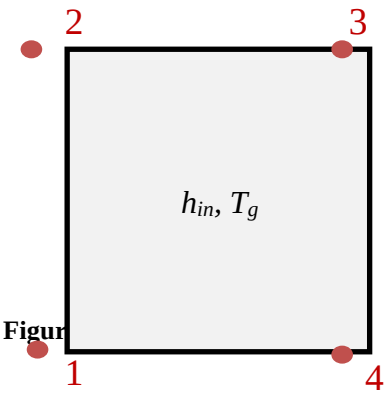

Figur

In Eq. **Error! Reference source not found.** the gas temperature is predicted from the node temperature at the pervious time step. This equation is included in the subroutine in order to estimate the enclosed air temperature. To adapt Eq. A.4-5 and simulate the convection within the void four different steps must be followed in the following order:

1. Temperature at the nodes of the void should be read from the output file at each time increment.
2. These temperatures should be substituted in Eq. **Error! Reference source not found.** to obtain the gas temperature at the next time step.
3. The calculated gas temperature should be assigned to the ambient temperature.

4. The calculated gas temperature should be passed to the next time increment and substituted in Eq. **Error! Reference source not found.**.

ABAQUS is set to write the temperature of the void nodes in an output file (.fil file). The .fil file can be opened and read with a URDFILE subroutine. Therefore, a URDFILE subroutine is implemented within the FORTRAN subroutine to open the output file and read the temperatures of nodes 1 to 4 (see **Error! Reference source not found.**) at each time increment. A FILM subroutine is the only subroutine which can assign a gas temperature and convection coefficient to the enclosed air temperature. Thus, a FILM subroutine is written to follow the URDFILE subroutine to enable CAE to compute convection. For each void surface node, a COMMON block is defined and the temperature of each node is allocated to the corresponding COMMON block.

The gas temperature is calculated and assigned to the enclosed air in the FILM subroutine. To calculate the gas temperature, Eq. **Error! Reference source not found.** is included in the FILM subroutine. Eq. **Error! Reference source not found.** consists of five variables. Four of these variables are the temperatures of the nodes around the square void and the fifth variable is the gas temperature at the previous time step. The temperature of each node is passed from the URDFIL subroutine with COMMON blocks and a new COMMON block is defined in the FILM subroutine to pass the value of the gas temperature from the previous time step to the next time increment.

The next section in the code is the assignment of the calculated gas temperature to the enclosed air. A SINK variable in the FILM subroutine represents the ambient temperature. Hence, the SINK variable is set to the calculated temperature. Additionally, the SINK variable is set to be equal to the relevant COMMON block to pass the value of the enclosed air temperature to the next time increment.

A.3 NUMERICAL RESULTS

This section illustrates the numerical results of the finite element and finite difference study of the benchmark model. **Error! Reference source not found.** shows the numerical results for bench mark model simulation. **Error! Reference source not found.**.a shows the temperature contour plot of the model estimated using FEM. **Error! Reference source not found.**.b-**Error! Reference source not found.**.d represents the temperature variations of nodes 6, 11 and 14. The red and black lines represent the FDM and FEM results, respectively. It is clear that the two are in good agreement.

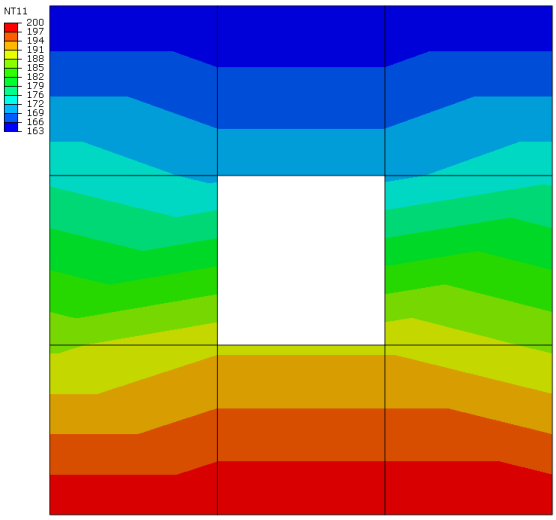

(a) ABAQUS temperature countour plot -°C

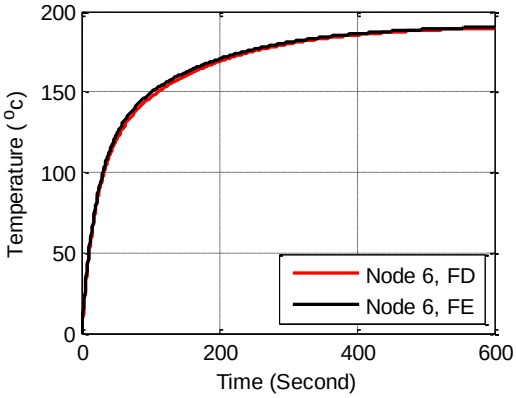

(b) Temperature history - node 6

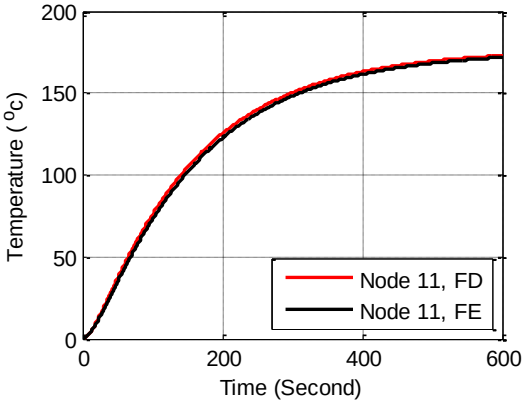

(c) Temperature history - node 11

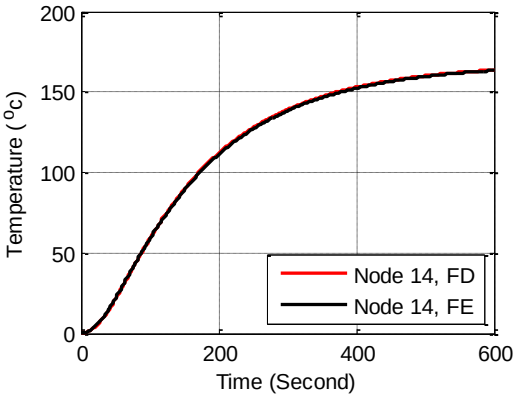

(d) Temperature history – node 14

Figure A.3-1 Square numerical results, heat transferred by radiation and convection inside the void

APPENDIX B - LIST OF PUBLICATIONS

- H.Atefi, A.Nadjai, F.Ali. (2017) Numerical and Experimental Investigation of the Structural Behaviour of Perforated Beams at Elevated Temperatures, *International Fire Safety Symposium. Italy. June 2017.*
- H.Atefi, A.Nadjai, F.Ali. (2017) Numerical and Experimental Investigation of the Thermal Behaviour Coated Cellular Beams with Intumescent Coating at the Elevated Temperature. *International Fire Safety Symposium. Italy. June 2017.*
- H.Atefi, S.Choi. (2012) Numerical Thermal Analysis of Intumescent Coatings, Using ABAQUS. Poster presentation section 2nd Asian Clay Conference, Korea.